Deformation behavior of Al-Al and Al-Cu laminated materials produced by Accumulated Extrusion

Gokula Krishna MURALIDHARAN

Supervisors:
Prof. Bert Verlinden
Prof. Marc Seefeldt

Members of the Examination Committee:
Prof. Omer Van der Biest (Chairman)
Prof. Jef Vleugels
Prof. Martine Wevers
Prof. Leo Kestens (U Ghent)
Prof. Kim Vanmeensel

Dissertation presented in partial fulfilment of the requirements for the degree of **Doctor of Engineering Science: Materials Engineering**

February 2018

Uitgegeven in eigen beheer, Gokula Krishna MURALIDHARAN, Leuven, Belgium

Summary

Plastic deformation is the process by which metals can be refined to enhance their microstructure and mechanical properties. Severe plastic deformation helps in achieving this in an effective manner by producing ultra-fine grained (UFG) microstructure materials. Every deformation process has a signature on the materials being deformed and it controls their grain refinement and texture properties. They in turn regulate the mechanical properties as well. A proper understanding of this and a correlation of the applied process with the material properties will help in having good control over the process and the desired material properties.

Accumulated Extrusion (AccumEx) is a novel SPD technique that has been introduced for the first time in this thesis. The processing technique was evaluated using experiments on commercially pure Al and Cu. The first study was done on Al-Al laminates. Stacks of Al were deformed up to 8 deformation passes. At the end of 8 passes, an UFG microstructure with an average equivalent grain size of 0.9 µm with high angle grain boundaries (HAGB) fraction of 70 %, and a texture with combination of plane strain compression and shear components were obtained. The mechanical properties were good only till 4 passes with a yield strength of near 200 MPa and elongation to failure of 6 %. Both the grain size and the hardness saturated after 4 passes. The process induced severe strain inhomogeneities within the material and they increased as the number of deformation passes was increased.

The effect of process induced shear on Al laminates was studied using the embedded-pin technique combined with continuum mechanics. True shear strains were derived to be a function of sample thickness after 1 pass and they accumulated after every deformation pass. They had a significant effect on the texture and microstructure of the material after 1 deformation pass, which were characterized using the EBSD technique.

Grain size saturation was studied with the help of ex-situ plane strain compression tests coupled with spatial EBSD characterization. Grain size saturation was found to be a microstructure accommodative phenomenon driven by mechanisms such as grain splitting/pinching and triple junction motion.

AccumEx was applied as a co-deformation technique for the production of Al-Cu laminated materials. The composite was fabricated in two configurations and deformed up to 4 AccumEx passes. Irrespective of the configuration type, the interfaces had a detrimental effect on the material's mechanical properties above 2 passes. The process produced an UFG microstructure in the Al part of the composite but a relatively coarser microstructure in the Cu part of the composite, due to strain inhomogeneities. The strain inhomogeneities developed due to the difference in the hardening properties between Al and Cu. It instigated complex interactions between the materials and thereby influenced the microstructure, texture and the hardening properties of Al.

AccumEx was compared with the most established SPD process - Equal Channel Angular Pressing (ECAP). AccumEx could produce an UFG microstructure in a comparatively rapid manner and the final properties were also comparable with each other. However, AccumEx was successful only up to 4 passes in Al-Al laminates and up to 2 passes in Al-Cu laminates which limited its ability as a successful SPD process only till medium high strains.

Samenvatting

Plastische vervorming is een proces waarbij de microstructuur van metalen verfijnd kan worden, waardoor hun mechanische eigenschappen verbeteren. Door middel van sterke plastische vervorming (SPD) kunnen ultra-fijne korrels (UFG) bekomen worden. Elk vervormingsproces laat een handtekening na in het materiaal waarop het toegepast wordt en bepaalt de verfijning van de korrels en de ontwikkeling van de textuur. Deze bepalen op hun beurt de mechanische eigenschappen. Inzicht in de relaties tussen het gekozen vervormingsproces en de eigenschappen van het materiaal helpt om een goede controle over het proces en de beoogde materiaaleigenschappen te bekomen.

Geaccumuleerde extrusie (AccumEx) is een nieuwe SPD techniek die in deze thesis voor het eerst beschreven wordt. De techniek werd experimenteel toegepast op Al en Cu met een commerciële zuiverheid. Het eerste deel van het onderzoek werd uitgevoerd op Al-Al laminaten. Al stapels werden tot hoogstens 8 passen vervormd. Een UFG microstructuur met een gemiddelde equivalente korrelgrootte van 0.9 µm met 70 % hoge hoek korrelgrenzen (HAGB) werd bekomen. De textuur bevatte zowel componenten van vlakke vervorming compressie als van afschuiving. De intensiteit van de afschuivingscomponent werd sterker van zodra 4 of meer passen uitgevoerd werden. De mechanische eigenschappen waren goed tot 4 passen. Zo werden een vloeispanning van 200 MPa en een vervorming bij breuk van 6 % behaald. Zowel de korrelverfijning als de hardheid namen niet sterk meer toe bij een verhoging van het aantal passen.

Het effect van procesgeïnduceerde afschuiving op Al laminaten werd bestudeerd aan de hand van een combinatie van de embedded-pin techniek en continuümmechanica. De ware afschuivingsvervorming bleek afhankelijk te zijn van de dikte van het monster na 1 pas en accumuleerde na elke vervormingspas. Door middel van de Electron BackScatter Diffraction (EBSD) techniek werd aangetoond dat de ware afschuivingsvervorming een significant effect had op de textuur en de microstructuur van het materiaal na 1 vervormingspas.

Met behulp van ex-situ vlakke vervorming compressietesten gekoppeld met EBSD karakterisatie, werd bestudeerd waarom de korrelverfijning na enkele vervormingspassen niet meer toenam. De microstructuur bleek zichzelf te herschikken zonder korrelverfijning. Dit proces werd gecontroleerd door mechanismen zoals korrelsplijting en beweging van triple junctions.

AccumEx werd toegepast als co-vervormingstechniek voor de productie van Al-Cu laminaten. Dit composiet werd geproduceerd in twee configuraties en vervormd tot hoogstens 4 passen. Onafhankelijk van de configuratie hadden de grensvlakken een erg negatieve invloed op de mechanische eigenschappen zodra meer dan 2 vervormingspassen toegepast werden. Het AccumEx proces produceerde een UFG microstructuur in het Al deel van het composiet maar een relatief grove microstructuur in het Cu deel van het composiet. Dit was te wijten aan inhomogeniteiten in vervorming. Die werden veroorzaakt door het verschil in versteviging tussen Al en Cu.

AccumEx werd vergeleken met het meest gebruikte SPD proces - Equal Channel Angular Pressing (ECAP). AccumEx bleek sneller een UFG microstructuur te produceren en de eigenschappen van het uiteindelijke materiaal waren vergelijkbaar met die na ECAP. AccumEx kon maar toegepast worden tot hoogstens 4 passen bij Al-Al laminaten en hoogstens 2 passen voor Al-Cu laminaten, waardoor het als SPD techniek beperkt blijft tot matig hoge vervormingen.

Acknowledgements

This doctoral thesis was performed under the framework of IAP7/21 project – INTEMATE. I am grateful to BELSPO and to all the members of the IAP committee for the funding and inputs throughout my PhD. I would also like to thank MTM and KU Leuven for hosting me during this period.

I would like to offer my immense gratitude to my promoters, Prof. Bert Verlinden and Prof. Marc Seefeldt, who have strengthened this thesis with all the necessary scientific reinforcements isotropically. It is from them that I have learnt to approach research in the right way and acquired scientific intuition and decision-making skills in research. Their revered knowledge in the field of metals and deformation gave me an opportunity to explore a variety of aspects in this field which enabled me to not only acquire in-depth knowledge in the field but also diversify myself by applying this knowledge to other inter-disciplinary domains as well. My current job position at 3DSystems would not have been possible without all these.

My sincere thanks to all the members of my Examination committee, Prof. Jef Vleugels, Prof. Martine Wevers, Prof. Leo Kestens, Prof. Kim Vanmeensel and Prof. Omer Van der Biest for participating as the jury of my preliminary and public defense and providing their valuable remarks and feedback to the betterment of my thesis.

My research colleagues/friends, namely Diarmuid, Joris, Sathish, Jeroen, Xiebin, Ling and Xiaodong have been very helpful during my research. All the valuable chats with them have benefited me in different parts of my thesis. I would also like to extend a special thanks to Diarmuid for his contribution and for accepting to collaborate in some parts of my work. It was a great pleasure working with all of them.

I owe all that I have learnt in EBSD characterization to Tom Van der Donk, the electron microscopy expert at MTM and I thank him very much for this. Joop van Deursen and his magic mind always had a principal role in most of the PhD theses at MTM. For mine as well, he was instrumental in bringing all the technological ideas into reality. I would also like to thank Paul Crabbe for his assistance in metallography. He is absolutely indispensable despite the arrival of several automated techniques for the sample preparation. Besides them, I would like to extend my sincere thanks to all the other MTM technical assistants as well, for being there for me at different moments during my PhD. Also, a special thanks to Huub for all the administrative support during the past 7 years of my stay in MTM.

A number of colleagues/friends were part of my journey in this PhD. I am grateful to all of them. I would like to mention few special ones – Nachi, M&M, Andrea, Kim, Thomas, Suraj, Karel, Bey, Gaurav, Bensu, Nicolo and Miquel from MTM; Lore, Jan, Anh Dung, Pierre, Anthony, Wim, Inigo, Gautier, Sam, Wojciech, Peter, Manisha and Maxime from 3DSystems. I am very happy to have them all around me. They have brought in a lot of positive energy at my work. Let us continue that way in the future as well.

I would like to extend my heartfelt thanks to my most beloved friends - Hari, Mars and Susarans. They have been a very supportive family for me during all the tough and happy times. I will always remember and relish all the fun and fruitful moments that we shared together. Of course, a lot more to come as well. Special thanks to my other besties – Deepan, Prabhu, Venky, Sam, Ravi and Arun for all their support. I would also like to thank my ex-roomies and friends – Ilaya and Ashwin for all the nice moments during the period of my stay together with them.

Saving the best for the last and as dramatic as always, I would like to converge my happiness, thankfulness, gratitude and all my positive emotions and extend them to my mom and dad. I am non-existent (literally and otherwise) without them. I owe all my endeavors to them for they live my life more than theirs. Dear mom and dad: whatever I am now is because of you and just for you, I will become better, wiser and stronger.

Gokula Krishna Muralidharan
February 2018

List of symbols and abbreviations

σ	*A stress*
σ_{gb}	*Grain boundary surface tension*
C_y	*Strengthening constant*
d, D	*Grain size*
τ	*Shear stress*
λ	*An angle, grain boundary spacing*
m	*Schmid factor, mobility*
$\bar{M}$	*Taylor factor*
$\dot{\gamma}_s$	*Strain rate*
$\Theta, \phi, \psi, \varphi$	*An angle*
γ	*Shear strain, Grain boundary energy*
V	*velocity*
ε	*strain*
A_0, A	*Area*
n, N	*Number*
G	*Shear modulus*
b	*Burgers vector*
f_{lagb}	*Fraction of LAGB boundaries*
ρ	*Dislocation density*

AcccumEx	*Accumulated Extrusion*
ARB	*Accumulative Roll Bonding*
BCC	*Body Centred Cube*
CDRX	*Continuous Dynamic Recrystallization*
CP	*Commercially Pure*
CRB	*Cold Roll Bonding*
CRSS	*Critical Resolved Shear Stress*
CVD	*Chemical Vapour Deposition*
DMMC	*Deformation processed Metal-Metal Composites*
EBSD	*Electron Back Scatter Diffraction*
ECAP	*Equal Channel Angular Pressing*
ED	*Extrusion Direction*
EDS	*Energy Dispersive Spectroscopy*
ER	*Extrusion Ratio*
FCC	*Face Centred Cube*
FIB	*Focussed Ion Beam*

GBS	*Grain Boundary Sliding*
GNB	*Geometrically Necessary Boundaries*
HCP	*Hexagonally Closed Packed*
HPT	*High Pressure Torsion*
IDB	*Incidental Dislocation Boundaries*
LEDS	*Low Energy Dislocation Structures*
ND	*Normal Direction*
ODF	*Orientation Distribution Function*
PM	*Powder Metallurgy*
PSC	*Plane Strain Compression*
PVD	*Physical Vapour Deposition*
SEM	*Scanning Electron Microscope*
SFE	*Stacking Fault Energy*
SIBM	*Stress Induced Boundary Migration*
SPD	*Severe Plastic Deformation*
TD	*Transverse Direction*
U.T.S	*Ultimate Tensile Strength*
UFG	*Ultra-Fine Grained*
XRD	*X-Ray Diffraction*
YS	*Yield Strength*

Table of Contents

1. Introduction

1.1. History

Plastic deformation of metals is a classical field in metallurgy which has been in use for several thousands of years. Shaping of metals was part of man's livelihood since Bronze age and Iron age. At that time the main applications were weapons. As mankind evolved into a civilized set-up, new metals and alloys were discovered and the process of harnessing the ability of metals for desired applications became an important necessity. In the modern advanced era, it is termed as thermo-mechanical processing of metals and it deals with the science and engineering of shaping and forming of different classes of metals for desired microstructure and strength. Newer aspects were/are added to this field with the invention of several scientific methodologies combined with the increased knowledge gain of mankind. The process of understanding the behavior of material, assessing the strength of the shaped metals, the interrelationships between strength, microstructure, crystallography and process design are the subjects of widely performed scientific research in this domain. Some of the prominent discoveries which should be remembered for the advancement of this field are – Metallography by H.C. Sorby in mid-19th century [1], X-ray diffraction in early 20th century by the Braggs [2], use of dislocations for plastic deformation by Egon Orowan, Michael Polanyi, G.I Taylor in 1934 [3,4], Hall-Petch relation by Hall and Petch in mid-20th century, etc. With industrialization and globalization growing at its pace, processing of metals has been made more easy with mechanized set-ups. Even as a step further, the use of additive technologies has also begun to mark its territory in par with the established subtractive technologies.

1.2. SPD and its scientific journey

The process of Severe Plastic Deformation a.k.a SPD is an attractive field of study and has been in research for more than 60 years. The technique is inspired from the history of sword making which dates back to 300 BCE [5]. Wootz, Damascus, etc., were the historically famous swords known for their superior strength. However, in the modern era, it started when the Nobel laureate Bridgman reported in 1943 that[6],

"If a bar is twisted while a longitudinal compressive load is simultaneously applied, it is possible to twist the bar through much greater angles without fracture than is possible without the compressive load. At the same time the magnitude of the torque which the bar can support without fracture is increased."

The primary focus of his work was to study the effect of extreme pressures on metals. He was awarded the Nobel prize in physics for his discoveries in the field of high pressure Physics. Based on his observation and the historical significance from sword making, the field of SPD became of prime interest among the scientific community. Equal Channel Angular Pressing (ECAP) and High Pressure Torsion (HPT) are the first SPD techniques which were reported. The aim of SPD is to obtain nano-structured or ultra-fine grained materials and it works with the general principle of metal working. SPD combines materials processing through hydrostatic pressure and shear deformation. In definition form it is [7],

"SPD is a *metal forming method with extensive hydrostatic pressure and shearing conditions that imposes high strain and produces exceptional grain refinement in the bulk material"*.

It is categorized as a top-down approach to produce nanostructure/ultra-fine grain metals on a bulk scale. The advantage of SPD is that the dimensions of the nanostructured materials produced by SPD are comparable with real size structural applications unlike the bottom up approaches such as CVD, PVD, etc. In addition, the ability of the process to obtain materials with superior mechanical properties has made the field of study broader. Several follow up studies were performed over the past 3 decades. They can be generalized into two domains – (i) process development; (ii) study of material behavior in SPD.

The process development research was and still is focused on developing new SPD processing techniques. Some of the prominent ones were derivatives of other standard deformation processes such as – rolling, extrusion, compression, etc. Some of the techniques were also targeted on utilization of the SPD's ability in producing high strength high ductility materials in continuous processing industrial applications. However, most of them were only successful in lab setting. Examples of applications for SPD processed materials can be seen in the automotive and the aerospace sectors [7]. The main focus of the other research domain is on understanding the material behavior during SPD. A metal undergoing SPD evolves into a nanostructured material with several modifications in its microstructure and texture. They are very important to be understood and to correlate with their mechanical and other physical properties, depending on the applications. So, in parallel with the process development, lots of focus went also on understanding the SPD processes, their impact on the material behavior and the final properties. Some of the most widely studied SPD techniques are Equal Channel Angular Pressing (ECAP), High Pressure Torsions (HPT) and Accumulative Roll Bonding (ARB).

1.3. Enhanced properties in materials produced by SPD

Nanostructured materials have become scientifically and technologically very important in the world of industries. The use of nanostructured materials has become very common in microelectronics, surface engineering, aerospace, bio-medical and other advanced structural and functional applications. They have unique structural properties with exceptional mechanical strength, toughness, fatigue life, wear resistance, etc., making them suitable candidates for advanced engineering applications. Nanostructured materials are widely produced by chemical and powder metallurgy (PM) routes. It is commonly called a bottom-up approach. However, the general problems with materials produced through such techniques are that they are brittle and expensive. Owing to these problems, SPD offers a good alternative approach. With the help of SPD, bulk scale nanostructured materials can be produced with similar superior properties [7-11].

The dependence of strength on grain size was discovered and published in the 1950s by Hall and Petch which is now commonly known as the Hall-Petch relationship,

$$\sigma_y = \sigma_0 + C_Y d^{-1/2} \tag{1.1}$$

where, σ_y is the yield strength, σ_0 is a material yield stress to overcome the resistance to dislocation movement in a pure lattice without grain boundaries, C_Y is the strengthening constant and d is the mean grain size. The factor -1/2 is found mainly for smaller grain size systems.

Thus, from the above equation, it is clear that the materials' yield strength increases when the average grain size is reduced. So, improving the strength of metals is possible with a significant amount of grain refinement. However, maintaining the ductility at the same time is a great challenge. The use of SPD has helped in partially accomplishing this as well [7-15].

Strength and ductility are the major concerns for use of metals in structural applications. Metals which are processed by conventional cold working, increase their strength by strain hardening, but their ductility is severely compromised. On the other hand, materials processed by SPD show a similar increase in strength together with appreciable elongation properties. This was published by Valiev et al. as the *Paradox of strength and ductility in metals processed by severe plastic deformation* [16]. Figure 1-1 and Figure 1-2 give a few examples from this article. Figure 1-1 shows the strength and elongation (elongation to failure) properties of nanostructured Ti and Cu processed by SPD in comparison with the coarse-grained conventional cold rolled materials. It shows that materials processed by SPD achieve superior properties with good combination of strength and ductility. Figure 1-2 gives one such comparison of the strength and ductility of SPD processed (ECAP) and cold rolled copper (Figure 1-2(a)) and aluminium alloys (Figure 1-2 (b)). ECAP provides room to undergo deformation to higher strains without failure compared to its conventional cold-rolling counterpart. The yield strength in both cases shows an increase but for the SPD processed material, the ductility is not compromised [8,9]. Some of the SPD processing techniques which have been commonly used are presented in Appendix A. Each processing route follows a unique pattern in achieving the UFG material.

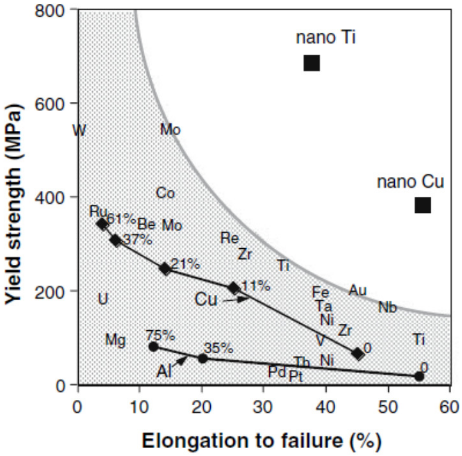

Figure 1-1 Superior tensile properties observed in SPD processed nano Ti and Cu [17].

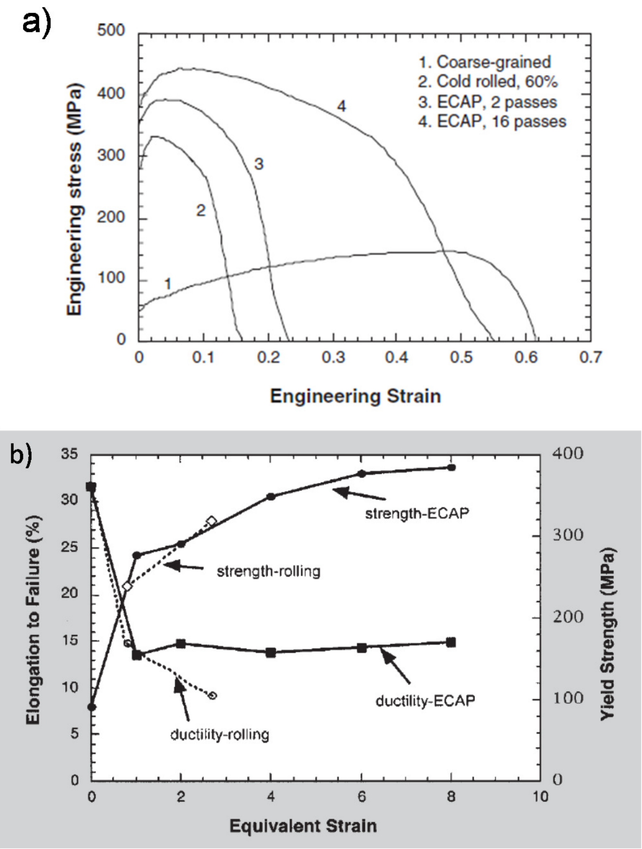

Figure 1-2 Comparison of ECAP and rolling on the yield strength and failure elongation (a) Copper, (b) Al alloy [17]

1.4. Accumulated Extrusion and thesis outline

Accumulated Extrusion or AccumEx, a plane strain compression deformation process is a derivative of a conventional extrusion process and works on a principle similar to Accumulative Roll Bonding (ARB). It is a novel severe plastic deformation process, introduced for the first time in this thesis [18]. The special design of the process will help in accumulating strain and in achieving ultra-high deformation strains within the sample. More details about the technique will be discussed in chapter 3, where the general information about the different processing techniques and characterization techniques which have been used in the thesis will also be presented. The necessary scientific prelude on mechanisms and concepts associated to plastic deformation and material properties which have been used in the thesis is briefly discussed in chapter 2. Besides, the thesis can be divided into two sections – AccumEx as SPD and AccumEx as co-deformation process.

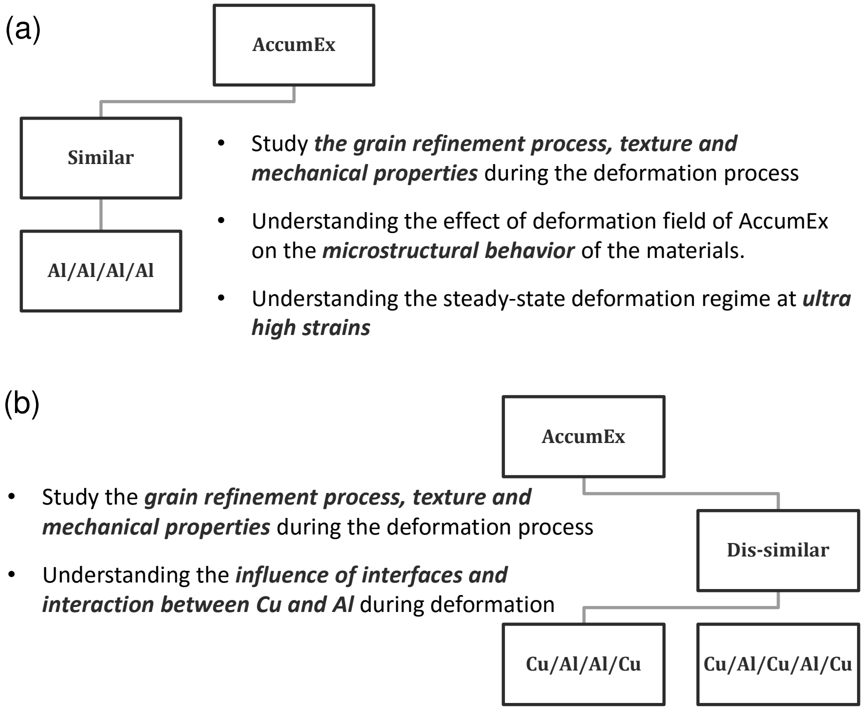

(a)

- Study ***the grain refinement process, texture and mechanical properties*** during the deformation process
- Understanding the effect of deformation field of AccumEx on the ***microstructural behavior*** of the materials.
- Understanding the steady-state deformation regime at ***ultra high strains***

(b)

- Study the ***grain refinement process, texture and mechanical properties*** during the deformation process
- Understanding the ***influence of interfaces and interaction between Cu and Al*** during deformation

Figure 1-3 Experiment matrix and the concept map applied in the thesis - (a) Similar materials; (b) Dissimilar materials and a short overview on their corresponding scientific approaches.

The main problem statement of the thesis is how AccumEx can be used as a SPD technique. And if that would be possible, what will the microstructure evolution, texture and mechanical properties be like? To start to answer this, an experiment matrix as shown in Figure 1-3 is planned using CP AA 1050 material and commercially pure oxygen free copper. The experiments are divided in to two sections – using similar and dissimilar materials. The choice of Al and Cu is due to the available vast literature knowledge and easy processing.

In chapter 4, the Al alloy is processed by AccumEx up to 8 deformation passes. It corresponds to an equivalent von-Mises strain of almost 13 and it produces more than 65000 interfaces within a sample thickness of 5 mm. The material is characterized for its microstructure, texture and mechanical properties from the initial condition till 8 passes. The results and observations obtained from this chapter motivated to take forth two interesting aspects for further study – 1. Deformation field of AccumEx, 2 – Microstructural accommodation mechanism of UFG material. They form chapter 5 and 6 respectively.

Each deformation technique has its signature on the material being processed. Similarly, AccumEx also has one. In Chapter 5, the deformation field of AccumEx is derived and its impact on microstructure and texture is studied. A new experimental procedure has been used for this – the embedded pin technique. It is an old technique to obtain information about the deformation field in rolling. However, in this work this has been adapted for AccumEx by coupling with continuum mechanics. A successful correlation of the calculated deformation field with the experimental microstructure and texture results has been made. Chapter 6 is a brief study on examining the accommodation processes of the UFG microstructure at extreme straining conditions. One of the striking observations obtained from chapter 4 is that the grain size saturates during the AccumEx processing after 4 passes. It is a common phenomenon in SPD and is termed as steady-state deformation regime. Till now, no proper understanding of this regime could be found in literature and remains almost an unknown territory, with very few experimental studies. In an effort to understand this process regime, ex-situ plane strain compression tests coupled with EBSD characterization have been performed on a grain size saturated sample. The microstructural changes at different strain increments are studied spatially and different accommodation mechanisms that can possibly be responsible for the saturation behavior have been proposed.

AccumEx produces layered or laminated materials. The magnitude of strain that is imposed by the process in a single deformation pass is around 75 % and is very high. This gives a possibility for using AccumEx in processing and producing dissimilar laminated/composite materials. In chapter 7, this is explored by deforming together commercially pure Al and Cu in two different configurations – Cu/Al/Al/Cu and Cu/Al/Cu/Al/Cu. Their microstructure, texture and mechanical properties are characterized and their interaction behavior is also studied.

Later in Chapter 8, the obtained microstructure and mechanical properties using AccumEx for both Al and Cu will be compared with the properties obtained through ECAP, for the same material. Finally, the general conclusions are presented in chapter 9 with possible suggestions and potential ideas for future work.

REFERENCES

1 Sorby, H. C. On the microscopical structure of crystals, indicating the origin of minerals and rocks. *Quarterly Journal of the Geological Society* **14**, 453-500 (1858).

2 Bragg, W. H. & Bragg, W. L. The Reflection of X-rays by Crystals. *Proceedings of the Royal Society of London. Series A* **88**, 428 (1913).

3 Orowan, E. Zur Kristallplastizität. III. *Zeitschrift für Physik* **89**, 634-659, doi:10.1007/bf01341480 (1934).

4 Taylor, G. I. Plastic strain in metals. *J. Institute of Metals* **62**, 307-324 (1938).

5 LANGDON, G. T. *Processing by Severe Plastic Deformation: Historical Developments and Current Impact*. *Materials Science Forum* **667-669**, 9-14 (Trans Tech, 2011).

6 Bridgman, P. W. Flow Phenomena in Heavily Stressed Metals. *Journal of Applied Physics* **8**, 328-336, doi:doi:http://dx.doi.org/10.1063/1.1710301 (1937).

7 Valiev, R. Z., Islamgaliev, R. K. & Alexandrov, I. V. Bulk nanostructured materials from severe plastic deformation. *Progress in Materials Science* **45**, 103-189, doi:http://dx.doi.org/10.1016/S0079-6425(99)00007-9 (2000).

8 Valiev, R. Nanostructuring of metals by severe plastic deformation for advanced properties. *Nat Mater* **3**, 511-516 (2004).

9 Lowe, T. & Valiev, R. The use of severe plastic deformation techniques in grain refinement. *Journal of Materials Science* **56**, 64-68, doi:10.1007/s11837-004-0295-z (2004).

10 Estrin, Y. & Vinogradov, A. Extreme grain refinement by severe plastic deformation: A wealth of challenging science. *Acta Materialia* **61**, 782-817, doi:10.1016/j.actamat.2012.10.038 (2013).

11 Valiev, R. Z. The new trends in fabrication of bulk nanostructured materials by SPD processing. *Journal of Materials Science* **42**, 1483-1490, doi:10.1007/s10853-006-1281-3 (2007).

12 Valiev, R. *et al.* Producing bulk ultrafine-grained materials by severe plastic deformation. *Journal of Materials Science* **58**, 33-39, doi:10.1007/s11837-006-0213-7 (2006).

13 Verlinden, B. Severe plastic deformation of metals. *Metallurgija* **11**, 165-182 (2005).

14 Divinski, S. V., Padmanabhan, K. A. & Wilde, G. Microstructure evolution during severe plastic deformation. *Philosophical Magazine* **91**, 4574-4593, doi:10.1080/14786435.2011.615349 (2011).

15 Azushima, A. *et al.* Severe plastic deformation (SPD) processes for metals. *CIRP Annals - Manufacturing Technology* **57**, 716-735, doi:10.1016/j.cirp.2008.09.005 (2008).

16 Valiev, R. Z., Alexandrov, I. V., Zhu, Y. T. & Lowe, T. C. Paradox of Strength and Ductility in Metals Processed Bysevere Plastic Deformation. *Journal of Materials Research* **17**, 5-8, doi:10.1557/jmr.2002.0002 (2011).

17 Zhu, Y. & Langdon, T. The fundamentals of nanostructured materials processed by severe plastic deformation. *Journal of Materials Science* **56**, 58-63, doi:10.1007/s11837-004-0294-0 (2004).

18 Muralidharan, G. K. and B. Verlinden (2016). "Novel severe plastic deformation technique—accumulated extrusion (AccumEx)." Materials Science and Technology: **32**(6), 547-555**.**

2. Literature Study

2.1. Deformation induced grain refinement – general principles

During plastic deformation, big grains break into small grains. This is commonly called ‘grain splitting’ and it has become a very popular field of study. Grain splitting leads to grain refinement and this is a key for increasing the strength of the metals. The process of breaking the grains has been identified to follow specific patterns and it is dependent on two major parameters – material and process. Material parameters are specific to the natural properties of the material and the process parameters are externally imposed variables through deformation. Irrespective of these parameters, the fundamental basis of grain refinement is provided by dislocations. They are the carriers of plastic deformation which provide the final structure of the grains depending on the material and the process parameters. According to Low Energy Dislocation Structures (LEDS) theory, it is believed that a material system which undergoes deformation always results in the most energetically favorable final microstructure [1]. Dislocations are line defects which are classified as edge, screw or mixed. The formation, interaction, annihilation, accumulation of these carriers, depending on the material’s basic property and the process conditions in the least energy expensive manner defines the final microstructure of the material after deformation. By varying each material parameter and process parameter, an enormous variety of microstructures can be achieved.

2.1.1. Materials parameters

2.1.1.1. Crystal structure and texture - a brief recap

Plastic deformation in metals usually proceeds by slip and twinning. Slip is a crystallographic phenomenon which occurs by the movement of dislocations over some crystal planes. These crystal planes are called slip planes. During deformation, dislocations are driven by the resolved shear stresses acting on their slip planes. When the magnitude of the shear stress reaches a critical value, slip will start. It is strictly plane and direction specific. Generally, the slip planes are the planes with the highest atomic packing density and the slip direction is the closest packed direction in that plane. They are represented together as slip systems. The critical resolved shear stress at which slip can be activated is the point of onset of plastic deformation and thus controls the yield strength of the material. Similarly, twinning is another crystallographic mechanism of plastic deformation but usually less dominant in metals, compared to slip. Twinning occurs by movement of atoms in a part of the crystal, which forms a mirror symmetry with the other part of the crystal. The plane of symmetry is represented as the twinning plane. Compared to slip, twinning is very localized and cannot satisfy the gross externally applied deformation strain, on itself. So, twinning is normally said to be seen only when there is lack of slip systems to accommodate the deformation or for some reason the critical resolved shear stress for the activation of slip system increases. It can be called as a secondary process and is commonly seen in HCP metals and in cubic metals when deformed at high strain rates or at cryo temperature [2,3].

The slip systems which are responsible for plastic deformation are crystal structure specific. It is known that there are in total 7 crystal systems and 14 Bravais lattices. Each lattice structure has its own sets of unique slip systems. The most common Bravais lattices which are used for metals are – FCC, BCC and HCP. FCC has 12 possible slip systems, BCC has 48 possible slip systems and HCP has 3 basal slip systems and sometimes additional prismatic and pyramidal ones depending on the c/a ratio. Depending on the available number of slip systems, the resistance to plastic deformation varies. For example, HCP with high c/a ratio has the lowest number of slip systems because of which they show low ductility in general and in most cases, extensive twinning.

Activation of slip systems involves the onset of plastic deformation and it greatly varies as a function of crystal orientation. For cubic systems, a crystal orientation can be represented for instance, as a plane-direction pair, in relation to the process reference frame. For example, consider a single crystal is being subjected to uniaxial tensile deformation. The crystal orientation of the single crystal will be given as <uvw> // tensile direction. Here the plane is not important because the constraint is along one single direction only. In another example, say rolling, where the same single crystal is constrained in two directions, the plane which is parallel to the rolling plane is also necessary for reference and the single crystal according to the process reference frame will be represented as {hkl} <uvw>, where {hkl} is parallel to rolling plane and <uvw> is parallel to rolling direction. Therefore, depending on the configuration of the crystal structure with respect to the applied principal stresses, the magnitude of the translated shear stresses on the slip planes will vary. The values of these resolved stresses can be analytically calculated, which was first given by Schmid, as presented in equation (2-1) [2,4]. To activate slip on the specific crystal orientation, the magnitude of shear stress, τ should be greater than or equal to τ_{CRSS}. Alternatively, this can be represented in terms of Schmid factor (m, equation (2-2). The Schmid factor helps in comparing the resistances between different crystal orientations to slip under a unique deformation mode, thereby gives an indication of which particular crystal orientation can slip faster over the others. The rule of thumb is, orientations with higher Schmid factor can slip easily and vice versa.

$$\tau = \cos\varphi . \cos\lambda . \sigma \tag{2-1}$$

$$m = \cos\varphi . \cos\lambda \tag{2-2}$$

Where τ is the shear stress acting on the slip plane, σ is the applied stress, m is Schmid factor, φ is the angle of the slip plane normal to the deformation axis, λ is the angle which the slip direction makes with the deformation axis.

So far, everything is discussed assuming the material is a single crystal. For polycrystalline materials, each grain or crystal orientation will have a unique Schmid factor for the imposed macroscopic constraint. This makes it difficult to know when the material begins to deform. Addressing this, two theories were introduced and debated – Sachs and Taylor theory [5-7]. In short, Sachs proposed that for a polycrystal an average of the Schmid factors of all possible random crystal orientations can be used as a good approximation to derive the theoretical yield strength for a polycrystal. It is called the iso-stress assumption. On the contrary, Taylor proposed that all the grains within the polycrystal must undergo the same amount of shape change as in the macroscopic state and therefore iso-strain is the fair assumption. For the former, it was noticed that the laws of continuity get defied and 3-dimensional defects will be generated. Therefore, the Taylor theory became the basis for the further understanding of the response of polycrystalline materials to deformation. However it has to be noted that Taylor theory violates stress equilibrium.

According to the Taylor theory, based on the rule of incompressibility, for each crystal orientation or here the grain, five independent slip systems are needed to accommodate any geometrically imposed shape change. In special cases, it can be achieved with fewer slip systems as well, depending on the degree of constraints and the morphology of the grains. The choice of the 5 slip systems is made by the minimum shear principle. This helps in deriving a relationship between the cumulative slip rates and the yield stress of the material. The ratio of the macroscopic stress and the critical resolved shear stress is defined as the Taylor factor for a given orientation and strain mode. A simplified form of this relation is shown in equation (2-3). Formally it resembles the inverse of the Schmid factor, under the reference frame of the externally imposed constraints. A crystal orientation with small Taylor factor can deform more easily than the one with larger Taylor factor.

$$\overline{M} = \frac{\sigma}{\tau_{crss}} \qquad \text{(2-3)}$$

Where $\overline{M}$ is the average Taylor factor, σ is the macroscopic stress and τ_{crss} is the critical resolved shear stress of all slip systems.

This expression can be useful in predicting the onset of yield for the material. However, once the yielding commences both $\overline{M}$ and τ_{crss} evolve and therefore the value of σ will change as well. This is because the crystal orientations change continuously during the deformation, due to lattice rotation. It is a prime aspect in the understanding of texture evolution. During plastic deformation of a polycrystal or single crystal by slip, the slip planes rotate to the most favorable configuration to minimize plastic work. When a single crystal material is deformed by uniaxial tension without lateral constraints, the gliding of planes will occur freely. However, under constraint at both ends, the slip planes tend to rotate during the deformation process to the most favorable orientation such that the material can accommodate the shape change and strain in a least energy expensive manner. Under such circumstances, the crystal orientation changes as the strain increment increases and therefore, the Schmid factor and the Taylor factor also constantly vary. This leads to de(re)-activation of slip system(s) with strain increments. The reorientation of the grains is given as lattice rotation. Together, the slip and the lattice rotation constitute the texture evolution. In the aspect of continuum theory, the process has been represented at crystal scale as a local velocity gradient tensor (l_{ij}). The local velocity gradient tensor can be decomposed into two parts – symmetric strain rate and anti-symmetric rotation rate (equations (2-4) and (2-5)). When the local velocity gradient is equated to the macroscopically imposed deformation mode (this will be discussed in the later section), one can solve for the slip rates and sub-sequentially the lattice rotation. Solving for the slip rates involves a proper choice of a series of assumptions and on itself is a vast field of study. Taylor, ALAMEL, VPSC, etc., are some of the successful models which have shown experimentally agreeable results[5,8-10].

$$d_{ij} = \sum_{s} \frac{1}{2}\left(M_{ij}^{s} + M_{ji}^{s}\right)\dot{\gamma}_{s} \tag{2-4}$$

$$\omega_{ij} = \mathrm{W}_{ij}^{l} + \sum_{s} \frac{1}{2}\left(M_{ij}^{s} - M_{ji}^{s}\right)\dot{\gamma}_{s} \tag{2-5}$$

Where, d_{ij} is the symmetric component of the velocity gradient tensor that comprises information of the strain, $\dot{\gamma}_s$ is the shear rate or slip rate on the sth slip system, M_{ij}^{s} is the geometric Schmid tensor associated with the slip system, ω_{ij} is the anti-symmetric rotational component of the velocity gradient tensor that comprises information of rate of rigid body rotation, W_{ij}^{l} and the rate of lattice rotation.

The distribution of the crystallographic or lattice orientations is thus of a prime importance for understanding the material's response to the applied plastic deformation and is commonly represented as pole figures, inverse pole figures and ODFs.

2.1.1.2. Stacking fault energy (SFE)

A stacking fault is defined as a defect or irregularity in the stacking sequence of the planes of a crystal structure. The energy associated with the planar irregularity is called SFE. It has an influence on the width of the stacking fault. A material with a high SFE only shows a few small SF. In case of a low SFE its stacking faults are wider. Stacking faults are included between partial dislocations. These dissociated partials show a different dislocation motion from normal slipping and alter the mobility of the dislocations. When the materials' SFE is high, the decomposition of the dislocations in two partials is unfavorable. This constraints the dislocation to move only along normal slip planes and directions and facilitates cross-slip along intersecting planes. On the other hand, when the SFE is low, the decomposition of dislocations into partials is favored. This lowers the mobility of the dislocations and in some cases facilitates twinning. All of them affect the deformation behavior of the material which is reflected in the type of grain substructures being formed. High SFE metals normally produce a deformation sub-structure which is a mosaic or cellular type while low SFE metals show banded sub-structures with linear arrays of dislocations. Properties such as strain hardening, texture evolution, ductility, grain refinement are closely interconnected with it. From one of the old studies of Hirsch et al., [6] the response of FCC metals with different SFE at different strains is described in Table 2-1. And from one of the recent studies [11], the influence of SFE on strain hardening rate as function of true strain for a similar starting grain sized material is also shown in Figure 2-1.

Table 2-1 - Characteristics of microstructure as function of stacking fault energy and strain [6]

SFE Strain	*High (Al)*	*Medium (Cu)*	*Low (High zinc brass)*
1. Low 0.1<ε<0.5	Grain elongation Deformation bands Equiaxed cells	Grain elongation Deformation bands Equiaxed cells Microbands	Grain elongation Deformation bands Stacking faults Deformation twins
2. Medium 0.5<ε<1.0	As above	As above Some clustering and alignment of microbands	As above Some alignment of twins Shear bands at higher strains
3. High ε>1	As above	As for 1 Extensive microband alignment and clustering Shear bands	As for 1 Twin alignment Continuing replacement of twinned structure by shear bands

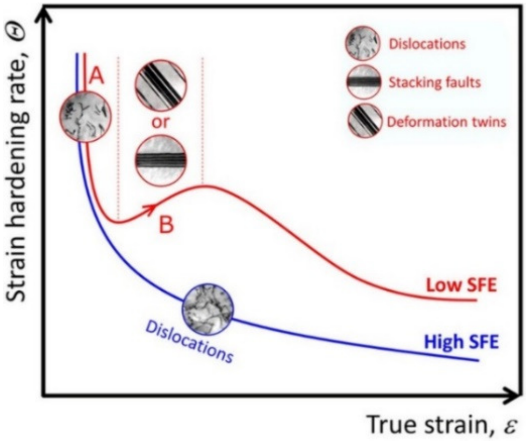

Figure 2-1 – Strain hardening behavior of low and high SFE materials. (A, B) are related to two typical strain-hardening stages of FCC materials with low SFE. Deformation patterns of dislocations, stacking faults and deformation twins are shown in inserts for different stages [11] .

2.1.1.3. Purity or solute effect

Purity or solute content is another material parameter that changes the material's response to applied deformation. Addition of alloying elements normally modifies the host material in two ways – solid solution formation and precipitate formation. For both cases, the secondary alloying elements affect the interaction of dislocations and their mobility. When the elements are in solution, the room temperature mobility or the activation energy required for the mobility of the dislocation is altered and when the elements are present in the form of precipitates, they hinder the motion of dislocations (depending on the type of the precipitates). Brass is a famous example for the former and precipitate or age hardened Al alloys are common examples for the latter.

In case of brass, the amount of alloying element (Zinc) modifies the SFE [6,12]. This directly modifies the deformation behavior of the material which is seen in the form of extent of twinning. Further, this also reflects in the type of texture, deformation sub-structures, rate of grain refinement and the mechanical behavior of Brass. Figure 2-2 shows, how the volume fraction of the Cu texture component changes as a function of Zn content and therefore strongly influences the anisotropy of the mechanical properties of the material after rolling. Other similar examples are – Al-Mg alloys, Al-Cu alloys, etc.

In case of age-hardened alloys, in general the precipitates act as barriers for dislocation motion and promote heterogeneous deformation behavior in their vicinity. The barriers increase the CRSS of the materials and modify the strain hardening properties. On a global scale, they directly affect the grain refinement process by modifying the rate of formation of sub-structures, their response to external process parameters such as temperature through (recovery and recrystallization), texture and mechanical properties of the material [13].

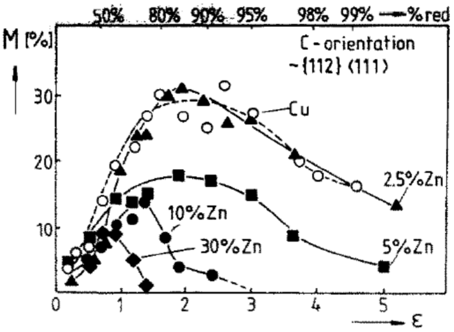

Figure 2-2 - Volume fraction, M_i of the C component {112}<111> in % as a function of the rolling strain for different CuZn alloys [6]

2.1.2. Process parameters

2.1.2.1. Deformation mode

The deformation mode is an external boundary condition which is imposed to the material subjected to plastic deformation. In terms of continuum theory, it is normally represented in a 3x3 matrix called the macroscopic velocity gradient tensor (L_{ij}). It can be decomposed into a stretch part (D_{ij}) and a spin part (W_{ij}), as presented in equations (2-6) and (2-7). Each deformation process can be macroscopically represented in the form of the velocity gradient tensor. Two of the most relevant deformation modes in the context of the thesis are pure shear and simple shear. They are shown in Figure 2-3 (A) [14]. Plane strain compression is an example of pure shear deformation and torsion is an example of simple shear deformation. Both the deformation modes are vastly employed in several SPD techniques – ARB is an example of pure shear and ECAP is an example of simple shear.

$$D_{ij} = \frac{1}{2}\left(L_{ij} + L_{ji}\right) \tag{2-6}$$

$$W_{ij} = \frac{1}{2}\left(L_{ij} - L_{ji}\right) \tag{2-7}$$

The two deformation modes have a different impact on the grain refinement process. As the local velocity gradient depends on the macroscopic velocity gradient, the choice of slip systems, slip rate, etc., will be very different and this gets directly reflected in the rate of grain refinement, hardening, texture evolution and the morphology of the grains. From a comparative study by Bhadeshia et al [15], a graph is presented in Figure 2-3 (B) which shows the rate of evolution of high angle grain boundaries. The calculations were done by theoretical modelling using principles of stereology and by applying homogeneous deformations to a tetrakaidecahedra in a variety of orientations. A simple shear mode requires an equivalent strain of 8.7 to achieve a similar grain boundary fraction (S_v/S_{v0}) which is achieved after equivalent strain of 3 after rolling. Higher strains are required to achieve a similar HAGB fraction when processed in simple shear mode. This gives a glimpse of how each deformation mode has its signature in the process of grain refinement. It should be noted that the above study was performed based on the assumption that the deformation is homogeneous and the effect of deformation bands, shear bands or other grain-subdivision mechanisms which gives rise to new mis-orientation boundaries were not taken into account.

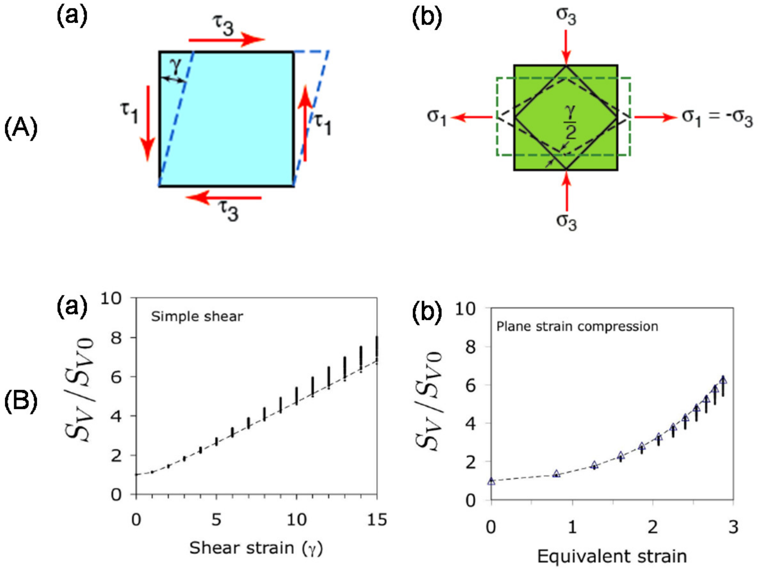

Figure 2-3 –(A) Schematic representation of simple shear (a) and pure shear (b) deformation modes [14]; (B) comparison of theoretically calculated geometrical changes in grains during (a) a simple shear process and (b) a plane strain compression process [15]. S_V/S_{V0} is the ratio of current over initial grain surface area per unit volume.

Of equal importance, the microscopic deformation field also influences the behavior of the material. It was presented in section 2.1.1.1 that to solve for the slip rates, in the Taylor model the local velocity gradient tensor is equated to the macroscopic velocity gradient tensor, $l_{ij} = L_{ij}$. However, this is not always true. Grain boundaries, deformation sub-structures and other entities in the microstructure are sites of dislocation interactions. The interactions affect the local stress field and in turn modify the local velocity gradient[5,16] and therefore, $l_{ij} \neq L_{ij}$. The effect of these local heterogeneities is usually assumed to be negligible for large grained materials (>100 µm), but as the material undergoes grain refinement and approaches towards UFG structures, this becomes very important in the process of continuous microstructural and texture evolution. Knowing the exact microscopic deformation field is difficult, but keeping into account the heterogeneity will help in understanding the microstructure of the material[17].

2.1.2.2. Temperature

Temperature is another important process parameter that affects the grain sub-structure evolution during grain refinement. Deformation processes can be performed at different temperatures – room temperature, cryo temperature, medium or high temperature. In the context of SPD, most of the processes are performed either at room temperature or at medium temperature. Higher processing temperature reduces the CRSS of the material for slip activation. Therefore, yielding occurs at lower stresses.

Besides, the mobility of dislocations increases and therefore more destructive interaction of dislocations are favored. They deter strain hardening and depending on the temperature, softening can also be favored. The softening of the material at high temperature regime is commonly described in three stages as recovery, recrystallization and grain growth. The first two will be of great relevance in the current context. Recovery is an internal energy reduction process that occurs at medium temperature range (usually $<0.4T_m$) to reduce excess stored energy that is usually present in the form of non-equilibrium lattice defects. When this process occurs during deformation simultaneously, it is termed dynamic recovery. Dynamic recovery is a common phenomenon in high SFE material at room temperature deformation to high strains. For low SFE materials, it is seen at medium processing temperatures. For understanding reasons, it can be stated the dynamic recovery works by setting a threshold value on the amount of energy stored within a specific material for a specific processing condition. The internal energy of the grains are not allowed to increase above this threshold value and is facilitated by annihilation of dislocations or rearrangement of dislocations into cellular structures forming low energy configurations, coalescence and sub-grain growth, etc. Dynamic recovery is very difficult to analyze experimentally as it occurs simultaneously with the deformation. However, it is believed to play a significant role in achieving UFG structures during SPD[13,18-21].

Similar to recovery, recrystallization is another high temperature mechanism which contributes to softening of the material. Usually, it is said to occur when a deformed material is subjected to temperatures above $0.4T_m$. The conventional static recrystallization involves nucleation of new grains which grow and replace the high energy neighboring sites. When this occurs during deformation, it is called dynamic recrystallization. With respect to the degree of strain and temperature involved, DRX has been reported by several authors based on different underlying mechanisms. They are called as - Discontinuous dynamic recrystallization, continuous dynamic recrystallization, geometric dynamic recrystallization [13].

Dynamic discontinuous recrystallization is pertinent to deformation processes which are carried out at temperatures above the recrystallization temperature ($>0.4T_m$). It is similar to static discontinuous recrystallization but occurs during the deformation simultaneously. New grains are formed by nucleation and growth of the recrystallization orientation components (for eg., cube in case of FCC) and they will eventually get deformed in the process. It occurs discontinuously. The driving force for the nucleation is difference in stored energy. The nucleation can occur at grain boundaries, at the precipitate affected zones, at deformation bands, at shear bands, etc [18,22].

Continuous dynamic recrystallization is a special category of recrystallization which some prefer not to classify as a recrystallization process but as extended recovery or in-situ recrystallization. The occurrence of such a phenomenon has been mainly reported for SPD processed materials. It is an elastic strain driven process. During deformation, the sub-grains which are formed at the low strains, through progressive rotation increase their misorientation with the neighboring sub-grains which eventually leads to conversion of the sub-grains into individual grains separated by HAGB. The exact driving force and the detailed mechanism of this process is still unclear but it has been counted as one of the dominant mechanisms for achieving fine grain equiaxed grain structures during SPD processing of metals [18,20].

Geometric dynamic recrystallization is another process which is commonly reported for Al and Al alloys, at high strains. During deformation, especially by rolling, grains become lamellar or flattened with formation of sub-structures. Subsequently at high strains, when the thickness of the grains approaches the size of the sub-grains, serrations are induced on the original high angle grain boundaries. These serrations may pinch off and results in smaller grain structures. They resemble the recrystallized grains, but this process should not be confused with the conventional recrystallization process[13,22].

2.1.2.3. Strain path

In the context of SPD, the strain path is another important process parameter that has an influence on the grain refinement and especially the final morphology of the grains. It can be described with the help of one of the famous examples from ECAP. ECAP processing is an established technique for grain refinement. It can be performed in three different routes – A, B and C. Each route has a different strain path and for each route, the rate of microstructure evolution varies, although the imposed magnitude of strain is the same. The details of them will be discussed in section 2.3.1. The strong dependence on strain path is said to be due to the changes in the strain hardening characteristics of the material facilitated by dislocation interactions and lattice strain. More information about this can be seen in the Ph.d. thesis of Van Boxel [23], and other strain path change studies [24-27].

2.2. Microstructure evolution

2.2.1. The general scheme

Aluminium is one of the most studied materials in terms of understanding the grain refinement process. It has been investigated for over 5 to 6 decades and several important contributions have been made that explain the evolution of grain (sub) structures as a function of material and process parameters. A generalized stage by stage process of grain refinement in commercially pure Al can be written as

1. Accumulation of dislocations.
2. Dislocation interactions and formation of a heterogeneous structure with regions of varying dislocation densities.
3. Re-arrangement of dislocations to form Geometrically Necessary Boundaries (GNBs) and Incidental Dislocation Boundaries (IDBs) that together form a mosaic or a cellular structure
4. Continuous refinement of cells with increasing misorientation and formation of high angle grain boundaries (HAGB).

The four different stages occur at different strain regimes. The first two are common during the initial regime (0.1-0.2 strain), the third one at above 0.2 strain and the fourth one at strains above 0.5. It must be noted that the above generalization is after assuming the starting grain size of the deforming Al is big. For Al with smaller starting grain size, a shift and overlap of the events can occur [28].

The formation of sub-structures in Al is very heterogeneous. They are formed at different scales – intragranular and intergranular. During the low strains, the intra-granular structures - cells, cell blocks, dislocation walls, microbands, etc., are dominant and form the basis for the microstructure at higher strains [12,29-32]. Figure 2-4 shows an idealized microstructure of Al after deformation and the commonly observed components. Figure 2-4 (a) shows a cell block structure with dense dislocation walls and equiaxed cells. Figure 2-4 (b) shows the formation of such a cell block structure initiated by slip patterns [12]. Cells are locally homogeneous regions of similar slip activities. They are confined within cell-blocks and the cell-blocks are separated by dense dislocation walls or microbands. Cell blocks are the second-degree homogeneous regions within the grains which are delineated by planar dislocation structures. Each cell block deforms with less than five slip systems, and at the grain level, several such cell blocks collectively accommodate the macroscopic strain. The DDWs act as separator between these regions of different slip activity. They are generally termed as geometrically necessary boundaries (GNBs). Microbands are also GNBs. They are seen in Al as double walled boundaries surrounding the cell-blocks. They are formed due to localized shearing and arrangement of dislocations along {111} slip planes. The boundaries which are seen between the cells are termed as incidental dislocation boundaries (IDBs), which are believed to form from the tangled dislocations due to slip activities[33-37].

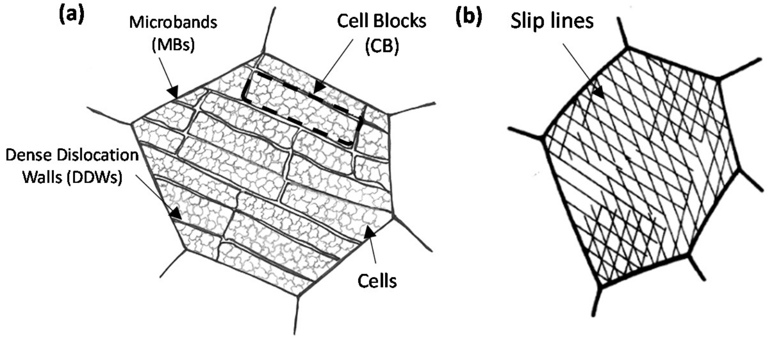

Figure 2-4 – (a) Schematic representation of the subdivision into cell blocks at low strain and (b) is a schematic of the slip line pattern that occurs within a gran that can lead to grain subdivision similar to that is shown in (a) [12]

Deformation bands and shear bands assist in formation of the grain sub-structures at intragranular level and sometimes at intergranular level as well. Examples of these are shown in Figure 2-5. They are not commonly seen at low deformation strains. Deformation bands separate big grains into banded regions and initiate lattice rotation by different slip activities. This eventually transforms the banded regions into different grains separated by grain boundaries. The characteristics of the formation of the deformation bands strongly depend on the parent crystal orientation. During rolling, this deformation banding is believed to contribute to the subdivision of the grains to form a lamellar microstructure [38-40]. Shear bands on the other hand are another category which occur due to strain localization. They are initiated due to local texture softening by rotation of primary slip planes to 45° with the compression direction. Shear bands are commonly seen to exist at 35 – 55° to the compression axis [41-43]. They facilitate local orientation changes which help in increasing the mis-orientation angle and formation of HAGB.

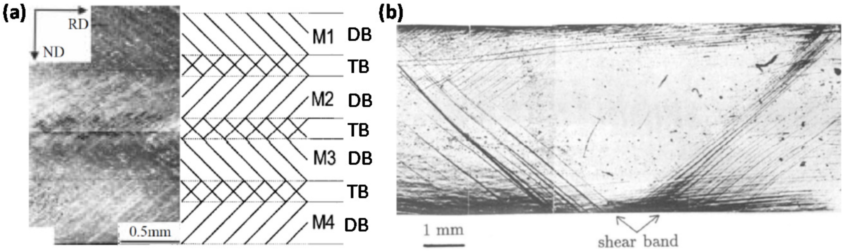

Figure 2-5 - (a) SEM channeling contrast image of cold rolled cube-oriented Al single crystal at 30 % strain and where the crystal split into deformation bands (DBs) (M1, M2, M3, M4) and transition bands (TBs) (regions in between the DBs) [38,39]; (b) Optical micrograph of shear band on the lateral face[44]

A general schematic of the process of transformation of big grains to smaller grained structures during rolling is shown in Figure 2-6, as reported by Humphreys et al. [28] Figure 2-6 (a) is the initial grain structure of Al with average grain size of diameter D_0. When a deformation is applied, the shape of the grains change according to the imposed constraints and the area fraction of grain boundaries increases. This is shown in Figure 2-6 (b) as a cellular structure. The size of the cell reduces with increasing magnitude of strain and subsequently or simultaneously, the misorientation between the cells also increases. Above strains of 1, a steady state is reached as the cell size approaches 0.2-0.5 µm. And subsequently, the misorientation between the sub-structures increase and some of the boundaries transform into medium and high angle boundaries. A lamellar microstructure is formed. Figure 2-6 (c) shows the formation of grain boundaries within the original grains. With continuous straining, to higher rolling strains, the original grain structure is completely modified and the spacing between the HAGB reduces till the size of the sub-grains. Figure 2-6 (d) shows the representative final microstructure. It is a fibrous structure, which should not be confused with the UFG structure obtained in SPD processes such as ECAP or HPT.

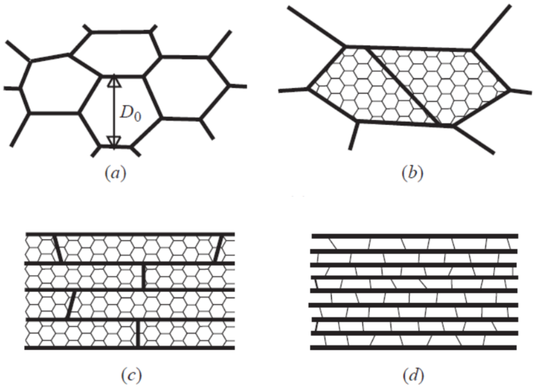

Figure 2-6 - Schematic diagram showing the development of microstructure with increasing strain by rolling; (a) Initial grain structure; (b) sub-grains and grain subdivision; (c) alignment of HAGB; (d) ribbon grain structure [28]

2.2.2. Microstructure after SPD

The main difference between the microstructures obtained from normal cold working and SPD is that the latter forms equiaxed UFG structures while the former takes the grain morphology specific to the applied deformation and is mostly anisotropic. Conventional cold working also produces near fine grained structures, however not effective enough to obtain HAGB equiaxed UFG as in SPD. In an example from [45], pure Al when deformed up to high strains by compression, shows similar grain size values as obtained after ECAP (1-1.2 µm). However, the morphological properties of the grains were not mentioned and it is highly possible that it would be anisotropic because of the unidirectional strain. The transformation of grains into equiaxed structures during SPD is a result of accumulating strain and the changes in the strain path imposed during processing. In conventional cold working, for eg., rolling, the GNBs which are formed during deformation are elongated in nature due to the defined process constraints. When these GNBs transform to a grain boundary, they remain elongated and therefore the equiaxed nature of the grain is destroyed (Figure 2-6). However, in SPD by imposing strain path changes, the elongated nature of the GNBs can be easily disrupted and depending on the strain path change, GNBs can be introduced in a three-dimensional manner. When such GNBs transform to HAGB, an equiaxed grain morphology can be obtained.

The development of the well-developed UFG equiaxed structures during SPD processing is not a single step process and occurs gradually by strain accumulation. In general, there is no established theory, as that of the grain sub-division models in cold working, to explain the formation of UFG equiaxed grain structures. The commonly used explanation involves grain sub-structures evolution, dynamic recovery and continuous dynamic recrystallization (CDRX). As mentioned in the previous section, CDRX is a local in-situ phenomenon driven by lattice rotations due to severe straining and is sometimes also referred as extended recovery. Dynamic recovery is a localized reduction in excess stored energy during the deformation process. Depending on the material's property, a combination of recovery and recrystallization drives the formation of the UFG material during SPD.

In the case of pure Al, dynamic recovery is dominant during room temperature deformation. This is because Al is a high SFE material. They favor cross-slip and therefore, the dislocations may annihilate locally. This dynamic annihilation nature does not allow enough dislocation accumulation and assists in forming cellular sub-structures during the initial deformation strains. These sub-structures later serve as a skeletal structure for the final UFG structure. This is said to be assisted by the process of CDRX. With repetitive deformation strains, the misorientation between the cellular sub-grains gradually increases due to strain accumulation and lattice rotations. This facilitates transformation of sub-grain boundaries into high angle grain boundaries which eventually leads to forming the UFG structures. An idealistic schematic explanation of this process has been described for HPT process by Liu et al. [46] and is presented in Figure 2-7. It is said that the size of the obtained final grain sizes is comparable with the size of the initially formed sub-structures.

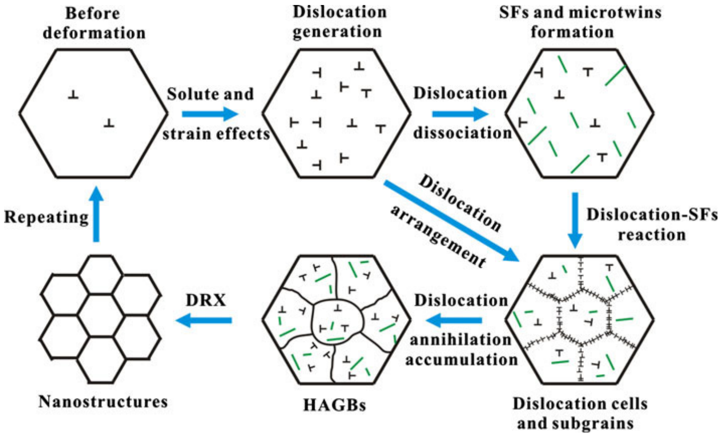

Figure 2-7 Schematic illustration of grain refinement process of Al alloys during HPT[46]

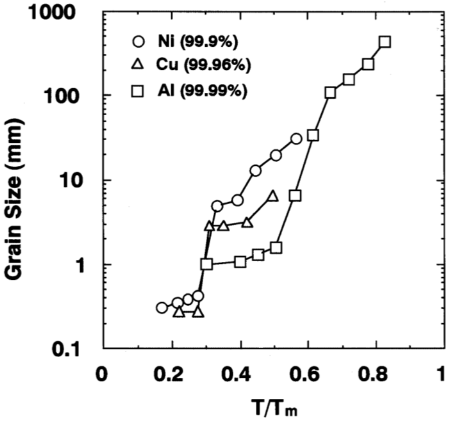

Figure 2-8 Grain size versus annealing temperature as a fraction of absolute melting temperature of pure Ni, Cu and pure Al after ECAP and annealing for 1 h[47]

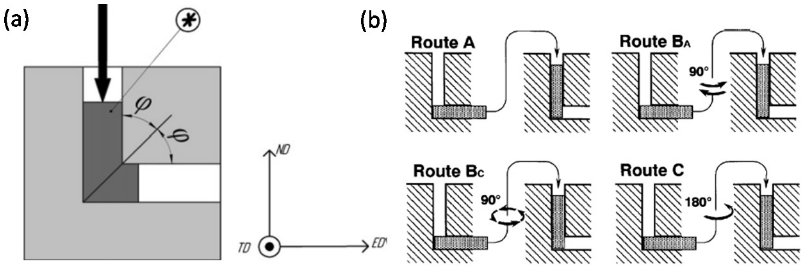

Figure 2-9-(a) Schematic of ECAP set-up [51]; (b) Different processing routes of ECAP[52]

Factors such as SFE, solute content, etc., modify the grain properties locally (as described in section 2.1.). An example on the effect of solute content can be explained from [45]. ECAP on pure Al and AA 6061 produced finer grain size for the latter than the former. Also, the saturation of hardness was much quicker and at lower equivalent strain in the pure Al than AA 6061. This is mainly because of precipitation hardening. Further, presence of precipitates provide resistance for dislocation motion and GNB movement. Therefore, the dynamic recovery property of Al is strongly hindered. This gives opportunity for higher dislocation accumulation and facilitates formation of finer sub-structures. When they gradually transform into grain boundaries by CDRX at extreme strains, a finer grain size is obtained compared to pure Al. As an example for the effect of SFE, a comparative graph on the obtained ECAP as-pressed grain sizes and grain sizes after 1 hour annealing at different homologous temperatures of Al, Cu and Ni is presented in Figure 2-8. Al has a SFE of 166 mJ/m^2, Ni has a SFE of 128 mJ/m^2 and Cu 78 mJ/m^2. From the figure, as the SFE reduces, a finer grain size can be obtained for similar magnitude of strains (at extreme range). Also, the change in grain size for different homologous temperature suggests that the stored energy is higher for low SFE material compared to high SFE material. This is because, for low SFE material, dynamic recovery is more difficult. This creates a complex sub-structure of dislocation network. At medium strains, these dislocation networks transform to GNBs and LAGBs and at large strains transform to high angle grain boundaries, thereby producing a finer grain size. Further, mechanisms such as deformation twinning are also favored which further facilitates grain size reduction. Therefore, SFE and purity play a major role in the grain size refinement. In many cases, addition of solutes also modifies the SFE of the material and therefore the nature of grain refinement also changes accordingly.

2.3. Comparison of SPD processes for Al

Commercial purity Al is one of the most studied materials in SPD [48,49]. Al is easily deformable and as such suitable to compare different SPD techniques under similar conditions. The most famous SPD techniques are – ECAP, HPT and ARB. Out of them, the most relevant ones are ECAP and ARB, which will be discussed in this section.

2.3.1. Al in ECAP

Equal Channel Angular pressing (ECAP) works on the principle of simple shear. ECAP is one of the most efficient techniques that can produce UFG and nanostructured Al. The ability of the process to impose large accumulative strains to the material assists the formation of UFGs. Hundreds of articles have been published on ECAP of Al. The schematic of the process is shown in Figure 2-9 (a). ECAP can be processed by 4 different routes and they are shown in Figure 2-9 (b). In the work of Iwahashi et al [50], high purity Al samples were processed by ECAP up to 4 passes. After each pass, the samples were sectioned and their microstructure was studied along three mutually perpendicular directions. The effect of strain path was also evaluated by performing the process in routes A, B_c and C. The respective change in grain size as function of the number of pressings along each plane and for the different routes was presented and is shown in Figure 2-10. The graph shows change in sub-grain size, grain size and combination of sub-grain and grain size as open, closed and half-open circular markers in function of number of pressings. It clearly shows that for route B the HAGB grains are formed at a faster rate compared to other routes. Route A is the slowest and route C is intermediate. This is because, the formation of substructures varied differently for different processing routes. The shearing pattern is different for each ECAP route and it influences directly the formation of the sub-structures and the grain refinement. It can be noticed that in route B, between the 3rd and the 4th passes, grain size along all the planes show a small increase in size. This was not explicitly addressed in the work. However, based on the understanding, one reason is that the observed difference can possibly be due to lack of enough statistics to infer an average, as the measurements were based on TEM micrographs. The other reason could be that the coarsening might have occurred because of the strain path change. Pass 4 has the same shear pattern as that of pass 1 which implies till pass 3, the imposed shearing pattern is compensated by rotation of 90° in its subsequent deformation, but as in pass 4 it starts over again, it would have resulted in a slight increase in the grain size along one of the directions.

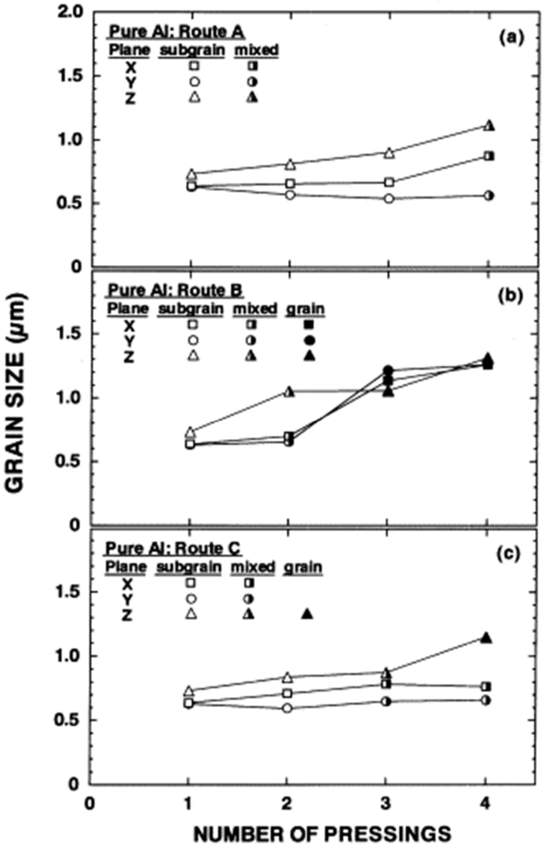

Figure 2-10- Different grain refinement patterns shown as change in grain size, sub-grain size and mixed along all sections of ECAP processed sample as function of number pressings[50].

In later work from several authors, the number of pressings was increased up to 8 and 16. As an example, some figures taken from the work of S. Poortmans[53] are presented in Figure 2-11. The evolution of the microstructure from the annealed state up to 16 passes of ECAP; route C is shown. The grain size reduced from 33 µm to less than 1 µm after 16 passes with equiaxed microstructure. Similarly, from another work by El Danaf et al., [24,54] the microstructures of Al after 8 passes of ECAP routes C and Bc were compared and it was reported that the average grain size obtained after route C is almost 1.5 to 2 times larger than after route B_c. Its corresponding effect was noticed in the mechanical properties as well, with Bc performing better than C. The yield strength of Al after 8 passes; Bc was 175 MPa and after 8 passes; C was 150 MPa.

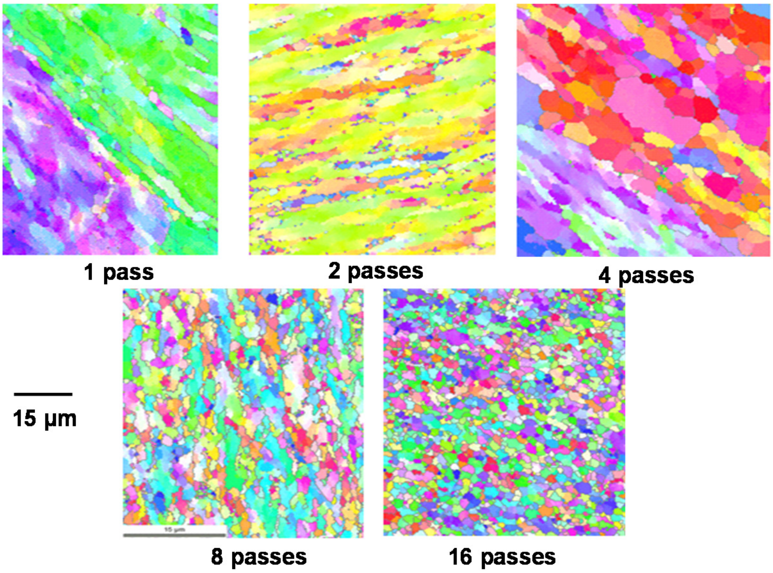

Figure 2-11 Microstructure evolution of AA 1050 processed by ECAP route C up to 16 passes [53]

The basis of grain refinement in the early passes of ECAP follows the path of the fundamental principles which was briefly described in sections 2.1 and 2.2. However, the formation of UFG structures greatly depends on the type of ECAP route and the magnitude of strains. The effect of strain path on microstructure during ECAP has been a very prominent field of study in the early 2000s. As mentioned in the earlier part of this section, each ECAP route exhibit different grain size and grain morphology. A work from Langdon [55] showed that for pure Al, an equiaxed grain structure can be easily attained using route B_c, at comparatively fewer number of passes. Similar results were obtained for other materials as well. This indicates the importance of the change in the strain path during deformation.

Strain path changes directly modify the strain hardening properties, dislocation interactions and the grain sub-structures of the material. By exploiting this in ECAP, the microstructures of the material can be partially tailored. A microstructure model suggested by Cheng Xu et al. [45] will be used to explain this. Each ECAP pass imposes a shear on the billet and the plane at which the shear is active is called as the macroscopic shear plane. When the billet is rotated (depending on the type of ECAP route) between every deformation pass, the orientation of the macroscopic shear plane within the billet gets varied. In this way, the accumulation of shear can be obtained at different angles with respect to the original configuration of the billet. The shear patterns imposed on the material after each ECAP pass for all the three routes along the three different planes of the billet are shown in Figure 2-12 (a). Corresponding to these shear patterns, the derived grain refinement on the X-Z plane of the billet will look as shown in Figure 2-12 (b). The red, mauve, blue and green lines indicate the orientation of the sub-structures which is linked to the direction of the primary slip plane during the ECAP 1, 2, 3 and 4 passes respectively. By comparing between all the three routes, route B_c has a higher total angular range of active slip systems. This suggests that the initial elongated GNBs oriented along the shear plane, gets fragmented by intersection of different slip systems due to the involved different macroscopic shear planes in the sub-sequent deformation passes.

This facilitates formation of a three-dimensional array of GNBs and therefore an equiaxed grain is obtained. Between route A and C, route A has slightly higher total angular range of active slip systems and therefore it has a less anisotropic grain structure than route C. Further, the grain refinement characteristics along the different planes of the billet also follow a similar pattern. The derivations from the described model showed a reasonable agreement with the experimental results, such that the model is now widely accepted.

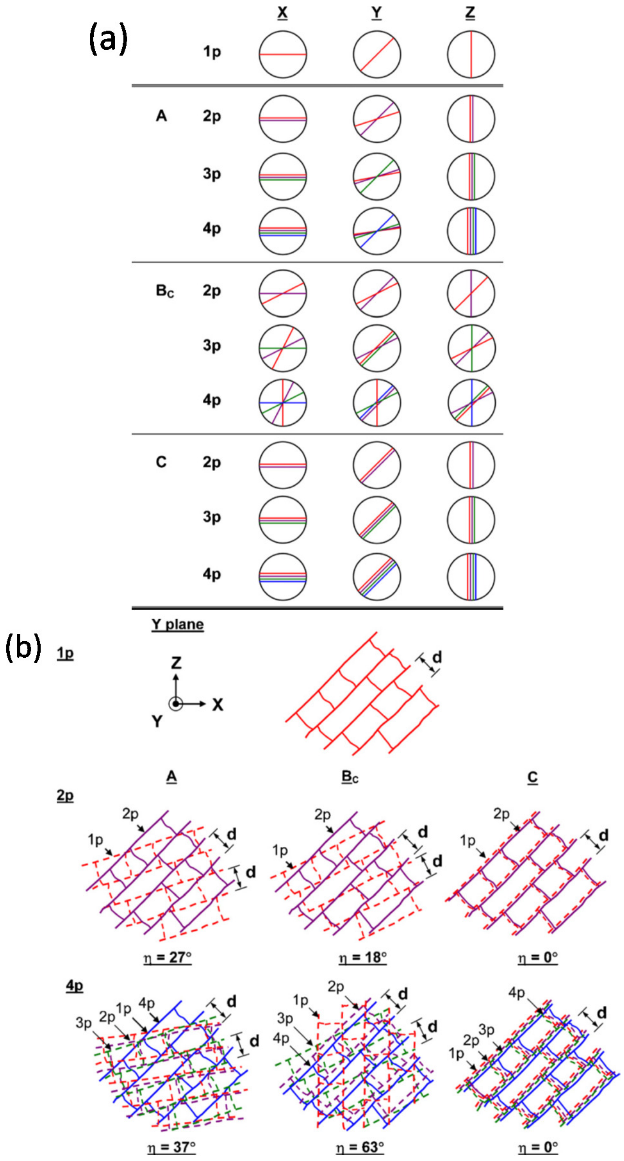

Figure 2-12 (a) The shearing patterns developed on the X, Y and Z planes after 1-4 passes using ECAP processing routes A, B_c and C; (b) A model for grain refinement in ECAP where sub grain bands are formed, with a width of d, with their long sides lying parallel to the primary slip plane: results are illustrated on the Y plane for 1, 2 and 4 passes using routes A, B_c and C;: the color red, mauve, green and blue correspond to first, second third and fourth pass through the die, respectively [55].

2.3.2. Al in ARB

Al was one of the first materials to be processed using ARB. ARB works on the principle of conventional rolling i.e., approximately plane strain compression [56]. However, the process is designed in such a way that the material can be processed n number of times so that ultra-high strains can be imposed. The experimental set up is shown in Figure 2-13. The amount of reduction per pass is mostly 50 %. However, adaptations and several experimentations have been performed over time for other reduction percentage as well.

AA 1100 was processed by ARB for the first time by Saito et al.,[56] and it was found that as the number of deformation passes increased, the yield strength of the material increased and a fine grained microstructure was obtained. In later publications, it was shown that fine grain lamellar structures with lamellar spacing of less than 500 nm could be achieved. The microstructure obtained was not equiaxed and was represented as a pan-cake UFG microstructure. Pirgazi et al. [58] processed AA1100 by ARB up to 10 cycles. An average grain size of 500 nm was achieved with a yield strength of nearly 275 MPa. Similarly, several articles have reported the achievement of UFG structures and good strength properties through ARB processing. Compared to conventional cold rolling, better grain refinement and mechanical properties were possible. For similar equivalent strains, in ARB, a higher rate in the generation of HAGB and misorientations was observed [56]. This is because of the mechanism of grain refinement being active in ARB. Lee et al. did an effort in quantifying the exact deformation field in ARB using an embedded pin technique [59]. The description of the technique can be found in [60]. Figure 2-14 (a) shows the deflected pin in the sample after ARB. The angle of deflection of the pin was measured and used in the calculation of the shear strain around TD along the RD-ND plane which gives the shear strain distribution as represented by equation (2-8) [59]. By this process, a strain distribution along the through thickness direction can be obtained and when plotted as function of thickness, it is as shown in Figure 2-14 (b) for 1 and more passes. As the process is continued by folding and rolling to increasing number of passes, the shear strain accumulation evolves in a complex manner. According to the shear strain, the grain size or the thickness of the grain lamella also varies as a function of thickness.

$$\gamma_1(x) = 13.6(0.5 - x)^2 + \ 288.4(0.5 - x)^6 \qquad \text{(2-8)}$$

Where γ_1 is the engineering shear strain and x is the depth position from the upper surface.

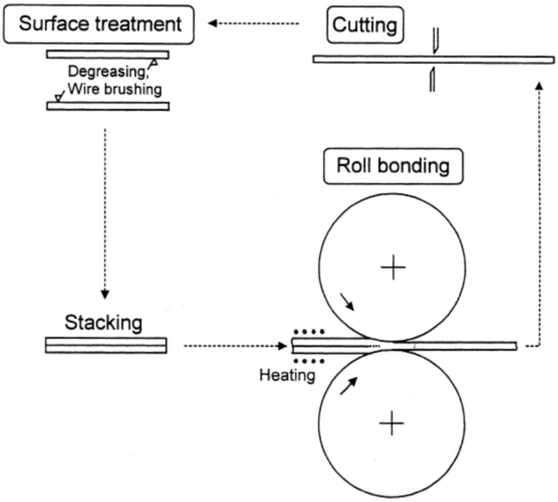

Figure 2-13-Schematic representation of Accumulative Roll Bonding (ARB) process [57]

The exact mechanism of grain refinement in ARB has not been studied as extensively as that of other SPD processes like ECAP or HPT. The only theory known is that during ARB, there is an accumulation of shear strain as derived by Lee et al [59]. During the initial passes of ARB, this shear strain plays a vital role in rapid grain refinement. This was attributed to shear induced different slip activities and deformation banding. Later, at higher deformation passes the formation of the UFG structures is facilitated by CDRX, as reported by Saito et al [56]. The deformation mechanics and strain path involved in ARB is a bit complex. From figure 2-14(b), at early deformation passes, a steep shear strain gradient is obtained. This gradient slowly homogenizes as the number of passes increases. But it should be noted that only the magnitude of the strain gradient homogenizes. The sign of the strain gradient follows a different pattern. The positive strain gradient can become negative or nullify depending on the position within the material. The magnitude of the strain gradient indicates the accumulation of the strain and the change in the sign of the gradient indicates the change in the strain path of the material. Combined, they can be effective in producing UFG material. A proper understanding on these aspects is still missing in literature.

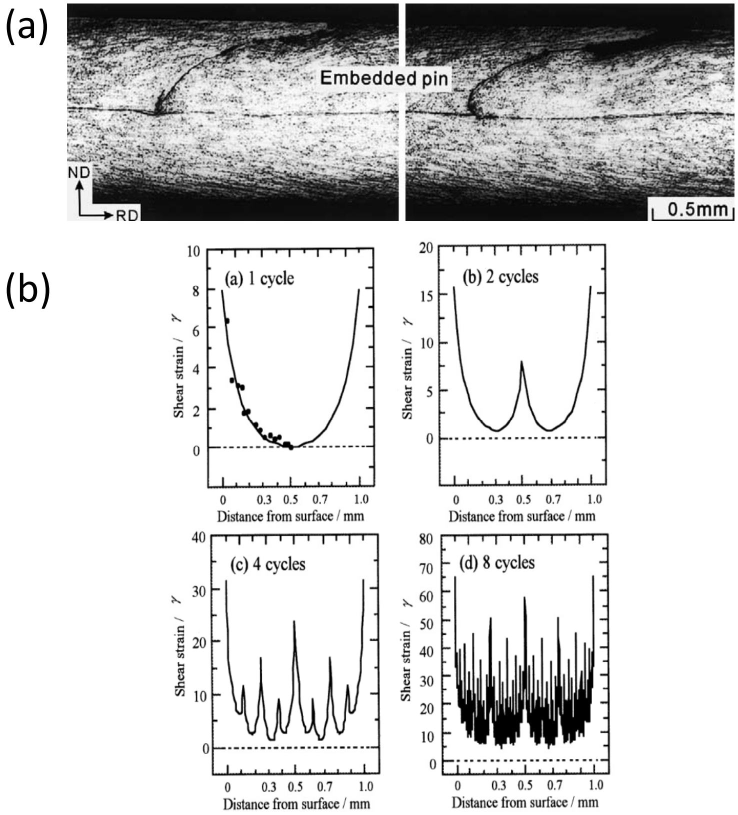

Figure 2-14 - (a) Optical microstructure showing deflection of the embedded pin in AA 1100 after ARB to one cycle; (b) Distribution of shear strain through thickness of the AA 1100 ARB processed by one, two, four and eight cycles [59].

2.4. Non-conventional accommodation mechanisms in UFG and nanostructured materials

Microstructure evolution in SPD starts by a conventional grain sub-division process. At strains above 500 %, the microstructure attains a steady state regime with a large fraction of HAGB and stable grain orientations. This steady state regime has been defined in literature as the state when the rate of formation of new dislocations is readily compensated by annihilation of dislocations [51,61]. Thus, material does not further strain harden and their grain size saturates. However, the question arises what happens at the level of the microstructure when the material of such a state is subjected to more deformation, as most of the SPD processes are carried out to equivalent strains well above 1000 %. The grain sizes remain almost constant, very slight modifications in grain orientations occur and the HAGB fraction also does not modify much. Several articles have acknowledged the occurrence of this steady state regime, but only very few have addressed the underlying mechanisms. Prominent observations revealed that the microstructure responded by re-structuring, re-organizing and coalescence of grains and grain boundaries which were facilitated by specific accommodation mechanisms such as grain boundary sliding, triple junction motion and stress induced grain boundary migration. They are not commonly expected mechanisms for room temperature deformation, but due to the extreme conditions of the materials being processed, the mechanism has gained relevancy [61-63].

2.4.1. Grain boundary sliding

Grain boundary sliding was first reported as a phenomenon in creep [64]. It is a dominant deformation mechanism for materials such as ceramics when deformed at high temperatures. It is proven to occur in nanocrystalline metals as well and was further established as one of the main reasons for their superplastic properties [61,65-67]. The occurrence of grain boundary sliding has been spotted prominently along the regions of triple junctions. Figure 2-15 shows a schematic of the various events that have been reported to possibly occur at a triple junction and which aid grain boundary sliding [68]. In the context of SPD, it is claimed that grain boundary sliding is a resultant of glide or movement of dislocations at the grain boundaries joining in the triple junction. Grain boundary sliding is very delicate and needs proper conditions with respect to grain size, strain rate, temperature and grain morphology to occur successfully. SPD processed nanostructured materials have managed to satisfy these conditions reasonably well. The presence of GBS was reported for many UFG materials and nanocrystalline materials which were processed by SPD [61]. It is an alternative for the conventional slip based deformation mechanism and it occurs without work hardening of the involved grains with or without change in grain orientation. Therefore, in the context of the steady state deformation regime, GBS becomes highly relevant and can play a vital part in the saturated behavior of the microstructure. However, owing to the magnitude of strain that the material undergoes in SPD, grain boundary sliding cannot be considered as the most prominent deformation mechanism [61,69]. The actual steady state regime is most likely the result of a collective process of several accommodation mechanisms, where GBS is a part of as well.

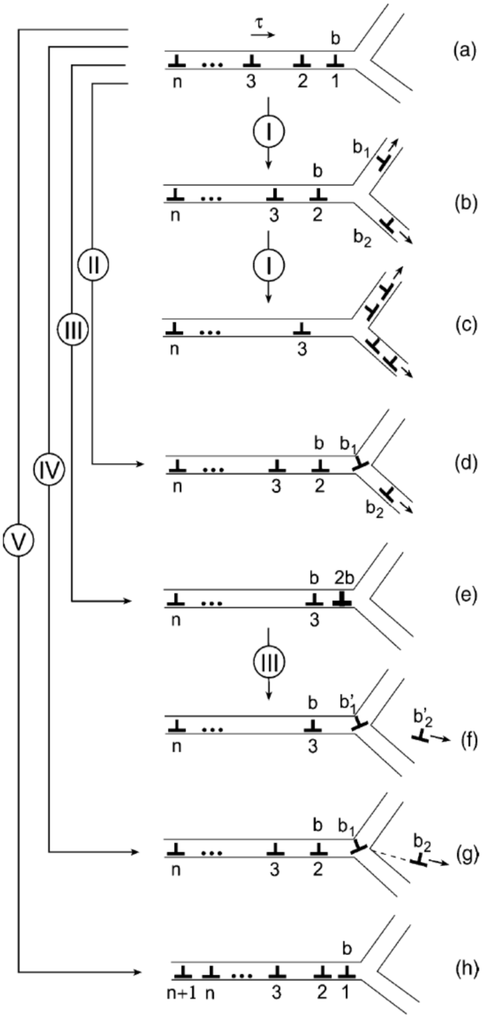

Figure 2-15 Transformations of grain boundary dislocation pile-ups at a triple junction of grain boundaries. (a) The dislocation pile-up stops at the triple junction. (b) The head dislocation of the pile-up splits into two mobile dislocations that move along adjacent grain boundaries. (c) The second head dislocation of the pile-up splits into two mobile dislocations that move along adjacent grain boundaries. (d) The head dislocation of the pile-up splits into an immobile grain boundary dislocation that stays at the triple junction and a mobile grain boundary dislocation moving along an adjacent boundary. (e) Two dislocations converge into a dislocation with Burgers vector 2b. (f) A dislocation with Burgers vector 2b splits into an immobile grain boundary dislocation that stays at the triple junction and a mobile lattice dislocation that moves in the grain interior. (g) The head dislocation of the pile-up splits into an immobile grain boundary dislocation that stays at the triple junction and a mobile partial dislocation which moves in the grain interior, with a stacking fault (dashed line) formed behind it. (h) New dislocations join the stopped dislocation pile-up [68].

2.4.2. Triple junction motion

Triple junctions play a major role in heterogeneity driven energy restorations which are associated with deformation. Triple junctions have been classified by Yu et al. [70] in three types – Y, r and H. They are shown in Figure 2-16. Y junctions are frequently observed in a lamellar microstructure with three lamellar grains, H junctions are interconnects between two lamellar grains and r junctions occur at any three interconnecting grain boundaries. H and r junctions are considered as stable junctions or in other words have low mobility as their interconnecting boundaries are comprised of low angle boundaries, as observed by Yu et al [70]. On the other hand, the Y junctions are comprised of high angle or medium angle boundaries and are comparatively more mobile[70,71].

Triple junction motion is a commonly observed phenomenon during a grain growth process at high temperatures. It is not exactly triple junction motion but triple junction driven migration of the grain boundary system. An equilibrium structure of a triple junction usually comprises three boundaries whose arrangement is shown in Figure 2-17 (a). The forces applied by the grain boundaries cancel out at the triple junction and by isotropic assumption, a dihedral angle of 120° is formed by each boundary at the junction.

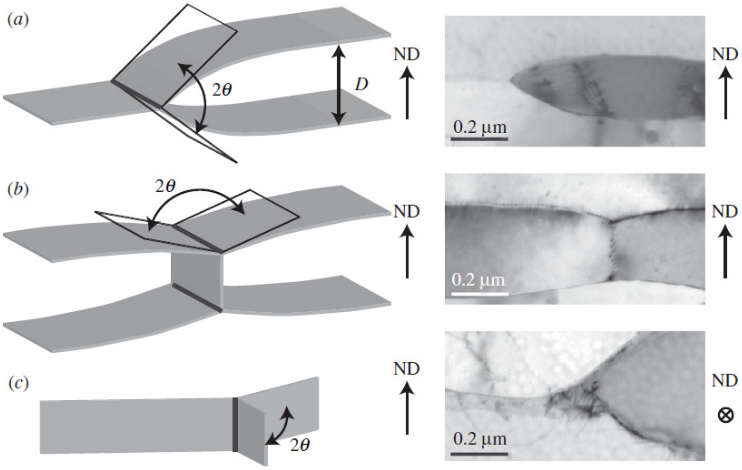

Figure 2-16 Illustrations and examples of three types of triple junctions in lamellar structures. (a) A Y-junction formed by three lamellar boundaries; (b) two H-junctions (an H-junction pair) formed by two lamellar boundaries and an interconnecting boundary between them; and (c) a random r-junction formed by three interconnecting boundaries. Triple junctions are highlighted in bold lines with dihedral angles 2θ indicated. Both Y-junctions and H-junctions are lying nearly parallel to the rolling plane, whereas r-junctions are oriented almost parallel to ND [70].

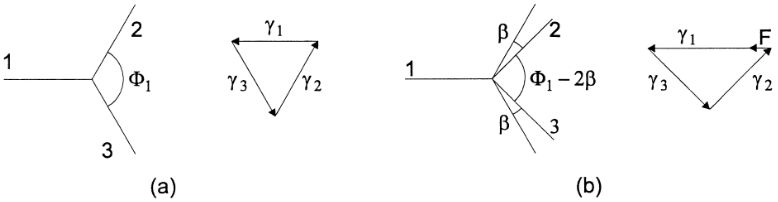

Figure 2-17 - The forces acting upon a triple junction: (a) equilibrated, at rest; (b) as the dihedral angle changes. F increases in response to the changing dihedral angle until it reaches its maximal value, F_{drag} [72].

When external forces come into play, the structure and the dihedral angles are modified and thus the force equilibrium at the triple junction gets disrupted. A resultant force due to deviation from equilibrium acts at the triple junction and has been defined as the drag force (Figure 2-17 (b)) [72]. Several factors such as triple junction mobility, grain boundary mobility, grain size and type of triple junction play a crucial role in the magnitude of the drag force. Further, these factors are dependent on the operating temperature and the dihedral angle as well [70,72,73]. Several studies have been reported to explain the triple junction driven migration of the grain boundary system. Two of the relevant equations to understand the kinetics of the triple junction system are given below,

$$\frac{2\theta}{2\cos\theta - 1} = \frac{m_{tj}a}{m_b} = \Lambda \qquad \text{(2-9)}$$

$$v = m_{tj}\sigma(1 - 2\cos\theta) \qquad \text{(2-10)}$$

where, Λ is a dimensionless parameter, 2θ is the dihedral angle, m_b is the grain boundary mobility, m_{tj} is the triple junction mobility, a is the grain size, v is the velocity of the triple junction, σ the grain boundary surface tension [72].

Equation (2-9) [74] introduces a dimensionless parameter that defines the steady state condition of a triple junction grain boundary system. It relates the dihedral angle with triple junction and GB mobility. When $\Lambda >> 1$, there is no drag due to the triple junction and therefore, the boundary system is controlled by grain boundary mobility and the dihedral angle 2θ will equal to $\pi/3$. However, when $\Lambda << 1$, the effect of triple junction mobility on the boundary system will be very prominent and the value of 2θ tends to become 0. The velocity of the motion of the entire boundary system is driven by grain boundary mobility in the former and grain boundary surface tension in the latter case. Equation (2-10) gives the relation to estimate the velocity of the grain boundary system as a function of triple junction mobility, dihedral angle and surface tension at the triple junction for the second condition [72]. Other than this, factors such as grain boundary curvature, grain size and temperature also contribute to the kinetics of the motion of the grain boundary system. At low temperatures, Λ is generally in the order of unity and therefore the mobility of triple junctions is comparable with grain boundary mobility. Experimental evidence proved that triple junctions have a finite mobility. However, it is largely dependent on the operating temperature, similar to the characteristics of grain boundary mobility. Therefore, at low temperatures, the mobility of triple junction is limited and it drags the motion of the grain boundaries. This leads to dihedral angles lower than equilibrium angles. At high temperatures, the TJ mobility increases. So, the drag of the triple junction greatly reduces and the motion of the grain boundary system is completely governed by grain boundary mobility. In Figure 2-18 it can be seen that, with increase in temperature, the motion of the grain boundary system shifts from triple junction dominated kinetics to GB dominated kinetics [75-77]. Therefore, at any given operating conditions, the dihedral angle of the grain boundary system reaches a meta steady-state and this is influenced by the grain size and the mobility of the triple junction and the grain boundaries in the system.

The above discussed aspects of triple junction dependent grain boundary motion were derived mainly in the context of grain growth at temperatures above the recrystallization temperatures. The relevance of such a mechanism is difficult to assess in the context of a saturated deformation regime during SPD. Recent work from Yu et al. gave more insight on this [70,71,78]. Heavy deformation in metals by rolling up to strains above 5 was followed by low temperature annealing, 100 – 200°C, so that only recovery is expected to be active. The deformed lamellar grain structures recovered by shortening of the lamellae into more equiaxed grain structures without any major modifications to the bulk texture. The shortening of the lamellae was facilitated by triple junction motion. Statistical analysis was done and it was concluded that a recovery process by triple junction motion was involved in the continuous removal of thin lamellae which had small dihedral angles and provided large surface tensions. From the understanding obtained so far, the applied external temperature could have modified the mobility of the triple junction which reduced the drag force and facilitated the migration of the grain boundary system. It is a type of a recovery mechanism. Such triple junction motions seem to have a strong role in the recovery kinetics of the materials with lamellar grain structures. However, the reported recovery was a temperature activated process and the significance of this in a room temperature SPD process is debatable. The answer to this was reported in another recent work from Yu et al [63]. It was shown that recovery by triple junction motion existed even at room temperature at extreme straining conditions. CP Al subjected to heavy rolling up to strains above 500 %, when deformed further up to 20 %, exhibited triple junction motion. It resulted in localised shortening of the lamella and re-configuration of the grain structures and was categorized as dynamic recovery. Not many follow up studies have been performed. Only one other similar work from Renk et al. reported the very same observation [69]. It will be a trial worth to explore this observation further to understand the relevamce of this process for grain size saturation.

Although there were a considerable number of articles which described triple junction motion kinetics in the aspects of force equilibrium and mobility, no clear study on the effect of local dislocations, dislocation pile-ups, grain orientation, etc., has been carried out. However, a very few studies mention that the effect of them is minimal and can be ignored. This can be true for coarse grained structures, but for materials with ultrafine grained structures, there can be possibilities that the said factors might influence the local steady-state condition of the triple junctions.

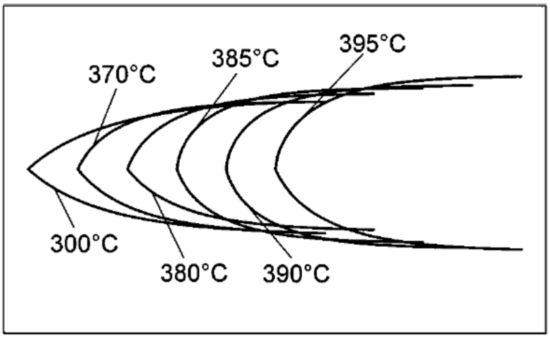

Figure 2-18 Evolution of the shape of the grain boundary system of a sample with symmetrical triple junction with increasing temperature [77]

2.4.3. Stress induced GB migration (SIBM)

Winning et al [79] reported that low angle and high angle boundaries can move under the influence of an external shear stress. The motion of grain boundaries is a commonly observed phenomenon during recrystallization and grain growth[80-82]. The associated factors that control this movement are a free energy gradient due to a gradient in stored energy and boundary curvature. LAGBs are low mobility structures comprising a periodic arrangement of dislocations. In contrast, HAGB are structures with less periodic dislocation arrangements and better mobility [83]. Therefore, most of the experiments on grain growth kinetics were focussed on mobility of HAGB only. In 1952, it was first reported that LAGBs responded to external shear stress, observed by optical microscopy [79,84]. Based on this observation, series of experiments were performed on bicrystals of Al with different grain boundary type to study the effect of external shear stress on a grain boundary [17,85]. Bicrystals with <112> and <111> tilt boundaries – planar and curved type with different misorientation angles were grown. These crystals were subjected to external shear stresses and their migration was observed. The activation enthalpies for the migration of the low angle and high angle boundaries were calculated and showed values very similar to those of activation enthalpies for volume diffusion and grain boundary diffusion respectively. A transition of the change in enthalpy was also seen at 12 - 14° (low to high angle boundary transition), but within the regime, no effect of degree of misorientation could be seen (except for <111> curved boundaries). Figure 2-20 shows the distribution of the calculated activation enthalpies of the <111> and <112> boundaries. The reason reported for the migration varied between the type of boundary – planar or curved. For planar boundaries, the migration is due to interactions of the local stress field in the grain boundary dislocations with the externally imposed shear stresses. For curved boundaries it is due to a combination of capillary forces due to boundary curvature and the stress-field interactions at the grain boundary [79]. The results were the evident proof that grain boundaries respond to stresses and migrate within the system. Around the same time, Cahn et al. published a paper with as title: *Coupling grain boundary motion to shear deformation* [86]. It was an extensive article explaining the response of grain boundaries to applied shear stresses with the help of molecular dynamics simulations. Figure 2-19 is a schematic from the article which shows two possible responses of a grain boundary to externally applied shear stresses. Several interesting inferences were made. The most relevant of all was that shear stress induced grain boundary migration produced shape and rotation changes in grains without diffusion or slip. It was propposed as a separate deformation mechanism, important for nanocrystalline materials, besides diffusional creep and slip which is characterized by grain size and temperature dependencies of the deformation rate [86]. In parallel, interesting experimental work was reported which showed mechanically induced grain growth of nanostructured metals which were subjected to indentation tests, compression and tensile loadings at room temperature. Stress induced grain boundary migration was claimed to be responsible for that, which facilitated local grain restructuring and coalescences and therefore an increase in grain size[87-90]. SIBM is a complex mechanism and the understanding of the process is not very clear till now. With the help of ideal experimental conditions (bi/tri crystals), the mechanism has been proven to exist but in reality, for polycrystalline and nanocrystalline metals, correlation of the mechanism at the level of microstructure is very difficult.

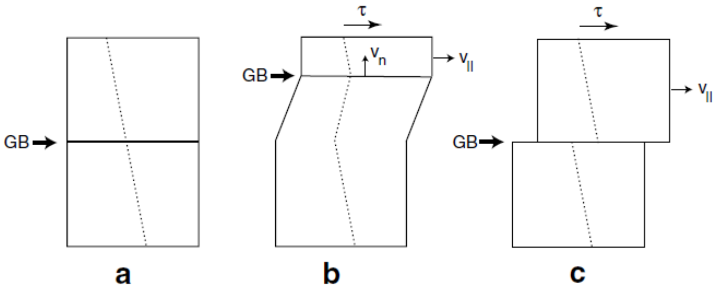

Figure 2-19 - Two types of response of a planar GB to an applied shear stress s. (a) Initial bicrystal; (b) GB motion due to coupling; (c) GB sliding. The dotted line crossing the GB represents a set of inert markers embedded in the lattice or any other fiduciary line. V_n and V_{II} are the velocities of normal GB motion and grain translation, respectively [86].

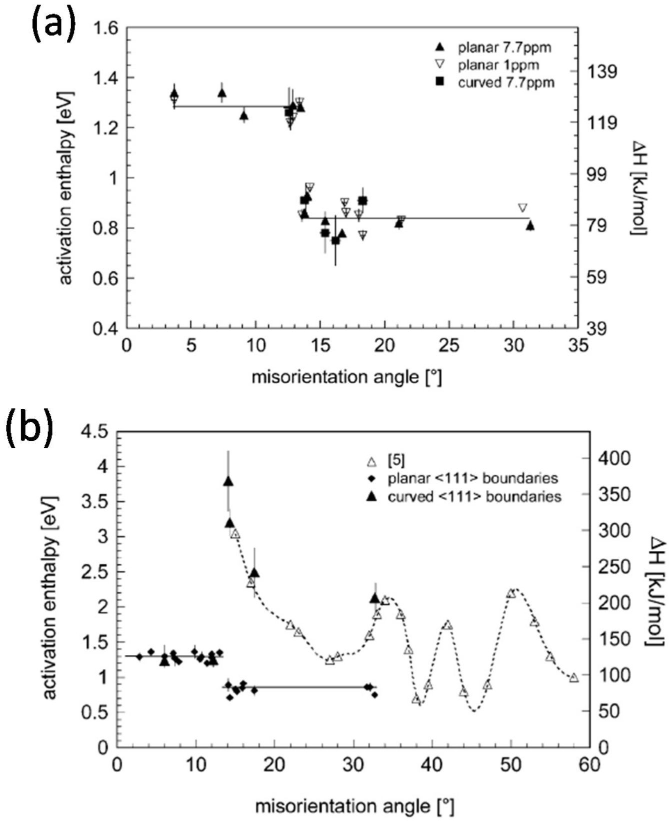

Figure 2-20 – (a) Activation enthalpy versus the misorientation angle for all experiments on symmetrical <112>-tilt boundaries; (b) Dependence of the activation enthalpy on the misorientation angle for the planar and curved <111>-tilt boundaries [85]

2.5. Bulk nano-structured composites

2.5.1. An Overview

Composite materials traditionally consist of a combination of two or more different phases with each of them contributing a unique property on the bulk scale. They are of many varieties starting from metals extending to ceramics and polymers. A lot of the metal and metal/ceramic composites have been produced by Powder Metallurgical (PM) routes or co-melting techniques at high temperatures. However, they have several drawbacks and are quite challenging to optimize in the desired way. Amidst them, the use of severe plastic deformation techniques for producing such composites was investigated and found to have a promising scope. Studies were performed from the 1960s especially on co-drawing of composite wires and later on other techniques such as cold roll bonding (CRB), accumulative roll bonding (ARB), etc. Such composites were coined as DMMC – Deformation processed Metal-Metal Composites[57,91-93].

Early investigations were mostly focused on Fe and Cu based DMMCs. The fascinating aspects of these DMMCs are that the Fe-Fe_3C composites (in case pearlite) produced by drawing possessed a very high ultimate tensile strength of nearly 6 GPa [93]. The high strength has been reported to be due to the extensive plastic deformation of the brittle Fe_3C phase in the dutile Fe matrix. Similarly, Cu-Nb alloys, also produced by drawing, exhibited up to 1.8 GPa of strength in combination with very good superconductivity properties [91,93-95]. Having found such interesting properties, several combinations of metals - FCC/FCC, FCC/BCC, BCC/BCC, HCP/HCP, etc., were investigated by co-deformation using SPD techniques. Examples of such composite materials are Al/Cu, Al/Cu/steel, Al/Fe, Al/stainless steel, Ag/Cu, Cu/stainless steel, Ag/Cu/Ag, Ni/Cu, Al/Zn, etc., and they are being used widely in the fields of automobiles, electronics, fuel cells, etc [91,96].

With the help of DMMC, material combinations of brittle and ductile materials, mechanical mixing/alloying of thermodynamically stable materials will be possible. More importantly, a better grain refinement can be achieved. Cu-Fe composites deformed by SPD exhibited grain sizes of 20-80 nm in the Cu part compared to 200 nm when Cu was deformed individually [62,91,96]. Therefore, DMMC combined with SPD will help in achieving a new range of properties which cannot be observed in conventional single phase processing. Efforts have been made to explore the positives of the co-deformation process on different metal combinations. Figure 2-21 shows a graphical explanation of the grain refinement that could be achieved with multi-phase materials through a co-deformation process. Besides, formation of UFGs/nanostructures and presence of interphase/interface regions as lamellar structures in the DMMC help in enhancing the strength properties of the composites as well [40,91,93,94,97,98].

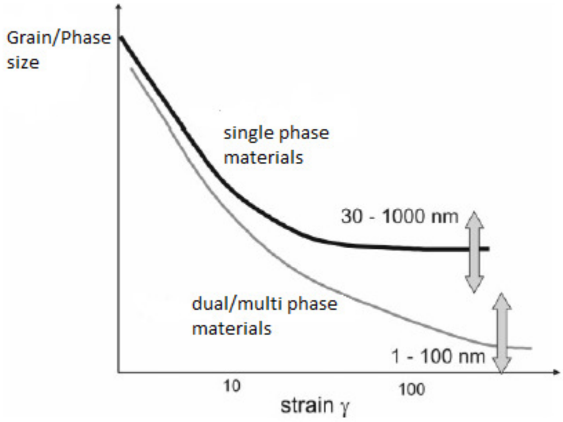

Figure 2-21-Grain refinement of single and multi-phase materials achieved through SPD [69]

The extent of mechanical bonding in the metal composites varies with respect to material and type of deformation process. Figure 2-22 gives an overview of a list of materials that can be cold bonded with other materials through cold (roll) bonding (CRB) and ARB processes. Further, the bond strength achieved through such deformation processes depends on the extent of deformation introduced. Each materials pair requires a minimum threshold deformation to achieve a successful bond. Figure 2-23 shows this threshold deformation in reduction % for different materials pairs which are processed by a CRB process [18].

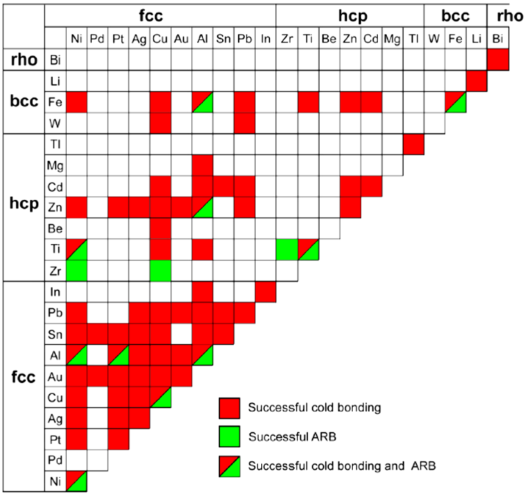

Figure 2-22-Successful ARB and cold (roll) bonding for different combination of materials [99]

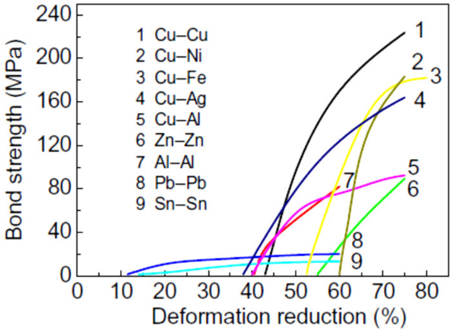

Figure 2-23-Bond strength as function of deformation reduction for different metal composites in CRB[99].

2.5.2. Microstructure, interfaces and strengthening properties

The deformation process of a composite material is not as straight-forward as in a single-phase material. For example, two materials – A and B - are rolled together in the sequence ABA. A is the clad material (c) and B is the matrix material (m). Their corresponding Mohr’s circle when deformed as a single phase can be seen in Figure 2-24 (a) and (b). The plane strain rigid-perfectly plastic shear yield strength of B is higher than the one of A. When these materials are rolled together, theoretically the Mohr’s circle for the composite will look like as shown in Figure 2-24 (c). However, in reality the Mohr’s circle will be as shown in Figure 2-24 (d). The softer material is imposed under compressive residual stress and the hard material under tensile residual stress [100,101]. This gives an example of how residual stresses and internal stresses are created during a co-deformation process.

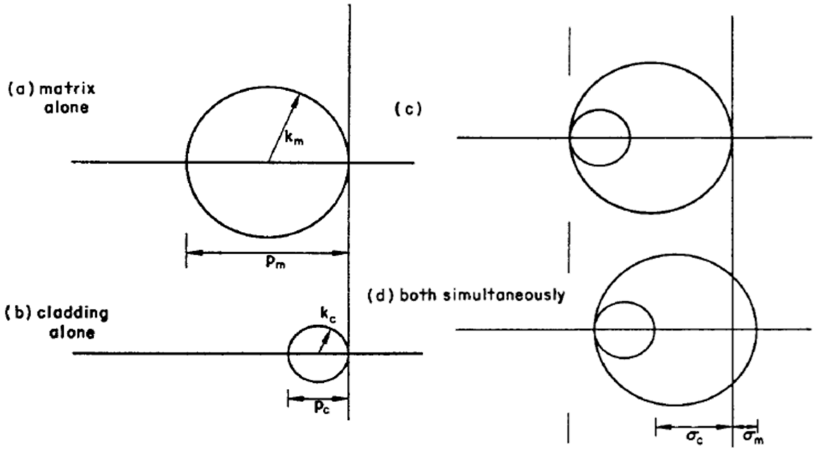

Figure 2-24-Mohr's circle for plane strain compression of a sandwich – (a) when deforming matrix alone; (b) when deformation the cladding alone; (c) theoretically expected stress state when deformed as a sandwich; (d) actual stress state when deformed as a sandwich, showing tensile residual stresses in the matrix [100,101] p_m and p_c are the magnitude of compressive stress of the matrix and clad respectively, k_m and k_c are the plastic shear yield strength of matrix and clad respectively and σ_m and σ_c are induced tensile and compressive stresses in matrix and clad respectively.

Different types of strengthening mechanisms are activated in the co-deformed material. Firstly, co-deformation promotes higher grain refinement and therefore facilitate grain boundary strengthening. Secondly, the mechanical interfaces formed during the co-deformation act as interface strengthening [91,93,102]. During SPD of composites, processed through repetitive straining by extrusion, rolling, etc., the number of interfaces per unit area increases with increasing deformation. The sites of interfaces serve as barrier for the dislocation motion and increase the resistance to deformation. Thirdly, the residual stresses and internal stresses which are developed at the interfaces significantly affect the hardening properties and the strength of the material [103-106]. The factors which affect the development of these residual and internal stresses are strength ratio of the co-deforming materials, thickness ratio, thickness of each layer, composite arrangement, morphology and the magnitude of strain being imposed [100,104,105]. Fourthly, it has been found that under extreme straining conditions, single-slip transfer is promoted across the interfaces. The extreme straining conditions are believed to modify the local structure of the interfaces, their crystallography and the internal stresses and all of them contribute to the properties of the composite [93,106]. Fifthly, mechanical alloying is promoted by co-deformation which assists in intermixing of the dis-similar materials (miscible and non-miscible) at the interfaces. Dissolution of secondary phases at the interfaces, amorphization or solid-solution formation occurs [93,94,106-

[110], all of which contributes to a major fraction of the strength of the composite, sometimes also negatively.

Of all the mentioned mechanisms, the interaction at the interface facilitated by extreme straining became an important area of interest. The occurrence of mechanical alloying and other related observations such as dissolution of secondary phases, amorphization, solute segregation, etc., have been observed and are unique to the co-deformation process. They are mostly high temperature mechanisms which have been made possible due to extreme straining conditions at non-equilibrium conditions. Dislocations are believed to play as a driving force behind these observations [93,106,107,111]. From examining severely deformed Cu-X alloys, slip transmission across interfaces from one phase to another was reported. The occurrence of the slip transfer depended on the coherency of the orientation at the interface. For example, in FCC-FCC material combinations, they are observed to occur when both the phases share similar texture and in FCC-BCC material combinations, when the Kurdjumov–Sachs condition is satisfied at the interface [93]. Extending this mechanism further, chemical mixing at the interfaces has also been claimed to plausibly occur by such a slip transfer, not on one single slip system but on multiple slip systems. The mechanism has been described as dislocation-shuffling [93,106,112]. It proposes inter-phase plastic deformation on multiple slip systems which can trap small embedded particles in a matrix of the neighboring phase which can further cut through by new dislocations leading to dissolution of the phase in the other matrix or amorphization or just segregation. The schematic of the mechanisms is shown in Figure 2-25. These are some of the interesting observations and mechanisms pertinent only to a co-deformation process. With proper understanding of the material behavior during co-deformation at extreme straining conditions, several new interaction mechanisms can be unraveled and will be an interesting area of study.

In the aim of obtaining the best use of such observations, different material combinations have been fabricated by co-deformation with the help of several SPD techniques such as – roll bonding, milling, drawing, HPT and studied for their mechanical and microstructural properties [62,92,94,106,113-115].

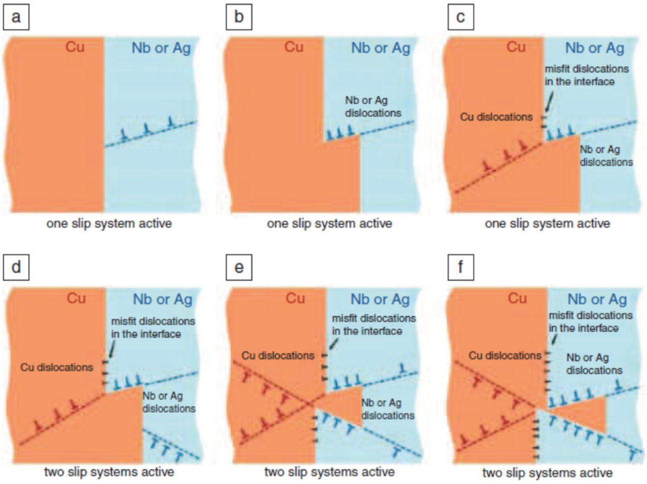

Figure 2-25-Dislocation shuffling mechanisms through multi-slip shear transfer followed by dislocation movement and chemical mixing [93]

2.6. Conclusion

The most prominent and successful SPD techniques are Equal Channel Angular Pressing (ECAP), High Pressure Torsion (HPT) and Accumulative Roll Bonding (ARB). ECAP is one of the most suitable SPD techniques for the processing of a wide range of metals and alloys. Many new techniques (ECAP conform, etc.) in par with ECAP and derivatives of ECAP have been designed and developed [116] and are still under research for commercial continuous processing. HPT is one of the best SPD processes in efficient production of ultra-fine grained materials down to 100 nm or even less [51]. However, it is limited to the processing of small discs. ARB is another potential technique which works on the principle of rolling. It is efficient in producing fine grained materials and has good scope for continuous production because of its feasibility supported by using a conventional cold rolling process set-up. Although the implementation of ARB is easier than any other techniques, it possesses certain drawbacks with respect to through thickness in-homogeneity of the microstructures, etc. Each of these methods has its own technical difficulties and are under progressive research to overcome them and successfully produce sound products. Numerous investigations are being conducted all over the world to harness the ability of SPD to produce UFG materials on large and continuous scale owing to the growing needs and applications among various fields [56,117].

Adding to the list, in this thesis a new SPD technique will be introduced. It is called Accumulative Extrusion (AccumEx). It is a derivative of Accumulative Roll Bonding (ARB) and works on the principle of plane strain compression. Instead of rolling, the process will be extrusion. Conventional rolling and plane strain extrusion share a similar strain behavior. Both the processes involve similar frictional forces at the lateral sides and undergo thickness reduction [118,119]. However, one advantage with AccumEx is that a higher through thickness variance in the sample can be achieved. In this thesis, the technique will be used to produce bulk UFG similar and dissimilar materials. The deformation field in the AccumEx process will be correlated with the microstructure and texture evolution. The response of UFG material to high strain deformation will be studied. The effectiveness of the technique in producing composite material will be tested.

REFERENCES

1 Gil Sevillano, J. & Aernoudt, E. Low energy dislocation structures in highly deformed materials. *Materials Science and Engineering* **86**, 35-51, doi:http://dx.doi.org/10.1016/0025-5416(87)90441-1 (1987).

2 Paupler, P. G. E. Dieter. Mechanical Metallurgy. 3rd ed., Mc Graw-Hill Book Co., New York 1986. XXIII + 751 p., DM 138.50, ISBN 0–07–016893–8. *Crystal Research and Technology* **23**, 194-194, doi:10.1002/crat.2170230211 (1988).

3 Hull, D. & Bacon, D. J. in *Introduction to Dislocations (Fifth Edition)* 43-62 (Butterworth-Heinemann, 2011).

4 Dehlinger, U. Kristallplastizität mit besonderer Berücksichtigung der Metalle. Von Prof. Dr. E. Schmid und Dr.-Ing. W. Boas. (Struktur und Eigenschaften der Materie, Bd. XVII). Verlag von Julius Springer, Berlin 1935. IV und 373 *Angewandte Chemie* **48**, 518-519, doi:10.1002/ange.19350483008 (1935).

5 Van Houtte, P. Deformation texture prediction: from the Taylor model to the advanced Lamel model. *International Journal of Plasticity* **21**, 589-624, doi:10.1016/j.ijplas.2004.04.011 (2005).

6 Hirsch, J. & Lücke, K. Overview no. 76. *Acta Metallurgica* **36**, 2883-2904, doi:http://dx.doi.org/10.1016/0001-6160(88)90173-3 (1988).

7 Taylor, G. I. Plastic strain in metals. *J. Institute of Metals* **62**, 307-324 (1938).

8 Kocks, U. F., Tomé, C. N. & Wenk, H.-R. *Texture and anisotropy: preferred orientations in polycrystals and their effect on materials properties*. (Cambridge University press, 2000).

9 Kanjarla, A. K., Van Houtte, P. & Delannay, L. Assessment of plastic heterogeneity in grain interaction models using crystal plasticity finite element method. *International Journal of Plasticity* **26**, 1220-1233, doi:10.1016/j.ijplas.2009.05.005 (2010).

10 Van Houtte, P., Kanjarla, A. K., Van Bael, A., Seefeldt, M. & Delannay, L. Multiscale modelling of the plastic anisotropy and deformation texture of polycrystalline materials. *European Journal of Mechanics - A/Solids* **25**, 634-648, doi:10.1016/j.euromechsol.2006.05.003 (2006).

11 Tian, Y. Z. *et al.* Significant contribution of stacking faults to the strain hardening behavior of Cu-15%Al alloy with different grain sizes. *Scientific reports* **5**, 16707, doi:10.1038/srep16707 (2015).

12 Bay, B., Hansen, N., Hughes, D. A. & Kuhlmann-Wilsdorf, D. Overview no. 96 evolution of f.c.c. deformation structures in polyslip. *Acta Metallurgica et Materialia* **40**, 205-219, doi:http://dx.doi.org/10.1016/0956-7151(92)90296-Q (1992).

13 Verlinden, B., Driver, J., Samajdar, I. & Doherty, R. Chapter 5 Softening mechanisms. *Pergamon Materials Series* **11**, 83-108, doi:http://dx.doi.org/10.1016/S1470-1804(07)80009-5 (2007).

14 Segal, V. M. Severe plastic deformation: simple shear versus pure shear. *Materials Science and Engineering: A* **338**, 331-344, doi:http://dx.doi.org/10.1016/S0921-5093(02)00066-7 (2002).

15 Zhu, Q., Sellars, C. M. & Bhadeshia, H. K. D. H. Quantitative metallography of deformed grains. *Materials Science and Technology* **23**, 757-766, doi:10.1179/174328407x157308 (2013).

16 Kashihara, K. The Relationship between Crystal Rotation Axis Orientation and Active Slip System in Pure Aluminum Tricrystal Deformed in Compression. *Materials Transactions* **49**, 419-423, doi:10.2320/matertrans.MBW200704 (2008).

17 Zaefferer, S., Kuo, J. C., Zhao, Z., Winning, M. & Raabe, D. On the influence of the grain boundary misorientation on the plastic deformation of aluminum bicrystals. *Acta Materialia* **51**, 4719-4735, doi:10.1016/s1359-6454(03)00259-3 (2003).

18 Sakai, T., Belyakov, A., Kaibyshev, R., Miura, H. & Jonas, J. J. Dynamic and post-dynamic recrystallization under hot, cold and severe plastic deformation conditions. *Progress in Materials Science* **60**, 130-207, doi:10.1016/j.pmatsci.2013.09.002 (2014).

19 Raghavan, R. S., Tiwari, S. M., Mishra, S. K. & Carsley, J. E. Recovery quantification and onset of recrystallization in aluminium alloys. *Philosophical Magazine Letters* **94**, 755-763, doi:10.1080/09500839.2014.975767 (2014).

20 Jazaeri, H. & Humphreys, F. J. The transition from discontinuous to continuous recrystallization in some aluminium alloys. *Acta Materialia* **52**, 3239-3250, doi:10.1016/j.actamat.2004.03.030 (2004).

21 Sakai, T. & Jonas, J. J. in *Encyclopedia of Materials: Science and Technology (Second Edition)* (eds Robert W. Cahn *et al.*) 7079-7084 (Elsevier, 2001).

22 McQueen, H. J. Development of dynamic recrystallization theory. *Materials Science and Engineering: A* **387–389**, 203-208,d (2004).

23 Van Boxel, S. *Anisotropic Work-Hardening and Strain Path Effects in an AlMn Alloy*, Ph.D. thesis, KU Leuven, (2010).

24 El-Danaf, E. A., Soliman, M. S. & Almajid, A. A. Effect of deformation path change on plastic response and texture evolution for 1050 Al pre-deformed by ECAP and subsequently plane strain compressed. *Materials Science and Engineering: A* **527**, 2547-2558, doi:10.1016/j.msea.2010.01.003 (2010).

25 Zhang, J., Gao, N. & Starink, M. J. Microstructure development and hardening during high pressure torsion of commercially pure aluminium: Strain reversal experiments and a dislocation based model. *Materials Science and Engineering: A* **528**, 2581-2591, doi:10.1016/j.msea.2010.11.079 (2011).

26 Todaka, Y., Umemoto, M., Yamazaki, A., Sasaki, J. & Tsuchiya, K. Effect of Strain Path in High-Pressure Torsion Process on Hardening in Commercial Purity Titanium. *Materials Transactions* **49**, 47-53, doi:10.2320/matertrans.ME200714 (2008).

27 Kawasaki, M. & Langdon, T. G. The significance of strain reversals during processing by high-pressure torsion. *Materials Science and Engineering: A* **498**, 341-348, doi:10.1016/j.msea.2008.08.021 (2008).

28 Humphreys, F. J., Prangnell, P. B., Bowen, J. R., Gholinia, A. & Harris, C. Developing stable fine-grain microstructures by large strain deformation. *Philosophical Transactions of the Royal Society A: Mathematical, Physical and Engineering Sciences* **357**, 1663-1681, doi:10.1098/rsta.1999.0395 (1999).

29 Hansen, N. & Juul Jensen, D. Development of microstructure in FCC metals during cold work. *Philosophical Transactions of the Royal Society A: Mathematical, Physical and Engineering Sciences* **357**, 1447-1469, doi:10.1098/rsta.1999.0384 (1999).

30 Hutchinson, B. Deformation microstructures and textures in steels. *Philosophical Transactions of the Royal Society A: Mathematical, Physical and Engineering Sciences* **357**, 1471-1485, doi:10.1098/rsta.1999.0385 (1999).

31 Hughes, D. A. & Hansen, N. High angle boundaries formed by grain subdivision mechanisms. *Acta Materialia* **45**, 3871-3886, doi:http://dx.doi.org/10.1016/S1359-6454(97)00027-X (1997).

32 Liu, Q. & Hansen, N. Deformation microstructure and orientation of f.c.c. crystals. *physica status solidi (a)* **149**, 187-199, doi:10.1002/pssa.2211490113 (1995).

33 Kuhlmann-Wilsdorf, D. & Hansen, N. Geometrically necessary, incidental and subgrain boundaries. *Scripta Metallurgica et Materialia* **25**, 1557-1562, doi:http://dx.doi.org/10.1016/0956-716X(91)90451-6 (1991).

34 Wert, J. A., Huang, X., Winther, G., Pantleon, W. & Poulsen, H. F. Revealing deformation microstructures. *Materials Today* **10**, 24-32, doi:http://dx.doi.org/10.1016/S1369-7021(07)70206-7 (2007).

35 Huang, X. & Winther, G. Dislocation structures. Part I. Grain orientation dependence. *Philosophical Magazine* **87**, 5189-5214, doi:10.1080/14786430701652851 (2007).

36 Winther, G. & Huang, X. Dislocation structures. Part II. Slip system dependence. *Philosophical Magazine* **87**, 5215-5235, doi:10.1080/14786430701591505 (2007).

37 Winther, G. Slip patterns and preferred dislocation boundary planes. *Acta Materialia* **51**, 417-429, doi:10.1016/s1359-6454(02)00423-8 (2003).

38 Liu, Q. & Hansen, N. Macroscopic and microscopic subdivison of a cold–rolled aluminium single crystal of cubic orientation. *Proceedings of the Royal Society of London. Series A: Mathematical, Physical and Engineering Sciences* **454**, 2555-2592, doi:10.1098/rspa.1998.0271 (1998).

39 Wert, J. A., Liu, Q. & Hansen, N. Dislocation boundary formation in a cold-rolled cube-oriented Al single crystal. *Acta Materialia* **45**, 2565-2576, doi:http://dx.doi.org/10.1016/S1359-6454(96)00348-5 (1997).

40 Hansen, N., Huang, X., Ueji, R. & Tsuji, N. Structure and strength after large strain deformation. *Materials Science and Engineering: A* **387-389**, 191-194, doi:10.1016/j.msea.2004.02.078 (2004).

41 Morii, K., Mecking, H. & Nakayama, Y. Development of shear bands in f.c.c. single crystals. *Acta Metallurgica* **33**, 379-386, doi:http://dx.doi.org/10.1016/0001-6160(85)90080-X (1985).

42 Hatherly, M. & Malin, A. S. Shear bands in deformed metals. *Scripta Metallurgica* **18**, 449-454, doi:http://dx.doi.org/10.1016/0036-9748(84)90419-8 (1984).

43 Shen, Y.-L. On the shear band formation in F.C.C. metals. *Scripta Metallurgica et Materialia* **25**, 1081-1085, doi:http://dx.doi.org/10.1016/0956-716X(91)90505-U (1991).

44 Harren, S. V., Dève, H. E. & Asaro, R. J. Shear band formation in plane strain compression. *Acta Metallurgica* **36**, 2435-2480 (1988).

45 Xu, C., Furukawa, M., Horita, Z. & Langdon, T. G. The evolution of homogeneity and grain refinement during equal-channel angular pressing: A model for grain refinement in ECAP. *Materials Science and Engineering: A* **398**, 66-76, doi:http://dx.doi.org/10.1016/j.msea.2005.03.083 (2005).

46 Liu, M. *et al.* Grain refinement in nanostructured Al–Mg alloys subjected to high pressure torsion. *Journal of Materials Science* **45**, 4659-4664, doi:10.1007/s10853-010-4604-3 (2010).

47 Neishi, K., Horita, Z. & Langdon, T. G. Grain refinement of pure nickel using equal-channel angular pressing. *Materials Science and Engineering: A* **325**, 54-58, doi:http://dx.doi.org/10.1016/S0921-5093(01)01404-6 (2002).

48 Kratochvíl, J. Mechanism of Grain Refinement Induced by Severe Plastic Deformation. *Materials Science Forum* **667-669**, 617-622, doi:10.4028/www.scientific.net/MSF.667-669.617 (2010).

49 Kaibyshev, R. & Mazurina, I. Mechanisms of Grain Refinement in Aluminum Alloys during Severe Plastic Deformation. *Materials Science Forum* **467-470**, 1251-1260, doi:10.4028/www.scientific.net/MSF.467-470.1251 (2004).

50 Iwahashi, Y., Horita, Z., Nemoto, M. & Langdon, T. G. The process of grain refinement in equal-channel angular pressing. *Acta Materialia* **46**, 3317-3331, doi:http://doi.org/10.1016/S1359-6454(97)00494-1 (1998).

51 Estrin, Y. & Vinogradov, A. Extreme grain refinement by severe plastic deformation: A wealth of challenging science. *Acta Materialia* **61**, 782-817, doi:10.1016/j.actamat.2012.10.038 (2013).

52 Valiev, R. Z. & Langdon, T. G. Principles of equal-channel angular pressing as a processing tool for grain refinement. *Progress in Materials Science* **51**, 881-981, doi:10.1016/j.pmatsci.2006.02.003 (2006).

53 Poortmans, S. From microstructure towards mechanical behavior of ultrafine grained aluminium alloys. *PhD dissertation* (2008).

54 El-Danaf, E. A., Soliman, M. S., Almajid, A. A. & El-Rayes, M. M. Enhancement of mechanical properties and grain size refinement of commercial purity aluminum 1050 processed by ECAP. *Materials Science and Engineering: A* **458**, 226-234, doi:10.1016/j.msea.2006.12.077 (2007).

55 Langdon, T. G. The principles of grain refinement in equal-channel angular pressing. *Materials Science and Engineering: A* **462**, 3-11, doi:http://dx.doi.org/10.1016/j.msea.2006.02.473 (2007).

56 Saito, Y., Tsuji, N., Utsunomiya, H., Sakai, T. & Hong, R. G. Ultra-fine grained bulk aluminum produced by accumulative roll-bonding (ARB) process. *Scripta Materialia* **39**, 1221-1227, doi:http://dx.doi.org/10.1016/S1359-6462(98)00302-9 (1998).

57 Saito, Y., Utsunomiya, H., Tsuji, N. & Sakai, T. Novel ultra-high straining process for bulk materials—development of the accumulative roll-bonding (ARB) process. *Acta Materialia* **47**, 579-583, doi:http://dx.doi.org/10.1016/S1359-6454(98)00365-6 (1999).

58 Pirgazi, H., Akbarzadeh, A., Petrov, R. & Kestens, L. Microstructure evolution and mechanical properties of AA1100 aluminum sheet processed by accumulative roll bonding. *Materials Science and Engineering: A* **497**, 132-138, doi:10.1016/j.msea.2008.06.025 (2008).

59 Lee, S. H., Saito, Y., Tsuji, N., Utsunomiya, H. & Sakai, T. Role of shear strain in ultragrain refinement by accumulative roll-bonding (ARB) process. *Scripta Materialia* **46**, 281-285, doi:http://dx.doi.org/10.1016/S1359-6462(01)01239-8 (2002).

60 Sakai, T., Saito, Y., Hirano, K. & Kato, K. Deformation and Recrystallization Behavior of Low Carbon Steel in High Speed Hot Rolling. *Transactions of the Iron and Steel Institute of Japan* **28**, 1028-1035, doi:10.2355/isijinternational1966.28.1028 (1988).

61 Pippan, R. *et al.* Saturation of Fragmentation During Severe Plastic Deformation. *Annual Review of Materials Research* **40**, 319-343, doi:10.1146/annurev-matsci-070909-104445 (2010).

62 Pippan, R., Wetscher, F., Hafok, M., Vorhauer, A. & Sabirov, I. The Limits of Refinement by Severe Plastic Deformation. *Advanced Engineering Materials* **8**, 1046-1056, doi:10.1002/adem.200600133 (2006).

63 Yu, T., Hansen, N., Huang, X. & Godfrey, A. Observation of a New Mechanism Balancing Hardening and Softening in Metals. *Materials Research Letters* **2**, 160-165, doi:10.1080/21663831.2014.886308 (2014).

64 Gifkins, R. C. Grain-boundary sliding and its accommodation during creep and superplasticity. *Metallurgical Transactions A* **7**, 1225-1232, doi:10.1007/bf02656607 (1976).

65 Warner, D. H. & Molinari, J. F. Effect of normal loading on grain boundary migration and sliding in copper. *Modelling and Simulation in Materials Science and Engineering* **16**, 075007, doi:10.1088/0965-0393/16/7/075007 (2008).

66 Kokawa, H., Watanabe, T. & Karashima, S. Sliding behavior and dislocation structures in aluminium grain boundaries. *Philosophical Magazine A* **44**, 1239-1254, doi:10.1080/01418618108235806 (2006).

67 Van Swygenhoven, H. & Derlet, P. M. Grain-boundary sliding in nanocrystalline fcc metals. *Physical Review B* **64**, doi:10.1103/PhysRevB.64.224105 (2001).

68 Fedorov, A. A., Gutkin, M. Y. & Ovid'ko, I. A. Transformations of grain boundary dislocation pile-ups in nano- and polycrystalline materials. *Acta Materialia* **51**, 887-898, doi:10.1016/s1359-6454(02)00433-0 (2003).

69 Renk, O., Hohenwarter, A., Wurster, S. & Pippan, R. Direct evidence for grain boundary motion as the dominant restoration mechanism in the steady-state regime of extremely cold-rolled copper. *Acta Mater* **77**, 401-410, doi:10.1016/j.actamat.2014.06.010 (2014).

70 Yu, T., Hansen, N. & Huang, X. Recovery by triple junction motion in aluminium deformed to ultrahigh strains. *Proceedings of the Royal Society A: Mathematical, Physical and Engineering Sciences* **467**, 3039-3065, (2011).

71 Yu, T., Hansen, N. & Huang, X. Recovery mechanisms in nanostructured aluminium. *Philosophical Magazine* **92**, 4056-4074, doi:10.1080/14786435.2012.704418 (2012).

72 Gottstein, G., King, A. H. & Shvindlerman, L. S. The effect of triple-junction drag on grain growth. *Acta Materialia* **48**, 397-403, (2000).

73 Gottstein, G., Ma, Y. & Shvindlerman, L. Triple junction motion and grain microstructure evolution. *Acta Materialia* **53**, 1535-1544, doi:10.1016/j.actamat.2004.12.006 (2005).

74 Zöllner, D. & Rios, P. R. Investigating the von Neumann–Mullins relation under triple junction dragging. *Acta Materialia* **70**, 290-297, doi:10.1016/j.actamat.2014.02.039 (2014).

75 Protasova, S. G., Gottstein, G., Molodov, D. A., Sursaeva, V. G. & Shvindlerman, L. S. Triple junction motion in aluminum tricrystals. *Acta Materialia* **49**, 2519-2525, doi:http://dx.doi.org/10.1016/S1359-6454(01)00142-2 (2001).

76 Czubayko, U., Sursaeva, V. G., Gottstein, G. & Shvindlerman, L. S. Influence of triple junctions on grain boundary motion. *Acta Materialia* **46**, 5863-5871, doi:http://dx.doi.org/10.1016/S1359-6454(98)00241-9 (1998).

77 Shvindlerman, L. S. & Gottstein, G. Grain boundary and triple junction migration. *Materials Science and Engineering: A* **302**, 141-150, doi:http://dx.doi.org/10.1016/S0921-5093(00)01366-6 (2001).

78 Yu, T., Hansen, N. & Huang, X. Linking recovery and recrystallization through triple junction motion in aluminum cold rolled to a large strain. *Acta Materialia* **61**, 6577-6586, doi:10.1016/j.actamat.2013.07.040 (2013).

79 Winning, M., Gottstein, G. & Shvindlerman, L. S. Stress induced grain boundary motion. *Acta Materialia* **49**, 211-219, doi:http://dx.doi.org/10.1016/S1359-6454(00)00321-9 (2001).

80 Exell, S. F. & Warrington, D. H. Sub-grain boundary migration in aluminium. *Philosophical Magazine* **26**, 1121-1136, doi:10.1080/14786437208227368 (1972).

81 Beck, P. A. & Sperry, P. R. Strain Induced Grain Boundary Migration in High Purity Aluminum. *Journal of Applied Physics* **21**, 150-152, doi:doi:http://dx.doi.org/10.1063/1.1699614 (1950).

82 Beck, P. A., Sperry, P. R. & Hu, H. The Orientation Dependence of the Rate of Grain Boundary Migration. *Journal of Applied Physics* **21**, 420, doi:10.1063/1.1699676 (1950).

83 Read, W. T. & Shockley, W. Dislocation Models of Crystal Grain Boundaries. *Physical Review* **78**, 275-289, doi:10.1103/PhysRev.78.275 (1950).

84 Li, C. H., Edwards, E. H., Washburn, J. & Parker, E. R. Stress-induced movement of crystal boundaries. *Acta Metallurgica* **1**, 223-229, (1953).

85 Winning, M., Gottstein, G. & Shvindlerman, L. S. On the mechanisms of grain boundary migration. *Acta Materialia* **50**, 353-363, doi:http://dx.doi.org/10.1016/S1359-6454(01)00343-3 (2002).

86 Cahn, J. W., Mishin, Y. & Suzuki, A. Coupling grain boundary motion to shear deformation. *Acta Materialia* **54**, 4953-4975, doi:10.1016/j.actamat.2006.08.004 (2006).

87 Rupert, T. J., Gianola, D. S., Gan, Y. & Hemker, K. J. Experimental Observations of Stress-Driven Grain Boundary Migration. *Science* **326**, 1686 (2009).

88 Jin, M., Minor, A. M., Stach, E. A. & Morris, J. W. Direct observation of deformation-induced grain growth during the nanoindentation of ultrafine-grained Al at room temperature. *Acta Materialia* **52**, 5381-5387, doi:10.1016/j.actamat.2004.07.044 (2004).

89 Mompiou, F. *et al.* In situ TEM observation of grain annihilation in tricrystalline aluminum films. *Acta Materialia* **60**, 2209-2218, doi:10.1016/j.actamat.2011.12.013 (2012).

90 Mompiou, F., Caillard, D. & Legros, M. Grain boundary shear–migration coupling—I. In situ TEM straining experiments in Al polycrystals. *Acta Materialia* **57**, 2198-2209, doi:10.1016/j.actamat.2009.01.014 (2009).

91 Russell, A. M., Chumbley, L. S. & Tian, Y. Deformation Processed Metal–Metal Composites. *Advanced Engineering Materials* **2**, 11-22, doi:10.1002/(sici)1527-2648(200002)2 (2000).

92 Bachmaier, A. & Pippan, R. Generation of metallic nanocomposites by severe plastic deformation. *International Materials Reviews* **58**, 41-62, doi:10.1179/1743280412y.0000000003 (2013).

93 Raabe, D. *et al.* Metallic composites processed via extreme deformation: Toward the limits of strength in bulk materials. *MRS Bulletin* **35**, 982-991, doi:10.1557/mrs2010.703 (2011).

94 Sauvage, X., Wetscher, F. & Pareige, P. Mechanical alloying of Cu and Fe induced by severe plastic deformation of a Cu–Fe composite. *Acta Materialia* **53**, 2127-2135, doi:10.1016/j.actamat.2005.01.024 (2005).

95 Thilly, L., Véron, M., Ludwig, O. & Lecouturier, F. Deformation mechanism in high strength Cu/Nb nanocomposites. *Materials Science and Engineering: A*

309–310, 510-513, doi:http://dx.doi.org/10.1016/S0921-5093(00)01661-0 (2001).

96 Goto, S., Kirchheim, R., Al-Kassab, T. & Borchers, C. Application of cold drawn lamellar microstructure for developing ultra-high strength wires. *Transactions of Nonferrous Metals Society of China* **17**, 1129-1138, doi:10.1016/s1003-6326(07)60238-6 (2007).

97 Cepeda-Jiménez, C. M., Pozuelo, M., Ruano, O. A. & Carreño, F. Influence of the thermomechanical processing on the fracture mechanisms of high strength aluminium/pure aluminium multilayer laminate materials. *Materials Science and Engineering: A* **490**, 319-327, doi:10.1016/j.msea.2008.01.034 (2008).

98 Jamaati, R. & Toroghinejad, M. R. Manufacturing of high-strength aluminum/alumina composite by accumulative roll bonding. *Materials Science and Engineering: A* **527**, 4146-4151, (2010).

99 Li, L., Nagai, K. & Yin, F. Progress in cold roll bonding of metals. *Science and Technology of Advanced Materials* **9**, 023001, doi:10.1088/1468-6996/9/2/023001 (2008).

100 Hawkins, R. & Wright, J. C. Observations on the deformation properties of sandwich materials. *International Journal of Mechanical Sciences* **14**, 875-878, doi:http://dx.doi.org/10.1016/0020-7403(72)90046-X (1972).

101 Atkins, A. G. & Weinstein, A. S. The deformation of sandwich materials. *International Journal of Mechanical Sciences* **12**, 641-657, doi:http://dx.doi.org/10.1016/0020-7403(70)90094-9 (1970).

102 Valiev, R. Z. *et al.* The Innovation Potential of Bulk Nanostructured Materials. *Advanced Engineering Materials* **9**, 527-533, doi:10.1002/adem.200700078 (2007).

103 De Giorgi, M. Residual stress evolution in cold-rolled steels. *International Journal of Fatigue* **33**, 507-512, doi:10.1016/j.ijfatigue.2010.10.006 (2011).

104 Semiatin, S. L. & Piehler, H. R. Formability of sandwich sheet materials in plane strain compression and rolling. *Metallurgical Transactions A* **10**, 97-107, doi:10.1007/bf02686412 (1979).

105 Hwang, Y.-M., Hsu, H.-H. & Lee, H.-J. Analysis of plastic instability during sandwich sheet rolling. *International Journal of Machine Tools and Manufacture* **36**, 47-62, doi:http://dx.doi.org/10.1016/0890-6955(95)92628-C (1996).

106 Raabe, D., Ohsaki, S. & Hono, K. Mechanical alloying and amorphization in Cu–Nb–Ag in situ composite wires studied by transmission electron microscopy and atom probe tomography. *Acta Materialia* **57**, 5254-5263, doi:10.1016/j.actamat.2009.07.028 (2009).

107 Raabe, D. & Hangen, U. Observation of amorphous areas in a heavily cold rolled Cu-20 wt% Nb composite. *Materials Letters* **22**, 155-161, doi:http://dx.doi.org/10.1016/0167-577X(94)00248-7 (1995).

108 Ohsaki, S., Kato, S., Tsuji, N., Ohkubo, T. & Hono, K. Bulk mechanical alloying of Cu–Ag and Cu/Zr two-phase microstructures by accumulative roll-bonding process. *Acta Materialia* **55**, 2885-2895, doi:10.1016/j.actamat.2006.12.027 (2007).

109 Sauvage, X. *et al.* Solid state amorphization in cold drawn Cu/Nb wires. *Acta Materialia* **49**, 389-394, doi:http://dx.doi.org/10.1016/S1359-6454(00)00338-4 (2001).

110 Sauvage, X., Thilly, L., Lecouturier, F., Guillet, A. & Blavette, D. FIM and 3D atom probe analysis of Cu/Nb nanocomposite wires. *Nanostructured Materials* **11**, 1031-1039, doi:http://dx.doi.org/10.1016/S0965-9773(99)00386-4 (1999).

111 Wang, T. L., Li, J. H., Tai, K. P. & Liu, B. X. Formation of amorphous phases in an immiscible Cu–Nb system studied by molecular dynamics simulation and ion beam mixing. *Scripta Materialia* **57**, 157-160, doi:http://dx.doi.org/10.1016/j.scriptamat.2007.03.006 (2007).

112 Ashkenazy, Y., Vo, N. Q., Schwen, D., Averback, R. S. & Bellon, P. Shear induced chemical mixing in heterogeneous systems. *Acta Materialia* **60**, 984-993, doi:10.1016/j.actamat.2011.11.014 (2012).

113 Sauvage, X., Wilde, G., Divinski, S. V., Horita, Z. & Valiev, R. Z. Grain boundaries in ultrafine grained materials processed by severe plastic deformation and related phenomena. *Materials Science and Engineering: A* **540**, 1-12, doi:10.1016/j.msea.2012.01.080 (2012).

114 Mozaffari, A., Danesh Manesh, H. & Janghorban, K. Evaluation of mechanical properties and structure of multilayered Al/Ni composites produced by accumulative roll bonding (ARB) process. *Journal of Alloys and Compounds* **489**, 103-109, doi:10.1016/j.jallcom.2009.09.022 (2010).

115 Min, G., Lee, J.-M., Kang, S.-B. & Kim, H.-W. Evolution of microstructure for multilayered Al/Ni composites by accumulative roll bonding process. *Materials Letters* **60**, 3255-3259, doi:10.1016/j.matlet.2006.03.001 (2006).

116 Segal, V. M. Materials processing by simple shear. *Materials Science and Engineering: A* **197**, 157-164, doi:http://dx.doi.org/10.1016/0921-5093(95)09705-8 (1995).

117 Cui, Q. & Ohori, K. Grain refinement of high purity aluminium by asymmetric rolling. *Materials Science and Technology* **16**, 1095-1101, doi:doi:10.1179/026708300101507019 (2000).

118 Deltombe, R., Dubar, M., Dubois, A. & Dubar, L. A new methodology to analyse iron fines during steel cold rolling processes. *Wear* **254**, 211-221, doi:10.1016/s0043-1648(03)00005-x (2003).

119 Güzel, A. *et al.* A new method for determining dynamic grain structure evolution during hot aluminum extrusion. *Journal of Materials Processing Technology* **212**, 323-330, doi:10.1016/j.jmatprotec.2011.09.018 (2012).

3. Experimentation and characterization methods

3.1. Introduction

The aim of this chapter is to introduce the experimental methods, characterization tools and the materials which will be used in the thesis. The first section will briefly describe the different deformation techniques used for the experiments. The second section will explain the characterization tools which have been used for the analysis of the material. And the third section will introduce the materials and their composition.

3.2. Deformation techniques

3.2.1. Accumulated Extrusion (AccumEx)

3.2.1.1. Process description

Accumulated Extrusion or AccumEx is a plane strain compression deformation process which works on the principle of Accumulative Roll Bonding (ARB). It is a novel severe plastic deformation process, introduced for the first time in this thesis [1]. The special design of the process helps in achieving ultra-high deformation strains within the sample. The schematic representation of the process is shown in Figure 3-1. The process works with 4 sheets of metal for each deformation pass. The dimensions of the sheets can be seen in the Figure 3-1. Stage I is cleaning and surface preparation, stage II is stacking and stage III is extrusion. The dimensions of the material after extrusion are 20x5x200 mm^3. This extruded sheet is then cut into 4 sheets of dimensions 20x5x50 mm^3. This is stage IV. The cut sheets are cleaned, re-stacked and re-extruded which can be repeated n number of times. A small flexibility is available during the first deformation pass. The count of the number of sheets is not constrained to 4. N number of sheets can be used as the starting material but the stacked dimension should comply with the global dimensions of stage III, 20x20x50 mm^3. Nevertheless, after 1 deformation pass, the sheet dimensions are constrained to the values shown in stage I.

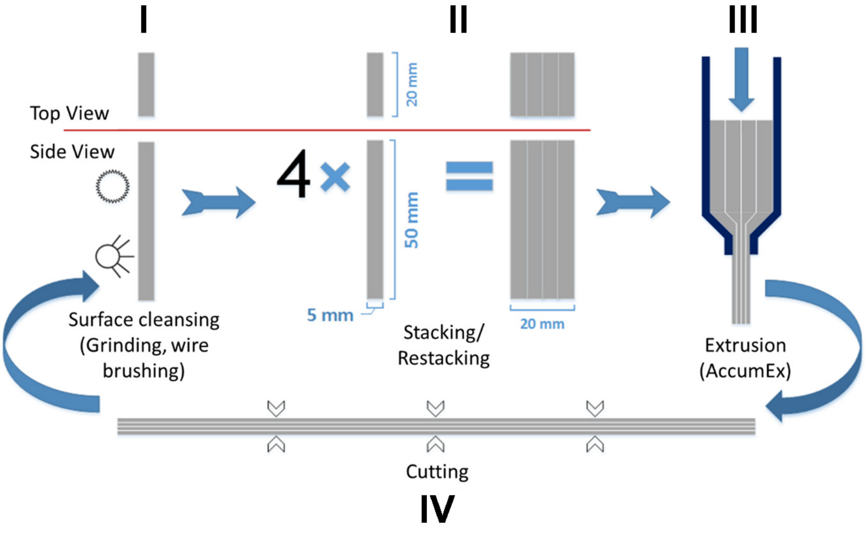

Figure 3-1 Schema of different stages of the AccumEx process

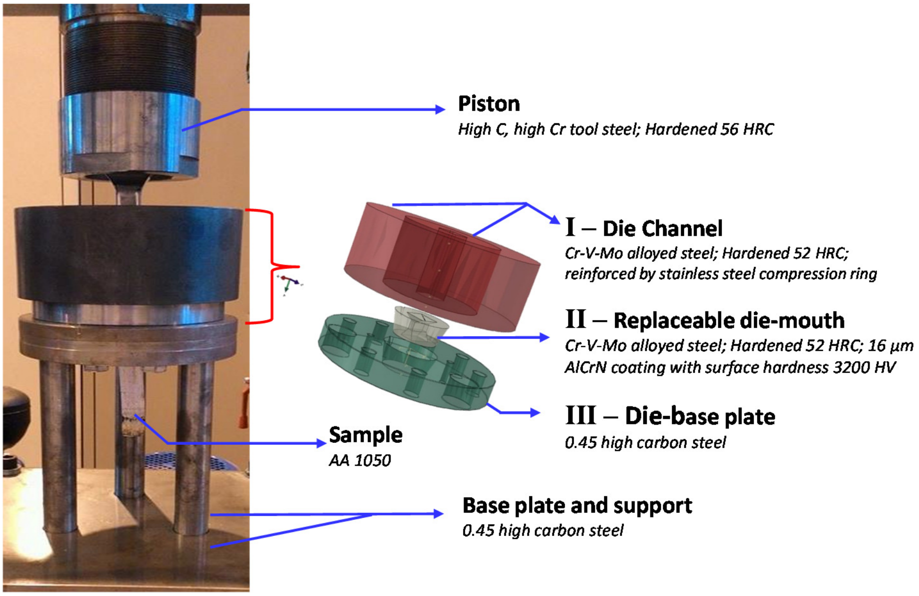

Figure 3-2 Experimental set-up of AccumEx

The experimental set-up of the AccumEx process is shown in Figure 3-2. The set-up is divided into four parts – piston, die, base plate and support. The die has three sub-parts – die-channel, replaceable die-mouth and die-base plate. The material is loaded in the die-channel and extruded at the die-mouth which is mounted on the die-base plate. The use of a replaceable die-mouth serves two purposes – it reduces the compressive stress on the die-plate and allows an easy replacement to perform experiments with different die angles (90° and 120°). The parts are marked in Figure 3-2. The replaceable die-mouth is made of a Cr-V-Mo alloy steel, hardened up to 52 HRC. The surface of the die is coated with AlCrN (by Balzers Oerlikon). The thickness of the coating is 16 um and the obtained surface hardness is around 3200 HV.

3.2.1.2. Process parameters

The processing of material in AccumEx consists of 4 steps as mentioned in Figure 3-1. Stage I – cleaning is an important step and it is done to remove any impurities present on the surface of the material. All the four sides of the metal sheets, which are subjected to AccumEx, are manually grinded using 80 grade SiC abrasive sheets. Followed by it, a manual wire brushing with 0.3 mm diameter steel wire is performed to scratch away the oxide layer on the metal sheets. Immediately after the wire brushing, the sheets are degreased and stored in ethanol/iso-proponal to guarantee minimum oxidation until final processing. Further, this surface preparation imparts high roughness on the sample surfaces which is expected to be useful in achieving good interlocking and bonding at the interfaces. The material is ready for stage II – stacking. 4 or more (depending on the experiment) sheets are assembled together and lubricated using MoS_2. The lubricant is applied manually using a sponge roller, but only along two sides of the assembled metal sheets. The faces where the interfaces are visible are not lubricated to be sure of minimal contamination at the interface regions, as it might hinder the bonding between the metal sheets. In stage III, the prepared assembly of metal sheets is extruded at room temperature and at a plunger velocity of 6mm/min. The die with a semi-die angle of 45° has been used for all the experiments (chosen based on trial and error experiments between 45° and 60°). The successfully extruded sheet is then ready for stage 4, where the sheet is cut in to 3 or 4 shorter sheets of initial dimensions using SiC cutting blade. The cut samples are further processed again for the 4 stages and the cycle continues up to N deformation passes.

3.2.1.3. Imposed strain

The imposed true strain ($\varepsilon_{\text{true}}$) and equivalent von-Mises strain ($\varepsilon_{\text{equiv}}$) during the AccumEx after each deformation pass can be calculated as,

$$\varepsilon_{\mathrm{true}} = \ln(\mathrm{ER}) * N \tag{3-1}$$

$$\varepsilon_{\mathrm{equiv}} = {}^{2}/_{\sqrt{3}} * \ln(\mathrm{ER}) * N \tag{3-2}$$

$$\mathrm{ER} = \frac{\mathrm{A_o}}{\mathrm{A}} \tag{3-3}$$

Where, ER is the extrusion ratio, $\mathrm{A_o}$ is the initial cross-sectional area and A is the final cross-sectional area. For N number of deformation passes, the strain value multiplies by a factor N.

In the present case, the applied geometrical reduction is 75 %. Therefore, $\mathrm{ER} = 4$. Now, applying the value of ER in equation (3-1) and equation (3-2), $\varepsilon_{\mathrm{true}}$ and $\varepsilon_{\mathrm{equiv}}$ can be calculated as 1.38*n and 1.64*n. With increasing deformation passes, the strain increases linearly.

3.2.1.4. Sample terminology

The sample reference system of the material before and after deformation is very important for characterization purposes. So, the coordinates of the sample are defined and represented in Figure 3-3. The figure also shows the names of different planes of the sample. ED is the extrusion direction, ND is the normal direction and TD is the transverse direction. After every deformation pass, the direction of ED is maintained for the sub-sequent deformation passes.

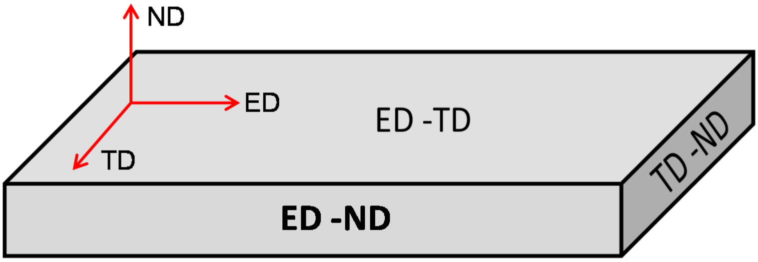

Figure 3-3 Lexicon of sections with respect to sample reference frame

3.2.2. Equal Channel Angular Pressing (ECAP)

ECAP is a very established SPD technique known for decades [2]. This technique will be used in this thesis to do comparative analysis with AccumEx with respect to the obtained microstructural and mechanical properties as a function of equivalent von-Mises strain. A short description of this process will be presented in this section.

3.2.2.1. Process description

ECAP is a simple shear deformation process. The process produces very little dimensional changes to the sample. Therefore, the material being deformed can be re-deformed multiple times. This helps in achieving ultra-high strains. It has been briefly described in Chapter 2. Of the different strain paths, route C will be used for the current study.

The ECAP set-up consists mainly of 2 parts – Die and Plunger. The die is divided into 3 sub-parts. They are the heating mantle, die support and central die. The die picture and a schematic representation of the die parts are shown in Figure 3-4 [3]. The heating mantle (1) is used for high temperature deformation of materials. The die support (2) is a tapered structure that supports the main central die (3), where the deformation takes place. The material is inserted via the inlet within the central die (3) which after extrusion, comes out of the outlet crossing through all the sub-parts (1, 2 and 3). The plunger, central die and die support are made of hardened tool steel. The dimensions of the material being processed are shown in Figure 3-5.

3.2.2.2. Process parameters

ECAP experiments performed in this thesis are all done at room temperature. The die-angles of the die used are 90° and 0° for Φ and Ψ, shown in Figure 3-5. The velocity of the plunger is maintained at 5 mm/min. MoS_2 lubricant is applied on all sides of the round billet before deformation.

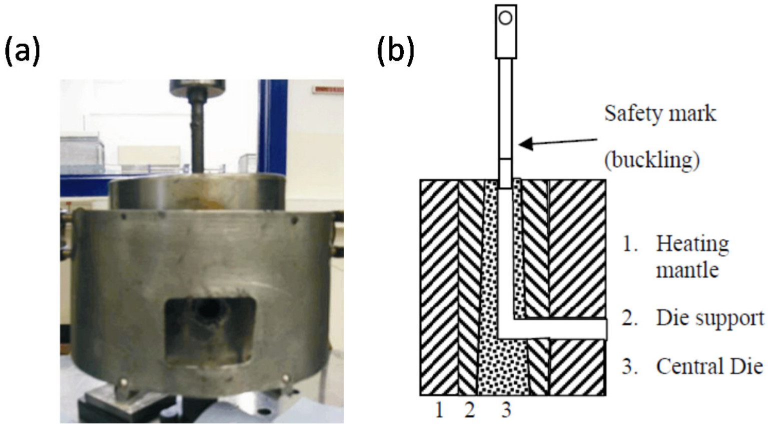

Figure 3-4 (a) ECAP experimental set-up; (b) schematic representation of the die [3]

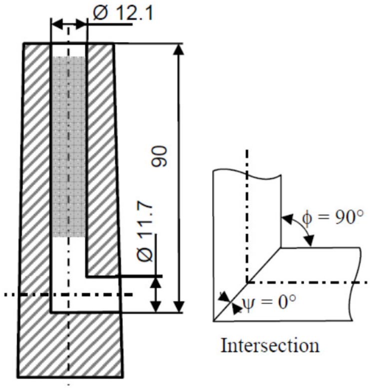

Figure 3-5 Die and sample dimensions of the ECAP experiment [3]

3.2.2.3. Imposed strain

ECAP is a simple shear deformation process. The imposed shear strain and the equivalent von-Mises strain can be calculated as,

$$\gamma = \mathbf{2}cot\left(\frac{\Phi + \Psi}{2}\right) + \Psi cosec\left(\frac{\Phi + \Psi}{2}\right) \tag{3-4}$$

$$\varepsilon_{equiv} = N/\sqrt{3}\left[2cot(\frac{\Phi + \Psi}{2}) + \Psi cosec(\frac{\Phi + \Psi}{2})\right] \tag{3-5}$$

Where, γ is the shear strain, Φ and Ψ are the die angles of the ECAP (Figure 3-5) and N is the number of deformation passes.[4]

In the current configuration set-up, $\Phi = 90°$ and $\Psi = 0°$. Substituting these values in equation (3-4) and (3-5), the shear strain can be calculated as 1 and the von-Mises equivalent strain can be calculated as 1.15*N. The magnitude of the strain increases linearly as a function of the number of passes.

3.2.2.4. Sample terminology

Similar to AccumEx, the sample reference system is very important for characterization purpose. The definition of the sample coordinates is represented schematically in Figure 3-6. ED is the extrusion direction, ND is normal direction and TD is the transverse direction. Also after every deformation pass, the ED is consistently maintained along the same direction for the sub-sequent deformation passes.

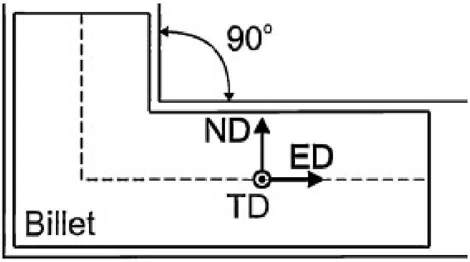

Figure 3-6 Lexicon of sample longitudinal-section showing its corresponding sample reference axes

3.3. Characterization methods

Several characterization tools have been used in the thesis to evaluate the material properties. For simplification purpose, they have been classified as – microstructural analysis, texture analysis, mechanical testing and others. The different tools used in each classification and their technical specification will be discussed in this section.

3.3.1. Microstructural analysis

The major part of the thesis focuses on the microstructural aspects of the material being studied. Three different types of microstructural images can be found in this thesis – Optical, Scanning Electron Microscopy (SEM) and Electron Back Scattered Diffraction (EBSD).

Optical images are acquired using a Leitz-Metalloplan light microscope. SEM images were acquired in FEI NOVA 450 NanoSEM using a SE detector. EBSD is a SEM based tool. It uses a EDAX Hikari super camera with a phosphor screen, attached to the FEI NOVA 450. Data collection is performed using TSL OIM data collection software. Measurements were done at a beam voltage of 20 kV, spot size 6 on a 70° tilted sample surface. A step size of 0.1 µm was used for fine scans and < 0.5 µm for coarse scan. The scan type is chosen based on the expected grain size and application of the measurement. The required images are later obtained by post-processing using the TSL OIM analysis software.

Two other SEM based complementary tools have also been used in this thesis – Energy Dispersive Spectroscopy (EDS) and Focussed Ion Beam (FIB). EDS is used to perform phase analysis which is coupled with EBSD to improve the quality of the measurements. It uses a EDAX detector, attached to FEI NOVA 450. FIB is used for milling sample surfaces to examine cross-sections of specific features. It is done using FEI NOVA 600 Nanolab, on a 52° tilted sample surface at an operating voltage of 30 kV. Rough milling is done at a current of 20 nA and fine mailing at 6.5 nA.

All the samples which are characterized using SEM and EBSD, were finely polished with mirror-finish prior to their characterization. This is done stage by stage using SiC grade grinding papers, diamond suspension and finally with 0.25 µm OPS colloidal silica suspension. At times etching for 1 min by immersing in Keller's reagent is also done. Longer polishing duration with OPS colloidal silica suspension is preferred to obtain better Kikuchi patterns [5].

3.3.2. Texture analysis

The crystallographic texture of the material can be measured at two levels – bulk and micro.

Bulk measurements provides information of the average texture of the whole sample surface under study. They are done using X-ray diffraction (XRD). It is a Siemens D-500 goniometer type machine which uses a Cu-Kα monochromatic source. Four pole figures - {111} {220}, {200} and {311} are measured. They are background corrected and post-processed using MTM-FHM software. Appropriate rotations and symmetry reinforcements are applied using this software and the ODF is calculated. ODFs are generally plotted as phi1 or φ2 sections depending on the crystal structure – BCC or FCC respectively.

Micro measurements provide region specific texture information which can be used for spatial studies. The measurement range can vary from millimetres to nanometres. It is done using EBSD. With the help of the TSL OIM analysis software, the orientation information of the scanned region, obtained from the EBSD measurements is used to calculate and plot the respective ODF sections.

3.3.3. Mechanical testing

The mechanical properties of the material processed in the thesis are measured using three methods – Vickers' micro-hardness, tensile test, compression test.

Vickers' micro-hardness is a very standard technique used in both AccumEx and ECAP processed samples. The measurements are performed with a FV-700, Future-Tech Corp machine. The samples are indented using a 300 g load cell with a dwell time of 15 s. The values are plotted as HV0.3.

Tensile tests are the main measurement technique to evaluate the mechanical properties of the AccumEx deformed samples. A non-conventional dog-bone design has been used due to the sample constrains. The dimensions of the design are shown in Figure 3-7 . The tests are performed using an INSTRON 4467 universal tensile tester at a strain rate of 10^{-3} /s (30 KN load cell). An extensometer is used to log strain instantaneously. Yield strength (Y.S), Ultimate tensile strength (U.T.S) and elongation to failure ($\varepsilon_{failure}$) are calculated for each measurement.

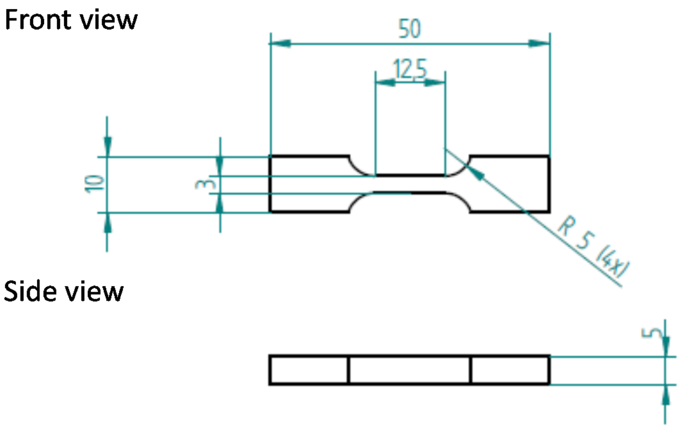

Figure 3-7 - Drawing of the tensile geometry used for tensile tests; All dimensions in mm

Compression tests are performed for the ECAP deformed samples. The design of the sample is very simple. It is a cylindrical sample with H/D (height to diameter) ratio 1.5. The tests are performed on an INSTRON 4505 with a load cell of 30 KN at a strain rate of 10^{-3} /s. The Yield strength (Y.S) is calculated for each measurement.

3.3.4. Others

Two other characterization tools are also used in this work – Inductively coupled plasma optical emission spectroscopy (ICP-OES) and x-ray tomography (µCT). The Varian 720 ES ICP-OES has been used to characterize the starting material for their chemical composition. A Tomohawk µCT has been used to evaluate the robustness of the material being processed by AccumEx.

3.3.5. Reference frame

To interpret the EBSD and texture results, knowing the sample reference frame is very important. In EBSD, the measurement is always performed using 3 sample reference axes – Axis 1, Axis 2 and Axis 3, as shown in Figure 3-8(a). Orientation maps plotted by the software show crystal planes perpendicular to Axis 3. However, the three axes can differ with respect to the section plane being analysed (section 3.2.1.4 and 3.2.2.4). Therefore, care must be taken to keep track of the sample reference axes in order to interpret the results and apply rotations using the correct reference frame.

Similarly, in bulk texture measurement using XRD, the software has a pre-defined sample reference frame (Figure 3-8(b)). The measurement positioning of the sample should match the sample reference frame or care should be taken to rotate the actual sample reference frame to match with the software's sample reference frame, which can be done post-measurement.

3.4. Materials and composition

In this section, the materials which have been studied in the thesis will be introduced. Al and Cu are the materials that have been chosen. This is mainly because, a lots of literature can be found on the SPD of the two metals and moreover, Al is one of the easiest material to deform. Further, Cu has a similar crystal structure like Al which reduces any complexity in the system. The supplier for both the metals is Salomons Metalen, Groningen, Netherlands.

3.4.1. Aluminium

The material used in this study is AA 1050, commercial purity grade aluminium. The Al purity is approximately 99.5 %. The exact composition of the alloy is determined by ICP analysis and presented in Table 3-1. The standard deviation reported for ICP analysis is normally around 10 %.

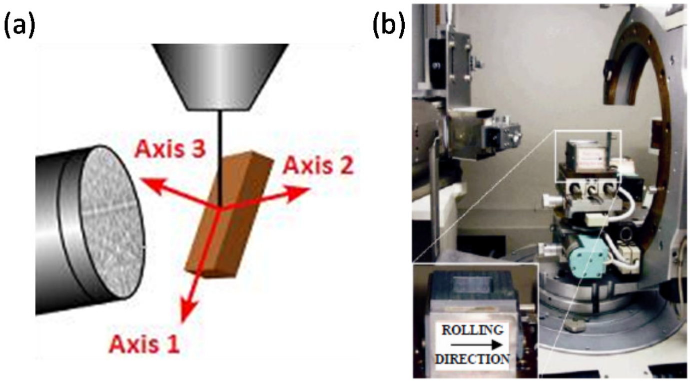

Figure 3-8 (a) EBSD measurement schematic showing the different sample reference axes with respect to measurement plane [6]; (b) XRD measurement tool showing sample being mounted with its rolling/extrusion directed towards right [3]

Table 3-1 Composition of AA 1050

Elements	Cu	Fe	Mg	Mn	Si	Ti	Zn	Ni	Cr	Al
Wt %	0.02	0.18	0.03	0.02	0.02	0.005	0.0015	0.005	0.005	rest

The material is received in sheet and cylindrical bar forms for AccumEx and ECAP respectively.

3.4.2. Copper

We used a commercial pure oxygen free (OF) copper with a commercial purity of 99.65 %. The exact composition of the material is determined by ICP analysis. It is tabulated in Table 3-2. The standard deviation reported for ICP analysis is normally around 10 %.

Table 3-2 Composition of of Cu

Elements	Ag	Al	As	Fe	Ni	Pb	Sn	Zn	Cu
Wt %	0.06	0.006	0.025	0.010	0.042	0.021	0.006	0.006	rest

The material is received in sheet, cylindrical tube and bar forms. Sheets are used in AccumEx and the tubes and bars in ECAP experiments.

REFERENCES

1 Muralidharan, G. K. and B. Verlinden (2016). "Novel severe plastic deformation technique—accumulated extrusion (AccumEx)." Materials Science and Technology: **32(6)**, 547-555.

2 Segal, V. M. Materials processing by simple shear. *Materials Science and Engineering: A* **197**, 157-164, doi:http://dx.doi.org/10.1016/0921-5093(95)09705-8 (1995).

3 Poortmans, S. From microstructure towards mechanical behavior of ultrafine grained aluminium alloys. *Ph.D. dissertation, KU Leuven* (2008).

4 Valiev, R. Z. & Langdon, T. G. Principles of equal-channel angular pressing as a processing tool for grain refinement. *Progress in Materials Science* **51**, 881-981, doi:10.1016/j.pmatsci.2006.02.003 (2006).

5 Vander Voort, G., Van Geertruyden, W., Dillon, S. & Manilova, E. Metallographic preparation for electron backscattered diffraction. *Microscopy and Microanalysis* **12**, 1610-1611 (2006).

6 EDAX. TSL OIM analysis 7.1 manual (2016).

4. Investigation of AA 1050 material processed by AccumEx

4.1. Introduction

Four decades of SPD research have been performed on different materials and the efficiency of the SPD process in producing UFG materials is in-debatable [1-8]. A key milestone in crossing borders from lab-scale to industrial level of SPD processing was the introduction of Accumulated Roll Bonding (ARB). However, also this process has limitations. The thickness of the starting material that can be processed has to be less than 2 mm. The bonding ability of the material is at the limit with respect to the applied deformation. A reduction ratio of more than 50 % is the rule of thumb to achieve sound bonding and at even higher ratios, the robustness of the bonding can be improved drastically [9,10]. Therefore, the control over the bond quality is a challenge in ARB.

Addressing these disadvantages, a new SPD technique - Accumulated Extrusion a.k.a AccumEx is introduced [11]. The detailed description of the process is explained in section 3.2.1. In this chapter, the testing of this process will be done. AccumEx experiments will be carried out using a commercial pure aluminium alloy. The property evolution of the material will be investigated at different stages of deformation.

4.2. Experiment

AA 1050 material of composition shown in table 3.1 is used. AccumEx deformation is carried out with this material up to 8 deformation passes. The dimensions of the starting material and after extrusion are shown in Figure 4-1. The material is used in the as-received starting condition - hot rolled; half-hardened state. Surface preparation and extrusion is carried out using the same parameters mentioned in section 3.2.1.

The equivalent von-Mises strain imposed in the sample is calculated using equation 3.2. The increasing strain has been calculated and is presented in Figure 4-2, as a function of number of deformation passes. A cumulative equivalent strain of 13.12 is achieved after 8 passes (without taking into account shear).

The number of laminates produced after each deformation pass can be calculated as 4^N, with n being the number of passes. Based on this, after 8 passes, more than

65000 layers are expected to be formed. This corresponds to an average theoretical layer thickness of approximately 80nm.

Characterization is performed for these AccumEx deformed material. Their microstructure, texture and mechanical properties will be studied and discussed in the following sections.

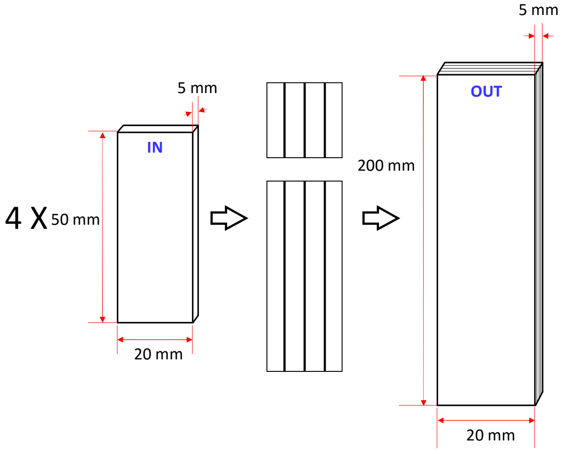

Figure 4-1 Input and output sample dimensions

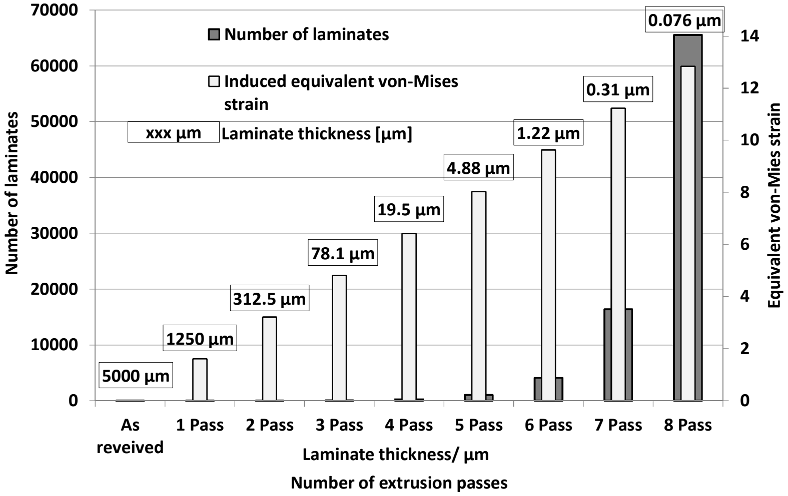

Figure 4-2 Number of extrusion passes vs Number of laminate sheets vs Lamellar thickness

4.3. Results

4.3.1. Microstructure analysis

4.3.1.1. Interfaces

SEM images of the interfaces at different stages are shown in Figure 4-3. All the images are captured along the ED-ND section. Interfaces are formed by mechanical bonding between the stacked material after deformation. With increasing number of deformation passes, the volume fraction of these interfaces increases. The formation of these interfaces is not clearly understood but several theories exist [12,13]. However, these microstructural features play a crucial role in the sturdiness of the material.

Figure 4-3(a-d) shows the pictures of interfaces. They were captured using SE contrast mode in SEM, after polishing and etching. Up to 4 passes, the interfaces remain straight. But after 4 passes severe bending is seen. The inclination is around 15 – 30° with respect to ED. The reason for this can be due to the reducing thickness of the laminates. The number of laminates increases by 4^N after each deformation pass. After 4 passes, the theoretical laminate thickness becomes 20 µm which further reduces to as low as 80 nm after 8 passes. Therefore, any strain in-homogeneity has a direct impact on the structure of the interfaces. At regions of higher bending, several defects such as macroscopic delamination and microscopic interface cracks are observed.

In another picture, at a slightly higher magnification Figure 4-3(d), due to effect of etching, the behavior of the grains locally at the interface can be seen. The grains seem to bend away from the interface. This gives the impression that a hard material is present at the site and deflects the flow of the material away from the interface. Based on literature evidence, it can be oxides entrapped during the deformation, however it was not possible to prove this using EDS analysis. So, a FIB sectioning is performed at this interface region (ED-ND section) to see the TD-ND section under the ED-ND plane (Figure 4-3 (e)). The TD-ND section that the defect is limited mostly to the surface level. The depth of the defect along TD is seen to be approximately 3.8 µm. However, such small defects might possibly pave the way to develop interface defects with increasing number of passes.

The robustness of the prepared samples is estimated using Tomohawk µCT measurement system. The measurement settings that were used are shown in Table 4-1. It is seen that up to 4 passes, the samples produced are defect free (Figure

4-4 (a), (b), (c)). However, after 8 passes, regions of defects are noticed. The defects are not continuous but rather intermittently seen. The dimensions of the cracks range from 7 µm to 3000 µm in length and approximately 9 to 10 µm in thickness. An example of them is shown in Figure 4-4(d) and (e). They deterred the sample's mechanical strength, especially the samples deformed above 6 passes.

Table 4-1 - µ-CT acquisition settings used for imaging the Al-Al laminates

Voltage	**Current**	**Filter**	**Voxel size**	**Rotation step, angle**	**Frame averaging**
85 kV	0.39mA	No filter	7.4 µm	0.3, over 187°	32 frames

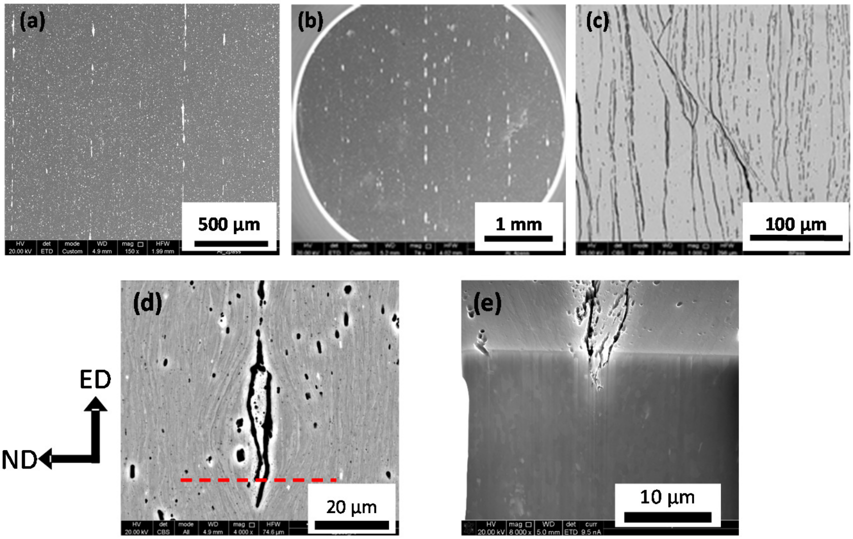

Figure 4-3 SEM images of interfaces - (a) 2 passes; (b) 4 passes; (c) 8 passes; (d) zoomed in 2 pass interface; (e) FIB sectioning of the interface along the red line shown in (d)

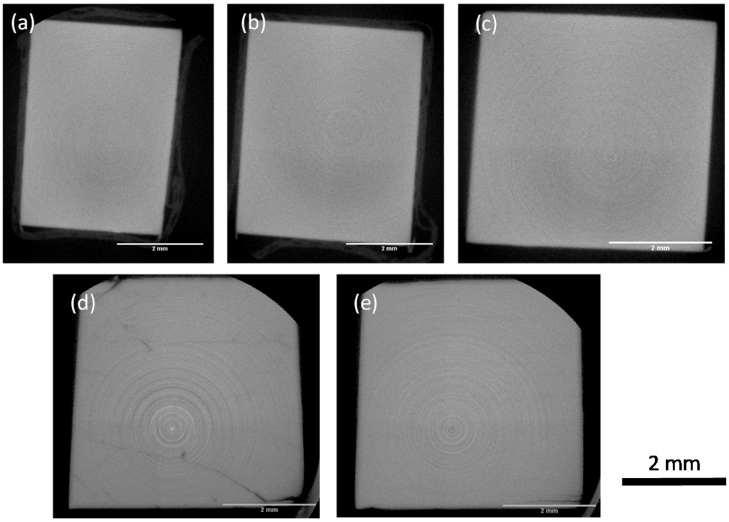

Figure 4-4 μCT cross-section images after (a) 1 pass; (b) 2 pass; (c) 4 pass; (d) 8 pass defect region; (e) 8 pass defect free region

4.3.1.2. Grain analysis

A 3D perception study is performed using EBSD for the as-received, 1, 4 and 8 passes samples. The microstructures and grain refinement are examined in all the three cross-sections for an increasing number of passes. Three EBSD scans of 100 x 100 µm² for strain below 6.4 and of 40 x 40 µm² for strains above 6.4 were used to calculate the average grain dimensions along each section. The grain size is measured manually by the intercept method in all the three planes with the help of ImageJ software [14]. An "equivalent" 3D grain size is calculated by assuming the grain volume as a sphere. It should be noted that, by mentioning grains, it refers to only regions separated by HAGB. HAGB fractions and average misorientation data are obtained with the help of TSL OIM analysis software. Figure 4-5 shows a descriptive analysis of the microstructures. Their corresponding statistical numbers are shown in Table 4-2. The evolution of average grain size, HAGB fraction and average misorientation angle as a function of the number of passes is plotted in Figure 4-6. A saturation is reported in figure 4-5, after 4 passes. This saturation is seen exclusively along the ND. Grain boundary spacing along ND reduced only by 25 % from 4 to 8 passes which corresponds to 650 % equivalent strain. Similarly, the HAGB fraction also showed a drop between 4 and 8 passes. This can be due to increasing formation of sub-structures which increases the LAGB fraction. This phenomenon will be explained with the help of the texture data.

(a) 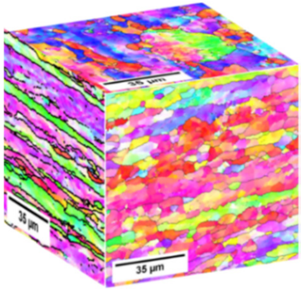	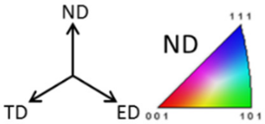 (i) As received The as-received Al sheets are hot rolled sheet; half hardened. They have elongated grains with rod-like morphology extending along ED. The equivalent grain size is 13 µm. Their average HAGB fraction and misorientation are 33 % and 12.07° respectively.	(b) 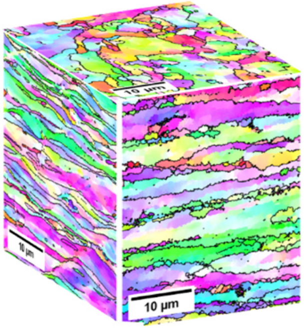	(ii) 1 Pass After 1 pass i.e., a strain of 1.64, severe elongation and fragmentation of grains are noticed. The shape of the grains develop into a pan-cake morphology with formation of several sub-structures (cells, sub-grains, etc.). The average equivalent grain size reduces to 6.5 µm. It corresponds to almost 55 % decrease from the as-received condition. The average HAGB fraction and misorientation angle increased to 45 % and 19° respectively. This implies, several sub-structures are formed which undergo large amounts of rotations developing HAGB.
(c) 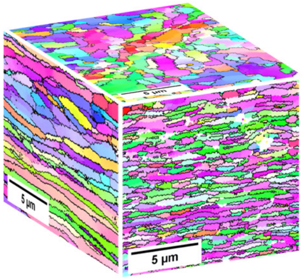	(iii) 4 Passes After 4 passes, i.e., after a strain of 6.56, the grains drastically reduce close to sub-micron level. The average equivalent grain size diameter becomes 1.16 µm. The pan-cake structure is maintained but a substantial reduction in the aspect ratio is seen. The structures become more equi-axed in the ED-TD plane. Bimodal grain structures are noticed along ED, broken and elongated. The average HAGB fraction and misorientation angle increase further to their highest – 77.3 % and 31°.	(d) 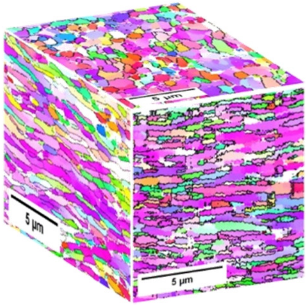	(iv) 8 Passes 8 passes of AccumEx equal a strain of 13.12. The grains retain their pan-cake structure with a very strong saturation seen along ND. The average equivalent grain size diameter reduced to 900 nm which is only 22 % reduction from 4 passes. Further to the point, the average HAGB fraction and misorientation angle reduced to 69% and 26° respectively. The reduction in grain size did not match the macroscopically applied strains.

Figure 4-5 Descriptive analysis of the EBSD images

Table 4-2 Grain size and grain boundary data along all three sections

Cross-Section	**ED-TD**			**ND-ED**			**ND-TD**			**Average grain size (assumed as a sphere)**
Samples (equiv. strain)	**TD [µm]**	**ED [µm]**	**HAGB %**	**ED [µm]**	**ND [µm]**	**HAGB %**	**TD [µm]**	**ND [µm]**	**HAGB %**	
As received (0)	15.4	19.89	20.92	21.59	4.22	37.98	14.14	5.01	34.61	12.8
1 Pass (1.64)	8.21	8.9	33.33	8.1	1.74	57.04	9.1	1.96	45.07	6.35
4 Pass (6.56)	1.33	1.55	66.7	1.35	0.41	84.34	1.36	0.34	78.66	1.14
8Pass (13.12)	1.13	1.23	62.5	0.98	0.31	74.6	1.02	0.35	68.33	0.9

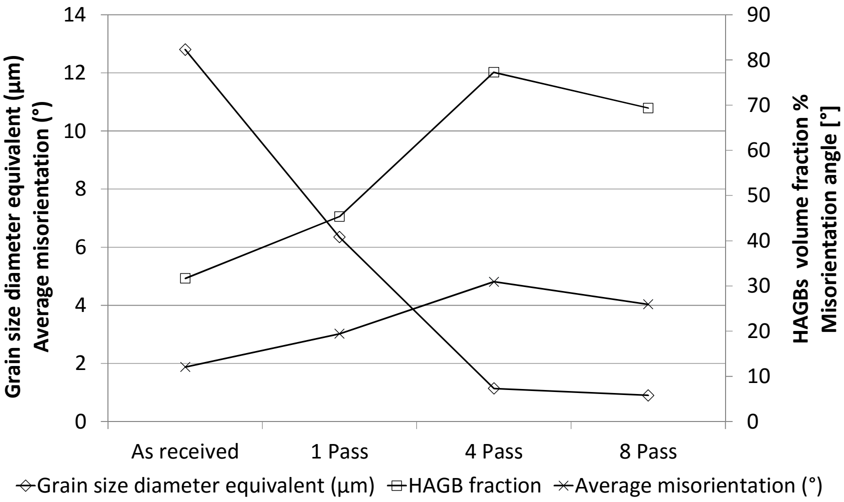

Figure 4-6 Statistics of gain size, grain boundaries and misorientation averaged in all 3 sections

4.3.1.3. Saturation

As mentioned in the previous section, grain size saturation along ND is seen very prominently after 4 passes of deformation. Along other directions, however the rate of refinement drastically reduced. If we disregard shear deformation near the outer sample surface, the deformation in AccumEx can be approximated as plane strain. Based on purely geometrical considerations, assuming that no grain splitting or coarsening occurs, we can calculate the dimensions of the grains after each pass and compare these figures with the actual experimental results. The ratio of the actual experimental values divided by the calculated "geometrical" values have been listed in Table 4-3. A value smaller than one tells us that the actual size is smaller than expected, hence that some grain splitting has occurred. Along ED after one pass a 4x elongation of the grains is expected, but in reality a reduction from 20.7 µm to 8.5 µm is observed, leading to a refinement factor of 0.1. After 8 passes the refinement along ED is 8.1 x 10^{-7} or in other words, the grains are more than 1.2 million times smaller than expected. Along TD a similar, but less impressive refinement is observed. On the other hand, along ND, the actual dimensions of the grains are larger than expected from pure geometrical considerations, which clearly indicates that the formation of smaller grains is a dynamic process and is more complex than just the formation of a new (sub)structure within the boundaries of the initial grains.

Table 4-3 Ratio of the actual experimental grain dimensions, divided by the values calculated based on the plane strain compression assumption

	ED	TD	ND	equiv. D
AR	1	1	1	1
1 pass	0.10	0.59	1.60	0.50
4 passes	0.000273	0.09	20.80	0.09
8 passes	8.13E-07	0.073	4686	0.070

4.3.2. Mechanical Properties

Micro hardness measurements and tensile tests are carried out to evaluate the mechanical properties of the deformed material.

Figure 4-7 shows the hardness values after each deformation pass. The measurements are performed along the ED-ND section. The as received material has a HV 0.3 of 44. Just after 1 pass, the hardness increases by about 30 %. With increasing passes, the hardness follows a linear increasing trend up to 4 passes to 68 HV 0.3 after which saturation is reached. It complies with the saturation behavior observed in the grain size analysis. Further, for samples above 6 passes, care was taken to measure hardness because, at certain instances, the indentation resulted in de-lamination of the interfaces which resulted in low hardness. They were not included in the calculation of the final average value.

Figure 4-8 shows the tensile test results. Engineering stress vs strain curves for as-received, 1, 2, 4 and 6 passes are plotted. The Y.S, U.T.S and the elongation to failure are also plotted in the insert of figure 4-8. The yield strength of the as-received material measured 102 MPa with an elongation to failure of 24%. After 4 passes, the yield strength increased to 195 MPa, but the elongation to failure drastically reduced to about 7%. Results obtained after 6 passes did not show any improvement from that of 4 passes. After 7 and 8 passes, the samples failed abruptly due to delamination of the weak interfaces. Besides, it can be noticed from the tensile data of 4 and 6 passes that at the onset of necking, their stress-strain curves become unstable with many bumps and dips. This is mainly due to the weak interfaces. It also supposedly has a huge impact on the elongation properties of samples processed after 4 passes. On the other hand, tensile tests for 1 and 2 passes samples are fairly homogeneous throughout the sample. They also showed a commendable yield strength – elongation to failure combination. The weakening of the interfaces at higher strains (above 4 passes) is due to the presence of de-lamination cracks at the interfaces.

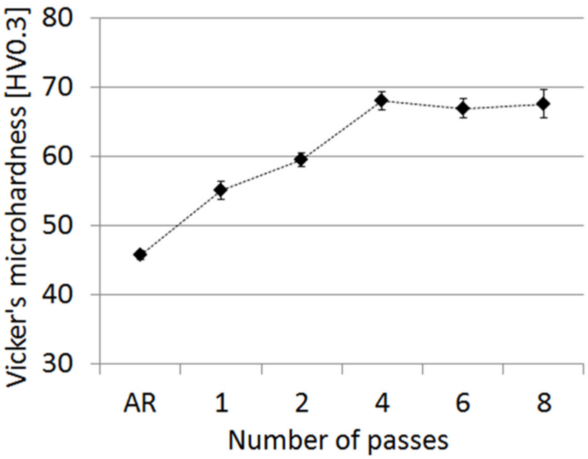

Figure 4-7 HV 0.3 micro hardness plot of samples processed by AccumEx, measured along ED-ND section

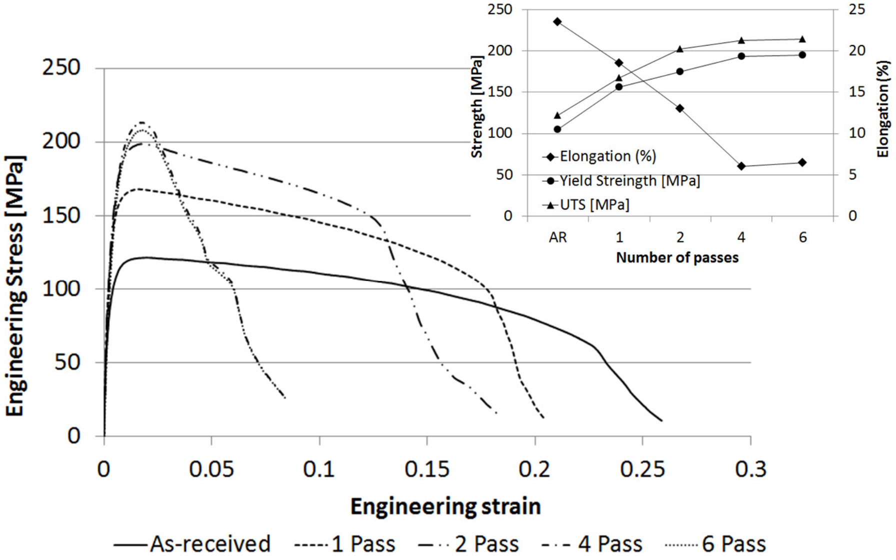

Figure 4-8 Tensile test results of AccumEx processed samples; insert shows the evolution of yield strength, ultimate tensile strength (UTS) and elongation to failure with number of passes

4.3.3. Texture

Bulk texture measurements are performed on the ED-ND sections of the AccumEx deformation samples. The φ_2 ODF sections are plotted by imposing monoclinic symmetry along TD, based on the series expansion method (Bunge method) using MTM-FHM software [15]. The ideal positions of the components are presented in Figure 4-9 for φ_2 = 0°, 45° and 65° ODF sections. Figure 4-10 shows the φ_2 = 0°, 45° and 65° ODF plots of the as received starting material and the AccumEx deformed samples after 1, 4 and 8 passes. The as received hot rolled sheets contain traces of Goss (011)[100] and Cube (001)[100] with a strong plane strain deformation texture: Brass (Bs) (011)[2-11], Copper (Cu) (112)[1-11] , Taylor (T) or Dillamore (D) (4 4 11)[11 11 -8] and S (123)[63-4]. By processing with AccumEx, the intensity levels of most of these deformation texture components increased along with the evolution of new components such as rotated cube (H) (001)[110] (shear component with (001) // ED and TD; [110] // ED). Figure 4-11 shows the orientation intensities f(g) as a function of strains/number of passes calculated within 10.5° of the corresponding ideal positions in Euler space.

With increasing number of passes, Cube and Goss weakened and reduced to negligible values after a strain of 6.4 (4 passes). S and Bs, the main components of deformation texture, intensify with strain but saturate between 2 and 4 passes. At strain 6.4 (4 passes), the shear component H increased. It showed corresponding weakening of Bs and S. Cu and T fraction increased consistently without any saturation throughout the deformation process. The increase became rapid after 2 passes, with a significant compensation by saturation and partial weakening of S. The ratio of their intensity levels along the course of deformation implies that deformation is typically plane strain till 4 passes but at higher strains, a strong effect of shear is noticed resulting in the weakening of the Bs and S components.

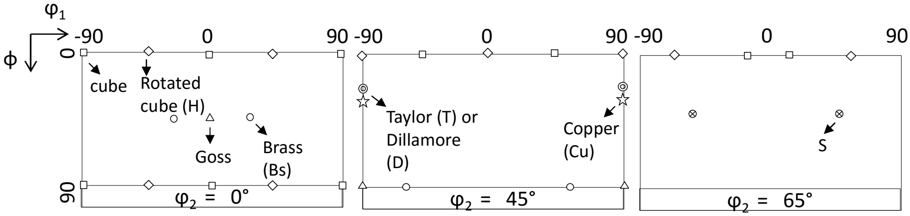

Figure 4-9 Ideal position of texture components in monoclinic symmetry along TD

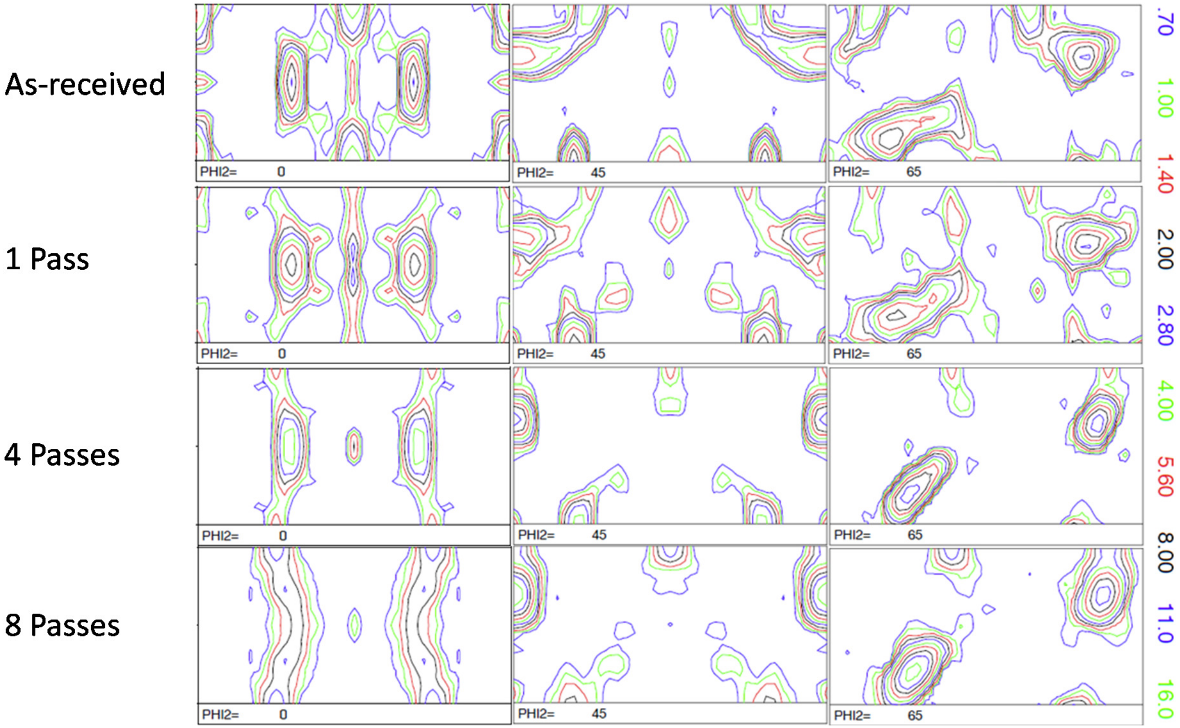

Figure 4-10 ϕ2 =0, ϕ2 =45 and ϕ2 =65 sections of AccumEx processed samples, measured on ED-ND section with monoclinic symmetry along TD.

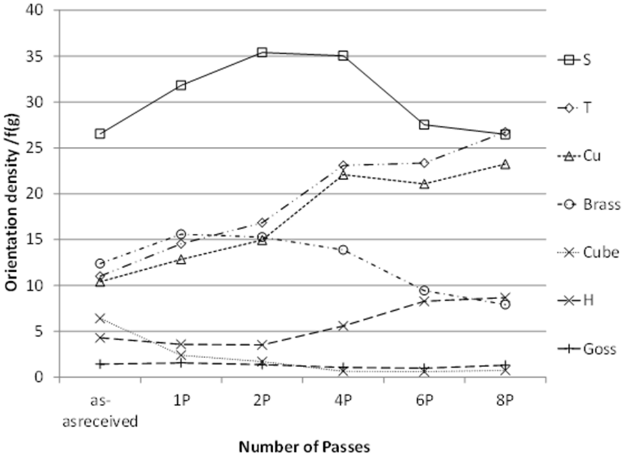

Figure 4-11 Plot on orientation density, f(g) with increasing number of passes

4.4. Discussion

The AccumEx process has been efficient in producing UFGs. A step by step refinement process is observed, as seen in other SPD techniques. The traditional grain sub-division mechanism involving grain fragmentation, sub-structural evolution, etc., [16-18] drives the refinement process during the deformation.

Along the statistical EBSD analysis, a significant observation is noted with respect to the change in HAGB fraction. The HAGB fraction after 4 passes was 80%, which implies that fully developed grains are formed with minor sub-structures. But with further deformation, it drops to about 70% which indicates that new LAGBs are generated or HAGB are being replaced by LAGBs. A similar reduction is observed in the average mis-orientation angle profile as well. The reason to both of the scenarios can be related to the evolution of the texture. Referring to figure 4-11, the decrease of Bs and S and the increase of Cu and T components after 4 passes creates a significant impact in the reduction of HAGB fraction. Most of the texture components shown in Figure 4-9, form a HAGB when they touch. But the orientation difference between Cu and T is either 8.05° or 60.5° with axis of rotation around <110>. Of the two, 8.05° <110> mis-orientation boundary theoretically corresponds to around 60% of all the different possible combination pairs between Cu and T. Those mutual grain boundaries will then contribute to the low angle grain boundaries fraction in the system. The EBSD scans and misorientation angle distribution shown in Figure 4-12 illustrate this point.

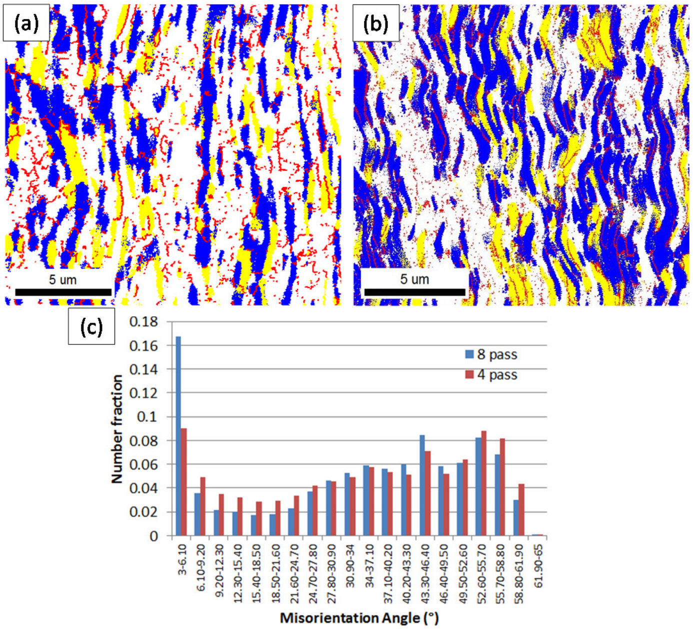

Figure 4-12 Orientation distribution maps for (a) 4 pass and (b) 8 pass, indicating Cu (yellow) and T (blue) oriented grains with LAGBs (red lines) (c) Misorientation angle distribution

Figure 4-12 (a) and (b) are crystal orientation plots showing only Cu and T grains (with a maximum deviation of 15°) after 4 and 8 passes. The distribution of LAGBs (misorientation boundaries of 3 – 14.9°) are plotted as red lines in the orientation map. A clear increase in the fraction of Cu and T orientations is noticed and along with this an increase in LAGBs. In numbers, the ratio of relative fraction of the LAGBs within the Cu and T grains to the overall LAGBs fraction is calculated and the numbers are 33% and 63% for 4 pass and 8 pass respectively. This can be further confirmed from the misorientation angle distribution chart (Figure 4-12 (c)). The boundaries in the 3-6° range shows an increase from 0.09 to 0.17 due to the increase in Cu and T neighbours. The increasing Cu and T grains also shows that they are more stable than the other components. This convergence of all components to Cu and T has also been reported in experiments of ARB [2] and predicted by theoretically models [19].

Two other unique differences with respect to the distribution of the texture components in comparison with ARB, are observed[20-22]. Firstly, in ARB the S component has always been weaker than the Cu component for the same equivalent strains. Especially at strains of 2 (more than 2 passes of ARB), the S components weakened, but in the case of AccumEx, this phenomenon is observed only after 4 passes (at strain 6.4). Secondly, in ARB the formation of H was seen after 4 cycles (strain of 3.2) but in case of AccumEx, it is observed at higher strains, above 4.8 (more than 3 passes). The formation of H implies the presence of shear in the sample. The source of shear is the redundant deformation occurring during the deformation process. The surface and the sub-surface of the material encounter this redundant deformation to its maximum (observed from the shear distribution [22-24]). With subsequent deformation cycles, they are transferred towards the centre which gradually contributes to the intensification of the H component. In the case of AccumEx, this observation is delayed and it might be because of the sample thickness or the degree of shear which is present. In most of the reports on ARB, sample thicknesses between 0.5mm and 2 mm are used [6,20,23,25], which is less than the sample thickness used in this study (5mm). Therefore, the volume fraction of the material undergoing homogeneous deformation at the centre is relatively larger in AccumEx. This implies that a higher number of passes is needed to expose the intensification of the H component.

Table 4-4 Comparison of yield strength achieved after deforming AA1050 through different SPD routes

Process route	Grain size [µm]	Yield Strength [MPa]	Elongation to failure (%)
AccumEx	0.9	195 @ $\varepsilon_{eq} = 6.4$	6 - 8
ECAP[27]	1.2	200 @ $\varepsilon_{eq} = 9.2$	20
ARB[16,28]	0.5	$200 - 260$ @ $\varepsilon_{eq} = 5 - 6$	5 - 6
Asymmetric rolling[29]	0.5	250 @ $\varepsilon_{eq} = 2.7$	< 5
High Pressure Torsion [30]	0.5	> 350 @ $\varepsilon_{eq} => 6$	< 5

The investigation of the mechanical properties provided good insights on the effect of interfaces. On a comparative scale with ARB, the strength achieved after AccumEx is marginally lower but their elongation to failure properties are good. In ARB, after 1 and 2 passes, though they exhibited a strength of more than 200 MPa, the corresponding elongation to failure were always less than 8% [3,6]. On the other hand, in AccumEx, for 1 and 2 passes which is 2 times that of the ARB equivalent strain, an elongation to failure of 18 % and 13% with yield strength of 154 MPa and 175 MPa respectively was achieved. At larger strains, a saturation of the strength combined with a low ductility is observed, due to the evolving defects (interface cracks). µCT confirmed their presence for samples deformed to high strain (> 4 passes) (Figure 4-4). The cross-sections showed intermittent cracks at different locations of the sample. They do not extend throughout the sample and are observed to be distributed very inhomogeneously along the interfaces. Such defects were reported for ARB but in a less harmful size [3,6,26]. The formation of these defects can be due to the occurrence of shear within the sample. Table 4-4 shows an overview of the yield strength values and elongation to failure achieved in AA1050 through several other SPD processes.

4.5. Conclusion

AA 1050 as-received was deformed using a novel SPD processing route – Accumulated Extrusion (AccumEx). The material was deformed up to 8 passes, equivalent strain of 12.8. A fully developed pan-cake UFG microstructure was observed with an average equivalent 3D grain size of 0.91 µm and a HAGB fraction of 70 %. A single deformation pass produced a refinement of 54% and after 4 passes the structures refined to ultra-fine grain range. With higher passes, above 4, more equi-axed structures were produced. The tensile properties of the materials were good after 1 and 2 passes, with good strength-ductility combination. Higher passes resulted in reduction of ductility, due to higher strain hardening and defect generation. The generation of interface cracks was due to intense shearing between laminates due to their reducing thickness with higher strains.

Evolution of texture with increasing strains was analysed. The effect of shear was visibly seen from the intensification of the shear component after 4 passes. The weakening of the deformation texture components – Bs and S followed by intensification of Cu and T gave a possible explanation for the reduction in the average misorientation angle and the HAGB fraction between 4 and 8 passes.

The two important observations from this chapter will be taken forward for a more detailed analysis in the upcoming chapters

(i) Deformation mode and its influence on the microstructural evolution (Chapter 5).
(ii) Grain size saturation, the mechanisms involved in it (Chapter 6).

REFERENCES

1 Figueiredo, R. B. & Langdon, T. G. Using Severe Plastic Deformation for the Processing of Advanced Engineering Materials. *Materials Transactions* **50**, 1613-1619, doi:10.2320/matertrans.MF200913 (2009).

2 Sun, P.-L., Li, W.-J. & Hsu, W.-C. Formation of a dominant Dillamore orientation in a multilayered aluminum by accumulative roll bonding. *Journal of Materials Science* **51**, 3607-3618, doi:10.1007/s10853-015-9682-9 (2015).

3 Su, L., Lu, C., Li, H., Deng, G. & Tieu, K. Investigation of ultrafine grained AA1050 fabricated by accumulative roll bonding. *Materials Science and Engineering: A* **614**, 148-155, doi:10.1016/j.msea.2014.07.032 (2014).

4 Toroghinejad, M. R., Jamaati, R., Dutkiewicz, J. & Szpunar, J. A. Investigation of nanostructured aluminum/copper composite produced by accumulative roll bonding and folding process. *Materials & Design* **51**, 274-279, doi:10.1016/j.matdes.2013.04.002 (2013).

5 Jamaati, R. & Toroghinejad, M. R. Manufacturing of high-strength aluminum/alumina composite by accumulative roll bonding. *Materials Science and Engineering: A* **527**, 4146-4151, doi:10.1016/j.msea.2010.03.070 (2010).

6 Pirgazi, H., Akbarzadeh, A., Petrov, R. & Kestens, L. Microstructure evolution and mechanical properties of AA1100 aluminum sheet processed by accumulative roll bonding. *Materials Science and Engineering: A* **497**, 132-138, doi:10.1016/j.msea.2008.06.025 (2008).

7 Saito, Y., Utsunomiya, H., Tsuji, N. & Sakai, T. Novel ultra-high straining process for bulk materials—development of the accumulative roll-bonding (ARB) process. *Acta Materialia* **47**, 579-583, doi:http://dx.doi.org/10.1016/S1359-6454(98)00365-6 (1999).

8 Saito, Y., Tsuji, N., Utsunomiya, H., Sakai, T. & Hong, R. G. Ultra-fine grained bulk aluminum produced by accumulative roll-bonding (ARB) process. *Scripta Materialia* **39**, 1221-1227, doi:http://dx.doi.org/10.1016/S1359-6462(98)00302-9 (1998).

9 Jamaati, R. & Toroghinejad, M. R. Cold roll bonding bond strengths: review. *Materials Science and Technology* **27**, 1101-1108, doi:10.1179/026708310x12815992418256 (2011).

10 Jamaati, R. & Toroghinejad, M. R. The Role of Surface Preparation Parameters on Cold Roll Bonding of Aluminum Strips. *Journal of Materials Engineering and Performance* **20**, 191-197, doi:10.1007/s11665-010-9664-7 (2010).

11 Muralidharan, G. K. and B. Verlinden (2016). "Novel severe plastic deformation technique—accumulated extrusion (AccumEx)." Materials Science and Technology: **32**(6), 547-555**.**

12 Li, L., Nagai, K. & Yin, F. Progress in cold roll bonding of metals. *Science and Technology of Advanced Materials* **9**, 023001, doi:10.1088/1468-6996/9/2/023001 (2008).

13 Raabe, D., Ohsaki, S. & Hono, K. Mechanical alloying and amorphization in Cu–Nb–Ag in situ composite wires studied by transmission electron microscopy and atom probe tomography. *Acta Materialia* **57**, 5254-5263, doi:10.1016/j.actamat.2009.07.028 (2009).

14 Schneider, C. A., Rasband, W. S. & Eliceiri, K. W. NIH Image to ImageJ: 25 years of image analysis. *Nat Meth* **9**, 671-675 (2012).

15 Van Houtte, P. *The MTM-FHM Software System, in: Katholieke Universiteit Leuven, Belgium, 2000*.

16 Kim, Y. S., Lee, T. O. & Shin, D. H. Microstructural Evolution and Mechanical Properties of Ultrafine Grained Commercially Pure 1100 Aluminum Alloy Processed by Accumulative Roll-Bonding (ARB). *Materials Science Forum* **449-452**, 625-628, doi:10.4028/www.scientific.net/MSF.449-452.625 (2004).

17 Bhattacharyya, A., El-Danaf, E., Kalidindi, S. R. & Doherty, R. D. Evolution of grain-scale microstructure during large strain simple compression of polycrystalline aluminum with quasi-columnar grains: OIM measurements and numerical simulations. *International Journal of Plasticity* **17**, 861-883, doi:http://dx.doi.org/10.1016/S0749-6419(00)00072-3 (2001).

18 Bay, B., Hansen, N., Hughes, D. A. & Kuhlmann-Wilsdorf, D. Overview no. 96 evolution of f.c.c. deformation structures in polyslip. *Acta Metallurgica et Materialia* **40**, 205-219, doi:http://dx.doi.org/10.1016/0956-7151(92)90296-Q (1992).

19 Hirsch, J. & Lücke, K. Overview no. 76. *Acta Metallurgica* **36**, 2883-2904, doi:http://dx.doi.org/10.1016/0001-6160(88)90173-3 (1988).

20 Raei, M., Toroghinejad, M. R., Jamaati, R. & Szpunar, J. A. Effect of ARB process on textural evolution of AA1100 aluminum alloy. *Materials Science and Engineering: A* **527**, 7068-7073, doi:10.1016/j.msea.2010.07.089 (2010).

21 Mishin, O. V., Juul Jensen, D. & Hansen, N. Evolution of Microstructure and Texture during Annealing of Aluminum AA1050 Cold Rolled to High and Ultrahigh Strains. *Metallurgical and Materials Transactions A* **41**, 2936-2948, doi:10.1007/s11661-010-0291-6 (2010).

22 Pirgazi, H., Akbarzadeh, A., Petrov, R., Sidor, J. & Kestens, L. Texture evolution of AA3003 aluminum alloy sheet produced by accumulative roll bonding. *Materials Science and Engineering: A* **492**, 110-117, doi:10.1016/j.msea.2008.03.005 (2008).

23 Kamikawa, N., Sakai, T. & Tsuji, N. Effect of redundant shear strain on microstructure and texture evolution during accumulative roll-bonding in ultralow carbon IF steel. *Acta Materialia* **55**, 5873-5888, doi:10.1016/j.actamat.2007.07.002 (2007).

24 Lee, S. H., Saito, Y., Tsuji, N., Utsunomiya, H. & Sakai, T. Role of shear strain in ultragrain refinement by accumulative roll-bonding (ARB) process. *Scripta Materialia* **46**, 281-285, doi:http://dx.doi.org/10.1016/S1359-6462(01)01239-8 (2002).

25 Hausöl, T., Höppel, H. W. & Göken, M. Tailoring materials properties of UFG aluminium alloys by accumulative roll bonded sandwich-like sheets. *Journal of Materials Science* **45**, 4733-4738, doi:10.1007/s10853-010-4678-y (2010).

26 Topic, I., Höppel, H. W. & Göken, M. Influence of rolling direction on strength and ductility of aluminium and aluminium alloys produced by accumulative roll bonding. *Journal of Materials Science* **43**, 7320-7325, doi:10.1007/s10853-008-2754-3 (2008).

27 Poortmans, S. & Verlinden, B. Mechanical Properties of Fine-Grained AA1050 after ECAP. *Materials Science Forum* **503-504**, 847-852, doi:10.4028/www.scientific.net/MSF.503-504.847 (2006).
28 Rezayat, M. & Akbarzadeh, A. Fabrication of aluminium matrix composites reinforced by submicrometre and nanosize Al2O3via accumulative roll bonding. *Materials Science and Technology* **28**, 1233-1240, doi:10.1179/1743284712y.0000000060 (2012).
29 Jiang, J., Ding, Y., Zuo, F. & Shan, A. Mechanical properties and microstructures of ultrafine-grained pure aluminum by asymmetric rolling. *Scripta Materialia* **60**, 905-908, doi:10.1016/j.scriptamat.2009.02.016 (2009).
30 Arzaghi, M. *et al.* Microstructure, texture and mechanical properties of aluminum processed by high-pressure tube twisting. *Acta Materialia* **60**, 4393-4408, doi:10.1016/j.actamat.2012.04.035 (2012).

5. Impact of shear in AccumEx processing of AA 1050

5.1. Introduction

The aim of this chapter is to understand the process of AccumEx in the perspective of strain distribution and its influence on the AA 1050 material. All SPD deformation processes have their unique effect on the nature of grain refinement of the material and its final properties. It is characterized by the strain path, microstructure and texture of the material being deformed. For example, in ECAP, the main parameter that influences the evolution of grain refinement is strain accumulation and shear strain. Different routes of ECAP produce different shear strain patterns in the material. These accumulated shear patterns effectively break the big initial grain structures into ultra-fine grains [1,2]. Similarly, in ARB, a combination of plane strain compression and shear effectively helps in reducing the grain size[3-5].

AccumEx is also a SPD process. Similar to ARB, extensive compressive strain in combination with process induced shear is imposed on the material during deformation. In this chapter, an effort has been made to quantify the effective strains, study their influence on the microstructural and textural properties in their early stages of deformation of AA 1050.

5.2. Experiments and characterization

5.2.1. Embedded pin technique

The embedded pin technique is a special technique used in rolling to calculate the strain profile within the sample as a function of thickness and processing conditions of the sheet. It is done by inserting a pin of similar material up to half the thickness of the sheet which is then rolled under normal conditions. The change in the dimensions of the pin will be used to calculate the exact shear and compression strains at each thickness position, with the help of equations reported by Lee et al[6].

In the present experiments, the technique is slightly modified. A cylindrical annealed, soft Cu pin of 2 mm diameter and 20 mm length is inserted in the structure of the 4-piece material system of AA 1050 in as-received state, at the center of the ED-TD plane parallel to the ND, as shown in Figure 5-1. The material with the pin is deformed by AccumEx to 1 pass. During extrusion, the Cu pin deforms along with the material. The shape profile of the pin is captured before and after deformation using µCT. Their images are shown in figure 5-1. The Cu pin which is straight and cylindrical before deformation transforms into a parabolic shape after deformation. This is due to the surface friction between the sample and die-wall and the redundant shears. The change in the shape of the pin will be used to derive the deformation gradient tensor of the process, in other words the actual deformation field of the process.

5.2.2. Through thickness EBSD measurement

Through the embedded pin technique, it could be seen that strain (shear and compressive) in the material varies from center to surface after the first pass AccumEx deformation (figure 5-1). This impacts the material properties in two ways – microstructurally and texturally. To understand it, EBSD measurements are done along the ED-ND sections of 1 pass and 2 pass AccumEx deformed samples, along ND from center to surface (0 mm to 2.5 mm), as shown in Figure 5-2(a). Each measurement covers an area of 200 x 100 µm^2 (ED x ND). A total of 25 measurements are performed to obtain information along the specified region.

A second set of through thickness EBSD measurements (similar scan area as above) are also done at the die-mouth, when the material is deformed half way. The measurements are performed at different ND positions as shown in Figure 5-2(b). The results of these measurements will be utilized in describing the strain path of the process in later sections.

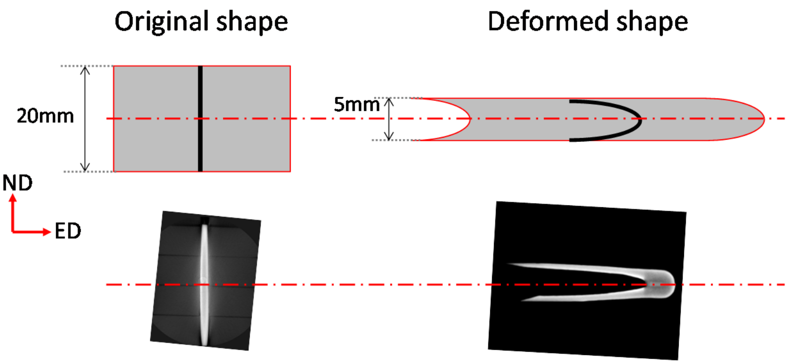

Figure 5-1: Pin profile - before and after deformation shown schematically and imaged using µCT.

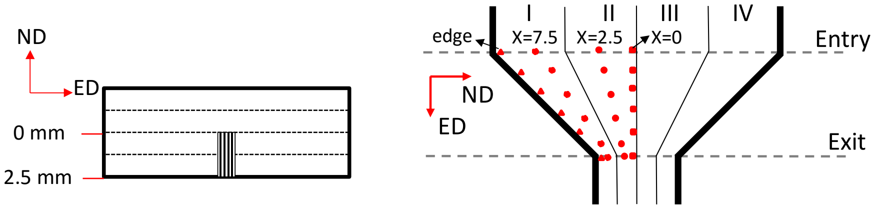

(a) (b)

Figure 5-2: (a) The rectangular contour shows the area of EBSD measurement on the ED-ND plane from position 0 mm till 2.5 mm; (b) die-mouth cross-section with material half-deformed showing the different locations of EBSD measurements

5.3. Quantification of shear

The experiments performed with the embedded pin helped in visualizing the deformation profile of the AccumEx process in terms of change in shape of the pin. The parabolic profile of the pin contains the information of strain. By mapping the final position of the pin to the initial position, the hidden strain information can be quantified. This can be done by applying basic continuum mechanics theory.

The initial and final position of the pin is equated mathematically using equation (5-1) and (5-2). Here (X1, X2) and (x1, x2) are the coordinate system of the initial and the final position respectively (Figure 5-3). With the help of this relation, a deformation gradient tensor is derived (equation (5-3)), as a function of thickness. The derived deformation gradient tensor is used to calculate the exact strain values for each thickness position. More information on the derivation is given as appendix B.

The position of the pin with respect to its co-ordinates can be written as,

$$x_1 = X_1\lambda_1 - \alpha\lambda_2^2 X_2^2 + C \quad (5\text{-}1)$$

$$x_2 = X_2\lambda_2 \quad (5\text{-}2)$$

Where λ_1 and λ_2 are process parameters, α is a function of extrusion ratio and pin length and C is a constant

After applying boundary conditions (Appendix B), the deformation gradient tensor is derived as,

$$F = \begin{bmatrix} \frac{t_i}{t_f} & -\frac{l_p}{t_i^2} X_2 \\ 0 & \frac{t_f}{t_i} \end{bmatrix} \tag{5-3}$$

Where t_i and t_f are initial and final thickness of the deformed sample, l_p is the length of the deformed parabolic pin (Figure 5-3) and X_2 is the initial position along ND which ranges between 0 and 10 mm.

Based on the derivation, the strain distribution has been plotted as a function of thickness (along ND) in Figure 5-44. The magnitude of the corresponding rigid body rotation is also plotted in Figure 5-5.

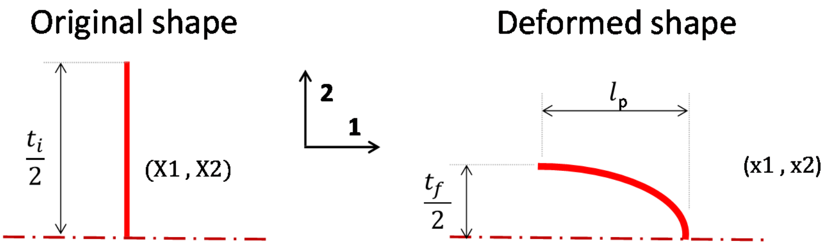

Figure 5-3: Dimensions and coordinates of the pin in its original and deformed shape

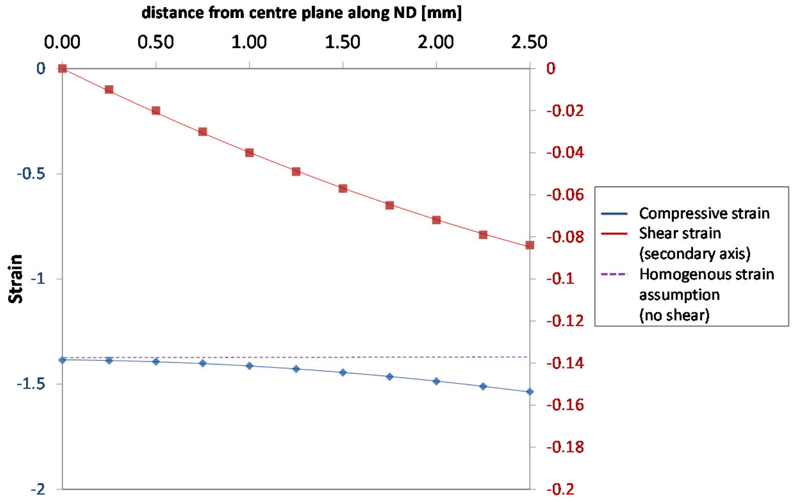

Figure 5-4: True Strain (Compressive ε$_{22}$, Shear ε$_{11}$) distribution calculated based on the calculated deformation gradient tensor as function of the position along ND in the reference frame (X1, X2)

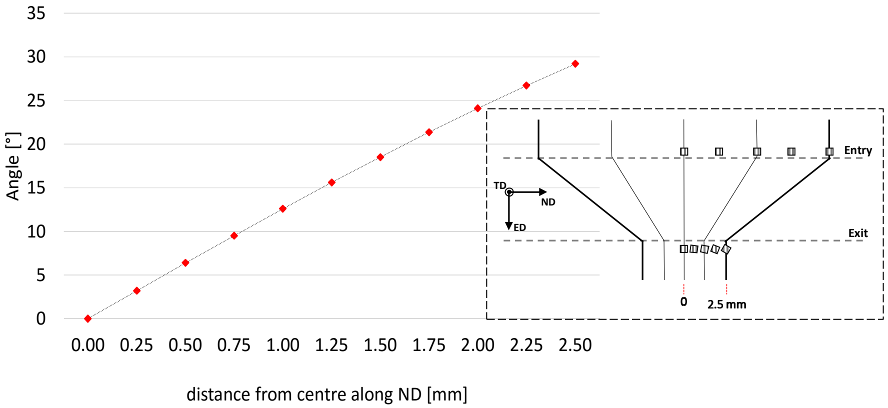

Figure 5-5: Rigid body rotation along the through thickness direction, at the exit of the deformation zone; insert – shows the schematic of the rigid body rotation around TD.

The strain distribution in the through thickness of the sample (ND) shows that a significant amount of shear is present on the surface. Comparing the obtained shear values with that of the ARB process, it looks like the amount of shear in AccumEx is small [3,6-8]. This is because, the strain values have been reported with respect to the reference frame (X1, X2) after applying rotation (Appendix B). The values reported in literature does not take into account the reference frame and therefore, the numbers cannot be directly compared. Some literature calculate redundant shear strains in ARB of values up to 8 (without lubrication) and 1 (with lubrication) after 1 pass [3]. In another work, to quantify shear in ARB using FE simulations, the values were reported to be up to 2 and a rigid body rotation of 40° at the surface. However, their texture simulations with the obtained strain values showed deviations from the observed experimental texture [9]. Therefore, the obtained strain profile in the current study will be directly evaluated by using a texture prediction model – ALAMEL rather than comparing with literature. ALAMEL, (Advanced LAMEL model) is used for predicting texture using the derived deformation gradient tensor. The model is reported to predict accurate texture in deformations such as rolling. The specialty of the model is that it works on pairs of orientations. It considers a planar boundary between the orientation pair which as a system collectively satisfy the macroscopic deformation. By this, it allows the individual orientation to choose its own velocity gradient, under the condition that they collectively conform to the macroscopic deformation. For the given texture, many such orientation pairs are considered and the model characterizes their respective grain and grain boundary orientations. This helps in taking into account the grain and grain boundary interactions also in the process of microstructure evolution [10,11]. Also, simultaneously and subsequently the strain distribution in AccumEx will be correlated with the texture and microstructural properties of the Al-Al laminates.

5.4. Effect of shear on texture

5.4.1. Manifestation of shear in Texture

Texture results presented in figure 4-10 showed that in AccumEx deformation of Al, the typical shear component-H intensifies with increasing deformation passes but becomes significantly visible only after 4 passes. Till 4 passes the presence of shear is not clearly known in the material's texture properties. Ideal positions of the different components and the fibres are schematically shown in Figure 5-6(a). Apart from the typical plane strain compression and recrystallization components, there are other components - H, A, A*, A' and B, which are classified as shear components. They exist in a fibre form – the {111} fibre and <110> fibre and can be seen in the φ_2= 45° ODF section. The {111} fibre comprises A, A* and A' components and the <110> fibre comprises rotated Goss (RG), A, B and H. Formation of either these components are not prominent after AccumEx, except for H (after 4 passes).

However, from the current experiments, a different type of fibre has been identified along the φ_2= 0° ODF sections (Figure 5-6(b)) and its presence has been found relatable with the shear strain in the material. The fibre can be seen after 1 pass (figure 4-10) and intensifies with increasing number of passes. It is not a typical fibre described in literature, but is commonly seen in all the texture results reported for ARB. The origin of the fibre is the Bs component (35, 45, 0), and migrates towards H through rotations in both positive and negative directions of φ_1 and positive direction of Φ. Therefore, it will be chosen to be described as B-H fibre. This fibre is visible up to medium high strains of 9, above which it reduces in intensity.

5.4.2. Formation of B-H fibre

The ODF sections which show the B-H fibre, correspond to surface texture measurements performed on the complete ED-ND sample plane. Texture measurements performed in the bulk of the material closer to the centre, do not show this B-H fibre. This can be attributed to the derived shear gradient in the ED-ND section, illustrated by the embedded pin method. To relate this experimentally, ODFs are plotted from the through thickness EBSD measurements of the 1 pass sample in Figure 5-7. φ_2 = 0° and 45° sections of different positions along ND from center to surface of the material are shown. From the figure, a clear displacement of the components along Φ and φ_1 can be seen. The components of the φ_2 = 0°

section show a good orthorhombic symmetry at the center (components at ideal Bs position) and with varying position along ND towards the surface, the symmetry is lost due to rotation of components away from the ideal position. When an average bulk texture is measured on such an ED-ND surface, the mentioned rotations are cumulatively measured in the form of the B-H fibre. φ_2 = 45° sections also show small rotation of the Bs position towards the {111} - fibre away from center.

The varying positions of the components in the B-H fibre are plotted as a function of Φ and φ_1 angles for 8 positions from the mid-plane to the surface in Figure 5-9. The ideal Bs position (35, 45, 0) is the origin. In the centre of the sample, the measured peak is very close to the ideal Bs position. With increasing ND position, away from the center, the Euler angles of the component move away from Bs towards increasing $\varphi_1$and Φ values. At 2500 µm i.e., at the surface, the component rotates to ~(43, 65, 0) which is approximately 20 - 25° to the Euler position of the H component – (45, 90, 0) along the <001> axis of rotation. Similarly, the other half of the sample which undergoes shear in the opposite direction will impose an inverse rotation of the components towards H (45, 0, 0), contributing constructively to a B-H fibre. With increasing number of passes, the rotation increases and results in a stronger B-H fibre. This proves that the gradient of shear reflects in the texture of the material by rotation of some specific texture components.

5.4.3. Validation of the deformation field using ALAMEL texture prediction

The starting texture used for the model is the average texture of the as-received AA 1050 sheet, measured on the ED-ND plane. The φ_2= 0° and 45° ODF sections are plotted with triclinic symmetry. The starting texture is discretized into a set of 5000 grain orientations. {111} <110> slip systems were used for the calculation of the slip rates and Taylor factors. The simulation is performed for the first deformation pass. The velocity gradient tensor was applied based on the equation (5-3). Five different simulations were executed for five different positions along ND – 0, 0.25, 0.5, 0.75, 1 with 0 in the center and 1 on the surface. Their corresponding φ_2 = 0° and 45° sections are plotted in Figure 5-8.

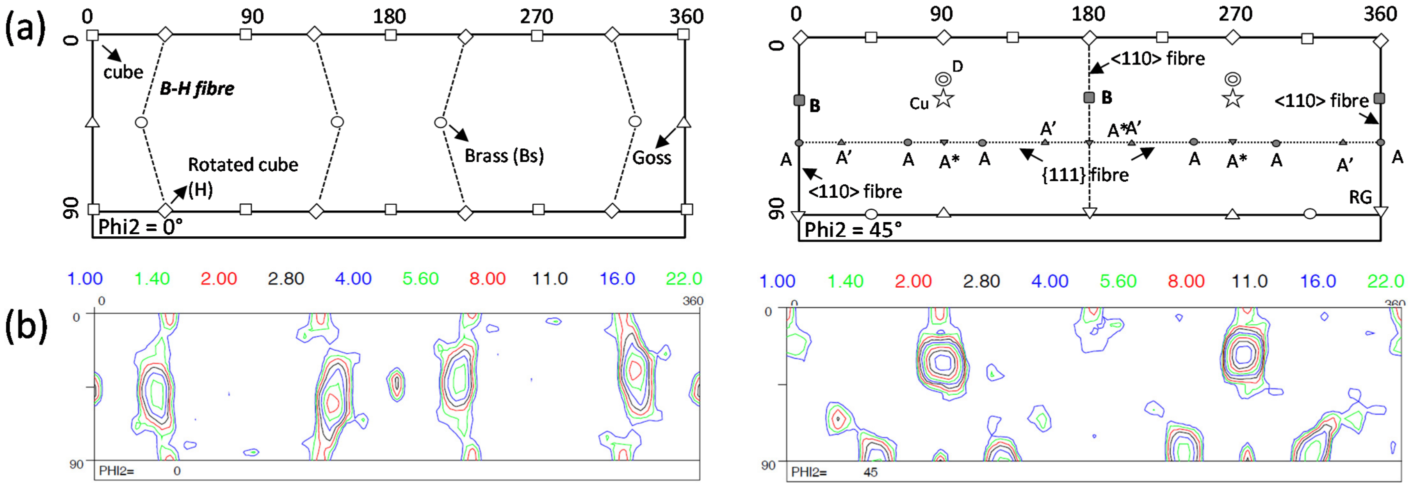

Figure 5-6: (a) Ideal position of common texture components plotted in φ 2 = 0° and 45° ODF sections; (b) φ 2 = 0° and 45° ODF sections of 4 pass samples, measured along the ED-ND plane.

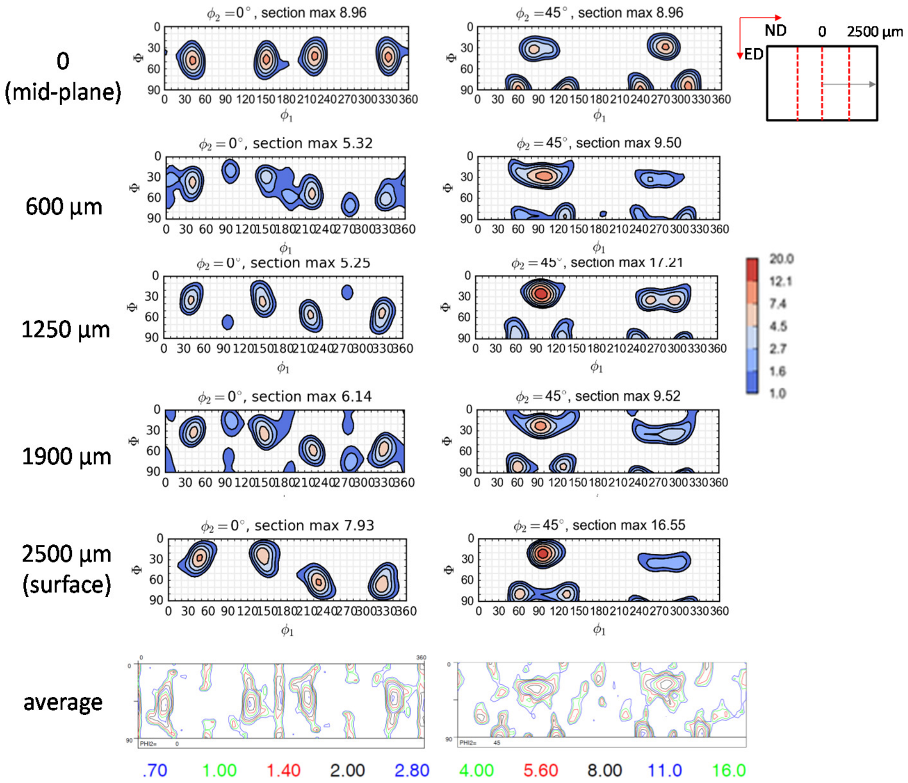

Figure 5-7 ODF sections of 1 pass at different thickness position, measured along ND in ED-ND section; direction of measurement is shown by arrow mark; average is the measurement obtained from X-ray measurements on whole ED-ND section.

The ODF plots show a very good correspondence with the experimental ODFs. The results clearly indicate that the presence of the texture gradient is due to shear. At the center, orthorhombic symmetry of the components is noticed but with increasing ND position towards the surface, the symmetry is lost. The rotation of components in the φ_2 = 0° section is clearly visible, indicating the presence of the B-H fibre. And in the φ_2 = 45° section, the migration of Cu components towards D is noticed. Both the rotations occur along TD, indicating a monoclinic symmetry around TD.

The rotation from center to surface is plotted in Figure 5-9. Comparing with the experimental values, they show a good agreement, although a general shift in Φ values is observed in the predicted values. The reason for the shift is unknown. It can be likely due to small mis-alignment of the measurement plane in the EBSD, due to sample preparation. Otherwise, the only mismatch is seen between the positions

2200 µm and 2500 µm, but on a relative scale in the Euler space, the difference can be considered as small. In comparison with other prediction results reported for ARB in literature, a better match is observed in the present work with respect to showing the spatially resolved texture changes as function of position along ND [3,8,9,12]. This implies that the derivation of strains using the embedded pin technique is more realistic and has helped in tracking the rotations of components in a very distinct manner.

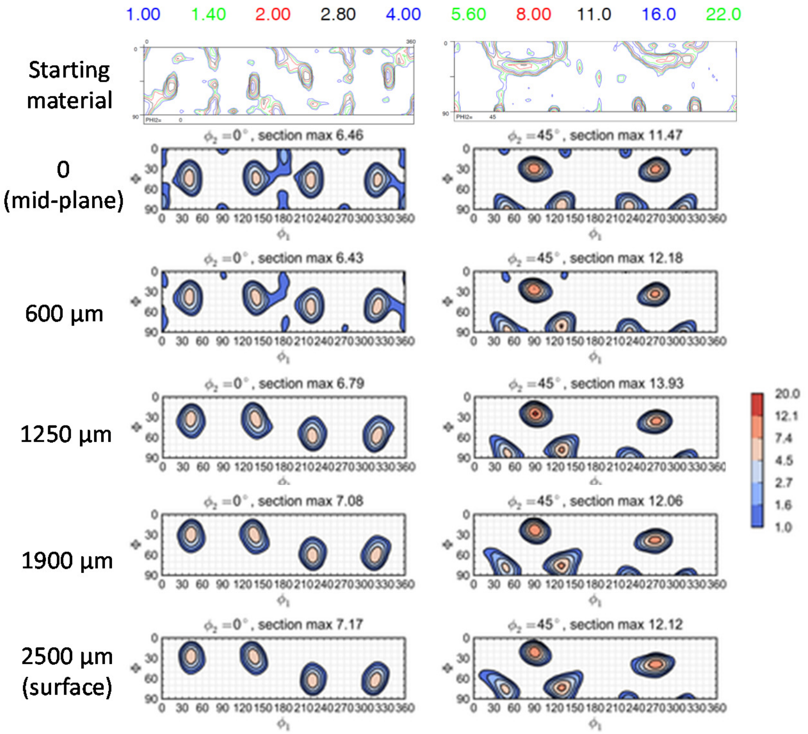

Figure 5-8: ODF sections of 1 pass sample of different thickness positions (same as Figure 5-7) predicted by ALAMEL for the derived deformation gradient tensor

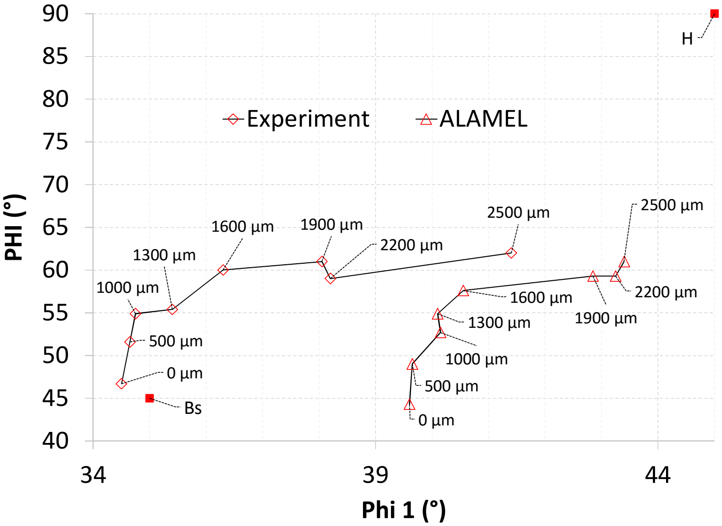

Figure 5-9: Rotation of component from Bs position towards H, plotted as function of Euler angles φ_1 vs Φ (experimental and ALAMEL). Data legends show the measured position along ND

5.5. Effect of shear on the microstructure

5.5.1. 1 pass

Figure 5-10 shows ED-ND boundary maps of the deformed sample at different positions along ND. The maps show a clear effect of shear on the microstructure. At the center, where shear is null, a widely spaced lamellar microstructure is observed. With increasing distance from the center, shear increases which results in finer lamellar structures. Figure 5-11 indicates the observation in numbers. The 15° boundary spacing shows smaller boundary spacing at the surface and sub-surface regions, whereas the “all boundary” spacing is almost homogeneous across the thickness. This implies that the geometrically imposed strain is uniform throughout the sample and the influence of shear is seen majorly in the HAGB structures. The average misorientation and HAGB fraction also follow the pattern which complies with the presence of shear strain. The region with higher shear produces higher HAGB fraction and higher average misorientation.

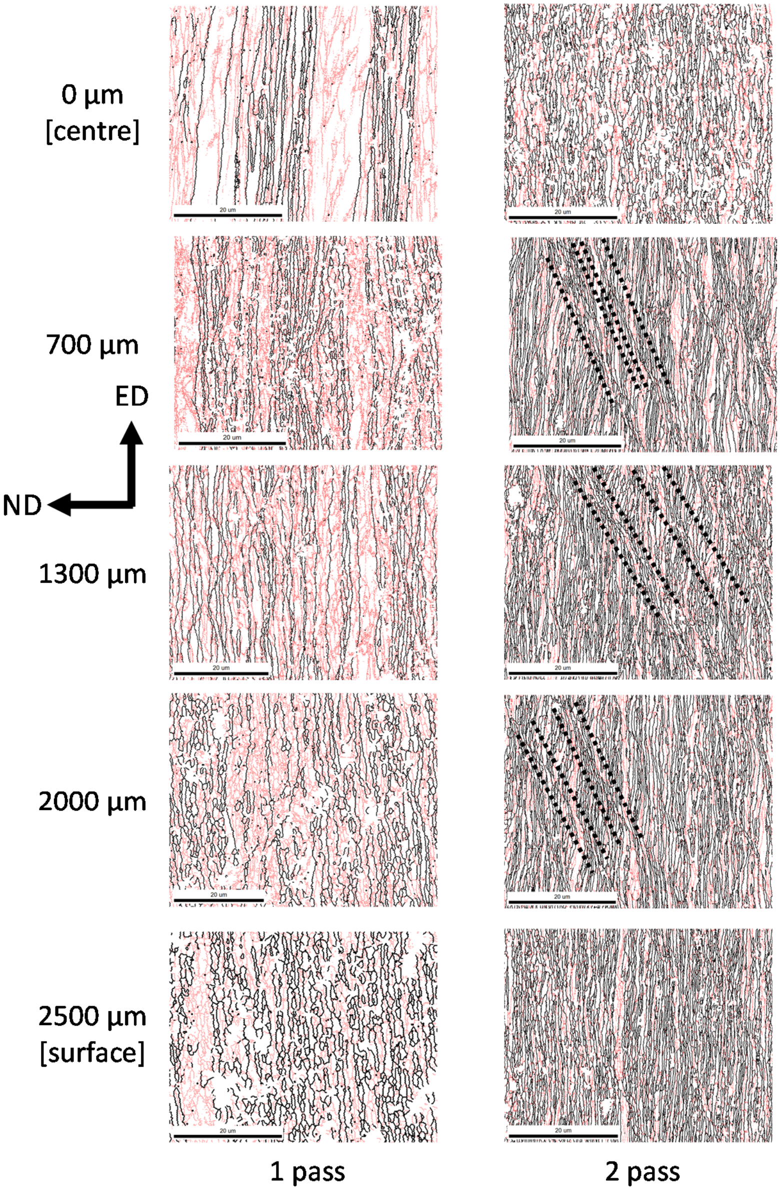

Figure 5-10: Boundary maps measured at different positions along ND after 1 and 2 passes; black lines - >15° misorientation boundaries, red lines - 2 - 14.9° misorientation boundaries; black dotted lines indicate the shear bands

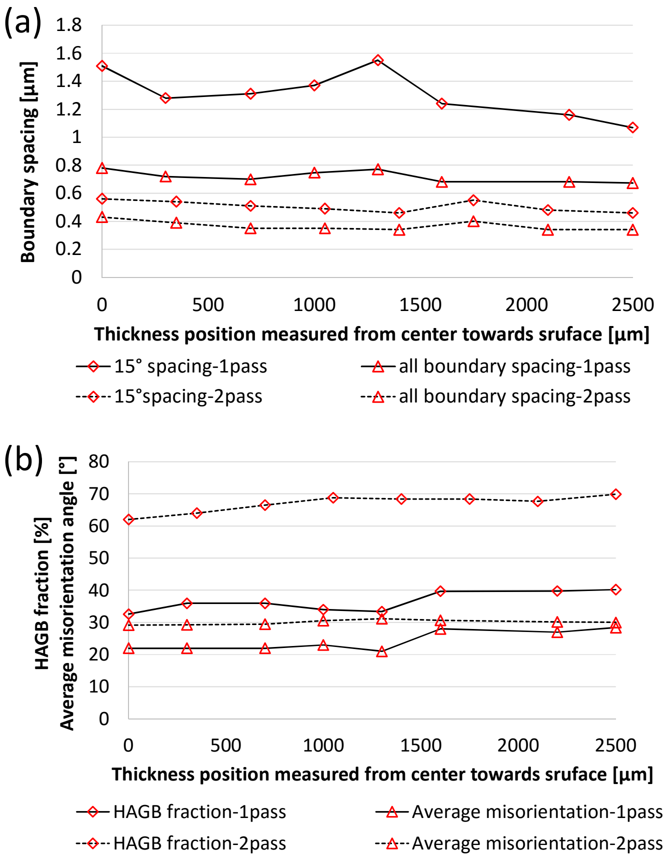

Figure 5-11: (a) Boundary spacing and (b) HAGB fraction, average misorientation angle profiles measured along different thickness positions from center (0 µm) to surface (2500 µm)

5.5.2. 2 pass

ED-ND boundary maps of the 2 passes deformed sample at different positions are presented in Figure 5-10. Compared with the 1 pass, the first impression is that there is a substantial grain refinement, homogeneously throughout the ND position. Several shear bands are observed in the sample and they are mainly located in the non-center and non-surface regions. The grain boundary spacing shows homogeneous distribution both for 15° and all boundaries. The effect of shear on the grain boundary spacing is almost null. The distribution of HAGB fraction and average misorientation is also homogeneous. This implies that the evolution of grain structures and rotations are homogeneous across the thickness. The impact of shear on the microstructures is not visible anymore. However, it should be noted that the shear has become redundant only with respect to showing gradient in the results. Its effect on the development of the grain structures during the deformation process cannot be ignored. Further, at the surface of the 2 pass sample, a possible presence recrystallization nuclei can be observed, however they could not be affirmed from the available data and will need further investigation.

5.6. Strain path

5.6.1. Accumulation of strain

In all SPD processes, accumulation of strain is a prime factor for grain refinement. The accumulation of shear and compressive strain for AccumEx has been calculated and presented in Figure 5-12, from center to surface. With respect to the shear strain distribution, the magnitude of strain increases throughout the thickness from center to surface. The distribution and the number of peaks and dips of shear increases with increasing number of passes due to sub-sequent re-assembling of the deformed sample. It evolves very similar to ARB [6], but at a rapid rate. It should be noted that only the magnitude of the plotted shear strains has been indicated and the actual sign or the direction of the shear has not been taken into consideration. Similarly, the compressive strain also shows peaks and dips, however owing to the magnitude of the overall global compressive strain, the amplitude of the peaks and dips are much less and therefore the overall strain distribution looks rather homogeneous across the thickness of the sample.

Although, it is certain that the pattern seen in the process of shear accumulation contains peaks and dips, it is not observed to reflect on the texture evolution. ODF sections along the thickness of 2 passes deformed sample do not indicate the history of shear from the previous deformation. For example, after 2 passes, the center region of the sample has a shear strain of magnitude 0.07. Theoretically, it should be visible in the texture. But, it is not. The phenomenon is explained in Figure 5-13. φ_2 = 0° ODF sections of center and surface regions after 1 pass and 2 passes are plotted schematically. After 1 pass, the center region shows a plane strain compression texture. At -2500 µm, a positive shear and at +2500 µm, a negative shear is seen. The φ_2 = 0° ODF section shows the difference in the direction of shear in the form of different direction of rotation of the components. After 2 passes, the layers obtained after 1 pass will become re-assembled in the order shown in Figure 5-12(b). It should be noted that only half the thickness of the sample is shown. So, by applying the obtained shear conditions from 1 pass, at -2500 µm position, a positive shear is present and at 0 µm position, a negative shear is present before the strain imposition of the second pass. After application of 2 passes, the texture of the negative shear at 0 µm position is erased and a plane strain compression texture is formed. At -2500 µm position, the shear is accumulated which is seen in the form of higher degree of rotation than it was in its 1 pass state. Therefore, the progressive re-position of the shear strain with sub-sequent deformation pass creates a constructive increase of shear in the texture evolution only at the sub-surface. Regions more close to the center realizes a very strong influence of the imposed compressive strain resulting in plane strain compression texture. In that process, the direction of shear is also reversed. This implies that with increasing passes, shear undergoes a constructive or destructive interference on the materials' texture property, depending on the location. Similar observations were reported for ARB as well[3,8,13-15]. In [8], the described observation was reported between 6 and 7 cycles of ARB. In [16], this was referred as racheting mechanism. The shear component formed in the surface during the previous pass, when moved to the center region is rotated back to the Cu component. This repetitive racheting mechanism results in predominant increase in the D component (intermediate between H and Cu) at the expense of Bs and S, as reported in figure 4-11, chapter 4.

The highly varying strain values and differing strain path along the sample thickness therefore helps in the homogenization of the grain structure along the thickness. The reported grain size statistics after 1 and 2 passes prove this point. Shear and strain path changes are believed to assist in the formation of several dislocations and GNBs that create higher grain refinement with formation of stable grain structures [3,6,16,17]. Such phenomena are expected to occur at a higher rate in this process. Therefore, the degree of refinement is very rapid for AccumEx. The effect which was seen in ARB after 5 passes is already seen after 2 passes in the present case. The process in some ways is comparable with the mechanism of ECAP as well. In route A; ECAP, shear is accumulated and the direction is the same for different passes. In route C; ECAP, shear is accumulated and the direction is reversed for every even deformation pass. Both passes are reported to produce efficient refinement, however, the route C produced better equiaxed structures [1,18]. In AccumEx, the surface region behaves similar to route A and the central region similar to route C. Regions in-between effectively have a combination of route A and C depending on their history and the position.

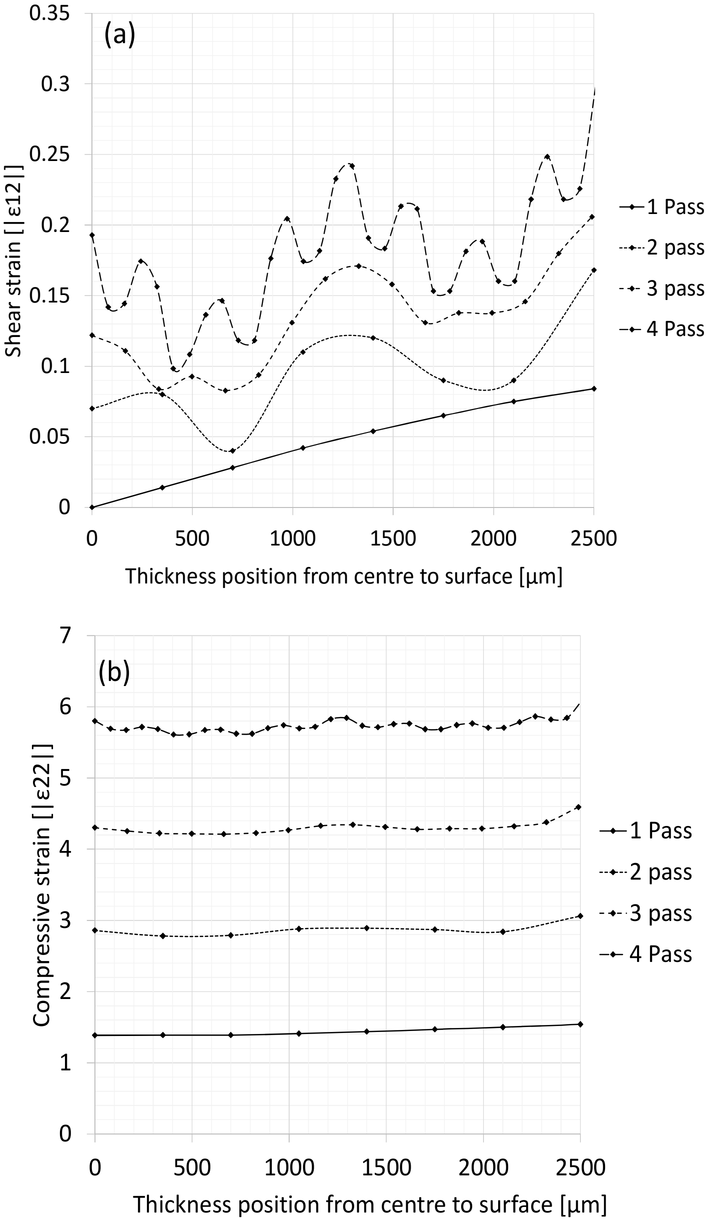

Figure 5-12 – (a) Shear strain distribution and (b) compressive strain distribution along ND from center to surface after every deformation pass up to 4 passes

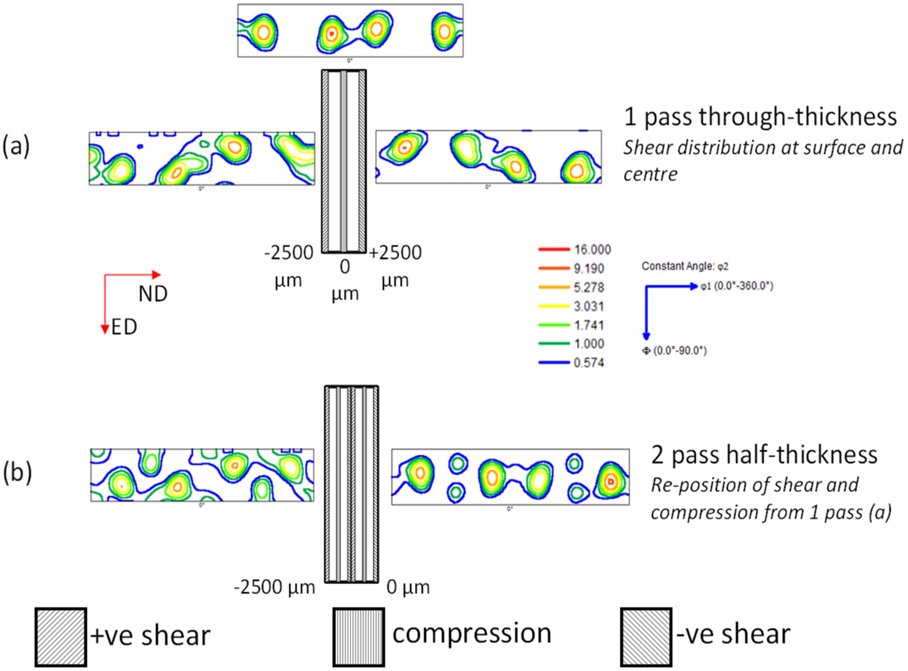

Figure 5-13 (a) ϕ₂ = 0° sections at surface and center of 1 pass sample; (b) ϕ₂ = 0° sections at surface and center of 2 pass sample

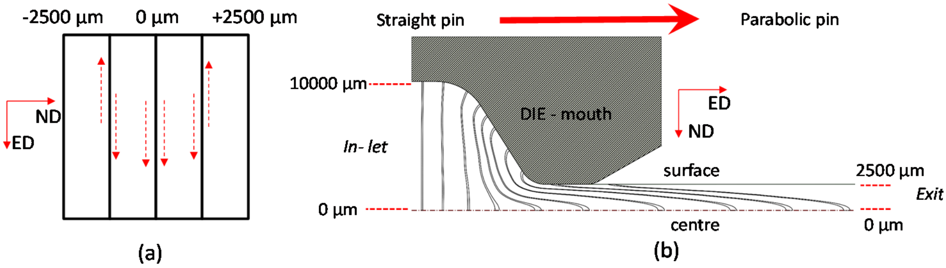

Figure 5-14 (a) shear direction at interfaces during initial deformation; (b) FE result showing the strain profile along the die-mouth

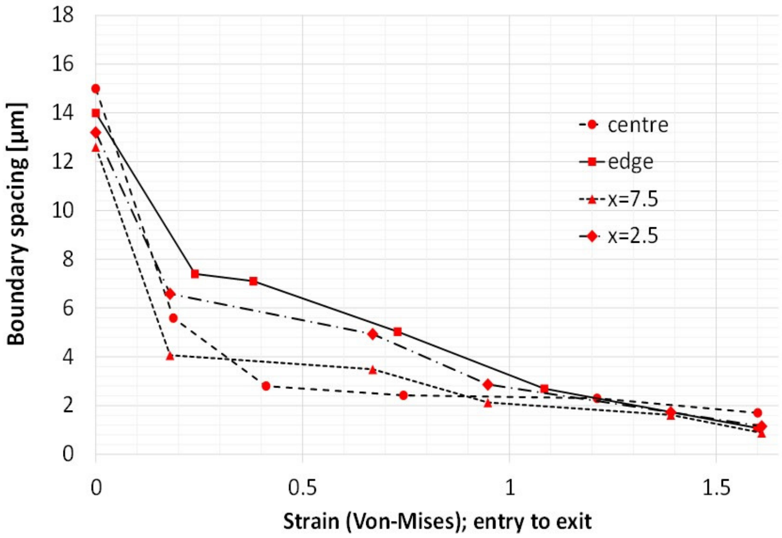

Figure 5-15 Rate of refinement of 15° boundary spacing along the die-mouth at different ND position shown in Figure 5-2(b)

5.6.2. Strain affected interface zone

Besides the positive effect of the complex strain path, a negative side-effect has to be mentioned: de-bonding of the interfaces. As reported in section 4.3.1.1, interfaces de-bond at higher deformation passes. The bending behavior prior to de-bonding is the hindsight of the influence of shear on this. With increasing number of passes, the volume fraction of material that undergoes shear increases (Figure 5-12). Further, with the reduction in the laminate thickness, the interfaces become part of the material flow rather than behaving as a separate entity. Based on the strain profile derived using the embedded pin technique, it is learnt that a heterogeneous field of shear and compressive strain is present across the thickness, i.e., ND position. These heterogeneities affect the material flow and at the interface, it can be visualized in the form of shear as shown in Figure 5-14(a). The interfaces remained straight even with the differences in the flow behavior in the initial deformation passes. This implies, the bulk part of the material between the interfaces compensates the heterogeneities without showing any adverse effect on the interfaces. However, as the number of deformation passes increases, the distance between the interfaces reduces and the effect of the heterogeneities begin to reflect on the structure of the interfaces. From the SEM analysis of the interfaces, above 4 passes, where the interface distance reduced to below 20 µm, it was noted that the interfaces began to bend and shear between each other visibly. To get a better picture on the evolution of these heterogeneities, the deformation path of the pin from the straight cylindrical shape to the parabolic form will be needed. An approximate estimation of the deformation path of the pin was derived with the help of Finite Elements (FE) simulation and is shown in Figure 5-14(b). The intermediate positions of the flowing Cu pin can be seen and suggest two observations – (i) more than 75% of the shear is seen to occur only after an equivalent strain of 56 %; (ii) the rate of compression of material is not the same along ND, for different ED positions. The presence of this heterogeneity is captured in the grain refinement as well. Figure 5-15 shows the decreasing 15° boundary spacing from entry to exit of the die (along ED), at different ND positions in the start of the deformation (center, x=2.5, x=7.5 and edge), measured during 1 pass, as shown in Figure 5-2(b). The rate of refinement along ED is different for different ND positions. The surface shows a late refinement, x=2.5mm shows a linear refinement and x=7.5 mm and center show a huge jump at the start. However, all the refinement converges to similar values near the exit. The difference in grain refinement across the thickness implies difference in compression rate across the thickness between the interfaces. The difference in the grain refinement is seen to exhibit in the formation of shear bands within the grains and the difference in the compression rate across the thickness is exhibited in the form of bending, shearing which eventually contribute to interface cracks and delamination.

5.7. Conclusion

The strain distribution in the AccumEx process was successfully calculated using the embedded pin technique and cross-verified using the ALAMEL model. The predicted texture was in good agreement with experimental texture. The strain distribution showed a shear gradient along ND which was visible in the sample’s texture by formation of a B-H fibre. The effect of this gradient was seen on the microstructure after 1 pass. After 2 passes, a more homogeneous microstructure was achieved. A complex strain path was derived for the process with increasing strains. The accumulation of strain proved to be helpful in the rapid homogenization of the microstructure. The complex flow pattern of the material was understood to be detrimental to the structure of interfaces at higher deformation strains (> 4 passes) as the distance between the interfaces reduces.

REFERENCES

1 Valiev, R. Z. & Langdon, T. G. Principles of equal-channel angular pressing as a processing tool for grain refinement. *Progress in Materials Science* **51**, 881-981, doi:10.1016/j.pmatsci.2006.02.003 (2006).

2 Lee, D. N. An upper-bound solution of channel angular deformation. *Scripta Materialia* **43**, 115-118, doi:http://dx.doi.org/10.1016/S1359-6462(00)00377-8 (2000).

3 Kamikawa, N., Sakai, T. & Tsuji, N. Effect of redundant shear strain on microstructure and texture evolution during accumulative roll-bonding in ultralow carbon IF steel. *Acta Materialia* **55**, 5873-5888, doi:10.1016/j.actamat.2007.07.002 (2007).

4 Saito, Y., Tsuji, N., Utsunomiya, H., Sakai, T. & Hong, R. G. Ultra-fine grained bulk aluminum produced by accumulative roll-bonding (ARB) process. *Scripta Materialia* **39**, 1221-1227, doi:http://dx.doi.org/10.1016/S1359-6462(98)00302-9 (1998).

5 Estrin, Y. & Vinogradov, A. Extreme grain refinement by severe plastic deformation: A wealth of challenging science. *Acta Materialia* **61**, 782-817, doi:10.1016/j.actamat.2012.10.038 (2013).

6 Lee, S. H., Saito, Y., Tsuji, N., Utsunomiya, H. & Sakai, T. Role of shear strain in ultragrain refinement by accumulative roll-bonding (ARB) process. *Scripta Materialia* **46**, 281-285, doi:http://dx.doi.org/10.1016/S1359-6462(01)01239-8 (2002).

7 Kang, J.-H., Inoue, T. & Torizuka, S. Effect of Shear Strain on the Microstructural Evolution of a Low Carbon Steel during Warm Deformation. *Materials Transactions* **51**, 27-35, doi:10.2320/matertrans.MB200916 (2010).

8 Kamikawa, N., Tsuji, N., Huang, X. & Hansen, N. Through-Thickness Characterization of Microstructure and Texture in High Purity Aluminum Processed to High Strain by Accumulative Roll-Bonding. *Materials Transactions* **48**, 1978-1985, doi:10.2320/matertrans.MA200702 (2007).

9 Li, S., Sun, F. & Li, H. Observation and modeling of the through-thickness texture gradient in commercial-purity aluminum sheets processed by accumulative roll-bonding. *Acta Materialia* **58**, 1317-1331, doi:10.1016/j.actamat.2009.10.036 (2010).

10 Van Houtte, P., Kanjarla, A. K., Van Bael, A., Seefeldt, M. & Delannay, L. Multiscale modelling of the plastic anisotropy and deformation texture of polycrystalline materials. *European Journal of Mechanics - A/Solids* **25**, 634-648, doi:10.1016/j.euromechsol.2006.05.003 (2006).

11 Vanhoutte, P. Deformation texture prediction: from the Taylor model to the advanced Lamel model. *International Journal of Plasticity* **21**, 589-624, doi:10.1016/j.ijplas.2004.04.011 (2005).

12 Pirgazi, H., Akbarzadeh, A., Petrov, R., Sidor, J. & Kestens, L. Texture evolution of AA3003 aluminum alloy sheet produced by accumulative roll bonding. *Materials Science and Engineering: A* **492**, 110-117, doi:10.1016/j.msea.2008.03.005 (2008).

13 Kamikawa, N., Tsuji, N. & Minamino, Y. Microstructure and texture through thickness of ultralow carbon IF steel sheet severely deformed by accumulative roll-bonding. *Science and Technology of Advanced Materials* **5**, 163-172, doi:10.1016/j.stam.2003.10.018 (2016).

14 Pirgazi, H., Akbarzadeh, A., Petrov, R. & Kestens, L. Microstructure evolution and mechanical properties of AA1100 aluminum sheet processed by accumulative roll bonding. *Materials Science and Engineering: A* **497**, 132-138, doi:10.1016/j.msea.2008.06.025 (2008).

15 Li, B. L., Tsuji, N. & Kamikawa, N. Microstructure homogeneity in various metallic materials heavily deformed by accumulative roll-bonding. *Materials Science and Engineering: A* **423**, 331-342, doi:10.1016/j.msea.2006.02.028 (2006).

16 C. P. Heason, P. B. P. Grain Refinement and Texture Evolution during the Deformation of Al to Ultra-High Strains by Accumulative Roll Bonding (ARB). *Materials Science Forum* **396-402**, 429-434 (2002).

17 Cui, Q. & Ohori, K. Grain refinement of high purity aluminium by asymmetric rolling. *Materials Science and Technology* **16**, 1095-1101, doi:doi:10.1179/026708300101507019 (2000).

18 Segal, V. M. Materials processing by simple shear. *Materials Science and Engineering: A* **197**, 157-164, doi:http://dx.doi.org/10.1016/0921-5093(95)09705-8 (1995).

6. Microstructural response of saturated CP AA 1050 deformed to additional straining

6.1. Introduction

This chapter aims at understanding the microstructural transformations in a saturated CP Al. It was learnt from chapter 4 that when CP Al was deformed up to 8 passes, the grain size and hardness values of the material reached a saturation after 4 passes. Such a limitation in grain refinement is a commonly observed phenomenon in all the SPD processes. However, only very few studies have been performed to address the underlying factors and reasons behind this grain size saturation.

CP Aluminium (AA 1050) was processed by Accumulated Extrusion (AccumEx) up to a true strain of 1100 % (8 passes). A 3D equivalent grain size was calculated from measurements along all the three perpendicular sections after every deformation pass (see figure 4-5). Lamellar structures of grains were formed and their grain boundary spacing along ND gradually reduced with increasing strain. The reduction in the grain size was significantly noticed up to 4 passes, but additional deformation up to 8 passes only had minimal reduction in the equivalent grain size. The average grain dimensions along ND and ED after 4 passes were 400 nm and 1 µm respectively while after 8 passes 350 nm and 800 nm respectively. The additional true strain of more than 600 % did not seem to have its equivalent effect on the corresponding grain size value. In order to visualise this and emphasize on the impact of grain size saturation behaviour at ultra-high deformation regime, a ratio is calculated between the experimental grain size and the geometrically expected grain size along ED and ND, from 0 to 8 passes and plotted in Figure 6-1(a). Here, the geometrically expected grain size is calculated by considering a unit grain volume and translating the externally imposed true strains, corresponding to the number of AccumEx deformation passes, to dimensional changes along the ED and ND of the unit grain volume. Associated with this, two assumptions have been considered which are, no size change along TD and no grain fragmentations or formation of grain boundaries along any directions, which implies the volume of the grain is conserved. This implies for any given true strain along ED and ND, the grain changes dimensions only along ED and ND. In the Figure 6-1(a), any non-zero value implies a deviation from the theoretically calculated ideal geometric grain dimension. After 1 pass, a small deviation is seen along ND and a large deviation along ED. This implies, along ND the compression and the grain size change more or less match, while along ED, occurrence of grain fragmentations leads to shortening of the grains and therefore a deviation from 0 is seen. As the number of deformation passes increases, the deviation begins to increase along both directions and the increase becomes exponential. For the direction ED, increased grain fragmentation is the primary reason. On the other hand, the ratio increase along ND lacks explanation. Theoretically, the obtained grain size along ND is several 1000 times larger than what is geometrically expected. In the context of mere numbers, it reflects grain coarsening. Such figures can be extracted from other SPD processes as well. A possible reasoning behind such a deviation in the geometrical expectations can be lack of fragmentation which implies no new grain boundary formation and coalescence of existing grain boundaries that can increase the grain size consistently everywhere in the sample. However, from a microstructural point of view there is more to it.

Humphreys et al. proposed that for rolling the high angle grain boundary spacing (λ_g) can be mathematically calculated based on equation 6.1, as a function of true strain, for the given starting lamellar grain boundary spacing (λ_0) [1,2]. The value of λ_0 is obtained from experimental data. As AccumEx is also a plane strain compression process, the measured high angle grain boundary spacing along ND (H_g) for different true strains of AccumEx is plotted against the curve derived from equation 6.1 (λ_g) in Figure 6-1(b). Up to true strain values of 1.5-1.8, a decent agreement could be seen between both the curves. Above true strains of 1.8 and till 2.8, the rate of grain size reduction noticed from the experimental data increases slightly compared to the rate of grain size change obtained from the mathematically derived values. Above 2.8, the rate of refinement for the experimentally obtained values almost reached null, indicating saturation. On the other hand, the values obtained from equation (6-1) show continuous refinement but at a significantly reduced rate. Their corresponding grain size values are also very small than that of the experimental values (the observed deviations might be different for different materials and different processing conditions).

$$\lambda_g = \lambda_0 \exp(\varepsilon_{true}) \qquad (6\text{-}1)$$

Where λ_g is the theoretically expected lamellar spacing, λ_0 is the initial lamellar spacing and ε_{true} is the applied compressive strain. In the counterpart, H_g is the spacing between high angle grain boundaries along the ND, experimentally measured from the EBSD maps belonging to the ED-ND sections.

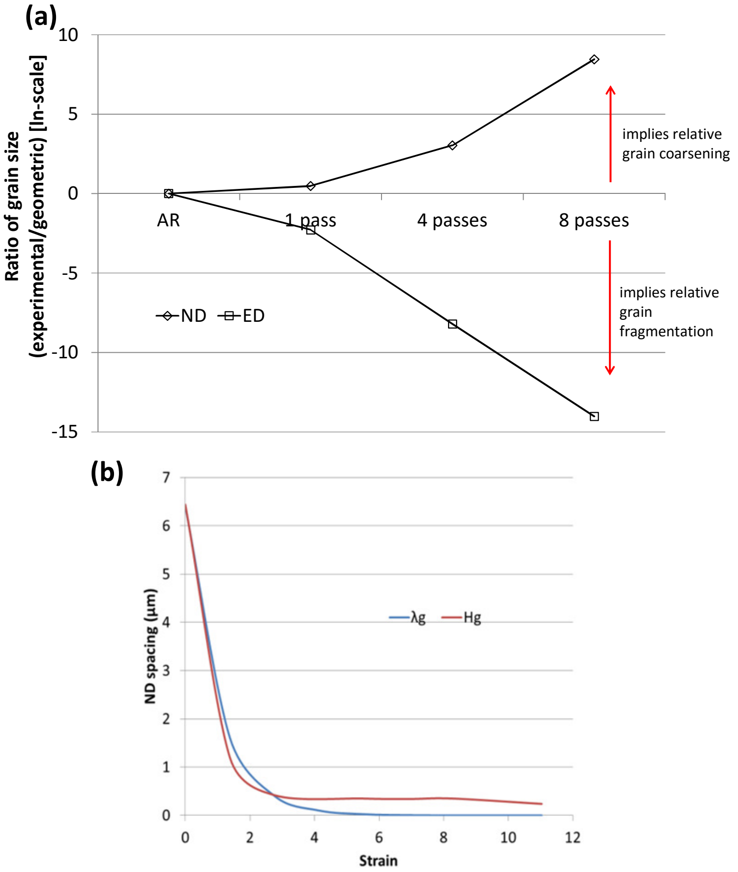

Figure 6-1 (a) plot of ratio of experimental grain size to theoretical grain size along ED and ND directions; (b) graph of ND grain boundary spacing as a function of strain – experimental (H_g) and theoretical (λ_g)

The agreement of grain size values at smaller true strain values and disagreement at higher strain values indicate that the model is very simple. This further indicates that the grain size evolution in metals subjected to room temperature deformation up to ultra-high strains (true strain >1) cannot be simplified and more experimental insights are needed to understand it. In general, the properties that influence the threshold size limit for the saturation are material purity, deformation temperature, stacking fault energy and strain mode [1-6]. Irrespective of these material and process variables, there are a few mechanisms which assist in obtaining the constant grain size characteristics. They are grain boundary sliding and grain boundary migration. More information on these mechanisms have been provided in the Chapter 2 (cf. section 2.4). Grain boundary sliding is not a process which can be easily tracked, unless TEM based study is performed. Therefore, this chapter will focus on the accommodation mechanisms that involve grain boundary migration, which can be visualised using EBSD technique. AccumEx processed saturated Al samples will be subjected to additional deformation strains and the microstructural modifications occurring between each strain interval will be studied. The obtained microstructural information will be analysed and their relevance for the grain coarsening behavior or grain size saturation will be interpreted.

6.2. Ex-situ plane strain compression test on split samples

6.2.1. Experimental set-up

Ex-situ plane strain compression is performed on CP Al samples which were pre-deformed up to a true strain of 550 % (4 passes) by AccumEx. The schematic of the PSC set-up is shown in Figure 6-2(a). Samples of 10 x 5 x 5 mm^3 dimensions are split in two halves (along ED and perpendicular to TD shown in dotted lines in Figure 6-2(b)) and the two new planes are polished and marked by hardness indentations (Figure 6-2(c)). The split sample is then reassembled, placed in the set-up and plane strain compressed to true strains of 11 %, 26 % and 38 %. The split sample allows us to perform microstructural characterization after every increment, without the effect of the surface frictions. EBSD measurements are done using 80 nm step size, consistently on one of the polished sides of the sample after every strain increment (as deformed) at a fixed region of interest. Hardness indentations are used as markers to track the region of interest after every strain increment step (as shown in Figure 6-2(c)). In this way, the same regions of the sample can be observed and their response to the applied plane strain deformation along the ED-ND plane can be studied.

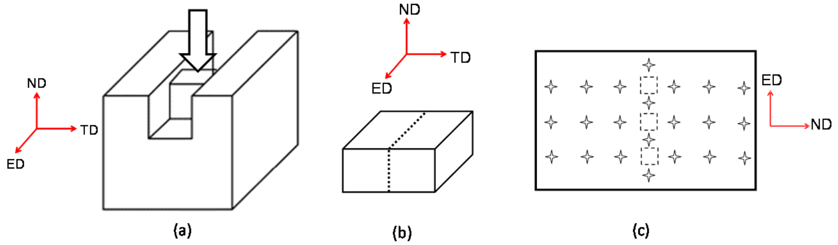

Figure 6-2 - (a) PSC set up; (b) Split sample with the split plane shown as dotted lines; (c) Plane of measurement marked by hardness indentions for spatial EBSD characterization

6.2.2. General microstructure evolution

Figure 6-3 shows the EBSD maps of one of the regions of interest, overlaid above their image quality after different strain increments. The starting microstructure of the material processed in PSC has a pan-cake ultrafine grained structure with an average grain size of nearly 1 µm. The bulk texture has stable orientations with the major fractions being S and Cu/T components. When additional deformation is given, microstructural changes are observed. Firstly, a highly heterogeneous microstructure is developed. The evolution of the grain boundary morphology suggests that the imposed deformation is first, during the first strain interval of 11%, accommodated by homogeneous compression in ND and corresponding stretching in ED and subsequently, during the strain intervals up to 26 and 38%, also by shear localization in the form of shear bands. Intergranular shear bands making an angle of 20-35° with ED were formed after 26 % increment strain. After 38 %, the frequency of these bands increased. The shear bands were nearly 100 µm long, spaced at 10 – 20 µm between each other and 2 to 4 grains thick. The bands modified the direction of material flow towards the shear direction. Because of this, lamellar grains which were initially elongated along ED deviated away from ED. An example of a shear band is shown in

Figure 6-4 (a). Figure 6-4 (b) shows the distribution of the inclination angles of the grains' major or elongation axis (assuming them as ellipse) with ND. A drop in the number fraction for 90° oriented grains with ND and increase in 69 and 79° orientated grains with ND is an indication that the ED elongated grains changed their lamellar direction away from ED.

Throughout the microstructure, no formation of new grain boundaries based on conventional slip based in-grain sub-division processes were spotted. The overall texture of the microstructure and the ratio of the component fractions (calculated with 15° standard deviation from their ideal position) remained almost the same. Such a contradiction from the conventional grain fragmentation behaviour can be attributed to the fine microstructure of the material. At this size of the microstructure the complete grain could possibly prefer to deform together as a single entity than by parts. However, shear driven microstructural heterogeneities occurred at several places locally which created new grain boundaries and grain sub-divisions.

Shearing and shear bands are commonly seen in FCC metals at two scales – macroscopic and microscopic. The formation of these shear bands during room temperature deformation generally depends on factors such as stacking fault energy, degree of reduction, grain morphology and grain size [7-10]. Stacking fault energy influences the crystallographic nature of the shear bands being formed – Bs type shear bands for low SFE and Cu type shear bands for increasing SFE. Al which is a high SFE material is not commonly reported to encourage shear bands. However, when it is deformed at higher degrees of reduction (greater than 60 %), shear bands do form in Al as well. Besides these, grain morphology and grain size play a crucial role. Lamellar grains or a layered grain structure are more prone to create shear bands. Paul et al. [7] says that layered microstructure is one of the most important factors in shear band formation and it is believed to be influential irrespective of the stacking fault energy of the material. This is because, the boundaries between layers act as barriers for dislocation motion and impose high stress concentration at the grain boundaries. This creates localised plastic slip which leads to formation of shear bands. The last factor is grain size [7]. It influences formation of shear bands especially at micro-scale. Reports say that one of the primary modes of deformation in UFG metals irrespective of crystal structure, degree of reduction, SFE, etc., is by shear localization [11,12]. Micro-shear bands have been attributed to the limitation in achieving good elongation properties during tensile tests. The low work hardenability rate due to high rates of dynamic recovery facilitates early onset of plastic instability by shear bands [13-15]. AccumEx deformed Al falls under the category of layered ultra-fine grained microstructure and therefore micro and macro shear bands will be major entities in the deforming material. This is the reason for early occurrence of shear bands just after 26 % deformation, compared to 60 % for coarse grained materials.

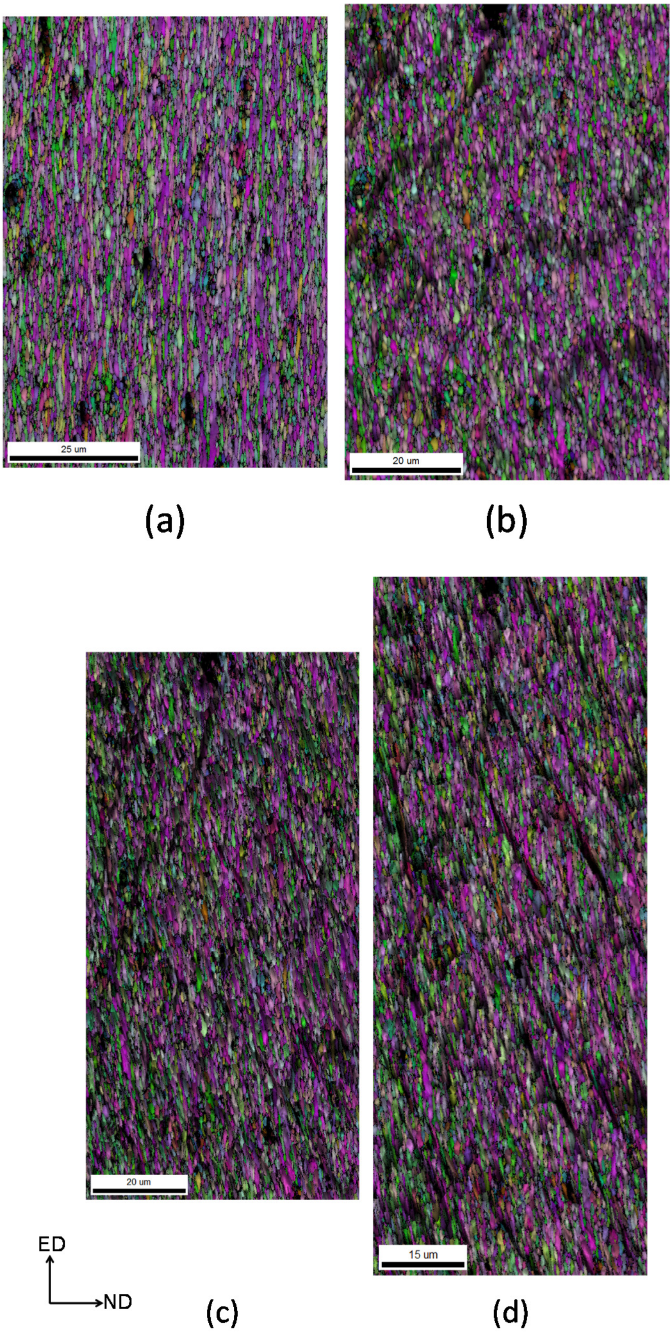

Figure 6-3 - Region of microstructure in the as-extruded state (a) and after 11 % (b), 26 % (c) and 38 % (d) strain increment

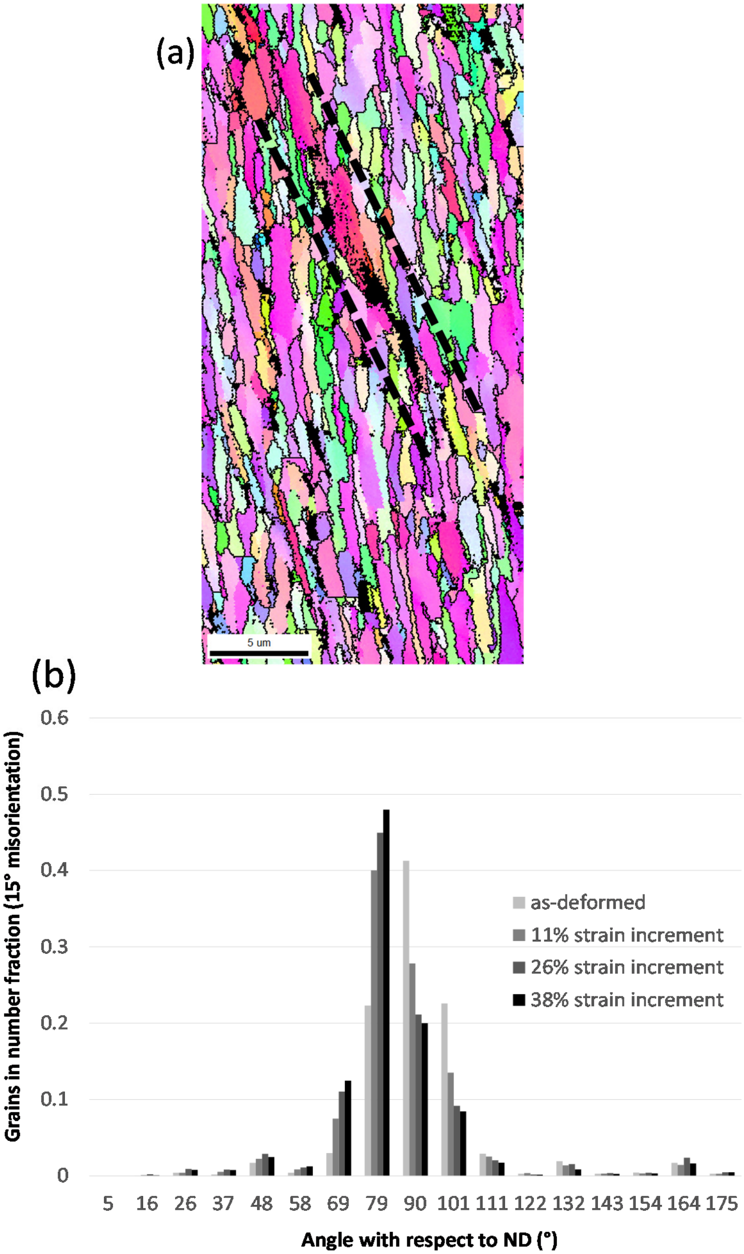

Figure 6-4 – (a) EBSD map showing a localized shear band; (b) Grain elongation axis angle distribution with respect to ND

6.3. Accommodation mechanisms

Microstructures obtained from the ex-situ compression tests, after every strain interval, were gathered and compared locally for local microstructural changes within and between grains. The changes are expected to be in grain size, grain morphology, crystallographic orientation or alignment of grain boundaries. Through careful examination of the microstructures, two mechanisms have been spotted which construe to play a vital role in the process of grain size saturation. They are grain splitting/pinching and triple junction motion. Grain splitting and they have been grouped as a single mechanism for easier interpretation. Grain splitting/pinching is observed to be focussed on high aspect ratio grains and the triple junction motion at the Y-type triple junctions, which are both constituents of lamellar grains [16]. Both the processes resulted in length reduction of the lamellae and in re-structuring of grains and grain boundaries locally. Following such events, disappearance of grains and coarsening of grains occurred and they can be found to occur either independently or at the expense of each other. In this section, both the mechanisms will be described in brief and the drivers of these mechanisms will also be discussed.

6.3.1. Grain splitting/ pinching

Grain splitting/pinching is not a commonly observed phenomenon in large equiaxed grain structures. Grain splitting is similar to grain fragmentation or grain sub-division which occurs by formation of a low angle grain boundary within a grain. Here, a lamellar grain is split into sub-grains by formation of one or several transverse low angle grain boundaries. Grain pinching on the other hand is separation of the grain into two or more independent entities. Through observations, it is found that sometimes, grain pinching can occur at the transverse low angle grain boundaries. Therefore, both the mechanisms have been grouped in a single mechanism as the point of interest here is reduction in the length of the grain lamellae. The grain splitting/pinching mechanism in general is pertinent to thin grains with high aspect ratio. In the current work, long and thin grains are noticed to pinch off into two or more separate entities between the strain intervals. The occurrence of splitting/pinching is found to be dependent on local grain arrangement, flow heterogeneity and the neighbouring grain interactions. Therefore, for understanding purpose, the observations have been classified into two types and each of them will be explained with a specific example.

6.3.1.1. Type 1

Type 1 involves both grain splitting and pinching. This type of grain splitting/pinching is driven by intra-grain strain heterogeneity induced by the direction of the material flow. Figure 6-5 presents an example of this. It is one of the striking examples that captures the sequence of splitting and pinching between the strain intervals in a clear manner. Lamellar grain A which is more than 8 µm long and around 600 nm wide, appears to be separated into 4 entities or individual grains at the end of 38 % strain increment. This separation occurs stage by stage and is mostly seen to be associated with local low angle transverse boundaries which are already in existence or newly formed within the long lamella as the straining proceeds. The colour code of the grain A after each strain increment indicates that its average orientation undergoes slight changes at different locations along the grain in this process.

Figure 6-6 (a) is the as-extruded initial position of the grain. Its corresponding (111) pole figure is shown alongside. The grain does not seem to have a single orientation but is sub-divided into regions with small misorientation (5-6° LAGBs). Based on the misorientation, regions - 1, 2, 3 and 4, are marked in the figure.

After 11 % strain increment (Figure 6-6 (b)), the grain inhomogeneously reduces in its width and inclines slightly away from ED. The inclination of the grain is also not homogeneous. Part 1 inclines 5° from its initial position and divides itself into 1a and 1b by forming a new transverse LAGB. Part 2 divides itself into two parts (2a and 2b). 2a inclines – 3° and 2b inclines 9° from their original axes. Part 3 and part 4 couples together to a single orientation (part (3,4)) and inclines 9° from its original state. All the mentioned divisions have been suggested based on the formation and disappearance of the LAGBs within the grain entities. Further, the associated small changes in the orientations are also captured in the corresponding (111) pole figure. The orientation spread from figure 6-6 (a) increased slightly in figure 6-6 (b).

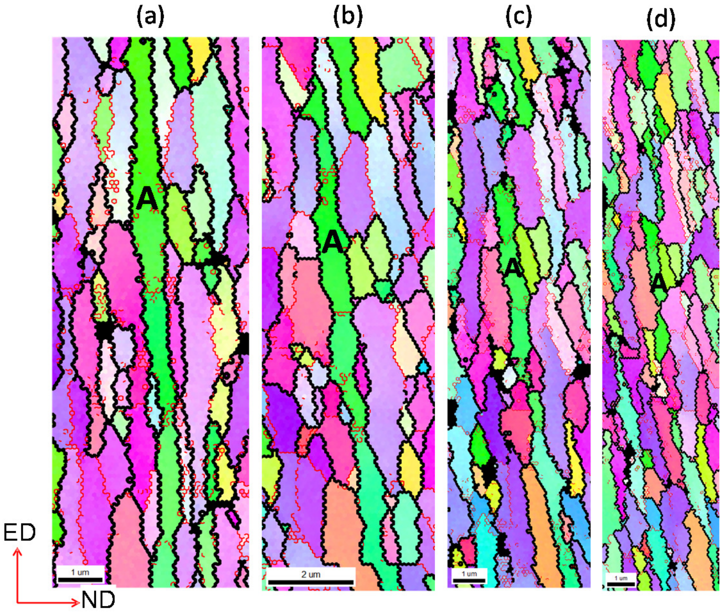

Figure 6-5-Grain splitting observed in grain A; (a) as-extruded; (b) 11 %; (c) 26 %; (d) 38 % strain increments

After 26 % strain increment, the grain further reduces in width, and again inhomogeneously (Figure 6-5 (c)). The degree of inclination seems not to vary a lot except for the tail part (2b, 3, 4). This preferential inclination of the tail leads to pinching of the grain at the LAGB interface between 2a and 2b. Alongside, another pinch off occurs at the LAGB interface of 1a and 1b. In the (111) pole figure, these changes are noticed in the form of increasing spread and rotation of the poles from their previous state. Along with the pinch off, part of the grain entity disappears. This gives an indication that the accommodation of the applied deformation might not be 2D anymore and some 3D effects are also possible to occur. More discussions on this aspect will be done in the later sections.

After 38 % strain increment, a significant reduction in width is seen and the inclination is seen to increase mainly in the part (3,4) (Figure 6-5 (d)). The grain entity is now inclined around 17° away from its starting position. Part 1(b) and 2(a) pinch off and some of the regions of the grains disappear. The pole figure shows higher rotation of poles with wider spread in the distribution of the poles.

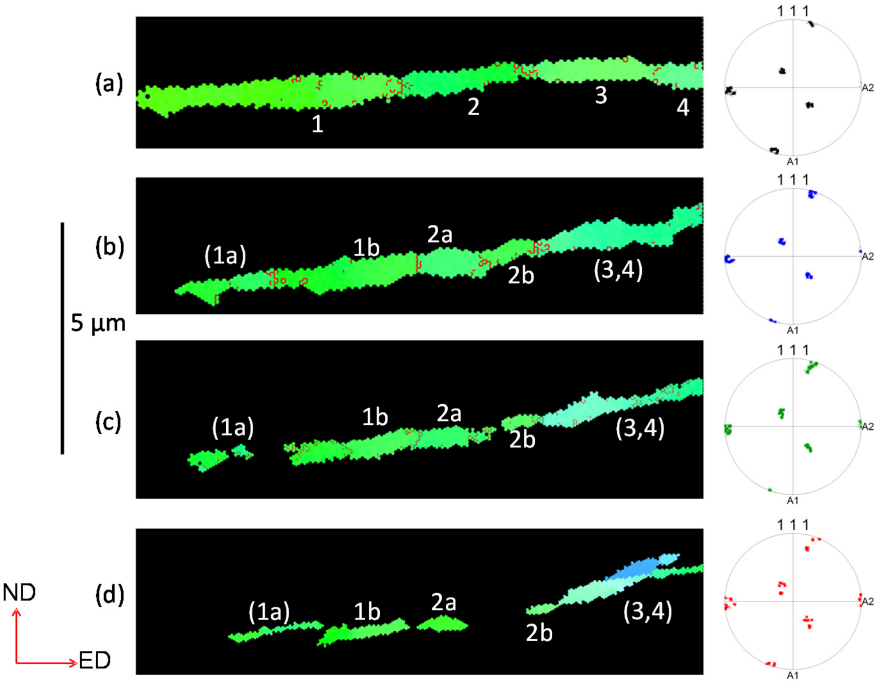

Figure 6-6 - Sequence of grain splitting of Grain A and its respective (111) pole figure from its as-extruded (a) to 11 % (b) , 26% (c) and 38 % (d) strain increments.

The sequence of steps which was described cannot be seen as an independent process. The change in orientation, formation and disappearance of LAGBs, grains pinching at transverse boundaries, etc., have some common link that drives the grain to its final point. Both change in orientation and inclination are observed to occur simultaneously. Grain A pinched off into 4 different entities. Of the 4 entities, entity or part (3,4) showed the highest alteration in both the orientation and the inclination, as noticed from the colour code and the geometry. To know if they are related, the change in angle of the longitudinal axis of the grain before and after the strains are measured and the measured angle have been used to rotate the crystal orientation of the entity rigidly. This is then be matched with the original crystal orientation of the entity. Results obtained from this exercise are presented in figure 6-7. The entity part (3,4), is measured to have changed its elongation axis by 17° after 38 % strain from its initial configuration. Its corresponding crystal orientation at as-extruded state and after 38 % strain are plotted in the pole figure as black and red dots respectively. Now, the original grain (part (3,4) only) orientation is rotated along TD(A2) rigidly by 17° and plotted in the same pole figure as blue points. The pole figure shows that there is a close relationship between the rigid rotation of the grain around TD and its corresponding crystal orientation. It indicates a possibility that the occurring orientation changes are mere resultant of rigid rotation of grains around TD, triggered by flow heterogeneities. Likewise, all the entities which observed crystal orientation changes showed a small link with their morphological inclinations. However, as the changes are subtle, it could not always be shown within the pole figure. Further, the formation of new transverse boundaries is also an indication of the varying rotation of the grain entities due to different inclination behavior.

It implies from this example that the main reason for the occurrence of grain splitting and pinching here is possibly due to the difference in the direction of flow of the material.

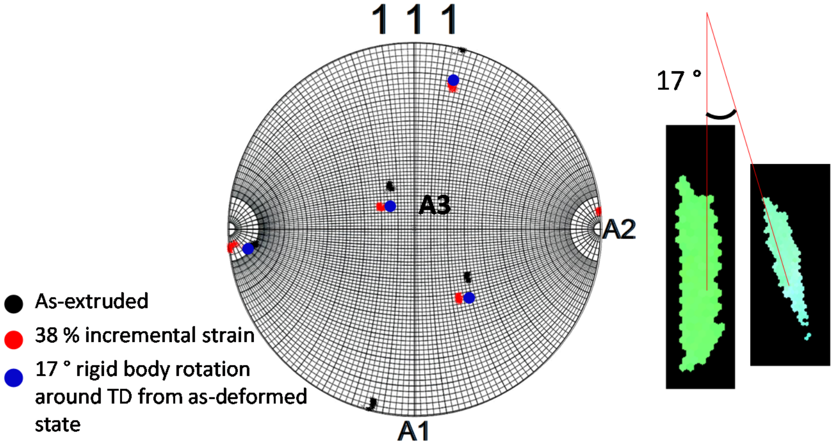

Figure 6-7-Comparision between the orientation of entity (3,4) after 38 % strain increment and 17° rigid body rotation. Wolff net is overlaid over the (111) pole figure. A1 – ED; A2 – TD; A3 – ND. Axis of rigid body rotation is A2

6.3.1.2. Type 2

Type 2 involves only grain pinching. Figure 6-8 (a) and (c) is an example which shows the grain pinching in a high aspect ratio grain. The process is found to be facilitated by differences in Taylor factor between the grains. Unlike type 1, type 2 seems to be a single step process and here it is noticed between 11% and 26% strain interval. The sizes of each grain and their orientations after 11 % and 26 % strain increments are shown in Table 6-1. Only grains 2 and 3 showed reduction in their width with a small change in their orientations. By observing the pictures, one can get an impression that grain 1 is harder than 2. In the language of crystal plasticity, the hardness of a grain can be represented using the Taylor factor. The plastic response of grains to a deformation mode varies with respect to the orientation. The Taylor factor is a measure of the plastic response of a crystal orientation. It is a function of activation of slip systems for a specific orientation in the applied specific deformation mode [17-19]. In simple words, an orientation with easier slip activation or which require lower stresses to activate shearing in its slip systems has a lower Taylor factor and vice versa. Therefore, the grain with higher average Taylor factor for a certain deformation mode is more resistant to deformation or needs higher magnitude of stress to realize the same amount of strain (c.f. section 2.1.1). The Taylor factor maps (for plane strain compression) for each microstructure are presented in Figure 6-8 (b) and (d). Before pinching, the average Taylor factors were 3.7, 3.35 and 3.43 for grains 1, 2 and 3 respectively. After pinching, the average Taylor factor of grain 1 increased to 4 and remained almost the same for grains 2 and 3. This implies that grain 1 is more resistant to plane strain compression than grains 2 and 3. This is the possible reason for the fact that grain 1 did not show any size change while grain 2 and 3 showed reduction in grain size and further grain 2 underwent pinching. Also, other possible reasons such as local morphology and 3D strain might also have its influence.

The increase in Taylor factor observed in grain 1 is due to an orientation change of the grain. The orientation change occurs homogeneously throughout the grain. The grain rotates around 2.5° almost around TD between 11 % and 26 % strain increment. The number is very small to prove if it is a resultant of rigid body rotation. Therefore, the orientation of the grain is traced back in its zero-strain increment state i.e., as-extruded and is plotted in a (111) pole figure in Figure 6-9. Now the orientation of the grain after 11 % and 26 % are also plotted in the same pole figure. Observing from the points, a clear indication of rotation of the poles around TD is noticed. The rotation angle is around 10-12°. Therefore, there is a high probability that the observed increase in Taylor factor due to change in orientation is a result of rigid body rotation of the grain. However, from the observed microstructure it cannot be said that the observed rigid body rotation is due to the change in the inclination of the grain. It is possible that the observed change in orientation is only a lattice rotation around TD.

Table 6-1 Grain width and average orientations (Euler angles) of the grains involved in Type 2 splitting

	Width (11 %)	**Width (26 %)**	**Average Orientation (11 %)**	**Average Orientation (26 %)**	
Grain 1	0.79	0.80	83.5, 29.2, 280.3	86.6, 31.4, 277.5	
Grain 2	0.66	0.46	54.2, 36.2, 341.5	56.5, 35.9, 339.9	49.9, 37.7, 346.9
Grain 3	0.83	0.71	272.5, 21.5, 44.9	270.4, 20.7, 49.4	

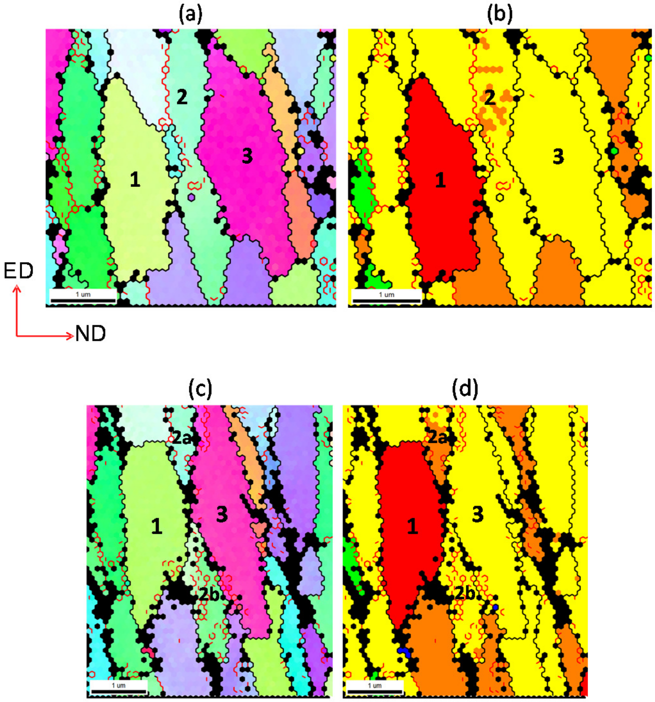

Figure 6-8 Splitting of grain 2 between 11 % (a) and 26 % (c) strain increment. Taylor factor maps (b) and (d) for plane strain compression deformation mode (🟨 - 3-3.5; 🟧 - 3.5 – 4; 🟥 - 4 – 4.5);

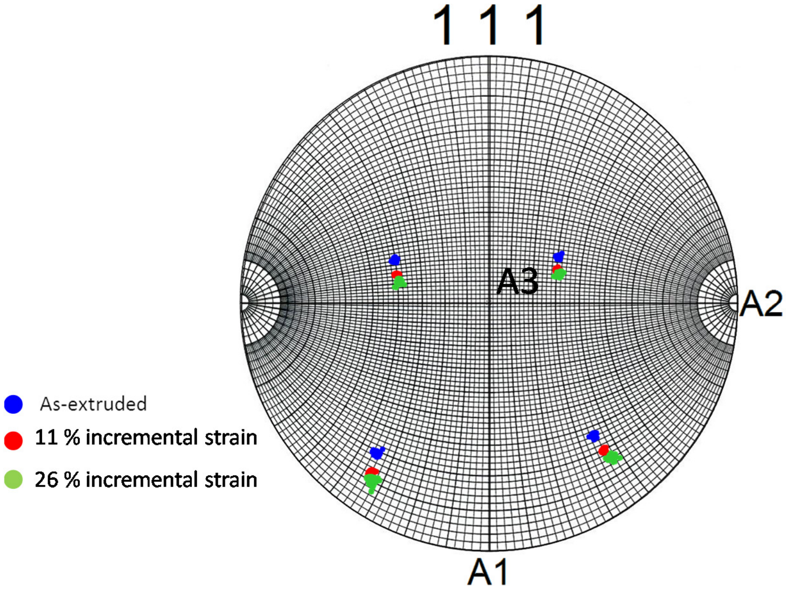

Figure 6-9 (111) pole figure overlaid over Wolff net of grain 1 (figure 6-8) in its as-extruded, 11 % and 26 % strain increment showing rotation around TD; A1 - ED; A2 - TD; A3 - ND

6.3.1.3. A shear driven process

Two examples of grain splitting/pinching were discussed – Type 1 and Type 2. Type 1 was intra granular in nature. A heterogeneity in the morphological rotation of the grain entities or the sub-divided grain regions resulted in grain splitting/pinching of the parent grain into several entities. Associated with it, crystallographic orientations also occurred and was found to be a rigid body rotation around TD as per its corresponding morphological inclination. Type 2 was inter granular in nature. Each grain has a resistance to deformation. The heterogeneity of the grains' resistance to deformation is further modified by change in crystallographic orientation of specific grain(s) which resulted in grain pinching of the neighboring grain. The crystallographic orientation change was found to be a rigid body rotation around TD. In both cases, local grain orientation changes – both morphological and crystallographic formed the primary cause for the grain splitting/pinching mechanism.

Rigid body rotation is not a commonly observed phenomenon in plane strain compression deformation mode. It has been always associated with simple shear deformation mode. The conclusions derived from the examples suggest that the observed rigid body rotations are due to the flow heterogeneity associated with the morphological inclination of the elongated grains. The source of these grains' inclinations is localized shear. It was mentioned in the section 6.2.2 that shear bands were seen after 26 % strain interval. Figure 6-4 (a) showed an example of a shear band. In the shear band regions and in the vicinity of the shear bands, the grain changed its elongation direction and rotated morphologically around TD in the ED-ND plane. Between each shear bands, a gradient in the inclination can also be seen. Such morphological rotation of the grains at times modifies the crystallographic orientation of the grains, depending on the texture of the grain. And in most cases the change in orientation is a rigid body rotation around TD or near TD. Microstructural factors which influence this process are grain thickness, grain aspect ratio, neighboring grain morphology and the grain's and grain neighbors' crystallographic orientations.

The local deformation mode at the level of microstructure is not always the same as which is applied macroscopically. In the continuum mechanics, this is represented as macroscopic and microscopic velocity gradient (more information in cf. section 2.1), which accounts for both deformation and rotation [20]. For most coarse-grained materials, the macroscopic and the microscopic deformation fields are assumed to be equal (Taylor's hypothesis). However, in reality there can be a strong deviation between the applied and the realised local deformation field. In fine grained materials, the possibilities are even higher because the presence of large fraction of grain boundaries create in-homogeneities in strain transfer between grains. Studies have proven this phenomenon both experimentally and through modelling. Quoting from the work of Kanjarla et al., [21] *'grain boundaries tend to induce opposite shear rates in the neighbouring grains and depending on the severity, new orientations tend to form at the vicinity of the grain boundary, irrespective of the grain orientation'*. The local texture evolution is modified [13,22,23]. Like such examples, the localized shearing observed in the current work modified the local deformation tensor. Equation (6-2) shows the macroscopically applied plane strain compression deformation is being modified locally as a combination of shear and compression. The value of x in the deformation tensor might vary as function of the position within the microstructure. The result is similar to what was derived in chapter 5.

$$\begin{bmatrix} 1 & 0 & 0 \\ 0 & 0 & 0 \\ 0 & 0 & -1 \end{bmatrix} => \begin{bmatrix} 1 & 0 & x \\ 0 & 0 & 0 \\ x & 0 & -1 \end{bmatrix} \tag{6-2}$$

6.3.2. Triple junction motion

Triple junction motion is the second type of accommodation mechanism which was part of the observation from the EBSD maps. Y-type triple junction with very small dihedral angles migrated at different strain increments and reduced the length of the lamellae which led to local increase in the size of the neighbouring grains. In this section, the triple junction motions which were observed during the ex-situ study will be briefly described with the help of three examples and an interpretation on the possible driving forces will be stated. Most of the differences are observed at micron-level and therefore, the results will be considered as a qualitative indicator. In order to be as precise as possible, care was taken to align the samples for EBSD measurements after every strain increment with the help of the hardness indenter markers. Further, the EBSD measurement was performed at 80 nm resolution which ensures a reliable observation on the changes in the measured microstructure.

6.3.2.1. Example 1

Figure 6-10 (Example 1) is an example of two triple junction motions noticed between the steps of 26% and 38% strain. Both are all HAGB junctions and are noticed at the junctions shared by grains 2 and 3 with 1 and 4. Between 26 % and 38 % strain, grains 2 and 3 indicate a reduction in size. The measured change in length for grains 2 and 3 are 0.5 µm and 0.3 µm respectively and their corresponding areas changed from 2.6 and 1.6 μm^2 to 1.3 and 1.5 μm^2 respectively. For grain 1, the average width remained almost constant in spite of the fact that the length of the grain increased from 4.2 µm to 5.2 µm. This shows that even after an incremental strain of 12 %, grain 1 stayed almost the same at the expense of the grain 2 and grain 3, facilitated by triple junction motion.

6.3.2.2. Example 2

Figure 6-10 (Example 2) is another example of a triple junction motion. It comprises 2 HAGB and 1 LAGB. The migration is seen in the strain interval between 26 and 38 %, pointed with an arrow. The misorientation angle of each boundary is shown in the figure. The highlighted grain reduces in area from 1.61 μm^2 to 0.96 μm^2, although its corresponding width remains unchanged at around 0.48 µm. The almost 40 % reduction in the grain area is due to the change in length of the grain and is facilitated by triple junction motion of the grain.

Example 1

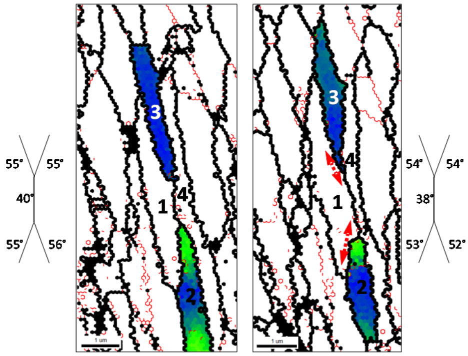

(a) (b)

Example 2

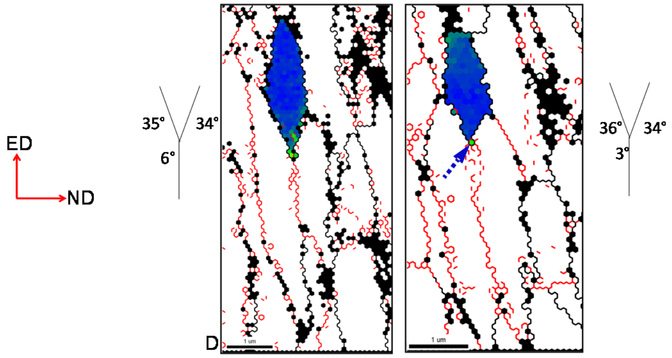

(a) (b)

Example 3

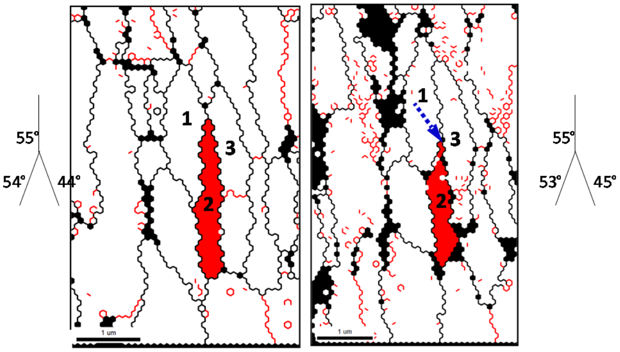

(a) (b)

Figure 6-10 Examples showing triple junction motion. The moving junctions are marked in each figure

6.3.2.3. Example 3

Figure 6-10 (Example 3) shows another example of a triple junction motion that is observed between 11 and 26 % strain. It is an all HAGB junction. Grain 2 reduces in area from 0.75 μm^2 to 0.64 μm^2. The width of the grain stays almost constant at around 300 nm. On the other hand, the length of the grain reduces from 2.4 µm to 2 µm due to the triple junction motion. Because of the change in area of grain 2, grain 1 and grain 3 coarsen locally. Their corresponding changes in area can be seen to be as 1.02 to 1.2 μm^2 and 0.72 to 1.15 μm^2 respectively.

Based on all the observed cases, two common points can be noted. The dihedral angle of the lamellar grains which show triple junction motion is low, roughly around 20-40° and the region which is swept by the triple junction motion has an average lamella spacing of only less than 250 nm. However, the exact driving force for the occurrence of such a mechanism is unclear.

Triple junction motion is not a commonly reported phenomenon in room temperature deformation. This is because it needs a higher temperature for activation [24-27]. However, from recent studies it was learnt that triple junction motion can occur as a restoration process in places of localised excess strain energy. The work from Yu et al., stated that when a heavily deformed lamellar microstructure of Al was subjected to low temperature annealing (less than 150° C), it immediately exhibited triple junction motion [16,28,29]. It led to shortening of thin lamellar grains. And as the duration and temperature was increased, they develop into near equiaxed structures. When similar experiments were done in this work, comparable results were obtained (not presented in the thesis). Therefore, triple junction motion certainly can be counted as a recovery mechanism for the grains to reduce their stored energy. In line of this, another work by Renk and Yu et al. reported triple junction motion during room temperature deformation of Al and Cu [18,30]. The degree of change in length of lamellae is less significant compared to high temperature involved experiments, however, they cannot be considered insignificant. In the absence of high temperature, the activation of the triple junction was not clear and was proposed as a stress-driven process. Howsoever, triple junction motion which was considered as a phenomenon occurring during static recovery, from their work and with further proofs from the current work, can now be established as also one of the phenomena occurring during a dynamic recovery process as well.

6.3.2.4. Stress-assisted process

Based on the understanding of triple junction motion in a grain growth process and the arguments from literature, the driving force for a triple junction motion should be something very local. With absence of high temperature, as suggested by Renk and Yu et al., stress induced activation can be suggested as a possible reason [4,5,31]. Derived from grain growth kinetics, the velocity of the triple junction motion can be written as [25,27],

$$V_{tj} = m_{tj}\sigma(2\,cos\theta - 1) \tag{6-3}$$

The migration velocity V_{tj} is proportional to surface tension (σ), dihedral angle (2θ) and mobility of the boundary (m_{tj}). Here mobility is a temperature dependent property. Surface tension is dependent on the grain boundary energy (γ) and the dihedral angle and it is believed to act on the TJ. This can be estimated using a sine-law relation [28,32],

$$\frac{\gamma_1}{sin\,2\theta_1} = \frac{\gamma_2}{sin\,2\theta_2} = \frac{\gamma_3}{sin\,2\theta_3} \tag{6-4}$$

If one considers only interfacial energies to be present in the system, the vector sum of forces will be 0 to maintain equilibrium. Therefore, at equilibrium, the dihedral angle can be calculated as 120° by assuming that grain boundary energies are same for all the three grain boundaries at the junction. When there is any change in the dihedral angle due to influence of external factors, the whole system diverges away from equilibrium which creates a net surface tension at the triple junction. This surface tension can be estimated as a function of dihedral angle and grain boundary energy. By assuming the same grain boundary energy for all the three boundaries at the triple junction, the surface tension can be given in an equation form as,

$$\sigma = (2\,cos\,\theta_1 - 1)\gamma \tag{6-5}$$

Where θ_1 is half-dihedral angle opposite to grain boundary 1. The equation suggests that with increasing dihedral angle from 0 to 120°, the ratio of surface tension to grain boundary energy reduces from 1 to 0. Substituting this observation in equation (6-3), for smaller dihedral angles, the velocity of a triple junction will be higher. This inference will be very relevant for the current observations. However, although the triple junction should be mobile at room temperature, it needs an activation to make it mobile. This activation has been claimed by some authors to be stress assisted [31].

It is well-known that in plastically deformed metals, grain boundaries are regions containing dislocations [24,25]. One of the unique properties of these grain boundaries that have been found is, they are responsive to shear stresses. It was established with the help of in-situ experiments on bicrystals with different types of edge type grain boundaries (axis-angle pair) of different misorientation angles that grain boundaries migrate as a response to an applied external shear stress at room temperature and high temperatures. It is claimed that the external stress field couples with the stress field at the grain boundaries which result in grain boundary motion. This has been called as stress induced grain boundary migration [31]. Factors such as capillary forces, misorientation angles, temperature, etc., show some influential effects. Triple junctions are also structures defined by intersection of grain boundaries and can certainly share similar characteristics. Moreover, triple junctions are known to have stress concentration zones and strain heterogeneities due to the occurrence of dislocation interactions and pile-ups [13,21]. From these arguments, it can be suggested that the observed triple junction motion can be a stress-assisted process. However, there is no evidence to assert this argument based on the available information. TEM studies or tri-crystal experiments will be necessary to substantiate it which will be suggested for future work.

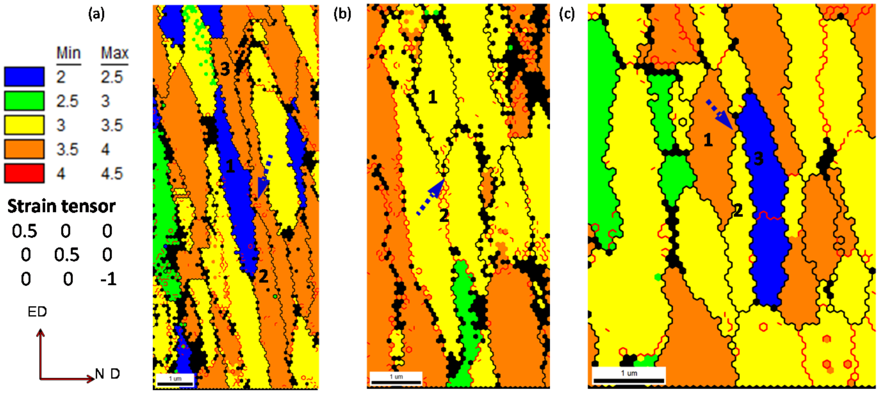

Figure 6-11 Taylor factor map of the grains from examples 1, 2 and 3 of figure 6-10 which migrated by triple junction motion and their neighbours for deformation mode with TD material flow; ε_{11} – ED; ε_{22} – TD; ε_{33} – ND

6.3.2.5. Flow heterogeneity driven process

Flow heterogeneity along ED was widely discussed in the previous sections. It plays a major role in grain splitting/pinching. It is speculated that it might be influential in the occurrence of triple junction motion as well. The flow heterogeneity of interest here is along the TD direction. The plane strain compression tests have been performed on a split sample. Although the dimensions are constrained in accordance to the specifications of the plane strain compression test, use of split samples provide room for minute accommodative deformation along TD. Further, it was observed that the faces of the split samples that have been polished exhibit roughness at micro-scale after straining. This suggests that a small but significant flow of material along TD is possible. Moreover, the grain size of the samples being deformed is in UFG range and so even a micro-scale flow can have a very prominent effect on the grains of the material. This was noticed in the grain splitting/pinching mechanism as well, where some regions of grains seem to have disappeared. It is possibly due to 3D flow of the material. Similarly, such a 3D flow can be a likely suspect for the observed triple junction motion. To examine this, a Taylor factor study is done on the reported 3 examples of the triple junction motion. In this study, different strain tensors with (3D strain) and without (2D strain) flow along TD are used and their corresponding Taylor factors of the grains are plotted. By doing this, it was noted that when flow along TD (3D strain) is included in the strain tensor, a relation between the observed triple junction motion and the Taylor factor maps could be seen in 2 examples out of 3. Due to difference in flow properties between grains along TD, the grains which have a lower Taylor factor for a deformation mode which takes in to account flow along TD, can preferentially flow or deform more than their neighbours along TD. This can result in an apparent coarsening/triple junction motion in a 2D-section. Figure 6-11 shows the Taylor factor maps of the examples presented in the previous section for a theoretical deformation mode which includes flow in TD also (3D strain). The strain tensor which was used to calculate the Taylor factors is also mentioned in the figure. In Figure 6-11 (a) Grains 2 and 3 have 3.55 and 3.66 as their respective Taylor factors, which is greater than that of grain 1 (2.4). Triple junction motion is observed in both grains 2 and 3. With respected to this figure, the observed triple junction movement can be stated as coarsening of grain 1 at the expense of grains 2 and 3, due to preferential flow of grain 1 along TD. In Figure 6-11 (b), the Taylor factors of grains 1 and 2 are 3.23 and 3.25, almost the same. No relation with the observed triple junction motion is seen. In Figure 6-11 (c) the Taylor factors of grains 1, 2 and 3 are 3.67, 3.3 and 2.45 respectively. Triple junction motion is seen at grain 2. It can be interpreted as, grain 3 having the lowest Taylor factor of all, coarsened at the expense of grain 2. From Figure 6-11 (a) and (c), a perspective is derived where the grain with lower Taylor factor preferentially flow in TD (out of plane). This is observed on a 2D plane as grain coarsening at the expense of shortening of the hard-neighbouring grains (triple junction movement). Therefore, it will be more realistic to state that triple junction motion can be a perceptive observation of flow heterogeneity between grains along TD. However, to be completely certain about such an observation, further analysis will be needed. With the help of theoretical models such as VPSC, ALAMEL, CPFEM, etc., the basis behind the observed changes can be verified and evaluated. It has not been done in this work, but will be a strong future work suggestion.

6.3.3. Re-configuration of grains and grain boundaries

The two microstructure accommodation mechanisms - grain splitting/pinching and triple junction motion were discussed separately with the help of examples in the previous sections. Both the mechanisms instigate different changes in the local configuration of the microstructure. Some grains disappear, grains which never shared boundaries form new pairs with shared boundaries – both LAGBs and HAGB, some grains coarsen at the expense of the neighbouring grains, etc. Collectively, they result in a modification of the local microstructure in such a way that the average grain size along ND does not change much. In order to explain this, a series of accommodation mechanisms which were observed in the same region of the microstructure at different increment steps were captured and used for discussion.

In Figure 6-12, three pairs of microstructures are presented - (a,b), (c,d), (e,f). They all show the same region of the microstructure from as-extruded state to 11% (a to b), 11 % to 26 % (c to d) and 26 % to 38 % (e to f) strain increments. For clarity: (b) and (c), as well as (d) and (e) are the same measured scan, but the former shows the post-strain events of the previous strain increment and the latter shows the indication of the regions where the accommodation is expected to occur for the ongoing strain increment. The regions which show splitting/pinching and triple junction motion at each strain increment are marked in the figures and numbered in Roman numerals. More description about the markings are described in the caption of the figure. By comparing (a) and (b), 3 grain splitting/pinching and 9 triple junction motions are spotted. The triple junction motions at II and III enable local grain coarsening of their corresponding neighbouring grain and in another case at V, a combination of 1 grain splitting/pinching and 2 triple junction motions lead to local grain coarsening of the migrating grain. Besides, for both the cases, the grains which were not neighbours before the strain increment share new boundaries in the place of the disappeared grain region. The boundary is a LAGB for the former and a HAGB for the latter. Between 11 and 26 %, 3 splitting/pinching and 5 triple junction migrations are spotted. Two triple junction motions lead to disappearance of a whole grain and the others result in local grain coarsening in its neighbourhood. At the expense of the disappearing grains, new grain pairs are formed. Amongst the 5 triple junction motions, junction X was formed due to a grain splitting/pinching during the previous strain increment step. Between 26 and 38 % strain increment step, 3 grain splitting/pinching and 4 triple junction motions are observed. Of the four, two triple junction motions occur at the triple junctions formed from the previous deformation increment and all of them result in partial or complete disappearance of grains.

In total, 6 grain splitting events occurred between as-extruded and 38 % strain increment and they resulted in formation of 12 new triple junctions. Of the 12, 6 of them underwent triple junction motion in the sub-sequent processing. Including them, a total of 17 triple junction motions occurred between as-extruded and 38 % strain increment. 5 of them facilitated partial or complete disappearance of the grains, 4 in grain coarsening (equiaxed structures) and all of them led to formation of new grain pairs sharing a new LAGB or a HAGB. All the mentioned observations belong to only a single small representative region, 8 X 11 µm^2, of the complete microstructure. Likewise, several regions in different parts of the microstructure are likely to undergo different combinations of similar sequential events. Similar local reconfiguration of grain boundaries is also expected. Through these sequential events which are facilitated by the grain interactions, the local grain size is influenced. The local grain size is roughly conserved. This suggests a new perception of the grain size saturation. Theoretical concepts say that grain size saturation is a resultant of dynamic recovery. It is a generally accepted phenomenon for room temperature deformation but unlike medium and high temperature deformation, no proper experimental proofs have been reported. Learning from the above observations it can be suggested that triple junction motion is a dynamic recovery process and grain splitting assists in formation of such triple junctions. The grain interactions which instigate the splitting are facilitated by texture and local flow heterogeneities. They lead to partial/complete disappearance of grains, coarsening of grains, re-structuring of grain boundaries, etc., which in turn helps the microstructure to maintain a constant grain size or at times even grain coarsening for any degree of additional strains under similar conditions.

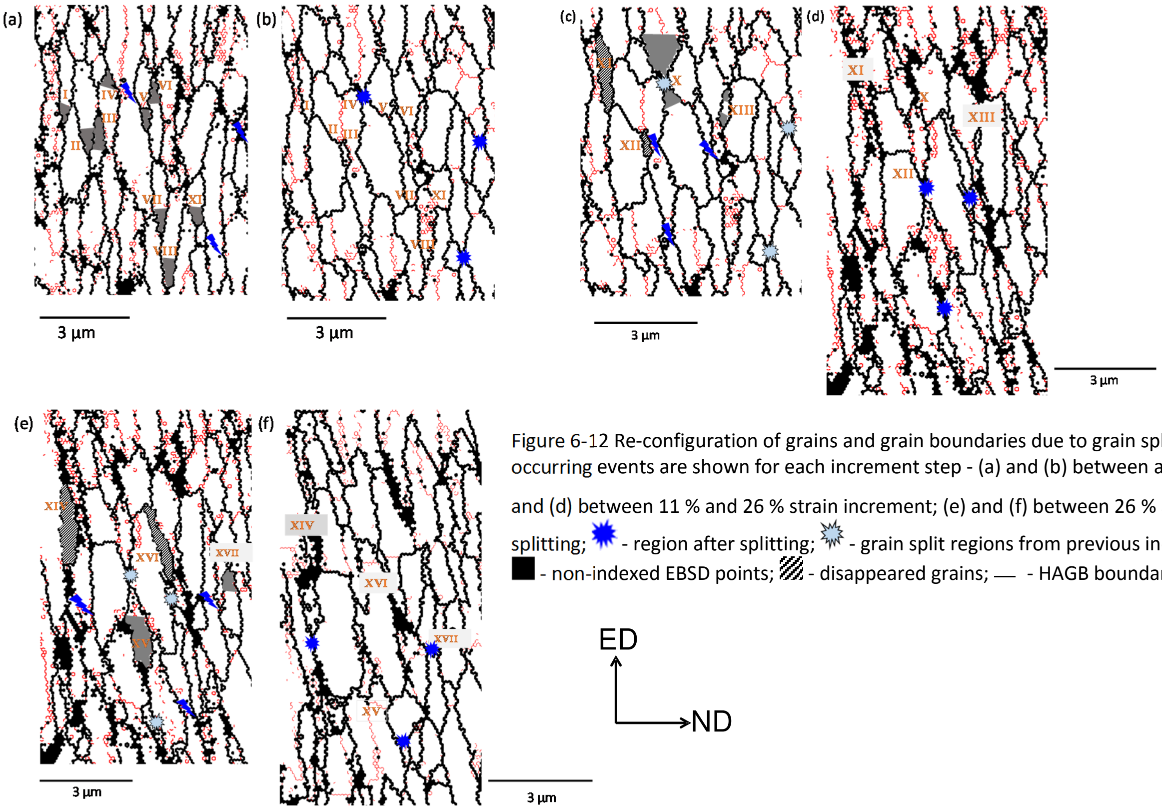

Figure 6-12 Re-configuration of grains and grain boundaries due to grain splitting and triple junction motion. The occurring events are shown for each increment step - (a) and (b) between as-extruded and 11 % strain increment; (c) and (d) between 11 % and 26 % strain increment; (e) and (f) between 26 % and 38 % strain increment. ⚡ - grain splitting; ✸ - region after splitting; ✺ - grain split regions from previous increment steps; ◼ - triple junction motion; ■ - non-indexed EBSD points; ▨ - disappeared grains; — - HAGB boundary; — - LAGB boundary.

6.4. Relevance for AccumEx

The plane strain compression ex-situ experiments revealed different microstructural accommodation mechanisms and those were described using examples. Also, possible reasons for the occurrence of the mechanisms were suggested. However, it still raises a question whether these observations are relevant in the context of AccumEx, since the main problem statement was why the grain size saturation is seen in spite of severe straining between 4 and 8 passes. This short section tries to assess the relevance with the help of a couple of graphical representations.

In Figure 6-4 (b), it was shown that the angle of inclination of the grains deviated from ED. This was attributed to the heterogeneous flow behavior of the grains facilitated by increased shear localizations in the form of shear bands during the PSC tests. A similar plot is presented for microstructures obtained after 4, 5 and 6 passes of AccumEx in Figure 6-13. It suggests that as the deformation proceeds from 4 to 6 passes, the number fraction of grains with their elongation axis 90° to ND significantly decreased. As a consequence, a significant increase in the grains with their elongation axis 10-30° away from ED can be noted. This is in a reasonable agreement with the observation made from figure 6-4. In addition, similar to the microstructure observed after PSC tests, several shear bands were noticed on the ED-ND plane, after 5 passes and they increased as the number of passes increased in AccumEx. This supports the hypothesis that the mode of deformation at the microstructure level is a combination of shear and compression for both cases, though likely at different ratios.

In another important observation from the performed PSC experiments, localized changes in the texture by rigid body rotations were noticed, associated with the shear heterogeneities. When the angles of rotation become higher, they can easily have an impact on the bulk texture of the material, when measured by XRD. This implies, if rigid body rotation is dominant in AccumEx as well, this should be reflected in the measured bulk texture of the material. Figure 4-11 suggested significant texture changes between 4 and 8 passes. To know if they are a result of rigid body rotation, a region of 100 X 200 μm^2 microstructure of pre-deformed sample (a reasonable representation of the bulk texture) is rigidly rotated up to 10 and 15° (suggested angle is derived from rigid body rotations which were observed from the PSC tests) around TD, both negative and positive with the help of TSL OIM Analysis software. The corresponding changes in the number fraction of the texture components are calculated and plotted in figure 6-14 and compared with the changes seen in figure 4-11. For both cases, Bs and S reduce in intensity and Cu and

H increase in intensity. On the other hand, component D reduces in intensity during the rigid body rotation, while during AccumEx, it increases in intensity. Except this outlier, the general effect of rigid body rotation around TD shows similar patterns of texture changes as what was measured between 4 and 8 passes of AccumEx. This indicates that localized shear can be an influential factor in the texture evolution. It should be noted that the presented study assumes that all the grains within the microstructure homogeneously undergo the same rigid body rotation. In reality, this is not true. The occurring shear along the ED-ND plane with axis of monoclinic symmetry around TD will be highly heterogeneous with different magnitude and sign for different regions within the microstructure. Therefore, their actual effect on texture evolution will be more complex, although exhibiting a similar trend.

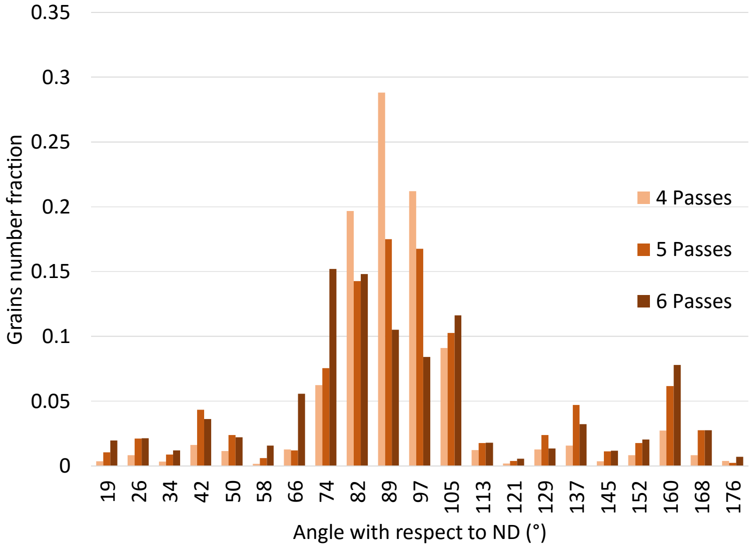

Figure 6-13-Grain elongation axis angle distribution with respect to ND after 4, 5 and 6 passes of AccumEx

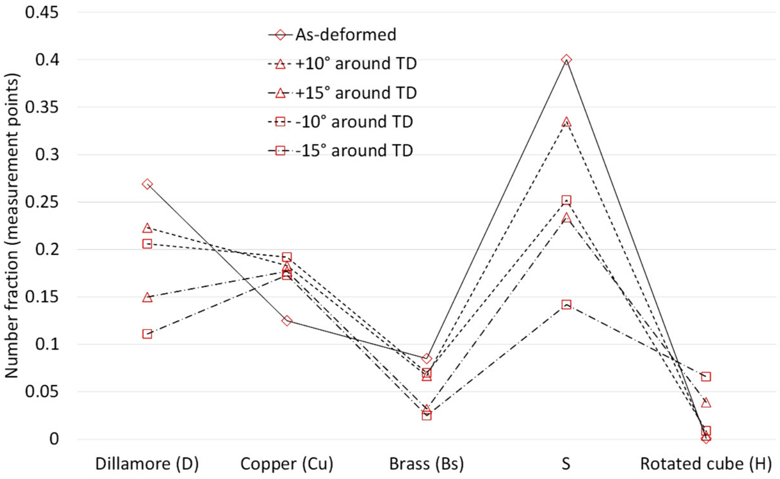

Figure 6-14 - Texture changes associated with rigid body rotation around TD of a region of the microstructure deformed up to 4 passes of AccumEx

Both analyses indicate that the results from the plane strain compression test can form a valid argument in the context of AccumEx deformation and can serve as a strong basis for exploring further.

6.5. Summary and conclusions

The steady state deformation regime is known to be a common phenomenon in SPD processing. Grain size reduction stops and the change in macroscopic strength of the material reaches a constant value after a certain deformation strain. Often, it is claimed that at this point, the rate of formation of dislocations are compensated by annihilation of dislocations and they are assisted with the help of some dynamic recovery mechanisms [1,3,33,34]. This study showed that practically it has more to it. With the help of ex-situ plane strain compression tests coupled with spatial EBSD characterization the actual microstructure changes could be captured.

Grain splitting/pinching and triple junction motion have been identified as two important mechanisms to facilitate the grain size saturation behaviour. Grain splitting/pinching was observed to be a resultant of flow heterogeneity facilitated by localized shear while triple junction was speculated to be either due to a stress induced grain boundary migration or due to flow heterogeneity between grains along TD. Sequential occurrence of these microstructural mechanisms resulted in local reconfiguration of grain boundaries and grains in such a manner that a constant grain size could be maintained. The final configuration of the microstructure was comparable with the microstructure obtained after AccumEx deformation which asserts the relevance of the observations from the PSC test to the AccumEx process.

Some of the other key observations for this work were – (i) the effect of shearing and shear bands on the microstructure has been captured experimentally. Occurrence of micro-shear bands modified the local grain arrangement by creating heterogeneities in the flow behavior of the grains. The heterogeneities were seen both at inter and intra granular level and could be directly related with the occurring texture and morphological changes in the grains; (ii) triple junction motion has been categorized as one of the dynamic recovery process. It is not just one of the static recovery mechanism at medium temperatures, but also occurs at room temperature deformation of thin lamellar grain microstructure materials; (iii) material flow along TD has been found to be a strong possibility for the occurrence of the triple junction motion which was never considered in literature. This observation indicates that the resolved deformation at the micro-scale of UFG materials is very complex.

REFERENCES

1 Li, Y. S., Tao, N. R. & Lu, K. Microstructural evolution and nanostructure formation in copper during dynamic plastic deformation at cryogenic temperatures. *Acta Materialia* **56**, 230-241, doi:10.1016/j.actamat.2007.09.020 (2008).

2 Huang, Y. & Prangnell, P. B. The effect of cryogenic temperature and change in deformation mode on the limiting grain size in a severely deformed dilute aluminium alloy. *Acta Materialia* **56**, 1619-1632, doi:10.1016/j.actamat.2007.12.017 (2008).

3 Pippan, R. *et al.* Saturation of Fragmentation During Severe Plastic Deformation. *Annual Review of Materials Research* **40**, 319-343, doi:10.1146/annurev-matsci-070909-104445 (2010).

4 Pippan, R., Wetscher, F., Hafok, M., Vorhauer, A. & Sabirov, I. The Limits of Refinement by Severe Plastic Deformation. *Advanced Engineering Materials* **8**, 1046-1056, doi:10.1002/adem.200600133 (2006).

5 Estrin, Y. & Vinogradov, A. Extreme grain refinement by severe plastic deformation: A wealth of challenging science. *Acta Materialia* **61**, 782-817, doi:10.1016/j.actamat.2012.10.038 (2013).

6 Zhang, K., Weertman, J. R. & Eastman, J. A. Rapid stress-driven grain coarsening in nanocrystalline Cu at ambient and cryogenic temperatures. *Applied Physics Letters* **87**, 061921, doi:10.1063/1.2008377 (2005).

7 Paul, H., Driver, J. H., Tarasek, A., Wajda, W. & Miszczyk, M. M. Mechanism of macroscopic shear band formation in plane strain compressed fine-grained aluminium. *Materials Science and Engineering: A* **642**, 167-180, doi:10.1016/j.msea.2015.06.056 (2015).

8 Shen, Y.-L. On the shear band formation in F.C.C. metals. *Scripta Metallurgica et Materialia* **25**, 1081-1085, doi:http://dx.doi.org/10.1016/0956-716X(91)90505-U (1991).

9 Morii, K., Mecking, H. & Nakayama, Y. Development of shear bands in f.c.c. single crystals. *Acta Metallurgica* **33**, 379-386, doi:http://dx.doi.org/10.1016/0001-6160(85)90080-X (1985).

10 Hatherly, M. & Malin, A. S. Shear bands in deformed metals. *Scripta Metallurgica* **18**, 449-454, doi:http://dx.doi.org/10.1016/0036-9748(84)90419-8 (1984).

11 Sakai, T., Miura, H. & Yang, X. Ultrafine grain formation in face centered cubic metals during severe plastic deformation. *Materials Science and Engineering: A* **499**, 2-6, doi:10.1016/j.msea.2007.11.098 (2009).

12 Yu, C. Y., Kao, P. W. & Chang, C. P. Transition of tensile deformation behaviors in ultrafine-grained aluminum. *Acta Materialia* **53**, 4019-4028, doi:10.1016/j.actamat.2005.05.005 (2005).

13 Kanjarla, A. K., Van Houtte, P. & Delannay, L. Assessment of plastic heterogeneity in grain interaction models using crystal plasticity finite element method. *International Journal of Plasticity* **26**, 1220-1233, doi:10.1016/j.ijplas.2009.05.005 (2010).

14 Guo, Y., Britton, T. B. & Wilkinson, A. J. Slip band–grain boundary interactions in commercial-purity titanium. *Acta Materialia* **76**, 1-12, doi:10.1016/j.actamat.2014.05.015 (2014).

15 Lee, T. C., Robertson, I. M. & Birnbaum, H. K. TEMin situdeformation study of the interaction of lattice dislocations with grain boundaries in metals. *Philosophical Magazine A* **62**, 131-153, doi:10.1080/01418619008244340 (1990).

16 Yu, T., Hansen, N. & Huang, X. Recovery by triple junction motion in aluminium deformed to ultrahigh strains. *Proceedings of the Royal Society A: Mathematical, Physical and Engineering Sciences* **467**, 3039-3065, doi:10.1098/rspa.2011.0097 (2011).

17 Takayama, Y. & Szpunar, J. A. Stored Energy and Taylor Factor Relation in an Al-Mg-Mn Alloy Sheet Worked by Continuous Cyclic Bending. *MATERIALS TRANSACTIONS* **45**, 2316-2325, doi:10.2320/matertrans.45.2316 (2004).

18 Renk, O., Hohenwarter, A., Wurster, S. & Pippan, R. Direct evidence for grain boundary motion as the dominant restoration mechanism in the steady-state regime of extremely cold-rolled copper. *Acta Mater* **77**, 401-410, doi:10.1016/j.actamat.2014.06.010 (2014).

19 Hu, X., Gaspérini, M. & Van Houtte, P. Strain Localization Observed during Shearing of Some Aluminium Alloys and Texture Softening Predicted by FC Taylor and Advanced Lamel Model. *Solid State Phenomena* **105**, 363-370, doi:10.4028/www.scientific.net/SSP.105.363 (2005).

20 Kocks, U. F., Tomé, C. N. & Wenk, H.-R. *Texture and anisotropy: preferred orientations in polycrystals and their effect on materials properties*. (Cambridge University press, 2000).

21 Kanjarla, A. K. *On the Mesoscale Heterogeneity in Polycrystal Plasticity*, KU Leuven, (2010).

22 Ma, A., Roters, F. & Raabe, D. On the consideration of interactions between dislocations and grain boundaries in crystal plasticity finite element modeling – Theory, experiments, and simulations. *Acta Materialia* **54**, 2181-2194, doi:10.1016/j.actamat.2006.01.004 (2006).

23 Raabe, D., Zhao, Z. & Mao, W. On the dependence of in-grain subdivision and deformation texture of aluminum on grain interaction. *Acta Materialia* **50**, 4379-4394, doi:https://doi.org/10.1016/S1359-6454(02)00276-8 (2002).

24 Gottstein, G., Ma, Y. & Shvindlerman, L. Triple junction motion and grain microstructure evolution. *Acta Materialia* **53**, 1535-1544, doi:10.1016/j.actamat.2004.12.006 (2005).

25 Protasova, S. G., Gottstein, G., Molodov, D. A., Sursaeva, V. G. & Shvindlerman, L. S. Triple junction motion in aluminum tricrystals. *Acta Materialia* **49**, 2519-2525, doi:http://dx.doi.org/10.1016/S1359-6454(01)00142-2 (2001).

26 Shvindlerman, L. S. & Gottstein, G. Grain boundary and triple junction migration. *Materials Science and Engineering: A* **302**, 141-150, doi:http://dx.doi.org/10.1016/S0921-5093(00)01366-6 (2001).

27 Gottstein, G., King, A. H. & Shvindlerman, L. S. The effect of triple-junction drag on grain growth. *Acta Materialia* **48**, 397-403, doi:http://dx.doi.org/10.1016/S1359-6454(99)00373-0 (2000).

28 Yu, T., Hansen, N. & Huang, X. Linking recovery and recrystallization through triple junction motion in aluminum cold rolled to a large strain. *Acta Materialia* **61**, 6577-6586, doi:10.1016/j.actamat.2013.07.040 (2013).

29 Yu, T., Hansen, N. & Huang, X. Recovery mechanisms in nanostructured aluminium. *Philosophical Magazine* **92**, 4056-4074, doi:10.1080/14786435.2012.704418 (2012).

30 Yu, T., Hansen, N., Huang, X. & Godfrey, A. Observation of a New Mechanism Balancing Hardening and Softening in Metals. *Materials Research Letters* **2**, 160-165, doi:10.1080/21663831.2014.886308 (2014).

31 Winning, M., Gottstein, G. & Shvindlerman, L. S. Stress induced grain boundary motion. *Acta Materialia* **49**, 211-219, doi:http://dx.doi.org/10.1016/S1359-6454(00)00321-9 (2001).

32 Read, W. T. & Shockley, W. Dislocation Models of Crystal Grain Boundaries. *Physical Review* **78**, 275-289, doi:10.1103/PhysRev.78.275 (1950).

33 Sakai, T., Belyakov, A., Kaibyshev, R., Miura, H. & Jonas, J. J. Dynamic and post-dynamic recrystallization under hot, cold and severe plastic deformation conditions. *Progress in Materials Science* **60**, 130-207, doi:10.1016/j.pmatsci.2013.09.002 (2014).

34 Trautt, Z. T. & Mishin, Y. Grain boundary migration and grain rotation studied by molecular dynamics. *Acta Materialia* **60**, 2407-2424, doi:10.1016/j.actamat.2012.01.008 (2012).

7. Investigation of AccumEx as a co-deformation process for dissimilar materials – Al and Cu

7.1. Introduction

Co-deformation is a process of deforming two or more dissimilar materials together. The material behavior when deforming as a single phase and when deforming in co-deformation is very different, especially at high strains. The application of the co-deformation technique can be widely seen in wire form where a combination of hard and soft metals is used to produce ultra-high strength materials. Famous examples are Cu-Nb and pearlite wires. The specialty of the two materials is that they possess one of the best combination of yield strength value greater than 2 GPa with ductility and conductivity [1]. Factors such as material compatibility (solubility), thickness ratio and temperature significantly influence the interaction between the dissimilar material pair during the deformation process and facilitate strengthening from bulk to nano scale depending on the deformation condition. Referring to an example from Pippan et al., [2] the grain size of Cu was reduced to less than 100 nm when deformed together with Fe compared to 200 nm when deformed alone. This was attributed to deformation induced local dissolution of Fe in Cu. In another example from [1], co-deformation of Cu-Nb to extreme strains resulted in amorphization at the interfaces facilitated by deformation induced diffusion. More examples have been reported for Cu-Ag, Cu-Nb, Cu-Fe, etc [1,3,4]. Studies claim that non-equilibrium processes such as dislocation induced diffusion and slip induced solid-solution formation are possible when co-deformation is performed to extreme strains. In this chapter, the new SPD process AccumEx will be used as a co-deformation technique to fabricate dissimilar metal composites. Al and Cu will be co-deformed using AccumEx up to 4 deformation passes in two different configurations and their grain refinement, texture and mechanical properties will be discussed.

7.2. Experiments

The AccumEx processing of Al-Cu has been carried out in two configurations

(i) Cu-Al-Al-Cu
(ii) Cu-Al-Cu-Al-Cu

A schematic of the two configurations is shown in Figure 7-1. The aluminum used is commercially pure AA 1050, while the copper is oxygen-free commercially pure. Their composition has been presented in chapter 3 (table 3-1 and 3-2). The thickness of each material used in the two configurations is different. In type 1 configuration, two 5 mm thick sheets of Al and Cu are used. In type 2 configuration, two 2.5 mm Cu sheets at the edge, one 5 mm Cu sheet at the center and two 5 mm Al sheets in between the Cu sheets are used. By this, a different area fraction of dissimilar metal interfaces can be introduced. Prior to deformation, the Cu sheets are annealed at 500°C in Argon for 4 hours, while the Al sheets are used in as-received condition (hot rolled state; half-hardened). This is done specifically to make sure that both materials have similar initial hardness. The samples are then prepared and processed by AccumEx as described in section 3.2.1.1, at room temperature. Both the configuration types are deformed by AccumEx up to 4 passes, which corresponds to an equivalent von-Mises strain of 6.4.

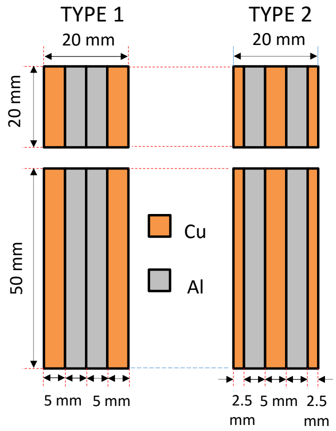

Figure 7-1 Two configurations of Al-Cu to be deformed by AccumEx

The choice of using Al and Cu for the co-deformation has been inspired from the knowledge of material behavior available for both materials under several processing conditions. Al and Cu are two of the mostly studied materials in the field of severe deformation. Besides, this gives the possibility to directly compare the deformation behavior of Al which will be derived from the current experiments with the results obtained from the previous chapters. Two composite arrangements have been proposed for the experiments. This gives the opportunity to evaluate the effect of area fraction of the dissimilar material interface on the deformation behavior and the mechanical properties of the composite.

7.3. Results

7.3.1. Optical micrographs

Figure 7-2(a) and (b) show representative optical micrographs of co-deformed Al-Cu by AccumEx up to 4 passes (type 2). All the pictures of figure 7-2(a) correspond to ED-ND sections. The general deformation behavior noticed in both the configurations is that after 2 passes, the Cu phase undergoes necking and breaks into lenticular structures, dispersed within the Al matrix. After 3 and 4 passes, they further sub-divide and form shorter lenticular structures. These lenticular structures are not perfectly lens-shaped but noticed to be skewed, bent and out of symmetry. The formation of lenses is not only seen in the ED-ND sections but also in the ND-TD sections (figure 7-2 (b)). The thickness distribution of these Cu lenses in the ED-ND sections is measured at different regions and plotted as box plots in figure 7-3. The distribution of thickness values is determined using line-intercept method with line spacing of 250 µm in 3 optical images of 2.7 x 2 mm^2 for each sample (type 1 and type 2). It has to be noted that the thickness of the Cu in its un-deformed state has not been included in the plot. Type 1 was processed using 5 mm thick Cu sheet while type 2 was processed with one 5 mm and two 2.5 mm thick Cu sheets.

Common observation points which can be made by correlating the optical images with the box plots are as follows. After 1 pass, a narrow distribution of the thickness profile is seen. It is because the interfaces are straight and continuous. After 2 passes, the Cu reduces in thickness, necks and fragments. This results in different thicknesses of Cu at different positions along ED. In the box plot, this is reflected as a downward shift in the median and a widening of the box along the y-axis respectively. After 3 passes, Cu reduces further in thickness with more fragmentation. The median in the box plot shifts more downward and the distribution range also increases further. After 4 passes, a similar trend continues both optically and in the box plot. However, the height of the box plot remains almost the same and only the lower limit shifts to smaller values. The effect of the starting thickness of Cu can be seen up to 3 deformation passes. A larger thickness distribution can be noted in the box plots of type 2 over type 1. Besides, the median thickness of the Cu lens is also slightly lower in type 2 compared to type 1, possibly because of the same reason. However, after 4 passes, both exhibit a very similar box plot which shows that the values are converging towards similar numbers.

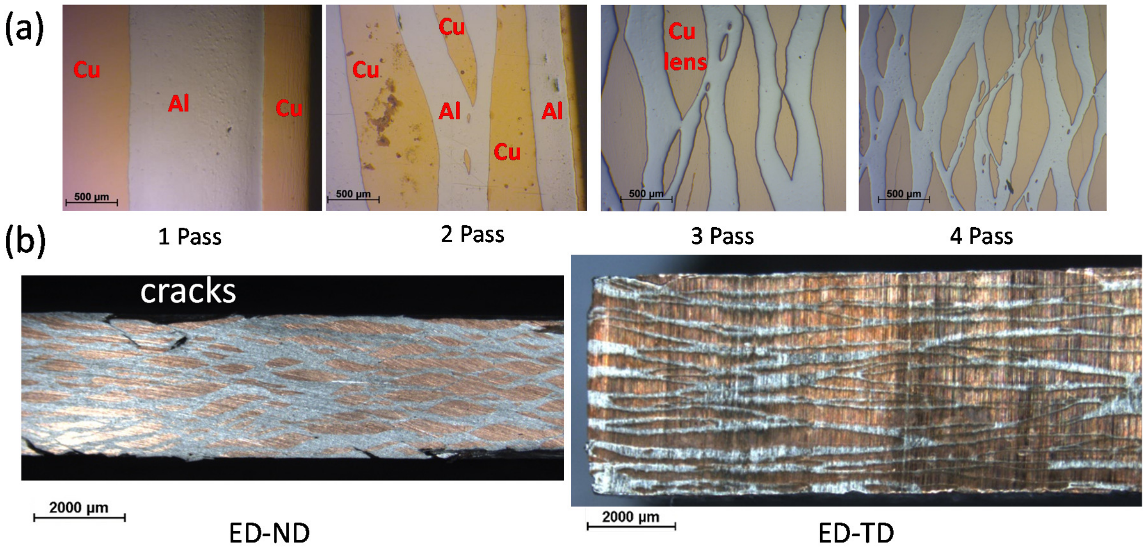

Figure 7-2 (a) Representative optical images of Al-Cu composite Type 2 deformed by AccumEx after 1, 2, 3 and 4 passes; (b) Images of ED-ND and ED-TD plane of Al-Cu composite type 2 deformed up to 4 passes of AccumEx showing networks of Al around Cu boudins

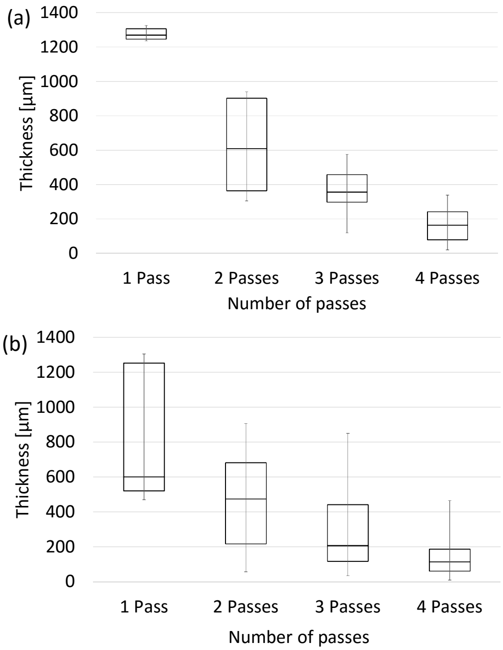

Figure 7-3 Box plot showing the distribution of thickness of Cu after each deformation pass for (a) Type 1; (b) Type 2

The box plot and the optical images suggest that the formation of Cu lenses appears as the most prominent feature of the composite deformation. The varying thickness distribution indicates that the strain distribution within the composite is very heterogeneous and the heterogeneity seems to increase as the deformation proceeds to higher deformation passes.

7.3.2. Effective strain

In this section an estimation of the strain distribution in both configurations has been done. Due to the complex shapes of the Cu lenses throughout the composite, an accurate estimation of the strain will be difficult, but unravelling the trend will already be useful in understanding the strain field. Observing from the micrographs in Figure 7-2, for each ED position, along the ED-ND section, a different strain distribution along ND for Al and Cu can be expected. Therefore, for a realistic estimation of the strain, the following will be performed for 2 and above passes.

On each optical micrograph, used for strain estimation, a set of 20 lines perpendicular to ED will be drawn. For each line along ND, one can see several Cu lenses with different thickness ranges. The thicknesses of all lenses in that line position are measured separately along ND. Now the thickness values are averaged for each line. The average is not calculated only based on the number of lenses that are visible in that ND line but also the interfaces within the lenses should be taken into account. This is because, after every deformation pass, the sample is cut into four pieces and are assembled together to extrude again. In that process, the Cu at the edges after the current deformation forms a Cu-Cu pair in the next deformation pass as they get assembled together. Therefore, depending on the number of deformation passes, the Cu lenses which are being measured might be either a single Cu or Cu-Cu pair with an interface in between. The line of interest which has been used for the measurement is approximately 2200 µm long along ND. This implies, after the first deformation pass, there will be no chance of having a Cu-Cu interface. After the second deformation pass, it is highly likely that there will be 1 Cu-Cu interface. After the third deformation pass, there will be 7 Cu-Cu interfaces and after the fourth pass, there will be 31 Cu-Cu interfaces. To properly incorporate this in the measurement, if the number of lenses measured in the line of interest is X, the average will be calculated by summing up all the thickness values and divide them by X for the first pass, divide by X+1 for the second pass, divide by 2*X for the third and fourth passes. True strain is then calculated for each of the 20 lines along ED for Cu. The averages of these true strains are plotted in Figure 7-4. The starting thickness used for the strain calculation of Cu is 5 mm for type 1 and 3.33 mm for type 2. Compared to the ideal strain that Cu is expected to undergo (red dotted line in Figure 7-4), after 3 and 4 passes, a significant under-straining can be seen. This is most probably due to the necking and fragmentation of Cu and the hardness incompatibility which is expected to arise as Cu strain hardens from its annealed state. If Cu is under-strained, on its counterpart, Al will be over-strained. Another notable observation from Figure 7-4 is, Cu in type 2 undergoes slightly lower effective strain than that of Cu in type 1.

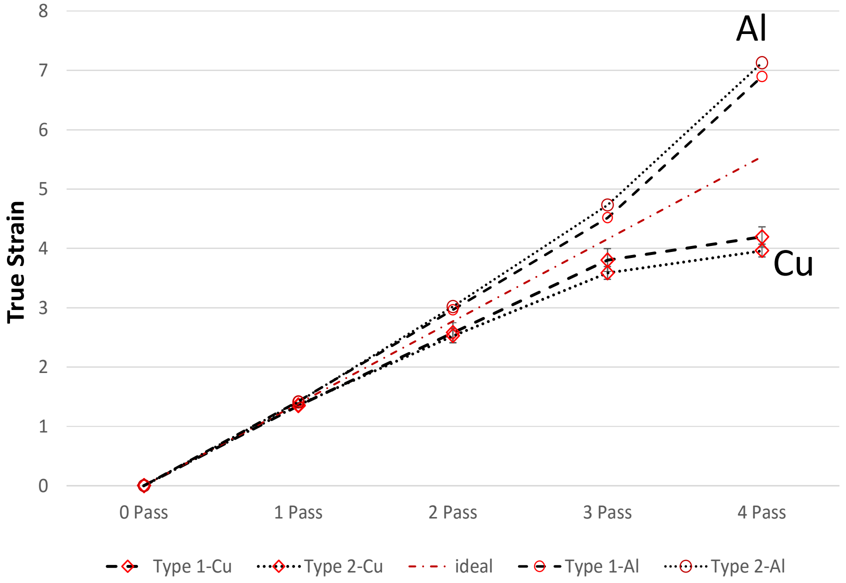

Figure 7-4 Effective cumulative compressive true strain on Al and Cu as function of number of passes; Error bars represents the scatter in the estimated average true strain values.

7.3.3. EBSD analysis

EBSD analysis on the deformed samples is carried out to obtain microstructure and texture information. In this section, we will discuss the microstructure evolution of Cu and Al. To keep it simple, the grains are monitored only along the ED-ND section. Maps of Cu and Al are shown in Figure 7-5 and Figure 7-6 respectively. The grain size and HAGB fraction are presented in

Table 7-1.

7.3.3.1. Cu

The starting microstructure of annealed Cu has big grains of approximately 32 µm in diameter. It also has annealing twins at several places. The grains are nearly equiaxed and have an average HAGB fraction of greater than 95 %. During AccumEx, the Cu grains are compressed and elongated, similar to what is observed for Al in chapter 4, just after 1 deformation pass. The grain boundary spacing is reduced to less than 5 µm in a single step. With further passes, the boundary spacing is reduced further and the long grains are fragmented into shorter grains. After 4 passes, an average equivalent grain boundary spacing of 2 µm and 3 µm in diameter is obtained for type 1 and type 2 configurations respectively. The grain refinement is facilitated by formation of several low angle boundary structures, through dislocation interactions and at places with assistance of mesoscopic bands such as shear bands. An example of a shear band can be seen in the EBSD image after 4 passes; type 2. Clearly, the microstructure is seen to refine into thin lamellar structures for both configurations.

The average HAGB fraction is very similar for both types. HAGB are formed because of increasing misorientation between grains during deformation assisted by dislocation structures and meso-bands. By forming lamellar structures, it is common that the HAGB fraction increases. However, 45 % HAGB is comparatively low for material deformed up to a strain of 6.56. Further, the final equivalent grain boundary spacing of 2 to 3 µm indicates that the effective strain observed in Cu is less or in other words, the externally imposed deformation can be said to be not effectively transferred to the Cu part of the composite. This can be seen complementing the observed effective strain distribution calculated in the previous section.

7.3.3.2. Al

The starting microstructure of Al is very different from that of Cu. Al is used in its as-received condition, which is hot rolled. It has a lamellar microstructure with an average equivalent grain size of 10 µm, aspect ratio of 3 and a HAGB fraction of around 40 %, almost the same as those of the Al used in chapter 4. AccumEx co-deformation reduced the grain size of Al and thin lamellar grains were formed. The lamellar grain boundary spacing reduced to 1.5 µm and 0.9 µm for type 1 and type 2 configuration after 1 pass. After 4 passes, it reduced to less than 500 nm for both type 1 and type 2 configuration. An average equivalent grain size of nearly 1 µm is obtained, which is similar to what was observed for Al during Al-Al AccumEx. The grain refinement occurs through typical sub-structural evolution and deformation banding which gradually transforms to HAGB structures. The HAGB fraction increases up to more than 60 % after 4 passes. However, it is comparatively low compared to Al-Al AccumEx.

Both the configurations show similar results at the end of 4 deformation passes. However, in the initial passes, especially the first pass, a significant difference can be noticed. The average equivalent grain size of Al type 1 is relatively higher than that of type 2. This difference of Al in type 2 can be attributed to the position of Al in the composite arrangement. Referring to figure 7-1, in type 1, Al is at the centre position of the configuration and the effective thickness of Al is 10 mm (2 sheets of Al). On the other hand, the position of Al is at 7.75 mm from the sample ends and the thickness is 5 mm. Now, with a short recap from the results of chapter 5, it was learnt that during AccumEx, a strong shear gradient is imposed. This shear gradient has a significant effect on grain size, especially in the first deformation pass. The equivalent grain size of Al in the centre was measured as 1.5 µm, while near the edge it was less than 1 µm. This information is very relevant with the current observation as well. The exact shear pattern is unknown in the Al-Cu co-deformation set up. However, it can be certain that a strong process induced shear gradient is bound to be present and can influence the grain refinement, especially in the initial deformation passes.

Table 7-1 - Grain size distribution and HAGB fractions of Al and Cu deformed by AccumEx

		Al (ND) [µm]	**Cu (ND) [µm]**	**Al (ED) [µm]**	**Cu (ED) [µm]**	**HAGB (Al) [%]**	**HAGB (Cu) [%]**
TYPE 1	0 pass	5.01 ± 0.12	35.7 ± 6.35	14.14 ± 9.9	30.67 ± 3.5	38	95
	1 pass	1.5 ± 0.1	3.13 ± 0.27	10 ± 3.7	24.39 ± 23	34	21.3
	2 pass	0.81 ± 0.2	1.39 ± 0.3	4.13 ± 1.13	15.63 ± 8.58	44.6	23.4
	3 pass	0.66 ± 0.06	0.62 ± 0.05	2.5 ± 0.57	3.89 ± 0.16	63.4	48.1
	4 pass	0.47 ± 0.02	0.5 ± 0.02	1.55 ± 0.22	2.66 ± 0.73	73.2	47.9
TYPE 2	0 pass	5.01 ± 0.12	35.7 ± 6.35	14.14 ± 9.9	30.67 ± 3.5	38	95
	1 pass	0.98 ± 0.06	4.5 ± 0.8	8.62 ± 5.24	38.04 ± 11.01	35.7	14.4
	2 pass	0.67 ± 0.04	2.5 ± 0.1	2.26 ± 0.19	21.06 ± 8.19	50.3	22.7
	3 pass	0.52 ± 0.03	1 ± 0.2	1.58 ± 0.57	6.48 ± 1.09	65.5	41.7
	4 pass	0.44 ± 0.02	0.7 ± 0.4	1.45 ± 0.6	5.54 ± 2.75	68.1	48

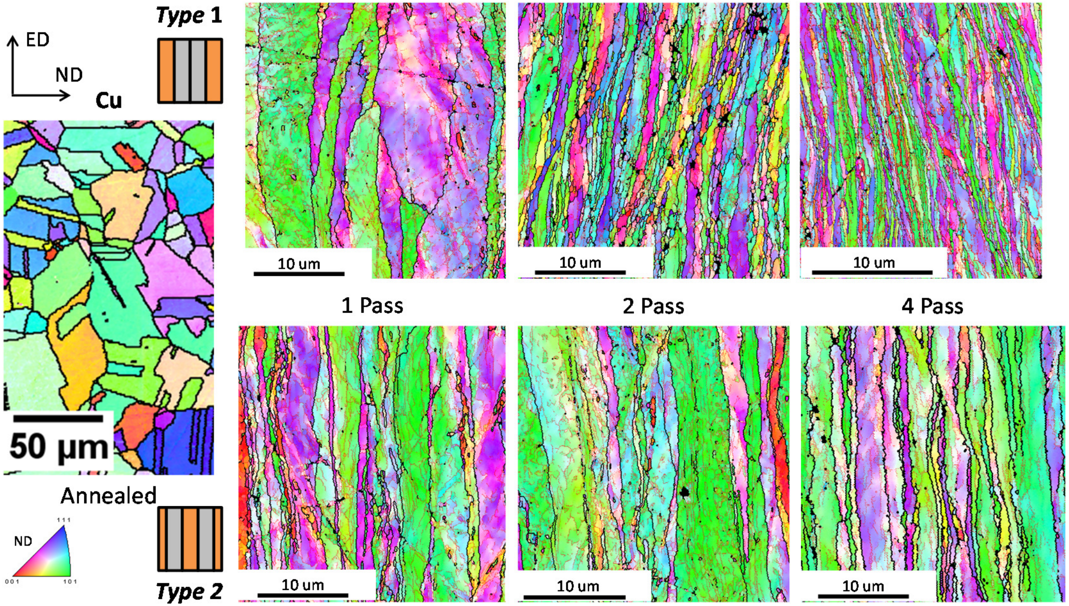

Figure 7-5 ND maps of Cu obtained by EBSD on the ED-ND section at different condition

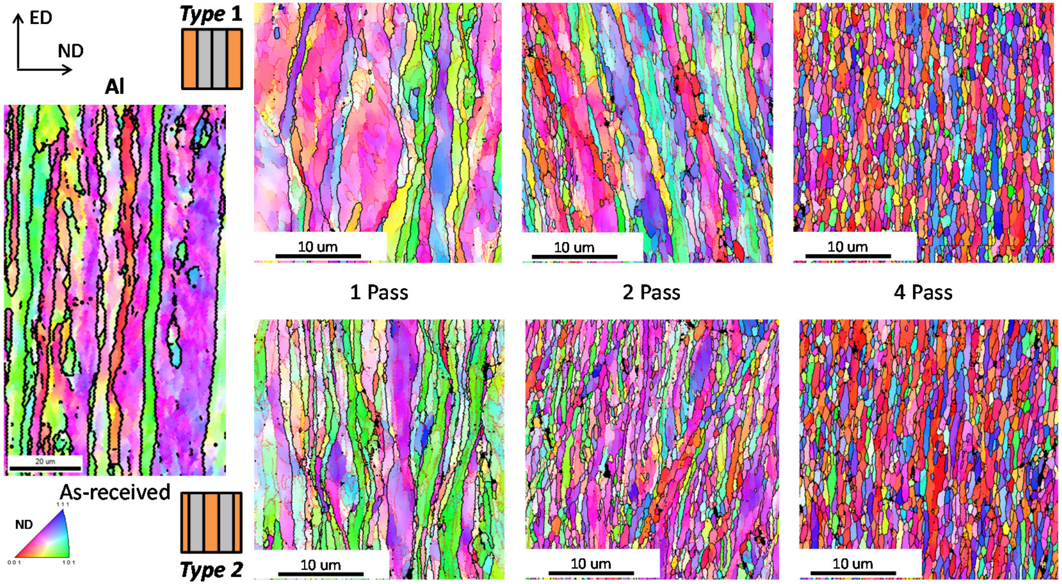

Figure 7-6 ND maps of Al obtained by EBSD on the ED-ND section at different condition

7.3.4. Microhardness

The Vickers' microhardness is measured on the ED-ND sections of the composite, for Cu and Al separately after every deformation pass and for both configuration types. Care is taken to ensure that the effect of the neighboring phase does not influence the measurements. Their respective results are presented in Figure 7-7. Cu undergoes rapid strain hardening after the first pass which increases the hardness from 55 HV0.3 to 140-150 HV0.3 in both the configurations. A small variation is noticed in the values between type 1 and type 2. Type 2 shows slightly lower hardness than type 1. However, after 2 passes, it catches up with type 1. Between 2 and 4 passes, the hardness remained almost constant. This gives a clear indication that there is lack of further strain hardening in Cu after 1 pass. The starting condition of Cu is in the annealed state and therefore it has the highest strain hardening capacity in the composite. Lack of strain hardening then implies that either the microstructure reached saturation or little to no additional strain is still imposed on Cu to obtain further strain hardening. Based on information from literature and hardness values obtained from other experiments (will be discussed in chapter 8), the former is most likely the case.

For Al, a much different scenario is seen. The hardness increased from 47 HV0.3, in the as received condition, to only 52 HV0.3 (type 1) and 50 HV0.3 (type 2) after 4 passes, compared to 70 HV0.3 for Al-Al reported in chapter 4. This implies that there is no strain hardening happening at all in Al for both the configurations. Also, the values do not correspond to the observed grain refinement as well. It was inferred from Figure 7-4 that Al undergoes higher effective strain during AccumEx, but no sight of its influence can be seen in the corresponding hardness data. Such a lack of strain hardening, despite all these said reasons can be possible only if dynamic annihilation of dislocations or recrystallization occur during deformation.

Dynamic recovery is very common for Al at room temperature. However, its influence cannot be expected to reduce the hardness to such low values, unless the deformation is performed at elevated temperatures. This is because there is enough driving force to completely reduce the stored energy in the system. The next possible reason is dynamic recrystallization. Dynamic recrystallization can be either continuous or discontinuous. Al does not favor dynamic dis-continuous recrystallization at all. And dynamic continuous recrystallization does not promote obtaining lower hardness values unless the deformation is performed at elevated temperatures. This leaves us to the only option to doubt on adiabatic heating during deformation. But, unless measured during deformation, it is difficult to answer this and it will need further experimental study. A brief extended study on this topic is done in section 7.2.2.

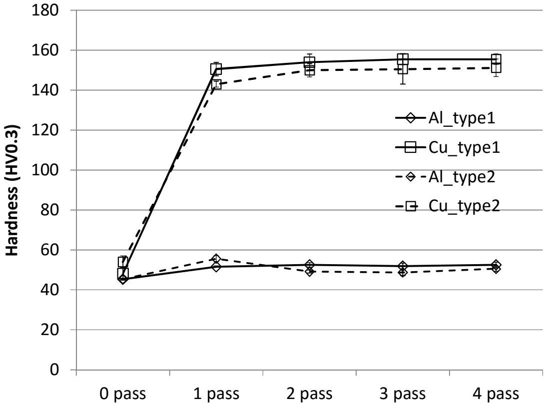

Figure 7-7 Hardness evolution in Cu and Al in type 1 and type 2 configuration, measured along the ED-ND plane. The error bars indicate the range of obtained values.

7.3.5. Tensile tests

The yield strength and elongation to failure of each sample deformed in type 1 and type 2 configurations are presented in Figure 7-8. The general understanding from the graph is type 1 performs better than type 2 up to 2 deformation passes. After 3 and 4 passes, both configurations show deteriorating properties.

The yield strength of the type 1 composite increases to 270 MPa with failure elongation strain of 15 % after 1 pass. This strength is 156 % larger than the one of Al in its as-received condition and 740 % larger than the one of Cu in its annealed condition. The rapid strain hardening of Cu is responsible for the single step increase in strength. After pass 2, the yield stress remains almost the same, but the elongation to failure property drops to 6 %. After 3 and 4 passes, both yield strength and elongation to failure strain properties deteriorate and reduce significantly.

Like type 1, the yield strength of type 2 increases to 225 MPa after 1 pass with failure elongation strain of 13 %. It is slightly lower than for type 1. After 2 passes, the yield strength remains almost the same, but failure elongation strain drops to around 5 %, also similar to type 1. After 3 and 4 passes, the yield strength drops subsequently along with the failure elongation strain.

Comparing type 1 and type 2, both show a very similar pattern of strength change but type 2 samples are always less strong than type 1 (till 3 passes). This can be explained with two possible reasons – composite arrangement, thickness of Cu lenses. Formation of Cu lenses occurs by necking and fracture in the ED-ND section after 2 passes in both type 1 and type 2. Along ND-TD section also Cu lenses form but after 2 passes (partially) for type 2 and after 3 passes for type 1. This difference is due to different starting thicknesses of Cu in type 2. The starting thickness of Cu sheets used in type 1 is 5 mm while in type 2 are 5 mm and 2.5 mm. The 2.5 mm thick Cu sheets initiate necking earlier than the 5 mm sheets due to the thickness to strength ratio. Hence, Cu lenses form already after 2 deformation passes along ND-TD in type 2. This is because the 2.5 mm Cu sheets show strain localization at comparatively lower stresses than the 5 mm sheets. Therefore, the yield strength of the composite is lowered.

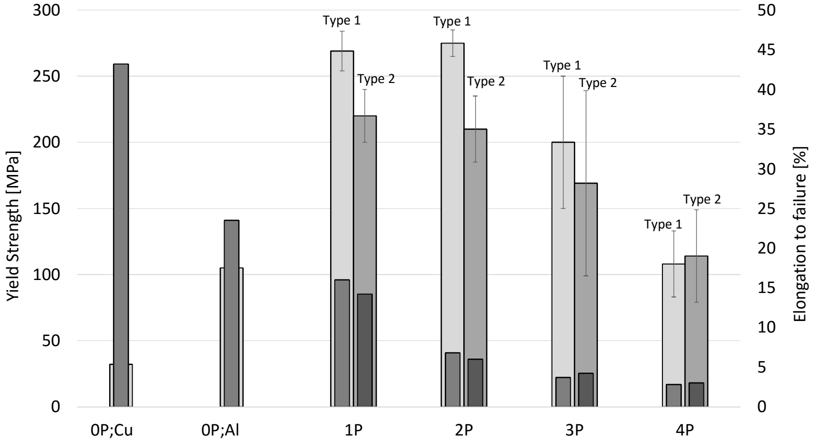

Figure 7-8 Yield strength and elongation to failure of the deformed composite as a function of number of passes. Light gray is the yield strength value of type 1 and type 2 while the dark gray (inside light gray) represent their respective elongation to failure.

Another observation which has to be addressed is that after 2 and above passes, the elongation to failure and yield strength dropped. Both composite arrangements are comprised with dissimilar interfaces. The interfaces are straight and un-interrupted only till the 1st pass. After 2 and above passes, the number of interfaces increase, begin to change direction and fragment as the Cu lenses are being formed. The influence of the interfaces becomes very localized around the Cu lens and the Al matrix, unlike in the first pass. Further, the morphology of the fragmenting lenses contains sharp vertices which creates a stress concentration zone in the Al matrix underneath. A cumulative effect of the increasing number of interfaces, heterogeneous alignment of interfaces and stress concentration zones create sources of instability and strain localizations within the composite during tensile loading. Failure analysis after tensile tests of a similar composite (Al-Fe), processed by AccumEx, showed cracking of the dissimilar interfaces and at places also Al-Al interfaces which formed the main reasons for early failure. In contrast to the expected strengthening effect, the increase of number of interfaces cause a detrimental effect on the mechanical properties of the Al-Cu composite, above 2 passes.

7.3.6. Texture

Bulk texture measurements are done on the ED-ND section of the deformed samples of type 1 and type 2. The φ 2 = 0 and 45° sections are shown in Figure 7-9 and Figure 7-10 for Cu and Al respectively. The volume fractions of the most common texture components are plotted in Figure 7-11.

7.3.6.1. Cu

The texture evolution in copper is very similar for both type 1 and type 2. In the annealed state, the Cu has a random texture with no significant strong texture components. After deformation, the texture evolves into a plane strain compression texture with increase in the intensity of the typical plane strain compression components – Bs, S, Cu and T. The components remain almost unchanged for both configuration types till 4 deformation passes. However, at higher passes, the effect of shear could be noticed in the form of a short B-H fibre in the φ2 =0° section. The local heterogeneities created in the formation of the Cu lenses are reflected in the form of the shear B-H fibre. Besides, the volume fraction of the components is quite similar for both configurations. This conforms to the understanding developed in chapter 5. AccumEx imposes macroscopic shear due to the process and with increasing passes, the shear is accumulated which is directly reflected in the texture evolution.

7.3.6.2. Al

Al has been deformed from its as-received deformation state. The starting texture is a hot rolled texture with combination of cube, Goss and other plane strain compression components. From the understanding developed in chapter 5, AccumEx imposes a strong shear gradient in the deforming material. The shear accumulates as the material from outside move inwards in the sub-sequent deformation passes. This can be learnt from the presence of the B-H fibre and formation of shear components such as H. However, the texture results obtained from the co-deformed Al are not so straight forward. Further, a noticeable difference in evolution between the two configurations also occurs. Therefore, the observation will be described separately for type 1 and type 2.

Type 1

The texture seen from the ODFs after 1 pass resembles the texture observed after 4 deformation passes of the Al-Al composite (figure 4.10). The presence of a long B-H fibre in the φ_2=0° section suggests the presence of a significant shear gradient within the Al part of the sample. Based on the understanding obtained from the chapter 5, this is most likely due to a flow heterogeneity between Al and Cu. This gradient increases and then weakens in the further deformation passes. This can be associated to the necking and fragmentation of Cu into lenses. Associated with this, the plane strain texture weakens and a random texture is obtained gradually after 4 passes (Figure 7-10, 4pass; type1). This can be seen in the volume fraction chart where the intensity of the plane strain compression components reduces and shear and recrystallization components are formed (Figure 7-11(a)).

Type 2

Similar to type 1, the ODF sections of type 2 also show a shear gradient after the first pass. A B-H fibre can be observed. However, the gradient seems to be slightly smaller than what is seen in type 1, which is defined based on the length of the observed fibre in the φ_2=0° section. This can be due to the thickness and the position of Al within the composite assembly and this does not imply that the magnitude of shear is lower. Noticing from ODFs and volume fraction of texture component in Figure 7-11, after 2 passes, a different texture is noticed for type 2. Unlike type 1, an immediate random texture is noticed. The plane strain compression components weakened, the B-H fibre deteriorated and a significant volume fraction of cube and Goss components could be noticed. The texture further remained random till 4 passes. Almost a static texture can be seen between 2 to 4 passes. This suggests that the deformation field of Al in type 2 could be different from that of type 1, specifically after 2 and 3 passes. This can also be linked to the observation that in type 2, Cu lenses are seen to be formed already after the 2nd pass and a comparatively higher fraction of Cu lenses is present in type 2 as compared to type 1. However, after 4 passes both reach similar texture values which is also comparable to the result obtained in the effective strain estimation.

A few prominent interpretations from the texture results are,

1. The deformation field in Al is controlled by the macroscopic deformation only up to 1st deformation. In 2 and above passes, it becomes very in-homogeneous irrespective of the configuration type. This is claimed to be due to the Cu lenses. Formation of Cu lenses modifies the flow of Al near the interface of Cu. Al begins to flow as a river around the Cu islands and Cu induces combinations of shear and compressive deformation fields on Al at the meso-scale. This meso-shear field, results in weakening of the texture (explained in detail in section 7.4).

2. The observation of cube and Goss components indicates the possibility for dynamic discontinuous recrystallization. If that is true, the driving force for this can be particle stimulated nucleation (PSN). Assuming the Cu lenses are large particles dispersed in the Al matrix, the deformation around these particles will be very complex with excess dislocation interactions. This can facilitate nucleation, provided enough temperature is attained by local adiabatic heating. To know if this is possible, an EBSD measurement is performed at the vicinity of the Cu lenses, and its orientation map and the ODF is presented in figure 7-12 (a) and (b). The average grain size is very similar to the bulk and no sign of micro-strain free grains or distortion free grains could be noticed. The most common texture components which can be noticed are rotated cube (H, shear), partial <111> fibre (shear), cube (recrystallization) and other plane strain compression components. This observation indicates that dynamic discontinuous recrystallization cannot be the reason for the random texture with recrystallization components and probably the complex flow/deformation field in Al around Cu lenses is a more realistic reasoning.

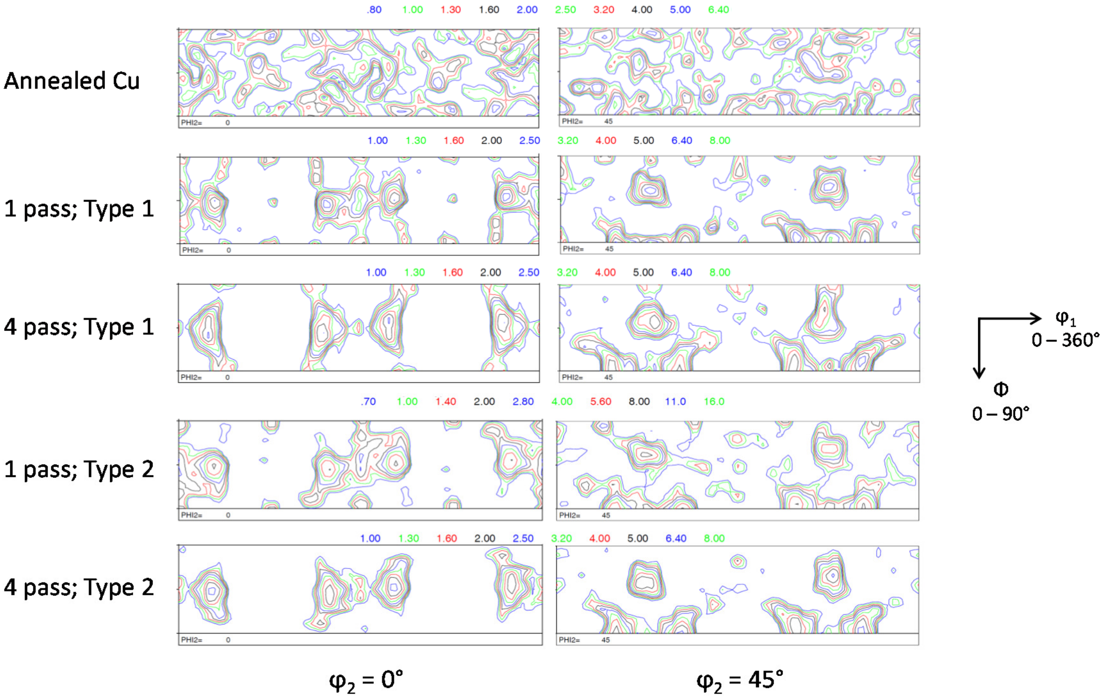

Figure 7-9 ODF plots of Cu

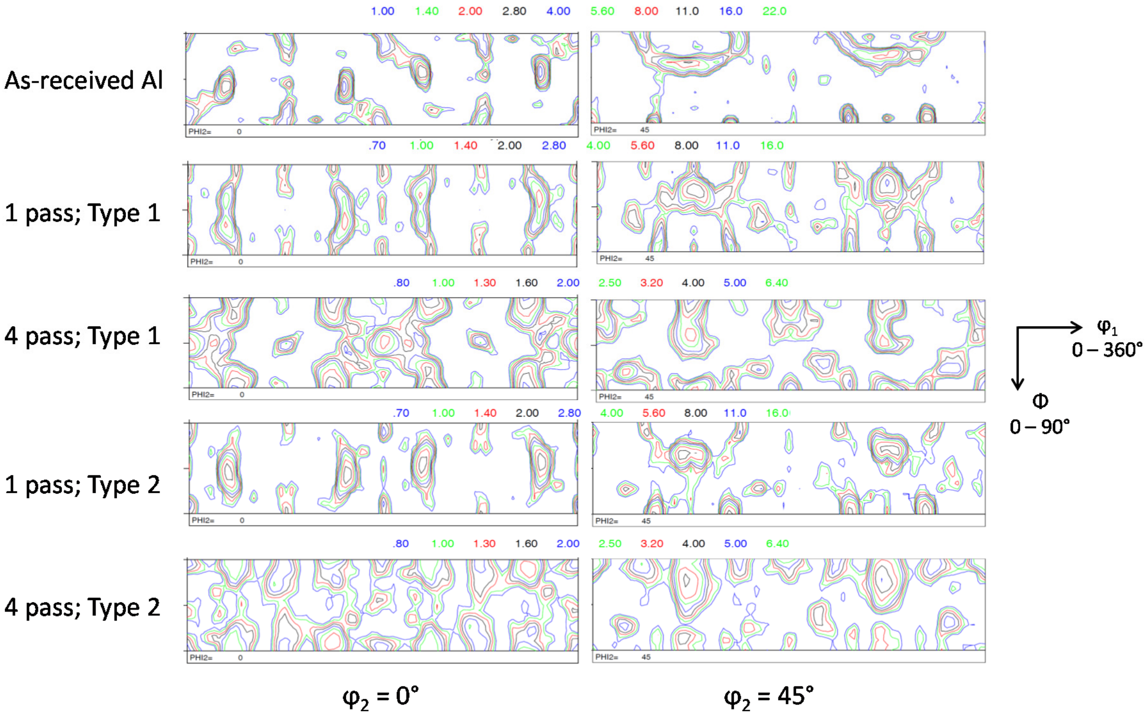

Figure 7-10 ODF plots of Al

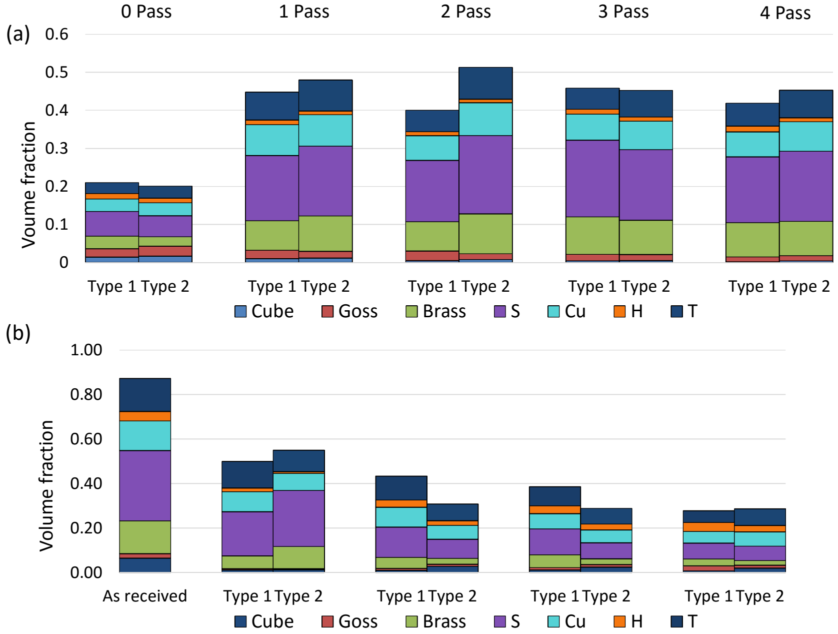

Figure 7-11 Volume fraction of components calculated using the MTM-FHM software. (a) for Cu; (b) for Al with increasing deformation passes for both type 1 and type 2 configurations

7.4. Discussion

7.4.1. Cu boudins and the local deformation field

Formation of Cu lenses is a common observation seen for both composite configurations after 2 and higher passes. They are formed by necking and fragmentation. These Cu lenses are described in literature as “boudins”, a terminology adapted from geology. The formation of such boudins is a commonly observed phenomenon in natural rock composites [5,6]. They form in different morphologies and sizes and the factors that influence them are viscosity, thickness ratio, rate of flow and bonding [6,7]. Viscosity is the resistance to flow, in other words decides the critical shear stress above which flow will be initiated. The thickness ratio between different phases determines the required force needed for the flow of the specific entity. The rate of flow indicates the rate of compression over a period of time and bonding specifies the interaction of the composite at the interface. Analogously, for metal composites, these properties can be translated to yield strength, thickness ratio, strain rate and interface bonding, which can possibly be major factors in the formation of boudins during deformation.

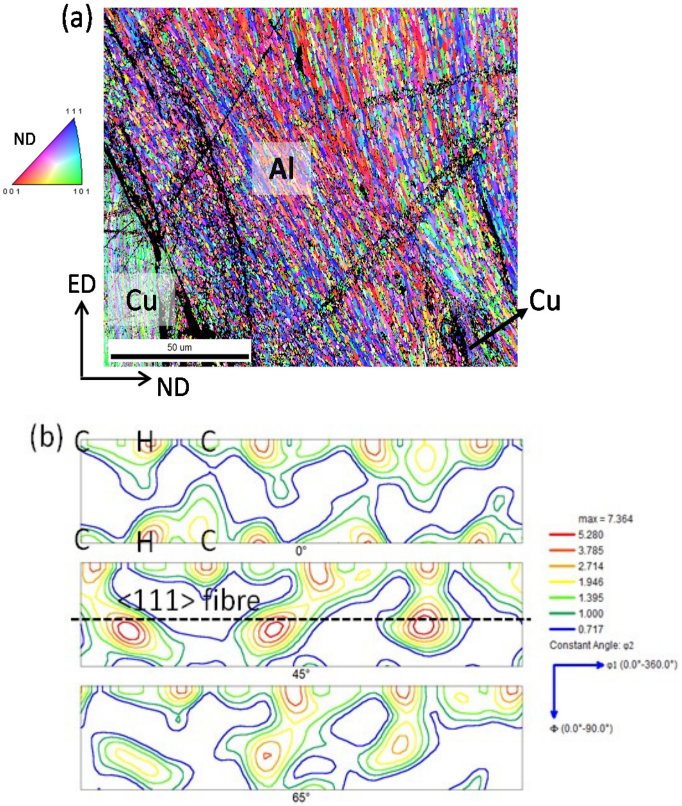

Figure 7-12-(a) ND map of Al region next to the Cu lens; (b) ODF sections of the Al region showing different texture components - Cube (C), rotated cube (H), partial <111> // ED fibre

Ideally, during co-deformation by plane strain compression, one would expect that the interfaces remain straight and continuous and a perfect lamellar structure can be obtained. In reality, this is untrue. A complex interaction between the dissimilar materials causes breaking of the hard phases [3,8-16]. These observations are not pertinent only to macroscopic structures but also in composites at nano-scale. Pearlite which is a nano-composite of ferrite and cementite, when deformed to high strains show breaking up of cementite into smaller fragments. The material with higher flow strength undergoes tensile internal stresses with magnitude proportional to the externally applied compressive strains [17,18]. This results in instability in the hard phase and formation of boudins [7,19-22]. Hwang et al. [19] introduced a model which can predict this instability for any metal composite during co-deformation by rolling. The model relates the strain hardening properties of the soft and the hard phases and to the thickness ratio at which plane strain compression deformation is performed and gives a prediction of the critical reduction at which the onset of plastic instability on the hard phase can possibly occur. The description of the equation and the respective calculations can be found in Appendix C. Applying this model to the Al-Cu system, it is calculated for the case of an Al-Cu system with 50-50 thickness ratio of Cu to Al that necking can be initiated at 70 % reduction during pass 1 and after 30 % critical reduction after pass 2. The different reduction % is due to different strain hardening properties of Al and Cu after 1 and 2 passes. This approximately matches with the observation that boudins were noticed only after the second pass. Further, it strongly indicates that the difference in strain hardening properties and the yield strength is the primary cause for the formation of the Cu boudins. And this will have a serious impact on the deformation field within the material. The formation of the boudins and the associated changes in the deformation field can be schematically explained as follows.

Two scenarios are considered,

(i) $\epsilon_{33}^{Al} \approx \epsilon_{33}^{Cu}$, for hardness ratio 1.17 (Cu/Al) which is representative for pass 1

(ii) $\epsilon_{33}^{Al} > \epsilon_{33}^{Cu}$, for hardness ratio 2.75 (Cu/Al) which is representative for pass 2 and higher.

For scenario (i), the hardness ratio says that Cu and Al have similar tensile strength. In this scenario, the applied compressive strain which is translated into elongation along the extrusion direction will be almost equal for both Cu and Al. It is a close representation of pass 1. The composite before and after deformation will look as shown in Figure 7-13(a) and (b). However, a small local shear gradient will always be unavoidable and is expected to be present at the interface. In scenario (ii), the hardness or yield strength of Al is 2.75 times smaller than Cu. For this case, the translation of the same applied compressive strain into elongation will be different for Al and Cu. For the same global stress values, the compressive strain and the elongation of Al will be higher than that of Cu. This represents the condition after 2 and higher passes, where hardening has happened in both Al and Cu. In this scenario, for the applied compression, the deformation will look as shown in Figure 7-13 (c) and (d) - (c) if the interface is considered free and (d) when the interface is considered ideally tied. Al undergoes a preferential compression over Cu and when the interface is tied, this flow heterogeneity induces a microscopic shear in Al, at the interface. For calculation purpose, this shear can be quantified as θ based on the geometry it takes, as shown in Figure 7-13 (d). The value of θ can be calculated by using basic trigonometry and sine law. For an applied specific strain on square geometry, if the constrained side does not elongate the non-constrained side compensates by elongating more in order to realize the applied strain. Therefore, depending on the magnitude applied strain the over-elongation of the non-constrained can be estimated and the thus formed angle between the elongated and the non-elongated side can then be calculated. For a square geometry (aspect ratio = 1), the θ will increase as a function of excessive compressive strain in Al as shown in Figure 7-14 (a). Higher excessive compression results in a larger θ and therefore implies higher shear. It has to be noted that the values of θ might be an over-estimate, and the aim here is to show the possibilities of extreme straining conditions. The actual θ specific to the current system is hard to be determined. Such localized flow heterogeneities create internal stresses on Al and Cu and they are shown with the arrows Figure 7-13 (d). The direction of the arrows indicates that Al undergoes compressive stresses and Cu gets subjected to tensile internal stresses. As the deformation proceeds the stresses progress towards the critical limit (yield strength of Cu), by when necking initiates and causes fragmentation. This is shown in Figure 7-13 (e). The manifestation of these internal stresses was noticed as shear bands at the onset of necking of the hard phase in Al based composites as reported by [15,23].

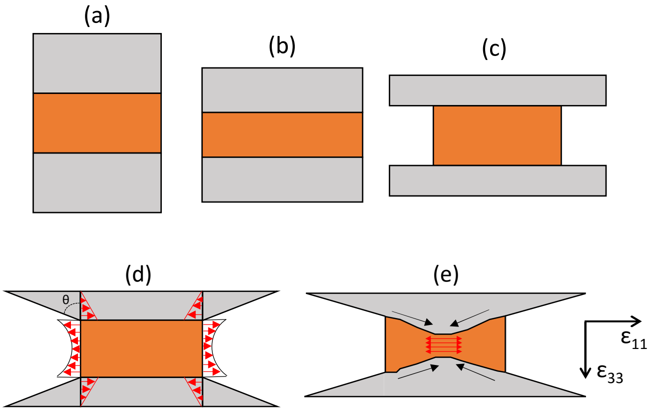

Figure 7-13 (a) Composite configuration before deformation; (b) deformation as explained for case (i); (c) ideal deformation state of case (ii) when interface is free; (d) Shearing, tensile stress, compressive stresses which occur due to tied interface; (e) Start of instability in the Cu sheet due to tensile internal stresses and modification of flow of Al

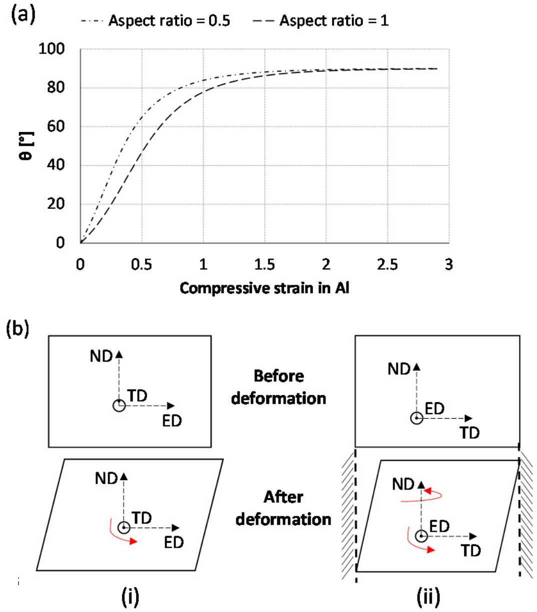

Figure 7-14 (a) Evolution shear angle as function of compressive strain in Al for different aspect ratios of Al (thickness to length); (b) (i) Shear in the ED-ND plane showing rigid body rotation around TD; (ii) Shear in ND-TD plane showing simultaneous rigid body ration around ED and ND due to flow constraint in TD

In either configuration, the existence of the induced shear can be expected to be present wherever the Cu boudins are being formed - along ED-ND and ND-TD sections, especially after 3 and 4 passes. This implies, at higher passes, on top of the complex compression and shear strains, two orthogonal shears act at the same time. Consider that the applied deformation is translated as compression along ND, shear along ED-ND and ND-TD locally at the vicinity of the Cu boudins in the composite. Compression encourages plane strain compression texture components. Shear encourages rigid body rotation of the texture components. A rotation of the plane strain compression components can be ideally a good guess. However, the rigid body rotation will be encouraged around two directions – TD and ED for ED-ND and ND-TD planes respectively. Besides, flow along TD is restricted and therefore, any flow initiated in the ND-TD plane along TD will result in a resolved rigid body rotation around ND as well. The representation of these rigid body rotations for both the planes is shown in Figure 7-14(b). With such complex rigid body rotations, compressive strains and strain localizations, the local texture gets modified depending on the configuration of Cu boudins in Al. Region specific EBSD is done in order to obtain local texture information at different locations and configurations.

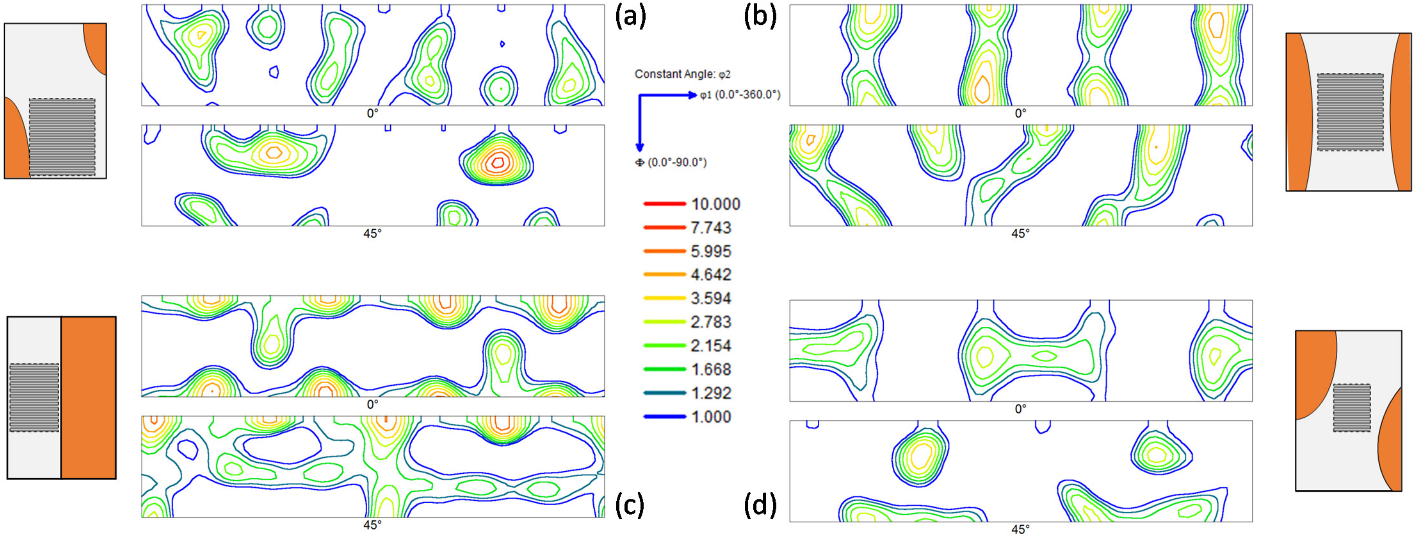

Figure 7-15 Different micro-shear textures observed by EBSD (a) PSC + shear (b) Huge shear gradient (c) Shear texture; (d)PSC + shear gradient + Goss; The orange colour regions represent Cu boudins, the white regions represents Al matrix and the grey area represents the area of EBSD measurement from which the corresponding adjacent ODFs were derived.

Micro-texture obtained from different regions in the Al part of a sample deformed up to 4 passes (both type 1 and type 2) are plotted in Figure 7-15 where their corresponding regions of measurement relative to the Cu boudins are also indicated. Figure 7-15 (a) is a combination of shear and compression. Figure 7-15 (b) is strong shear along both directions with less compression. Figure 7-15 (c) shows simple shear with H and gamma fibre. Figure 7-15 (d) shows the presence of Goss components together with compression and shear. Depending on the relative position with respect to Cu boudins, the micro-texture of Al varies distinctly. Spacing between boudins, positioning of boudins and magnitude of the compressive strain are the major factors that influence the local texture of Al. Cumulatively, when these different regions are measured at the bulk level, they are interpreted as weak and random texture. Further, the different Cu arrangement in type 1 and type 2 influences the flow behavior of Al. Type 2 has more Al-Cu interfaces than in type 1 and therefore, the flow heterogeneity will be higher. This affects the texture evolution of Al in type 2 more adversely than in type 1, during the initial deformation passes.

The dissimilar interfaces have a significant impact on the deformation field of the composite. Their effect is found to be more detrimental than reinforcing in the fabricated Al-Cu composites of both configurations, after 2 passes. Among type 1 and type 2, type 2 performed less than type 1 in terms of mechanical properties. This is because the flow behavior of Al is dominantly controlled by Cu in both types. In type 1, the deformation is commenced with two dissimilar interfaces while in type 2 it is with four dissimilar interfaces. As the deformation proceeds, the number of dissimilar interfaces in type 1 theoretically increases to 8, 32 and 128 after 2, 3 and 4 passes respectively, while in type 2 to 16, 64 and 256 respectively. When the effect of hardness incompatibility that is created between Al and Cu is related with this information, it suggests that type 2 might exhibit higher internal stresses and therefore the onset of heterogeneity will be faster. θ, a micro shear angle was introduced as a measure of induced shear strain in Al due to excessive compression of Al over Cu. The value of this θ is not only a function of the compressive strain but also varies with respect to aspect ratio of the Al sheet that undergoes compression (thickness to length ratio). For the same applied compressive strains, sheets with smaller aspect ratio show larger shear strains due to larger θ values. In the case of type 1 and type 2, the aspect ratio of Al in type 2 is 2 times smaller than in type 1 (based on the starting assembly). Therefore, the corresponding shear strain in Al of type 2 will be larger than that of type 1. Figure 7-14 shows the θ evolution for a sample with two different aspect ratios. Additionally, the number of dissimilar interfaces is also 2 times larger in type 2 than in type 1 after every deformation pass. Therefore, the volume fraction of the micro-shear regions will be at least 2 times larger in type 2. Cumulatively, all factors together contribute to the early onset of heterogeneity of Al in type 2, which is explicitly noticed in the texture evolution and on a lighter note also in the effective strain calculation. The magnitude of under-strain in Cu is slightly higher in type 2 than type 1.

7.4.2. Negligible strain hardening behavior in Al – a brief discussion

Another important aspect of the observed results is the anomaly in the measured hardness values of Al. The hardness of Al in both type 1 and type 2 does not increase with increasing deformation passes. The values are around 21 % lower than in its fully strain hardened state (figure 4-7) when deformed alone. Constant hardness values generally imply saturation in strain hardening. On the other hand, lower and constant hardness in the present case imply no strain hardening happening at all, which is an unexpected phenomenon to occur for a room temperature deformation up to ultra-high strains. This section will discuss all the associated factors which can contribute to the anomaly.

Hardness in general can be directly related to the tensile strength. From literature, a mathematical relation is introduced which shows the different parameters that influence yield strength. In a single equation, they can be expressed as shown below [24-27],

$$\sigma_y = \sigma_0 + \Delta\sigma_{gb} + M\Delta\tau_d \tag{7-1}$$

where, σ_0 is the yield strength of coarse grained pure Al which is approximately 28 MPa [24]. $\Delta\sigma_{gb}$ is due to grain boundary strengthening and $M\Delta\tau_d$ is the contribution of dislocation induced strengthening.

A. GB strengthening

It is well-known that grain size and sub-grain size influences the flow properties of metals. This is referred to as grain boundary strengthening (equation (7-2)). In Figure 7-16(a), a comparison between the average grain size (15° misorientation domains) and sub-grain size (2° misorientation domains) of Al in three forms - non-composite, type 1 and type 2 is presented. Their corresponding hardness values are also plotted with it. In figure 7-15(b), the HAGB fraction, average misorientation angle and kernel average misorientation (1 to 5 Kernels) of those Al samples deformed up to strains of 6-7 are plotted. Three important points can be inferred from the two graphs,

(i) The onset of saturation is seen to occur at slightly higher grain size values in the composite configuration. The sub-grain size and grain size of the Al in its composite configuration are around 20 % bigger than that of Al in its non-composite configuration after saturation.

(ii) After an equivalent von-Mises strain of 3.5, the hardness of the Al in the composite configuration is found to be independent of the grain size values, while for the Al in the non-composite configuration, it keeps changing.

(iii) The HAGB fraction and average misorientation angles are very similar for the Al in all the configurations.

Now, an estimation of the grain boundary strengthening using the obtained data will be performed for the Al of all the configurations. For comparison purpose, grain size information of Al in its as-received condition will also be used. To remind again, the hardness values of Al deformed in the composite form are comparable with the hardness of Al in its as-received state. GB strengthening can be presented as [24,27],

$$\Delta\sigma_{gb} = \alpha_2 G b \left[\lambda f_{LAGB}\left(\frac{1}{d}\right) + (1 - f_{LAGB})\left(\frac{1}{D}\right)\right] \qquad (7\text{-}2)$$

where G is shear modulus, b is Burgers vector, α_2 is a constant which has a value of 2 [24,28], f_{LAGB} is the fraction of LAGB, d is the average sub-grain size, D is the average grain size and λ is the ratio of sub-grain boundary strengthening contribution to grain boundary strengthening, which is estimated as 0.5 [24].

Table -7-2 Calculation of grain boundary strengthening

	Al-Al; 6 pass	Al; in Al-Cu type 1; 4 pass	Al; in Al-Cu type 2; 4 pass	as-received
$\boldsymbol{\alpha_2}$ (constant)	2	2	2	2
$\boldsymbol{f_{LAGB}}$ (LAGB fraction)	0.32	0.3	0.31	0.75
$\boldsymbol{d}$ (sub-grain size), µm	0.27	0.35	0.38	0.8
$\boldsymbol{D}$ (grain size), µm	0.801	1.01	1.02	15
$\boldsymbol{G}$, GPa	26 [29]			
$\boldsymbol{b}$, nm	0.28 [30]			
$\boldsymbol{\Delta\sigma_{gb}}$, MPa	18.6	17.4	17	7.07

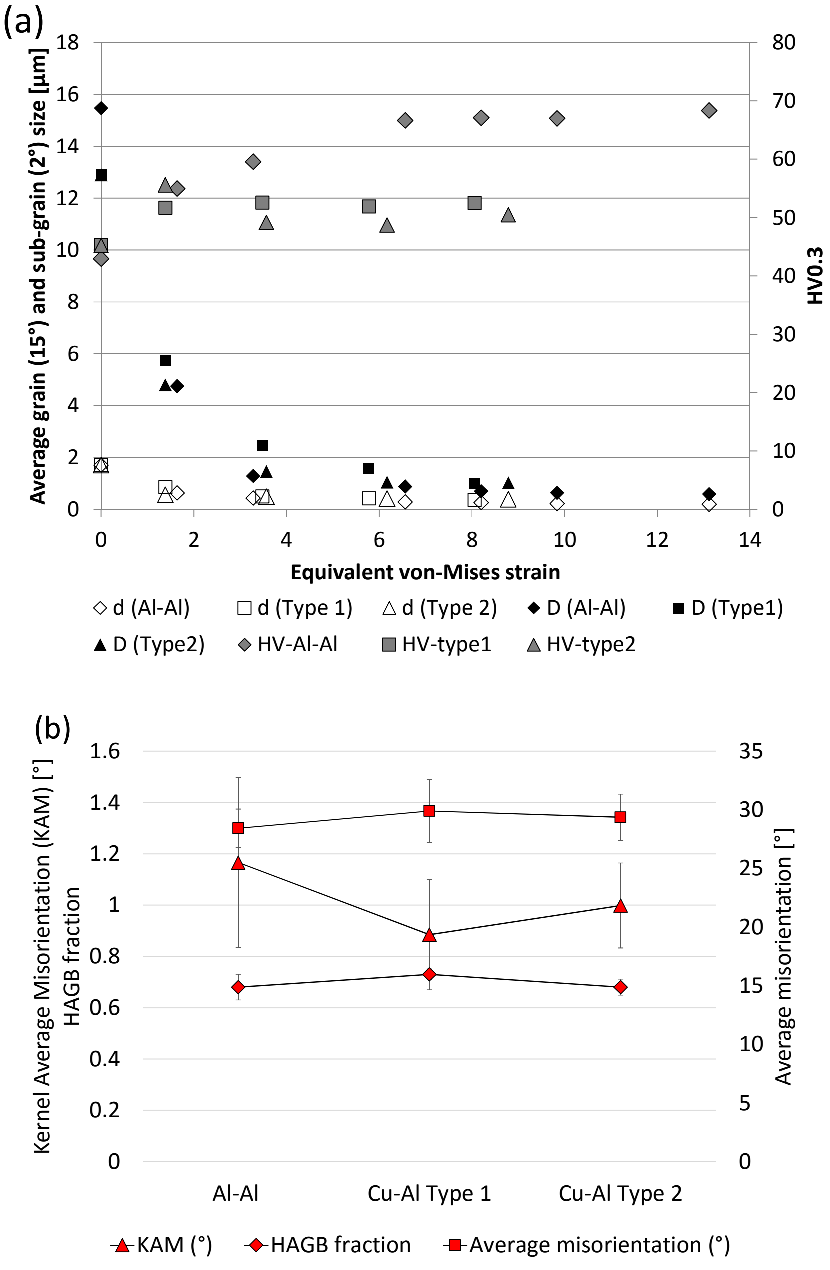

Figure 7-16 - (a) Grain size (D), sub-grain size (d) and hardness distribution of Al as function of equivalent von-Mises strain; (b) HAGB fraction, misorientation distribution of Al in its saturation state.

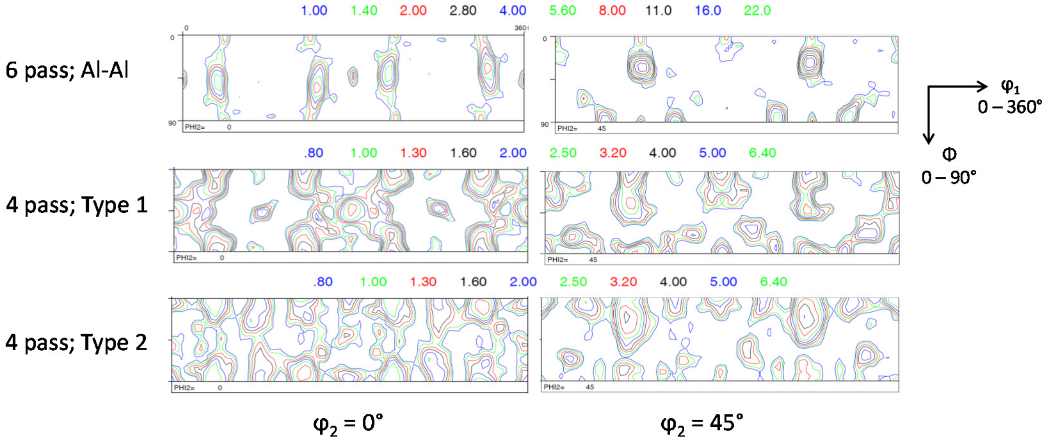

Figure 7-17 - ODF sections of Al in its saturation state after deformation in composite and non-composite configurations

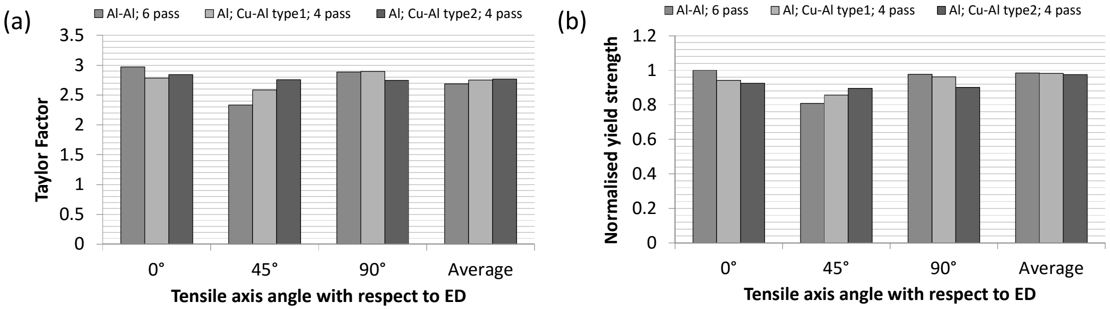

Figure 7-18 - (a) Taylor factor of Al for tensile deformation mode at different directions; (b) Normalized yield strength of Al predicted by the Taylor model for different directions

The calculated $\Delta\sigma_{gb}$ values of Al in the composite and non-composite configuration are presented in table 1. Two conclusions can be drawn from the calculation,

(i) All configurations of deformed Al, up to equivalent von-Mises strain of 6 to 7, show a similar grain boundary strengthening contribution despite the observed 20 % difference in their average grain size values. The difference is very insignificant due to the scale of grains size which are obtained after deformation.

(ii) The GB strength contribution is 2 times less for Al in its as-received state compared to AccumEx deformed Al, in any configuration. In spite of this difference, the hardness of Al in the composite form is comparable with the hardness of Al in its as-received state.

This clearly rules out the difference in grain size as a possible reason for the obtained low hardness values.

B. Influence of texture

In equation (7-1), the last term is the contribution due to texture (M) and dislocation strengthening ($\Delta\tau_d$). The Taylor factor, M is a representation of texture which has a significant effect on yield strength of the material. Figure 7-17 shows the φ2 = 0 and 45° section of the saturated Al, of Al-Cu type 1 and type 2 ; 4 pass and Al-Al; 6 pass. They correspond to similar equivalent von-Mises strains. The ODFs show a strong difference in the texture components and the texture strength, among the three samples. In order to evaluate the influence of this texture difference on the hardness, uniaxial tensile tests are simulated using the Taylor model [31] for all the three textures and the obtained yield stress values will be compared. Using uniaxial tensile deformation as a representation of hardness is not a good assumption and therefore, it has to be noted that this analysis is only to roughly estimate the effect of texture on the flow properties of the material, assuming all the other factors such as grain size and dislocation density to be identical.

The uniaxial tensile test simulations are done in seven different directions - 0°, 15°, 30°, 45°, 60°, 75° and 90° with respect to ED of the Al-Al; 6 pass and Al; Al-Cu type 2; 4 pass using the FC Taylor model [32]. The obtained yield stresses are presented in a normalized form, normalized with the stress value predicted for Al-Al; 6 pass; 0°. The average Taylor factor and the corresponding normalized stress values for the 0°, 45° and 90° samples are plotted in Figure 7-18 (a) and (b) respectively. The trend seen in the average Taylor factor is reproduced in their yield stress values. The normalized yield stresses of Al in Al-Cu type 1 and type 2; 4 pass along 0°, are around 5 % and 8 % lower than they are in Al-Al; 6 pass, respectively. Along 90°, they are 2 % and 8 % lower, respectively. And along 45°, they are 6 % and 10 % higher, respectively. It is an erratic difference in the flow properties along different directions. The difference becomes even more erratic when the values obtained for the other directions are also used in the comparison. However, taking an average of the normalized flow stress values along all the 7 directions results in neutralization of the differences between the yield stresses. The differences reduce to less than 1 % (Figure 7-18(b)). A similar effect can be expected for the hardness measurements. Unlike tensile deformation, the applied deformation field in hardness indentation is multidirectional, although the exact field is unknown. Therefore, a similar nullification of the effect of texture will be assumed in the process of indentation. This observation shows that the hardness indentation will not show a significant dependency on the average texture of the material.

C. Dislocation strengthening

Dislocation strengthening is the third part of the equation (7-1). It is also called as Taylor strengthening [33,34]. It is given as,

$$M\Delta\tau_d \tag{7.2}$$

$$\Delta\tau_d = \alpha_1 \mathrm{Gb}\sqrt{\rho} \tag{7.3}$$

where, M is the Taylor factor, G is the shear modulus, b is the burgers vector, ρ is the dislocation density and α_1 is a constant corresponding to dislocation mobility (around 0.3 for Al) [34].

Dislocation density is one of the prime factors that contribute to the strength of a material. The stored energy in the system is a function of dislocation density. It increases as function of strain and reaches a saturation wherein the strain hardening begins to saturate and the hardness remains almost constant. The hardness evolution observed in figure 4-7, is also a resultant of saturating dislocation density. It reduces when the material is subjected to annealing. This reduction depends on the type of softening phenomenon being active – recovery or recrystallization and of the duration of annealing.

Obtaining low hardness values for Al can be possible if the dislocation density of the material is low. It can be estimated theoretically that to obtain a 25 % drop in hardness i.e., from the saturated state (70 HV) to 50 HV0.3, almost 50 % reduction in dislocation density will be necessary, assuming all the other variables remaining the same. The only possible way to achieve this is through elevated temperature recovery or recrystallization. Static recovery of strain-hardened Al occurs at temperature range 150 – 300°C. Depending on the temperature and duration of annealing, around 20 % drop in hardness or more can be obtained, depending on the strain history of the material. For annealing temperatures at 300°C and above, recrystallization is favored and therefore a hardness drop of more than 50 % can be possible for just 5 min holding time in a strain-hardened Al. Al encourages dynamic recovery during deformation. However, a recovery similar to what can be achieved at temperatures of 150°C and above is hardly possible during the deformation, without an external source for the required high temperature. Similarly, recrystallization in Al is also not possible without the involvement of higher temperature. It was suggested in the section 7.3.6 that cube and Goss components, which are typical recrystallization components are observed throughout the deformation process between 1 and 4 passes. When Al is deformed alone, cube and Goss components disappear right away after the 1st pass (figure 4.10). This indicates a possibility for the occurrence of discontinuous recrystallization during deformation [35-38]. However, in the subsequent arguments in section 7.3.6, the claim was denied due to lack of experimental evidence. Therefore, although dislocation density can make a possible reason for the observed lower hardness, a valid reason for the occurrence of such a drop can occur for the present case is missing.

D. The unanswered question – further possibilities

Summarizing the above discussion,

1. Hardness did not change in spite of changing grain size
2. Effect of texture on hardness is minimal
3. Dislocation density has a direct effect on the hardness values, but there is not obvious reason to explain a large drop in dislocation density corresponding to the low observed hardness.

Residual stresses are very common in composite materials. A famous example is pearlite. Pearlite, a composite of ferrite and cementite, when deformed induces compressive residual stresses on ferrite and tensile residual stresses on cementite, due to plastic strain incompatibility [39]. A similar behavior is expected in Al-Cu composite as well (c.f. figure 7-12). Residual stresses modify the strain hardening properties of the metal [39-42]. The well-known example is shot peening. Shot peening induces compressive residual stresses at the surface of the metal and this increases the resistance of the metal to deform and also increases the surface hardness [43]. In this context, another example is presented in figure 7-19 (a), from the article [44]. An AA 8009 alloy was subjected to biaxial/uniaxial stresses (tensile and compressive) and hardness was measured using nano-indentation on the plane under the stress, while loaded. Compressive stresses increased the hardness and the tensile stresses reduced the hardness. The change in hardness was dependent on the magnitude of the applied stress [44]. From this information, residual stresses can have a significant impact on the value of the hardness. Based on this, a primitive characterization study is done on Al-Cu and Al-Al samples to evaluate the residual stresses in Al. XRD was done on Al-Cu (deformed up to 3 passes) and Al-Al (deformed up to 4 passes) along their ED-ND sections. Their respective 2-θ diffraction peak positions of all the measured planes of Al are noted. From the peak positions, their respective lattice strains can be calculated. In comparison with the lattice spacing of Al calculated for Al-Al, the lattice spacing of Al in Al-Cu is observed to be under tensile strain. The lattice strains calculated for six diffraction planes are shown in figure 7-19

Figure 7-19 (b). The comparison has been based between Al-Cu and Al, and not with an annealed Al as the concern here is hardness difference between Al in Al-Cu and Al in Al-Al. Comparing these results with that of obtained from literature, it can be said that the lower hardness of Al in Al-Cu can possibly be a consequence of tensile residual strain in Al. However, it is unclear on how the Al in Al-Cu is under tensile residual strain compared to that of Al in Al-Al. During the Al-Cu co-deformation, internal stresses are imposed on Al and Cu. After relaxation, one would expect that Al will be under compression rather than in tension. On the other hand, it has to be noted that during the deformation, the continuous Cu sheet breaks in to boudins. This implies that a part of the relaxation happens already during the breaking. Therefore, the degree of constraints between each other can become lenient which suggests that the state of the residual stresses in Al, at the meso-scale, around Cu undergoes transformations already during the deformation. Also, like in rolling, during extrusion, the heterogeneity in the plastic strain field across the sample thickness imposes macroscopic residual stresses from the surface to center. All these different contributions makes it difficult to understand the obtained results on lattice strain measurements. A combination of XRD and neutron diffraction and/or by XRD with stepwise layer removal would be needed to unravel the different contributions and in separating the meso-phase and the macroscopic residual stresses. This is a suggestion for future work. Another important point to be noted here is, from figure 7-19 (a), it is seen that a residual stress of 100 MPa induces a change of 7 % in their hardness values. The hardness difference noticed for the present case is 25 % or more. Therefore, even if it can be proven valid that tensile stresses are the reason for the lower hardness values, it will be hard to correlate this to the observed difference in hardness values. More experiments similar to that reported in [44] are needed to quantify the effect of stresses on the hardness values of AA 1050. This will be taken forth as a suggestion for future work.

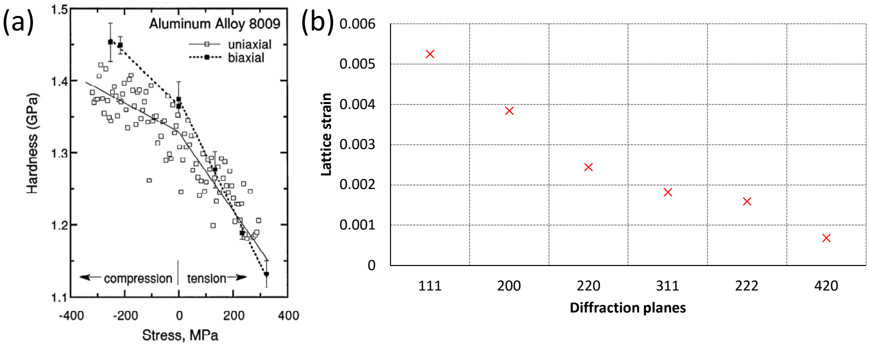

Figure 7-19 – (a) Figure taken from Tsui T et al [44] which shows nanoindentation measurements of the stress dependence of hardness for uniaxially and biaxially stressed specimens of aluminium; (b) Lattice strain of Al in Al-Cu composite, measured in reference to Al of Al-Al

7.4.3. A comparative discussion on the obtained material properties

Co-deformation of materials using rolling and wire drawing has been performed for several decades. Many combinations of metals – Al, Cu, Ni, Ti, Fe, etc., have been reported. The experiments which were performed by ARB showed robust properties with increasing number of passes. With respect to the material combination, different results were obtained. Al-Ti, Al-Ni and Al-Mg showed increasing tensile properties with increasing number of passes with lower ductility. The hardness of Al in all cases was greater than 65 HV [12,15,20,45]. In the case of three metal composites - Cu-Zn-Al and Al-Ti-Mg, a deteriorating strength after 4 cycles of ARB was reported [10,13,46]. The deteriorating results were attributed to the formation of intermetallics at the interface. With respect to Al-Cu composites, positive results were reported. Mehr et al [11] showed with deformation up to 12 cycles of ARB, the grain size of Cu was reduced down to 50 nm and of the one of Al down to 200 nm with good mechanical properties of more than 300 MPa yield strength and 6 % elongation to failure. By increasing the Al-Cu ratio, better properties were obtained. In similar work [47], Al-Cu was ARB processed up to 5 cycles and showed that a yield strength above 350 MPa with 8 % elongation to failure can be obtained. On the other hand for AccumEx deformed Al-Cu, the sample was robust only up to 2 passes of deformation. The effect of dissimilar interfaces worked out in the opposite way in the case of AccumEx. Contradictory to the reported articles, mechanical interfaces in AccumEx evolved into regions of irregularities instead of reinforcements. The bonding of the interface which was good up to 2 passes deteriorated badly after 3 and 4 passes.

With respect to texture evolution in Al during co-deformation, articles only reported partial weakening of plane strain compression components [9,48,49]. From the current work, it was possible to understand the underlying aspects of the weakening with reasonable spatial correlation. Due to the large difference in hardness, Al is observed to be very sensitive to the local deformation field and gets easily controlled by its co-material during the co-deformation process.

7.5. Conclusion

Co-deformation of Al-Cu composites was performed using AccumEx up to 4 deformation passes and in two different configurations. The grain refinement in Al and Cu, their individual bulk texture and the mechanical properties were characterized. An estimation of the effective strain distribution calculation revealed that Cu in general was less strained compared to Al. This is mainly due to the formation of Cu lenses or boudins. A lamellar microstructure is obtained for Cu and an ultrafine lamellar microstructure is obtained for Al. After 4 passes, the equivalent grain size of Al reached a saturated value of around 1 µm with aspect ratio of 2, while for Cu the final equivalent grain size was greater than 3 µm, with aspect ratio greater than 8. The texture study showed that after 4 passes, for Al a weak and random texture with combination of plane strain compression, shear and recrystallization texture components was noticed while for Cu, a typical plane strain compression texture was seen. The hardness of Cu increased from 50 HV to 150 HV after 1 pass but did not show any distinct change between 1 and 4 deformation passes. The hardness of Al showed a slight increase from 47 to 50 HV after 1 pass, but between 2 and 4 passes, no change was noticed. Tensile strength of the composites increased after 1 and 2 passes to around 240-260 MPa but after 3 and 4 passes, they deteriorated. Type 2 configuration in general showed lower strength than type 1.

The deformation behavior of Al and Cu played a significant role in the final properties of the composite. The extensive strain hardening of Cu induced heterogeneity in the flow behavior between Al and Cu. The hardness ratio of Cu to Al increased from 1.17 to 2.75 just after 1 pass and remained almost the same till 4 passes. Therefore, during deformation Al underwent overstraining for the same applied compressive stresses. This difference in the flow characteristics resulted in the fragmentation of the Cu sheets into boudins. Associated to this process, Al in the vicinity of Cu underwent micro-shear which modified the texture of Al. Region specific EBSD measurements revealed different texture properties in Al depending on the position of the Cu boudins. This formed an explanation for the observation random texture in Al during bulk measurements.

Use of two different configurations suggested that with increasing number of interfaces, more heterogeneities were imposed which turned detrimental to the properties of the material. Other differences were that Al in type 2 showed earlier onset of texture weakening than in type 1 and the tensile properties of type 1 were always better than the ones of type 2. The intention to use mechanical interfaces for improving the strength properties of composite material was realized in a negative manner when produced using AccumEx. The interaction of the process deformation field with the material's deformation field within the composite could be one of the major reason for that.

The saturated hardness of Al was found to be 25 % lower than when Al was deformed alone. Despite producing ultra-fine grained microstructure Al obtaining such a low hardness value was surprising, however no valid explanation could be found. Otherwise, in general co-deformation by AccumEx cannot be categorized as a successful processing method to deform dissimilar metal composites to high deformation strains with the current deformation settings. However, on a positive note, it was learnt that by tailoring the shape and morphology of the boudins with different combination of materials, a completely different material property can be obtained. The exact effect of these boudins is still not clear but, it can form an interesting study.

REFERENCES

1 Raabe, D. *et al.* Metallic composites processed via extreme deformation: Toward the limits of strength in bulk materials. *MRS Bulletin* **35**, 982-991, doi:10.1557/mrs2010.703 (2011).

2 Pippan, R., Wetscher, F., Hafok, M., Vorhauer, A. & Sabirov, I. The Limits of Refinement by Severe Plastic Deformation. *Advanced Engineering Materials* **8**, 1046-1056, doi:10.1002/adem.200600133 (2006).

3 Raabe, D., Ohsaki, S. & Hono, K. Mechanical alloying and amorphization in Cu–Nb–Ag in situ composite wires studied by transmission electron microscopy and atom probe tomography. *Acta Materialia* **57**, 5254-5263, doi:10.1016/j.actamat.2009.07.028 (2009).

4 Raabe, D. & Hangen, U. Observation of amorphous areas in a heavily cold rolled Cu-20 wt% Nb composite. *Materials Letters* **22**, 155-161, doi:http://dx.doi.org/10.1016/0167-577X(94)00248-7 (1995).

5 Goscombe, B. D., Passchier, C. W. & Hand, M. Boudinage classification: end-member boudin types and modified boudin structures. *Journal of Structural Geology* **26**, 739-763, doi:10.1016/j.jsg.2003.08.015 (2004).

6 Ramberg, H. Natural and Experimental Boudinage and Pinch-and-Swell Structures. *The Journal of Geology* **63**, 512-526 (1955).

7 Smith, R. B. Formation of folds, boudinage, and mullions in non-Newtonian materials. *Geological Society of America Bulletin* **88**, 312-320, doi:10.1130/0016-7606(1977)88<312:fofbam>2.0.co;2 (1977).

8 Jia, N., Zhu, M.-W., Zheng, Y.-R., He, T. & Zhao, X. Inhomogeneous Deformation of Multilayered Roll-Bonded Brass/Cu Composites. *Acta Metallurgica Sinica (English Letters)* **28**, 600-607, doi:10.1007/s40195-015-0237-5 (2015).

9 Qu, P., Zhou, L. & Acoff, V. L. Deformation textures of aluminum in a multilayered Ti/Al/Nb composite severely deformed by accumulative roll bonding. *Materials Characterization* **107**, 367-375, doi:10.1016/j.matchar.2015.07.011 (2015).

10 Motevalli, P. D. & Eghbali, B. Microstructure and mechanical properties of Tri-metal Al/Ti/Mg laminated composite processed by accumulative roll bonding. *Materials Science and Engineering: A* **628**, 135-142, doi:10.1016/j.msea.2014.12.067 (2015).

11 Yousefi Mehr, V., Toroghinejad, M. R. & Rezaeian, A. Mechanical properties and microstructure evolutions of multilayered Al–Cu composites produced by accumulative roll bonding process and subsequent annealing. *Materials Science and Engineering: A* **601**, 40-47, doi:10.1016/j.msea.2014.02.023 (2014).

12 Eslami, P., Karimi Taheri, A. & Zebardast, M. A Comparison Between Cold-Welded and Diffusion-Bonded Al/Cu Bimetallic Rods Produced by ECAE Process. *Journal of Materials Engineering and Performance* **22**, 3014-3023, doi:10.1007/s11665-013-0591-2 (2013).

13 Mahdavian, M. M., Ghalandari, L. & Reihanian, M. Accumulative roll bonding of multilayered Cu/Zn/Al: An evaluation of microstructure and mechanical

properties. *Materials Science and Engineering: A* **579**, 99-107, doi:10.1016/j.msea.2013.05.002 (2013).

14 Kim, I.-K. & Hong, S. I. Effect of heat treatment on the bending behavior of tri-layered Cu/Al/Cu composite plates. *Materials & Design* **47**, 590-598, doi:10.1016/j.matdes.2012.12.070 (2013).

15 Mozaffari, A., Danesh Manesh, H. & Janghorban, K. Evaluation of mechanical properties and structure of multilayered Al/Ni composites produced by accumulative roll bonding (ARB) process. *Journal of Alloys and Compounds* **489**, 103-109, doi:10.1016/j.jallcom.2009.09.022 (2010).

16 Yang, D., Cizek, P., Hodgson, P. & Wen, C. e. Ultrafine equiaxed-grain Ti/Al composite produced by accumulative roll bonding. *Scripta Materialia* **62**, 321-324, doi:10.1016/j.scriptamat.2009.11.036 (2010).

17 Semiatin, S. L. & Piehler, H. R. Formability of sandwich sheet materials in plane strain compression and rolling. *Metallurgical Transactions A* **10**, 97-107, doi:10.1007/bf02686412 (1979).

18 Hawkins, R. & Wright, J. C. Observations on the deformation properties of sandwich materials. *International Journal of Mechanical Sciences* **14**, 875-878, doi:http://dx.doi.org/10.1016/0020-7403(72)90046-X (1972).

19 Hwang, Y.-M., Hsu, H.-H. & Lee, H.-J. Analysis of plastic instability during sandwich sheet rolling. *International Journal of Machine Tools and Manufacture* **36**, 47-62, doi:http://dx.doi.org/10.1016/0890-6955(95)92628-C (1996).

20 Min, G., Lee, J.-M., Kang, S.-B. & Kim, H.-W. Evolution of microstructure for multilayered Al/Ni composites by accumulative roll bonding process. *Materials Letters* **60**, 3255-3259, doi:10.1016/j.matlet.2006.03.001 (2006).

21 Lee, J.-M., Lee, B.-R. & Kang, S.-B. Control of layer continuity in metallic multilayers produced by deformation synthesis method. *Materials Science and Engineering: A* **406**, 95-101, doi:10.1016/j.msea.2005.06.030 (2005).

22 Nowicke, F., Zavaliangos, A. & Rogers, H. C. The effect of roll and clad sheet geometry on the necking instability during rolling of clad sheet metals. *International Journal of Mechanical Sciences* **48**, 868-877, doi:10.1016/j.ijmecsci.2006.01.021 (2006).

23 Quadir, M. Z., Ferry, M., Al-Buhamad, O. & Munroe, P. R. Shear banding and recrystallization texture development in a multilayered Al alloy sheet produced by accumulative roll bonding. *Acta Materialia* **57**, 29-40, doi:10.1016/j.actamat.2008.08.056 (2009).

24 Qiao, X. G., Starink, M. J. & Gao, N. Hardness inhomogeneity and local strengthening mechanisms of an Al1050 aluminium alloy after one pass of equal channel angular pressing. *Materials Science and Engineering: A* **513-514**, 52-58, doi:10.1016/j.msea.2009.01.051 (2009).

25 Zhang, J., Gao, N. & Starink, M. J. Microstructure development and hardening during high pressure torsion of commercially pure aluminium: Strain reversal experiments and a dislocation based model. *Materials Science and Engineering: A* **528**, 2581-2591, doi:10.1016/j.msea.2010.11.079 (2011).

26 Starink, M. J. & Wang, S. C. A model for the yield strength of overaged Al–Zn–Mg–Cu alloys. *Acta Materialia* **51**, 5131-5150, doi:10.1016/s1359-6454(03)00363-x (2003).

27 Marthinsen, K. & Nes, E. A general model for metal plasticity. *Materials Science and Engineering: A* **234**, 1095-1098, doi:http://dx.doi.org/10.1016/S0921-5093(97)00349-3 (1997).

28 Nes, E., Pettersen, T. & Marthinsen, K. On the mechanisms of work hardening and flow-stress saturation. *Scripta Materialia* **43**, 55-62, doi:http://dx.doi.org/10.1016/S1359-6462(00)00363-8 (2000).

29 Kissell, J. R. & Ferry, R. L. Aluminium Structures: A Guide to their Specifications, Design. *(second ed.)John Wiley & Sons, New York* (2002).

30 Hutchinson, J. W. Elastic-Plastic Behavior of Polycrystalline Metals and Composites. *Proceedings of the Royal Society A: Mathematical, Physical and Engineering Sciences* **319**, 247-272, doi:10.1098/rspa.1970.0177 (1970).

31 Taylor, G. I. Plastic strain in metals. *J. Institute of Metals* **62**, 307-324 (1938).

32 Van Houtte, P., Li, S., Seefeldt, M., Delanney, L. Deformation texture prediction: from the Taylor model to the advanced Lamel model. *International Journal of Plasticity* **21**, 589-624, doi:10.1016/j.ijplas.2004.04.011 (2005).

33 El-Awady, J. A. Unravelling the physics of size-dependent dislocation-mediated plasticity. *Nat Commun* **6**, 5926, doi:10.1038/ncomms6926 (2015).

34 Ashby, M. F. The deformation of plastically non-homogeneous materials. *Philosophical Magazine* **21**, 399-424, doi:10.1080/14786437008238426 (1970).

35 Yu, H. *et al.* Microstructure evolution of accumulative roll bonding processed pure aluminum during cryorolling. *Journal of Materials Research* **31**, 797-805, doi:10.1557/jmr.2016.70 (2016).

36 Huang, Y. & Prangnell, P. B. The effect of cryogenic temperature and change in deformation mode on the limiting grain size in a severely deformed dilute aluminium alloy. *Acta Materialia* **56**, 1619-1632, doi:10.1016/j.actamat.2007.12.017 (2008).

37 Li, Y. S., Tao, N. R. & Lu, K. Microstructural evolution and nanostructure formation in copper during dynamic plastic deformation at cryogenic temperatures. *Acta Materialia* **56**, 230-241, doi:10.1016/j.actamat.2007.09.020 (2008).

38 Zhang, K., Weertman, J. R. & Eastman, J. A. Rapid stress-driven grain coarsening in nanocrystalline Cu at ambient and cryogenic temperatures. *Applied Physics Letters* **87**, 061921, doi:10.1063/1.2008377 (2005).

39 De Giorgi, M. Residual stress evolution in cold-rolled steels. *International Journal of Fatigue* **33**, 507-512, doi:10.1016/j.ijfatigue.2010.10.006 (2011).

40 Bolshakov, A., Oliver, W. C. & Pharr, G. M. Influences of stress on the measurement of mechanical properties using nanoindentation: Part II. Finite element simulations. *Journal of Materials Research* **11**, 760-768, doi:10.1557/jmr.1996.0092 (2011).

41 Ortiz, A. L., Tian, J. W., Villegas, J. C., Shaw, L. L. & Liaw, P. K. Interrogation of the microstructure and residual stress of a nickel-base alloy subjected to

surface severe plastic deformation. *Acta Materialia* **56**, 413-426, doi:10.1016/j.actamat.2007.10.003 (2008).

42 Sinclair, C. W., Saada, G. & Embury, J. D. Role of internal stresses in co-deformed two-phase materials. *Philosophical Magazine* **86**, 4081-4098, doi:10.1080/14786430600654438 (2006).

43 Kobayashi, M., Matsui, T. & Murakami, Y. Mechanism of creation of compressive residual stress by shot peening. *International Journal of Fatigue* **20**, 351-357, doi:http://doi.org/10.1016/S0142-1123(98)00002-4 (1998).

44 Tsui, T. Y., Oliver, W. C. & Pharr, G. M. Influences of stress on the measurement of mechanical properties using nanoindentation: Part I. Experimental studies in an aluminum alloy. *Journal of Materials Research* **11**, 752-759, doi:10.1557/jmr.1996.0091 (1996).

45 Liu, H. S., Zhang, B. & Zhang, G. P. Microstructures and Mechanical Properties of Al/Mg Alloy Multilayered Composites Produced by Accumulative Roll Bonding. *Journal of Materials Science & Technology* **27**, 15-21, doi:10.1016/s1005-0302(11)60019-4 (2011).

46 Ma, M., Huo, P., Liu, W. C., Wang, G. J. & Wang, D. M. Microstructure and mechanical properties of Al/Ti/Al laminated composites prepared by roll bonding. *Materials Science and Engineering: A* **636**, 301-310, doi:10.1016/j.msea.2015.03.086 (2015).

47 Eizadjou, M., Kazemitalachi, A., Daneshmanesh, H., Shakurshahabi, H. & Janghorban, K. Investigation of structure and mechanical properties of multi-layered Al/Cu composite produced by accumulative roll bonding (ARB) process. *Composites Science and Technology* **68**, 2003-2009, doi:10.1016/j.compscitech.2008.02.029 (2008).

48 Jia, N., Raabe, D. & Zhao, X. Texture and microstructure evolution during non-crystallographic shear banding in a plane strain compressed Cu–Ag metal matrix composite. *Acta Materialia* **76**, 238-251, doi:10.1016/j.actamat.2014.05.036 (2014).

49 Chang, H. *et al.* Texture evolution of the Mg/Al laminated composite fabricated by the accumulative roll bonding. *Scripta Materialia* **61**, 717-720, doi:10.1016/j.scriptamat.2009.06.014 (2009).

8. Comparative study of material properties of Al and Cu deformed by ECAP and AccumEx

8.1. Introduction

The micro-mechanics involved within a deformation process determine to a large extend the final properties of the material being processed. Different processing conditions resulted in different properties for the same material [1-7]. Especially in the field of SPD, the deformation path that the material undergoes to achieve a UFG structure is vitally dependent on the deformation mode and the nature of the process. Several SPD techniques and their characteristic features have been reported [3,8,9]. In this chapter, the results obtained from AccumEx processing of Al and Cu-Al, reported in the previous chapters will be compared with their ECAP counterpart. For this purpose, two sets of experiments are performed – ECAP of Cu and Cu-Al. ECAP on Al has already been studied by Poortmans [10] and the results obtained from that work will be utilized for the comparative study.

8.2. Experiments

8.2.1. ECAP

Two times a set of experiments is carried out on Cu and a Cu-Al composite. Both experiments are carried out by ECAP route C at room temperature up to 8 deformation passes. The description of the process can be found in chapter 3. The first set of experiments are performed on Cu bars with geometry as shown in Figure 8-1 (a) and composition as mentioned in table 3-2 . The material is used in its as-received condition (hot extruded). The second set of experiments are performed on a Cu-Al composite assembly. The geometry of the composite is shown in Figure 8-1 (b). An Al rod of 6 mm diameter with composition (table 3-1) is inserted inside a Cu tube of 12 mm outer diameter and 6 mm inner diameter. Prior to assembly, Cu and Al are annealed at 500°C for 4 hours and 400°C for 3 hours respectively. This is to ensure there is no remains of texture and microstructure from the previous hot working process, in this case axisymmetric extrusion. Later, the materials are surface treated by wire-brushing followed by cleaning with Acetone to remove oxides and assembled just before ECAP. .

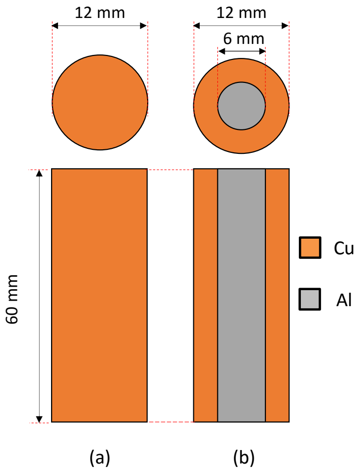

Figure 8-1 Geometry of (a) Cu; (b) Cu-Al ECAP samples

8.2.2. AccumEx

The results obtained from chapter 4 and 7 will be directly used for the purpose of this comparative study. In addition, another set of experiments which has not yet been reported yet will also be used - Al-Al similar AccumEx performed with annealed starting condition.

All the samples are studied for their microstructure using EBSD, their micro-hardness using Vickers micro-hardness testing and tensile properties using tensile tests. The data which will be presented correspond to the results obtained from the ED-ND section of AccumEx and ECAP deformed samples (figure 3.3 and 3.6). The values will be compared based on the same equivalent von-Mises strain. Strain 0 corresponds to the starting state of the material which can be annealed or as-received. Grain size and micro-hardness of Al and Cu will be studied separately. The comparison will be based between Al-Al AccumEx (as received/annealed starting), Cu-Al AccumEx (type 1 and type 2), Cu-Al ECAP, Al ECAP [10] for Al and between Cu-Al AccumEx (type 1 and type 2), Cu-Al ECAP, Cu ECAP for Cu. The yield strength will be compared globally between AccumEx, Cu-Al AccumEx, Cu ECAP and Al ECAP.

8.3. Results

8.3.1. Grain size analysis

The grain size is measured by the linear intercept method using 15° misorientation as a criterion for a high angle grain boundary. The value which is presented for each process is an average of the grain size measured along ED and ND. The grain size evolution is plotted as a function of the equivalent von-Mises strain for Al and Cu separately.

Figure 8-2 shows the grain size values of Al. Irrespective of the deformation mode, a general trend of grain refinement is observed for all tested conditions. The rate of refinement observed in AccumEx is very high. In the case of Al-Al AccumEx; as-received starting condition, a sub-micron grain size is obtained after an equivalent von-Mises strain of 5. In Al-Al AccumEx; annealed starting condition, a grain size of 1.5 µm is obtained after an equivalent strain of 6. The effect of the initial grain size is clearly visible. In ECAP, a sub-micron grain size is observed after an equivalent strain of 15 after a slower grain refinement. Moreover, the final grain size value after an equivalent strain of 15 is 30 % higher than the grain size values obtained in Al-Al AccumEx after an equivalent strain of 11. For the Cu-Al co-deformation processes, a different trend can be noticed. In co-deformation Cu-Al by AccumEx, grain size saturation is seen to occur at grain size values 20 – 40 % higher than in Al-Al AccumEx. Similarly, in co-deformation Cu-Al by ECAP, larger grain size values for Al are observed compared to its non-composite counterpart, however after a strain of 9, the values converged to similar numbers.

Figure 8-2 shows the grain size evolution of Cu. Up to an equivalent strain of 10, none of the processes resulted in a grain size of less than 1 µm. The rate of grain refinement showed similar trends for all processes till an equivalent strain of 4. The grain sizes obtained after AccumEx are smaller than their ECAP counterparts, both in composite and non-composite samples. However, a huge difference between the two composite arrangements of AccumEx is seen which was explained due to a difference in effective strain distribution within the composite. Another important point to be noted here is that the grain size obtained after co-deformation of Cu-Al by ECAP is higher than that of ECAP of Cu only.

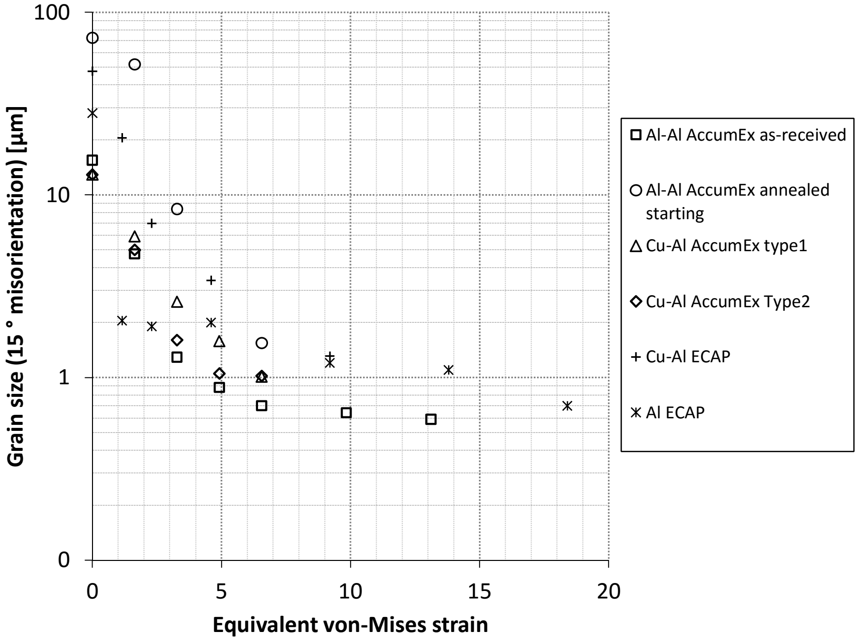

Figure 8-2 Grain size distribution of Al as function of von-Mises equivalent strain

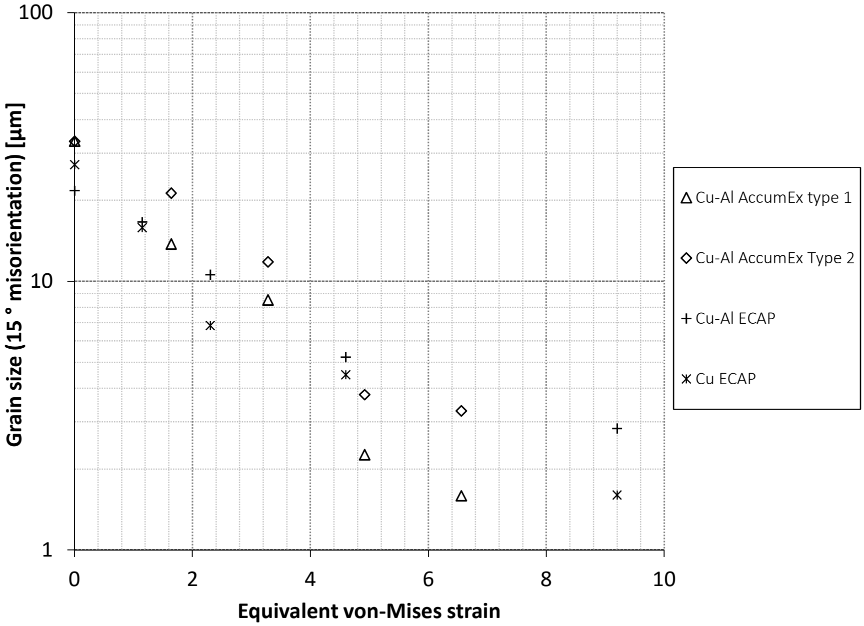

Figure 8-3 Grain size distribution of Cu as function of von-Mises equivalent strain

8.3.2. Micro-hardness

Vickers micro-hardness was measured for Al and Cu separately for all the different deformation routes performed. Data for Al ECAP have been taken from literature [11] for comparison purpose.

Figure 8-4 shows the hardness evolution of Al. The hardness of Al is 40-45 HV0.3 in its as-received condition and 20-25 HV0.3 in its annealed condition. After deformation, a significant strain hardening is seen in all the processes. The first major observation is that the hardness values of Al processed by AccumEx deformation are higher than the ones from Cu-Al co-deformation by AccumEx or ECAP. Despite of the difference in starting condition, the hardness of Al reached ~70 HV0.3 after an equivalent strain of 6 for both cases. In case of Al ECAP, the hardness crossed 60 HV only after 8 passes, an equivalent strain of about 9. In the co-deformation set up, both AccumEx and ECAP, the effect of strain hardening is seen to be negligible. The hardness values are about 25 % less than in its non-composite counterpart. Figure 8-5 shows the hardness evolution of Cu. From this figure, it is clearly noticed that, irrespective of the starting condition and type of the deformation process, the hardness of Cu increased to about 145 HV0.3 and saturated after deformation above an equivalent strain of 3.

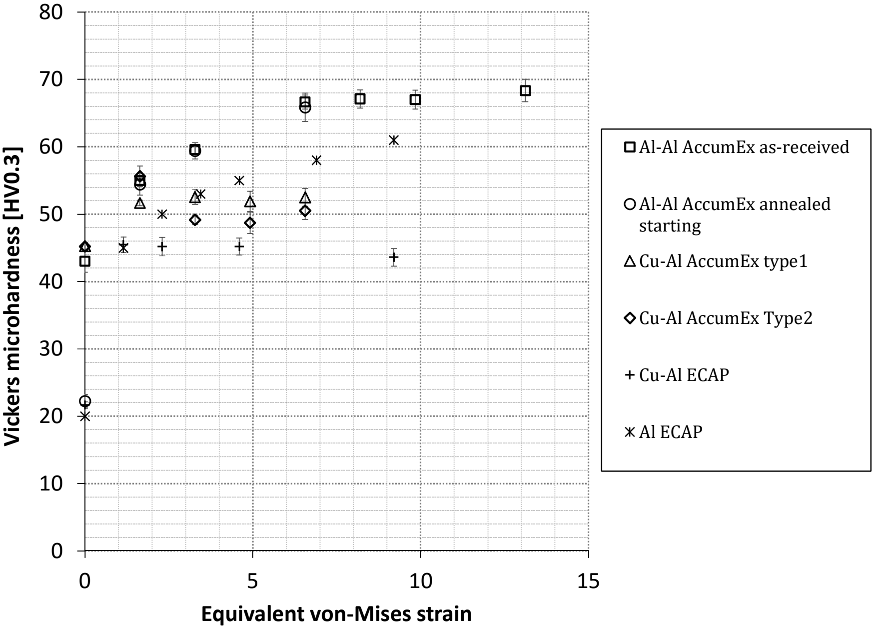

Figure 8-4 Micro hardness evolution of Al as function of equivalent von-Mises strain

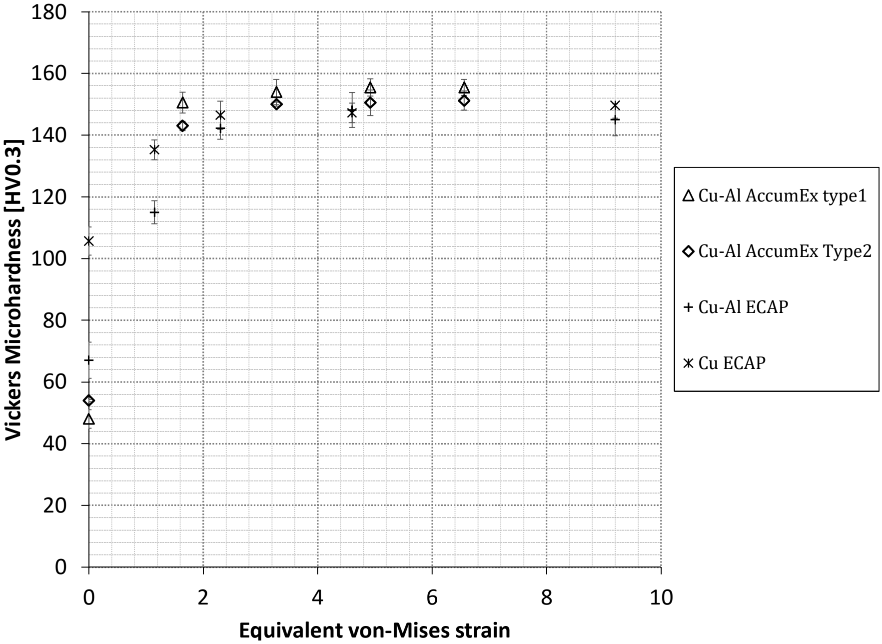

Figure 8-5 Micro hardness evolution of Cu as function of equivalent von-Mises strain

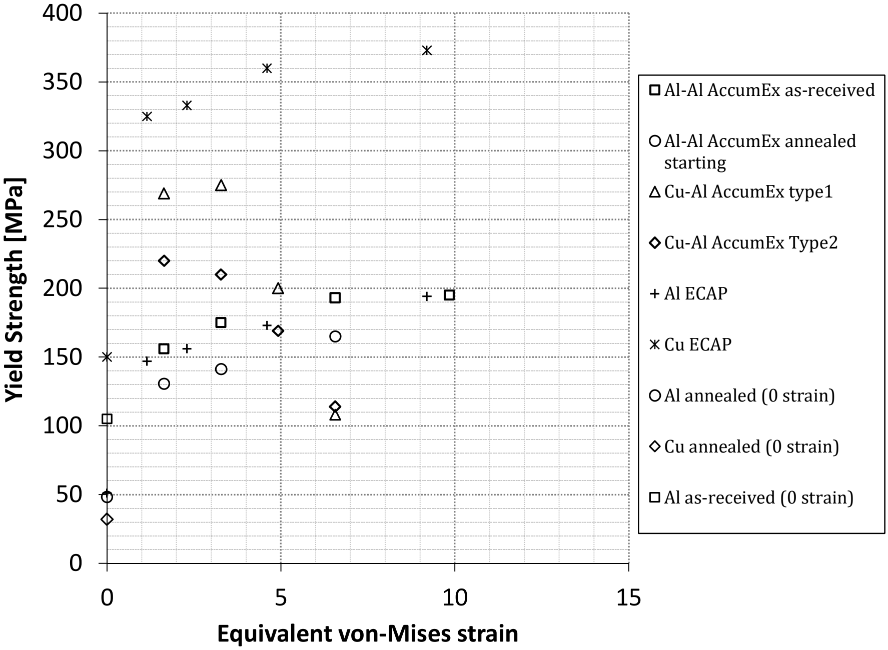

Figure 8-6 Yield strength evolution of deformed material as function of equivalent von-Mises strain

8.3.3. Yield strength

The Yield strengths of the AccumEx deformed Al and Cu-Al and the ECAP deformed Al and Cu samples are plotted in Figure 8-6. The highest value of all is obtained for ECAP deformed Cu. Second highest is for Cu-Al; type 1, co-deformed by AccumEx deformed up to an equivalent strain of 3.2. The yield strength values of ECAP processed Al and AccumEx processed Al; as-received showed similar values. AccumEx Al; annealed showed a relatively lower yield strength. Results obtained for higher strains by AccumEx are low and are attributed to the defects arising due to the processing conditions. However, till deformation strains of 3-4, the yield strength of the composite is as expected situated between the values for Cu and Al.

8.4. Discussion

Equation (8-1) is a representation of the yield strength (σ_y) involving the contribution of strain hardening and grain refinement [12-15], where σ_0 is the yield strength of the material in its annealed form, $\Delta\tau_d$ is the contribution to yield strength by grain boundary strengthening, $\Delta\sigma_d$ is the contribution to yield strength due to accumulation of dislocations and M is the Taylor factor. Grain boundaries and dislocations are major factors contributing to the strength of the material. Formation of grain boundaries implies grain refinement which is assisted by the formation of dislocations and grain rotations[16].

$$\sigma_y = \sigma_0 + \Delta\sigma_{gb} + M\Delta\tau_d \tag{8-1}$$

AccumEx can be idealized as a plane strain compression process. It is a pure shear deformation. However, results from chapter 5 proved that, simple shear deformation mode also exists and it accumulates with increasing equivalent strains. ECAP is a shear deformation process with no geometrical modifications. So, its deformation mode is represented ideally as simple shear.

The evolution of grain sub-structures is very different between pure shear and simple shear [8]. In pure shear mode, because of a huge geometrical reduction, most of the grain refinement happens by formation of GNBs and IDBs, triggered by textural evolution, i.e., rotation of grains towards more stable orientations with grain sub-divisions [17-20]. Further, depending on the magnitude of reduction in thickness and the material being processed, shear bands also assist in the grain size reduction. Therefore, the evolution of HAGB is rapid and thus grain refinement is faster. In the present case this is reflected in the fact that most of the microstructural modifications occur in the initial deformation passes. On the other hand, during simple shear, the deformation proceeds mostly by shear localization and formation of shear band structures. This confines the dislocation activities and sub-structure evolution, within the strain localized regions. Eventually, the grain structures develop with their boundaries directing towards the shear direction. However, for this to happen, higher deformation strains are needed which can impose enough grain rotations which will assist HAGB formation [3,8,21]. As a direct evidence, Figure 8-7 shows that in an ECAP process the rate of formation of HAGB is lower than in AccumEx. It is also reflected in the grain sizes and rates of strain hardening. Therefore, AccumEx helps in rapid grain refinement and obtaining finer grain size at lower equivalent von-Mises strain while ECAP proceeds by gradual structure modifications which can be controlled and modified by different strain path changes.

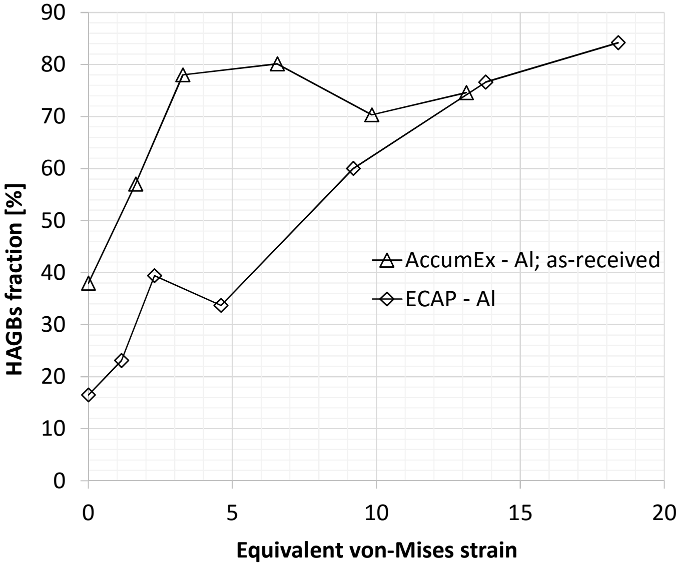

Figure 8-7 Formation of HAGB as function of equivalent von-Mises strain during deformation of Al by AccumEx; as-received and ECAP

The mechanical properties of non-composite samples processed by ECAP performed better than AccumEx. Poor properties in AccumEx are due to the process induced defects at the mechanically created interfaces which made it difficult to evaluate the bulk mechanical properties effectively. Addition of Cu as reinforcement deterred the strain hardening of Al in both AccumEx and ECAP. However, the reported grain size values show that they are in par with the non-composite counterpart. This implies that the observed lower hardness values is a common phenomenon in both

AccumEx and ECAP and remains a big question mark and needs further study to understand it. Further it gives a clue that the interaction between Al and Cu could have a significant role in it.

8.5. Conclusions

Experiments were performed using ECAP on Cu and Al-Cu samples. Their microstructural and mechanical properties were characterized. Grain size, micro hardness and yield strength were plotted as a function of equivalent von-Mises strain and compared between AccumEx and ECAP. The following conclusions were drawn,

1. Deformation in Al produced similar microstructure and mechanical properties in AccumEx and ECAP, but the latter achieved the same at higher equivalent strains.
2. Co-deformation of Al and Cu in both AccumEx and ECAP resulted in complex property changes in the Al part. The anomalous hardening behavior of Al was observed in both cases and remains a standing question.
3. Deformation of Cu was solely dependent on its observed effective strain. The microstructural and hardness values were very similar in all the deformation processes.
4. AccumEx imposed a more rapid modification in the microstructural and mechanical properties of the material than ECAP.

REFERENCES

1 Poortmans, S. & Verlinden, B. Mechanical Properties of Fine-Grained AA1050 after ECAP. *Materials Science Forum* **503-504**, 847-852, doi:10.4028/www.scientific.net/MSF.503-504.847 (2006).

2 Valiev, R. Z. & Langdon, T. G. Principles of equal-channel angular pressing as a processing tool for grain refinement. *Progress in Materials Science* **51**, 881-981, doi:10.1016/j.pmatsci.2006.02.003 (2006).

3 Segal, V. M. Materials processing by simple shear. *Materials Science and Engineering: A* **197**, 157-164, doi:http://dx.doi.org/10.1016/0921-5093(95)09705-8 (1995).

4 Estrin, Y. & Vinogradov, A. Extreme grain refinement by severe plastic deformation: A wealth of challenging science. *Acta Materialia* **61**, 782-817, doi:10.1016/j.actamat.2012.10.038 (2013).

5 Kratochvíl, J. Mechanism of Grain Refinement Induced by Severe Plastic Deformation. *Materials Science Forum* **667-669**, 617-622, doi:10.4028/www.scientific.net/MSF.667-669.617 (2010).

6 Azushima, A. *et al.* Severe plastic deformation (SPD) processes for metals. *CIRP Annals - Manufacturing Technology* **57**, 716-735, doi:10.1016/j.cirp.2008.09.005 (2008).

7 Pippan, R., Wetscher, F., Hafok, M., Vorhauer, A. & Sabirov, I. The Limits of Refinement by Severe Plastic Deformation. *Advanced Engineering Materials* **8**, 1046-1056, doi:10.1002/adem.200600133 (2006).

8 Segal, V. M. Severe plastic deformation: simple shear versus pure shear. *Materials Science and Engineering: A* **338**, 331-344, doi:http://dx.doi.org/10.1016/S0921-5093(02)00066-7 (2002).

9 Hirsch, J. & Lücke, K. Overview no. 76. *Acta Metallurgica* **36**, 2883-2904, doi:http://dx.doi.org/10.1016/0001-6160(88)90173-3 (1988).

10 Poortmans, S. From microstructure towards mechanical behavior of ultrafine grained aluminium alloys. *Ph.D. dissertation* (2008), KU Leuven.

11 El-Danaf, E. A., Soliman, M. S., Almajid, A. A. & El-Rayes, M. M. Enhancement of mechanical properties and grain size refinement of commercial purity aluminum 1050 processed by ECAP. *Materials Science and Engineering: A* **458**, 226-234, doi:10.1016/j.msea.2006.12.077 (2007).

12 Armstrong, R., Codd, I., Douthwaite, R. M. & Petch, N. J. The plastic deformation of polycrystalline aggregates. *Philosophical Magazine* **7**, 45-58, doi:10.1080/14786436208201857 (1962).

13 Zhang, J., Gao, N. & Starink, M. J. Microstructure development and hardening during high pressure torsion of commercially pure aluminium: Strain reversal experiments and a dislocation based model. *Materials Science and Engineering: A* **528**, 2581-2591, doi:10.1016/j.msea.2010.11.079 (2011).

14 Starink, M. J. & Wang, S. C. A model for the yield strength of overaged Al–Zn–Mg–Cu alloys. *Acta Materialia* **51**, 5131-5150, doi:http://dx.doi.org/10.1016/S1359-6454(03)00363-X (2003).

15 Gil Sevillano, J., Van Houtte, P. & Aernoudt, E. Large strain work hardening and textures. *Progress in Materials Science* **25**, 69-134 (1980).

16 Lopes, A. B., Barlat, F., Gracio, J. J., Ferreira Duarte, J. F. & Rauch, E. F. Effect of texture and microstructure on strain hardening anisotropy for aluminum deformed in uniaxial tension and simple shear. *International Journal of Plasticity* **19**, 1-22, doi:http://dx.doi.org/10.1016/S0749-6419(01)00016-X (2003).

17 Hughes, D. A. & Hansen, N. High angle boundaries formed by grain subdivision mechanisms. *Acta Materialia* **45**, 3871-3886, doi:http://dx.doi.org/10.1016/S1359-6454(97)00027-X (1997).

18 Mishin, O. V., Juul Jensen, D. & Hansen, N. Evolution of Microstructure and Texture during Annealing of Aluminum AA1050 Cold Rolled to High and Ultrahigh Strains. *Metallurgical and Materials Transactions A* **41**, 2936-2948, doi:10.1007/s11661-010-0291-6 (2010).

19 Hansen, N., Huang, X., Ueji, R. & Tsuji, N. Structure and strength after large strain deformation. *Materials Science and Engineering: A* **387-389**, 191-194, doi:10.1016/j.msea.2004.02.078 (2004).

20 Hansen, N. & Juul Jensen, D. Development of microstructure in FCC metals during cold work. *Philosophical Transactions of the Royal Society A: Mathematical, Physical and Engineering Sciences* **357**, 1447-1469, doi:10.1098/rsta.1999.0384 (1999).

21 Zhu, Y. T. & Lowe, T. C. Observations and issues on mechanisms of grain refinement during ECAP process. *Materials Science and Engineering: A* **291**, 46-53, doi:http://dx.doi.org/10.1016/S0921-5093(00)00978-3 (2000).

9. General conclusions and suggestions for future research

9.1. General conclusions

AccumEx is a novel SPD technique which has been studied for the first time in this thesis. The primary aim of this thesis was to evaluate the ability of the process to produce nano-structured materials – similar and dissimilar, and compare it with other SPD techniques. This was done with the help of experiments on the material combinations - Al-Al and Al-Cu. AccumEx is a new deformation technique and therefore understanding of the process and its effect on the material is crucial. This inspired to do a specific study which involved designing an experiment to quantify the deformation field imposed on the Al and further some specific characterization studies to correlate the derived deformation field with the microstructure and texture evolution of the Al-Al laminates. In the Al-Al AccumEx experiments, the material was deformed up to 8 deformation passes, which corresponds to an equivalent von-Mises value of 12.8. The grain boundary spacing of the material already reached a saturation of 400 nm after 4 passes and implied that an additional strain of almost 600 % had a negligible effect on the grain size. Few insights on this behavior were found in literature which inspired to take it as a topic of investigation. The main aspects of all the derived results will be summarised in this chapter.

Al-Al AccumEx

The first validation of AccumEx was done on AA 1050, commercially pure Al in which stacks of Al were deformed up to 8 passes of AccumEx at room temperature. Microstructural analysis showed that the average 3D grain size or the equivalent grain diameter was reduced from around 15 µm to 0.91 µm and the HAGB fraction was increased from 36 % to 70 %. Most of the grain refinement occurred during the first 4 passes, while between 4 and 8 passes, no major changes were noticed. Texture results showed that the average texture was mostly a typical plane strain compression texture till 4 passes and a combination of shear and plane strain compression texture after 4 passes. Micro-hardness saturated at around 70 HV after 4 passes and remained constant till 8 passes. Tensile results showed that the best properties were obtained after the first and second deformation passes. Above 4 passes, the samples failed catastrophically due to deterioration of the mechanical interfaces of the laminates. Use of higher reduction percentages and sample thicknesses in AccumEx showed a positive effect in the initial deformation passes by helping in achieving a robust mechanical bonding just after 1 and 2 passes. On the contrary, at higher deformation passes, the degree of heterogeneity increased and it directly affected the bonding of the mechanical interfaces by forming inter-lamellar volume defects. That in turn led to degradation of the material's mechanical properties. The study suggested that AccumEx was efficient in producing UFG microstructure in Al, but failed to produce mechanically robust samples, especially at higher strains. In many aspects, AccumEx is similar to ARB but at higher strains the process is not efficient.

Shear – a main component of the deformation field imposed by AccumEx

Although AccumEx is a largely plane strain compression process, shear was a major component in its deformation field. A new method – the embedded pin technique coupled with continuum mechanics was applied to derive the deformation field imposed by AccumEx on Al, during the first deformation pass. True compression and shear strains in the material were quantified and found to vary as a function of ND position or sample thickness position (along ED-ND plane). The magnitude of shear was nil at the centre of the sample and increased towards the surface of the sample. Further, at higher deformation passes, they accumulated as per position in the sample. Some important observations associated with this shear gradient were

(i) The B-H fibre, a new texture fibre was identified and proposed as an indication of the presence of shear or shear gradient. The presence of shear is normally visible in texture results as typical shear texture components – H, <111>//ND fibre (gamma), etc. In AccumEx also shear components (H) were visible, but only from 4 passes onwards (due to the accumulation of shear). The effect of shear on texture in the initial deformation passes was not clearly known. The correlation of the deformation field with the spatial micro-texture, measured after the first deformation pass revealed a rotation of texture components away from Bs and towards H (positive or negative), depending on the magnitude of shear and direction of the shear at the location of interest. This, at the bulk scale is averaged out and observed as a B-H fibre, when measured along the ED-ND plane. The length and the intensity of the B-H fibre changed with increasing number of deformation passes as the shear strain is accumulated.

(ii) The correlation of the grain size with the deformation field showed that after the first pass grain refinement was relatively faster at the surface and sub-surface of the Al-Al samples, where the shear is highest. After 2 passes, the effect of shear became negligible and the grain sizes were nearly homogeneous throughout the sample. However, it was learnt that shear begins to exhibit itself in other manners - inter-granular microscopic shear bands in the microstructure and inter-lamellar macroscopic shear bands at the interface regions, mostly clustered along the surface, sub-surface and half-mid thickness regions of the sample. They were formed due to the complex deformation path in the material and were regarded as the reason for the degradation of the mechanical bonding between the interfaces at higher deformation passes.

Grain size saturation – a microstructure accommodation phenomenon

A new ex-situ experiment was designed which coupled stepwise plane strain compression with EBSD characterization to monitor the microstructural response of a grain size saturated material to additional strains. A 4 pass pre-deformed Al-Al sample was deformed to additional strains of 11, 26 and 38 % and was spatially characterized for the microstructure evolution after each strain interval. Several interesting observations were made:

(i) It was learnt that grain size saturation can be visualized as an effect of few sequential microstructural events which involve shortening of grains, disappearance of grains and grain boundaries and re-arrangement of grain neighbors. The occurrence of such microstructural modifications helped in maintaining an almost constant grain size locally. Unlike the discussions that are seen in literature which describe the grain saturation behavior theoretically as an effect of dynamic recovery and dislocation interaction behavior, the current observations helped in relating the phenomenon directly at the level of microstructure.

(ii) Two mechanisms were identified as drivers for the above said microstructural modifications – grain splitting/pinching and triple junction motion. Grain splitting/pinching occurred in high aspect ratio grains and was facilitated by texture changes. The texture changes in turn were a resultant of inter and intra granular flow heterogeneity (shear) along ED in the ED-ND plane. Triple junction motion occurred at high aspect ratio grains with y-type triple junctions and small dihedral angles. It resulted in shortening of grains near the junction. The mechanism was proposed to be either a stress-assisted phenomenon or due to flow heterogeneity between grains along TD (a 3D-strain). The effect of triple junction motion on the grain(s) has been characterized as one of the type of dynamic recovery processes, which can be applicable for all lamellar materials. Both grain splitting/pinching and triple junction motion showed some dependency in their occurrence. The former helped in creating several triple junctions of large aspect ratio grains for the latter to materialize.

(iii) Rigid body rotation, a constituent of shear was characterized at the level of individual grains. It was correlated with the microstructure's morphological changes before and after the incremental strains, with the help of Taylor factor analysis.

(iv) The local deformation mode at the level of the microstructure was identified to be a combination of plane strain compression + shear with its axis around TD + extension along TD. They are not necessarily to be the same everywhere within the microstructure but qualitatively seem to vary depending on the grain orientation, grain morphology, grain boundaries and location with respect to the macroscopic deformation reference frame.

Al-Cu AccumEx

Al-Cu composites were fabricated in two different configurations – Cu-Al-Al-Cu (type 1) and Cu-Al-Cu-Al-Cu (type 2). The deformation was performed up to 4 passes and the microstructure, texture and mechanical properties were investigated for both Cu and Al. After 4 passes, the Cu part of the composite exhibited a coarser microstructure than Al, with an average grain size of 3 um and aspect ratio of greater than 8, and a typical plane strain compression texture. The Al part of the composite exhibited a UFG microstructure with grain sizes of around 1 µm. The texture was weak and almost random. The mechanical properties were good only till 2 passes. This is because the process could manage to fabricate a robust composite only till 2 passes and after 2 passes, the interface volume defects degraded the mechanical properties catastrophically. The dissimilar interfaces exhibited a detrimental effect rather than a strengthening effect on the composites. The general impression from the study was that AccumEx is not a suitable technique for producing UFG dissimilar materials.

The interaction of Al and Cu was an interesting aspect in the study. The difference in the strength properties and the strain hardening behavior between Al and Cu created flow heterogeneities at the Al-Cu interfaces. It led to strain differences between Al and Cu and led to generation of internal stresses. Thus, Cu fragmented into lens or boudins at 2 and above passes. Consequently, Al underwent over-straining over Cu. The microstructure and mechanical properties of Al became dependent on the local configuration of Cu boudins. Location dependent texture and negligible strain hardening in Al were examples of it. From literature review it was learnt that the behavior of a metal when deformed as a single material or co-deformed with dissimilar materials can be significantly different. It was explained with the help of examples of atomic scale and nano-scale interactions at extreme strains. However, from the current study the interactions were seen at micro and macro scale and already at medium strain levels. This indicates that irrespective of the size scale, the interaction behavior between the dissimilar materials during co-deformation can have a strong influence on the final properties of the composite of interest.

AccumEx vs ECAP

AccumEx in general imposed a higher rate of grain refinement and faster saturation in mechanical properties than ECAP. This was attributed to the difference in deformation modes between the two SPD techniques. In Al-Cu co-deformation both techniques exhibited complex material behavior, and it was regarded to be due to the interaction between the two materials during the deformation. Irrespective of the type of deformation being used, interaction of the dissimilar material is very dominant in deciding the final material properties of the composite.

9.2. Outlook and suggestions for future

(i) The study Al-Al AccumEx and the quantification of shear showed that an intense process induced strain in-homogeneity is present in the material and this affected the material’s integrity at higher deformation passes. This can be tackled by reducing the reduction % per deformation pass and/or reducing starting thickness of the sample being used (20 mm). A few follow up experiments were done using 66 % reduction per pass, keeping the sample thickness unchanged. The results were not positive and implied that the large initial sample thickness also needs to be re-designed to see an effect on the minimization of the strain in-homogeneities. This will require an extensive study on different combinations of reduction % and initial sample thicknesses. FEM based study can also be coupled with this to reduce experimental time.

(ii) AccumEx was performed on Al-Al laminates up to 8 deformation passes. Theoretically, the laminated material contains >65000 layers with an inter-laminate distance of ~80 nm. The measured average grain boundary spacing of the material was 400 nm which implied efficient material mixing at the interfaces. Literature suggests several theories for the occurrence of material mixing at interface regions, during extreme deformation. TEM-based studies

can help in investigating these theories and help getting insights in such non-equilibrium phenomena.

(iii) Use of embedded pin technique proved to be a promising way to map the mesoscopic deformation field in the material. It yields similar results as in FE modelling of the process. However from an experimental point of view. FEM cannot be applied to processes with extreme conditions due to the limitations in the method. Therefore, for such scenarios, this experimental technique can be helpful. Further, it will also be a useful tool in multi-scale modelling where the texture and microstructure evolution need to be directly correlated with the deformation field of the material. Multi-scale modelling requires a realistic representation of the process from micro to macro scale. From our study, it was learnt that the macroscopically applied deformation is not necessarily the same at the microscopic level. Therefore, use of embedded pin technique or derivative(s) of this technique will help in defining a realistic representation of the deformation process of interest.

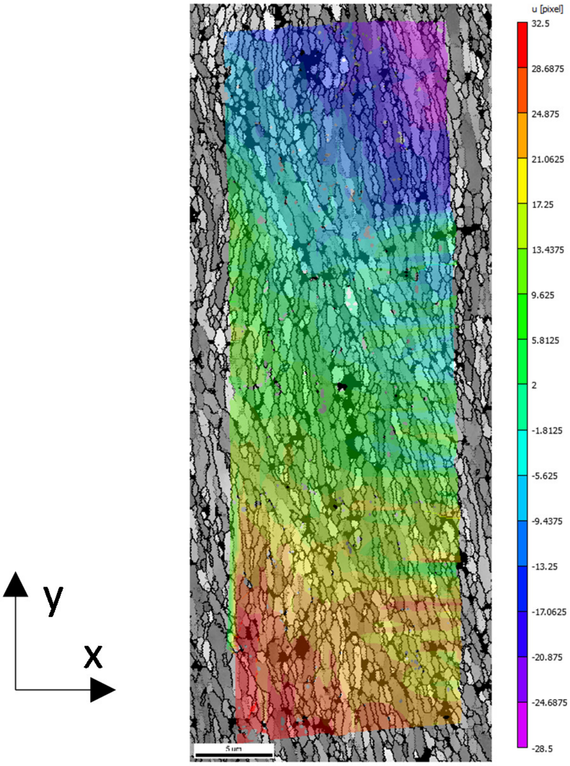

Figure 9-1 - Digital image correlation of the change in displacement (in µm) in the microstructure along x-axis after 9 % additional strain on 8 passes deformed sample.

(iv) It was learnt that interaction between grains are very critical at small grain sizes. The local resolved deformation mode is dependent on the grain orientations and the interactions. This is a complex observation which cannot be generalized. Several texture prediction models (ALAMEL, VPSC, etc.,) include interaction between grains and grain boundaries. However their accuracy could be found to be always in need for improvements. A proper statistical study on the different possibilities of interactions, as suggested in the current work, and their effects on local orientation changes will help in improving the predictability of the current models. Further, at different grain sizes, the interactions and their responses are different. For example, from a follow up study on 8 pass pre-deformed samples, it was learnt that additional strains result in some kind of rotational type of strain in the microstructure (an example Figure 9-1 is shown). Figure 9-1 shows a color map with displacement values of each pixel along x, measured by digital image correlation after 9 % strain increment. The displacement value within the selected region varies from -28 µm to +32 µm. The negative displacement is seen at the right top corner of the selected region, the positive displacement is seen at the left bottom corner of the selected region and almost a 0 displacement at the center. This approximately represents a rotational type displacement of the grains within the microstructure. Several reasons can contribute to it, even for example some misalignment in the positioning of the sample. Howsoever, this is a unique result. Understanding of such observations and exploiting such advanced techniques will open different ways of seeing the microstructural behavior of metals.

(v) The Al-Cu interaction behavior studied in this work is very complex and needs further understanding. Al showed negligible strain hardening behavior which was never reported in literature. The possible reasons were extended recovery and residual stresses. They were not studied in the current work. Extended recovery can help in reducing the dislocation density, however to achieve a drop of 50%, it cannot be a room temperature based phenomenon. In that case, it would be easier to evaluate this using a TEM study which can help understand the deformation structures in detail. Residual stresses are very high in co-deformation. Al is expected to undergo compressive residual stresses along ED while Cu tensile residual stresses. These stresses translate into other directions in different ways. They might influence the mechanical properties of the material. Therefore, a proper residual stress study (X-ray or neutron based) on Cu and Al at different deformation passes will give a better idea on the interaction between Al and Cu and possibly on its effect on Al's strain hardening properties.

APPENDICES

A. Different Severe Plastic Deformation techniques from literature [1,2]

Process name	Schematic process illustration	Process name	Schematic process illustration	Process name	Schematic process illustration
Equal Channel Angular Pressing (ECAP)	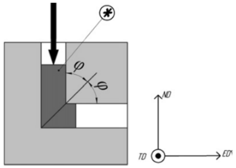	Repetitive Side Extrusion	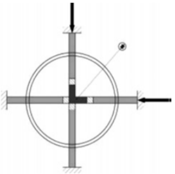	High Pressure Torsion (HPT)	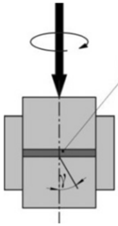
Rotary-die ECAP	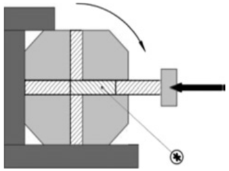	Accumulative Roll Bonding (ARB)	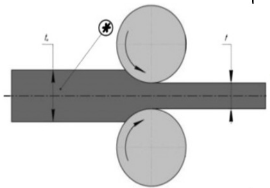	Cyclic Extrusion-Compression	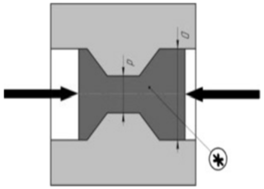

Process name	**Schematic process illustration**	**Process name**	**Schematic process illustration**	**Process name**	**Schematic process illustration**
Multi-axial Forging	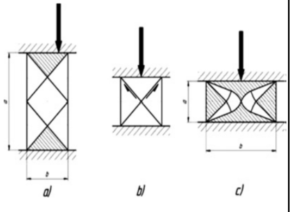	Cyclic Close Die Forging (CCDF)	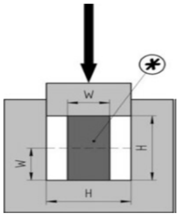	Twist Extrusion	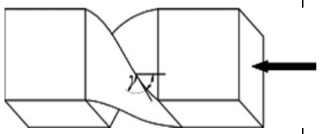
Repetitive Corrugated Pressing (RCS)	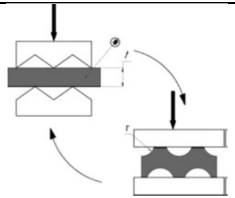	Integrated Extrusion + ECAP	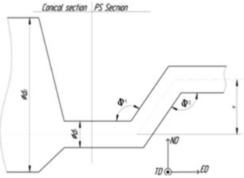	Parallel Channel ECAP (PC-ECAP)	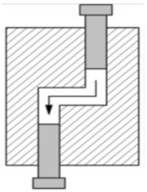

ECAP – Conform	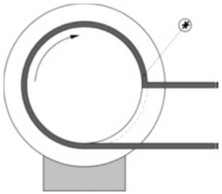	Con-shearing	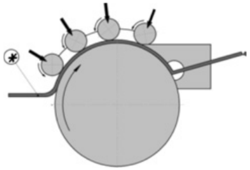	Continuous Confined Strip Shearing (C2S2)	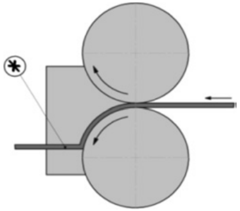
Process name	**Schematic process illustration**	**Process name**	**Schematic process illustration**	**Process name**	**Schematic process illustration**
Incremental – ECAP	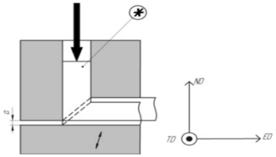	Continuous Repetitive Corrugating and Straightening (RCS)	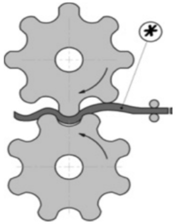	Tube Twisting	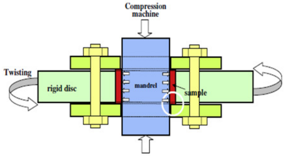

Continuous High-Pressure Torsion	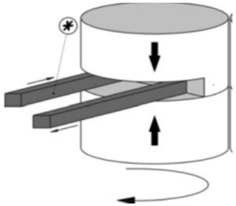	Asymmetric Rolling	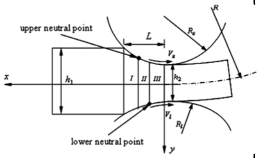	Equal Channel Angular Drawing (ECAD)	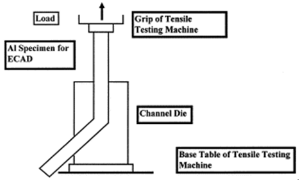
Accumulated Extrusion (AccumEx)	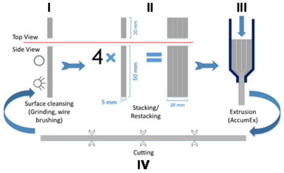				

REFERENCES

1 Estrin, Y. & Vinogradov, A. Extreme grain refinement by severe plastic deformation: A wealth of challenging science. *Acta Materialia* **61**, 782-817, doi:10.1016/j.actamat.2012.10.038 (2013).

2 Valiev, R. *et al.* Producing bulk ultrafine-grained materials by severe plastic deformation. *Journal of Materials Science* **58**, 33-39, doi:10.1007/s11837-006-0213-7 (2006).

B. Derivation of the velocity gradient and strain tensor

The position of the pin with respect to its co-ordinates can be written as,

$$x_1 = X_1\lambda_1 - \alpha\lambda_2^2 X_2^2 + C$$

$$x_2 = X_2\lambda_2$$

Where, λ_1, λ_2 and α are functions the dimensions of the pin and C is constant

The deformation gradient tensor is written as,

$$\mathrm{F} = \begin{bmatrix} \frac{\partial x_1}{\partial X_1} & \frac{\partial x_1}{\partial X_2} \\ \frac{\partial x_2}{\partial X_1} & \frac{\partial x_2}{\partial X_2} \end{bmatrix}$$

$$\mathrm{F} = \begin{bmatrix} \lambda_1 & -2\alpha\lambda_2^2 X_2 \\ 0 & \lambda_2 \end{bmatrix}$$

The values of F_{ij} can be calculated with the help of boundary conditions which are as follows,

(i) Constant volume

$$\det(F) = \lambda_1\lambda_2 = 1$$

$$\lambda_1 = \frac{1}{\lambda_2}$$

(ii) Relation between the initial and the final position
At,

$$dX = \begin{bmatrix} 0 \\ \frac{t_i}{2} \end{bmatrix} \Rightarrow dx = \begin{bmatrix} l_p \\ \frac{t_f}{2} \end{bmatrix}$$

We know that,

$$dx = FdX$$

This gives,

$$\lambda_2 t_i = t_f\ ;\ \lambda_2 = \frac{t_f}{t_i}$$

$$-2\lambda_2^2 t_f^2 \alpha = l_p;\ \alpha = \frac{-l_p}{2t_f^2}$$

Therefore, using the boundary conditions all the unknowns have been represented as a function of initial thickness, final thickness and the length of the extension. Now, the deformation tensor can be calculated as,

$$\mathrm{F} = \begin{bmatrix} \frac{t_i}{t_f} & -\frac{l_p}{t_i^2}X_2 \\ 0 & \frac{t_f}{t_i} \end{bmatrix}$$

The values of l_p, t_f, t_i are derived from the experiments as 20, 5 and 20 respectively.

Polar decomposition of F is given as

$$F = RU$$

Where, R is a rotational tensor and U is a right stretch tensor

The right Cauchy – Green deformation tensor is written as,

$$C = F^T F = U^2$$

$$U^2 = F^T F = \begin{bmatrix} \frac{1}{\lambda_2^2} & -2\lambda_2 \alpha X_2 \\ -2\lambda_2 \alpha X_2 & \lambda_2^2((2\alpha X_2)^2 + 1) \end{bmatrix}$$

The rotation tensor can be calculated as,

$$R = FU^{-1}$$

The true strain can be calculated as,

$$E_L = \ln(U)$$

Applying rotation,

$$E_{Lg} = R^T E_L \mathrm{R}$$

This implies, for each thickness position, the strain components will have different magnitude with respect to the choice of reference frame.

At X2 = 0

$$E_L = \begin{bmatrix} 1.39 & 0 \\ 0 & -1.39 \end{bmatrix}$$

$$E_{Lg} = \begin{bmatrix} 1.39 & 0 \\ 0 & -1.39 \end{bmatrix}$$

At X2 = 10

$$E_L = \begin{bmatrix} 0.73 & -1.35 \\ -1.35 & -0.73 \end{bmatrix}$$

$$E_{Lg} = \begin{bmatrix} 1.54 & -0.08 \\ -0.08 & -1.54 \end{bmatrix}$$

C. Prediction of Necking

In order to calculate the critical equivalent strain, ε_c and critical thickness reduction r_c for diffuse necking on the soft layer of the composite material during co-deformation the following equations can be used [1,2]

$$\varepsilon_c \geq \frac{n_h}{\sqrt{3}(1-H)\left(1-\frac{k_s}{k_h}\right)\varepsilon^{n_s-n_h}}$$

$$r_c = 1 - exp\left(-\frac{\sqrt{3}}{2}\right)\varepsilon_c$$

Where, ε_c is critical equivalent strain, H is initial thickness ratio of hard layer to total thickness of hard and soft layer, n_i and k_i denote the strain hardening exponent and the strength coefficient of soft ($i = s$) and hard layer ($i = h$) and ε is the applied compressive strain (1.38). The strain hardening exponent and the strength coefficient can be calculated using tensile test data fitted by Swift strain hardening law. The parameters for Cu and Al corresponding to pass 1 and pass 2 of AccumEx deformation are presented in Table 0-1. The plot of critical reduction vs critical equivalent strain is shown in *Figure 0-1*

Table 0-1 Swift parameters of Al and Cu obtained from tensile tests

Pass 1		**Pass 2**	
n_h	0.47	n_h	0.25
k_h	350	k_h	952
n_s	0.16	n_s	0.136
k_s	250	k_s	343.66

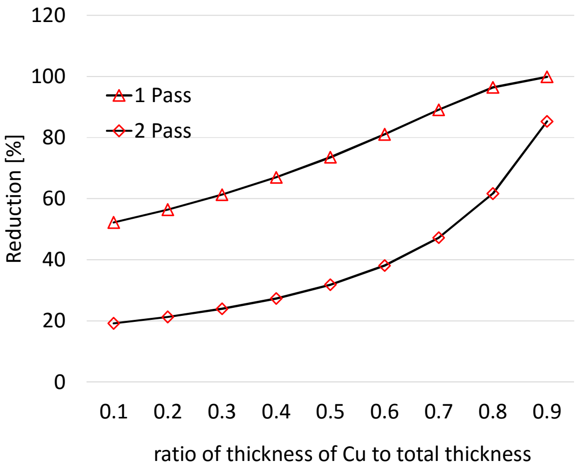

Figure 0-1 Critical reduction vs critical equivalent strain for AccumEx

REFERENCES

1 Hwang, Y.-M., Hsu, H.-H. & Lee, H.-J. Analysis of plastic instability during sandwich sheet rolling. *International Journal of Machine Tools and Manufacture* **36**, 47-62, doi:http://dx.doi.org/10.1016/0890-6955(95)92628-C (1996).

2 Nowicke, F., Zavaliangos, A. & Rogers, H. C. The effect of roll and clad sheet geometry on the necking instability during rolling of clad sheet metals. *International Journal of Mechanical Sciences* **48**, 868-877, doi:10.1016/j.ijmecsci.2006.01.021 (2006).

Curriculum Vitae

Gokula Krishna Muralidharan

Date of birth: 28-05-1989
Current address: Groenveldstraat 61/0201, 3001 Heverlee, Belgium
E-mail: mgkrishna89@gmail.com

Education background

PhD researcher 2012-2018
Department of Materials Engineering (MTM)
University of Leuven (KU Leuven)
Belgium
Thesis : Deformation behavior of Al-Al and Al-Cu laminated materials produced by Accumulated Extrusion

Master of Engineering 2010-2012
Department of Materials Engineering (MTM)
University of Leuven (KU Leuven)
Belgium
Thesis : Metallic Ceramics –MAX phase ceramics

Bachelor of Engineering 2006-2010
College of Engineering, Guindy Campus
Anna University Chennai
India

Professional Experience

Sr. Process Development Engineer, R&D 2017-present
3DSystems, Direct Metal Printing
Belgium

Researcher 2012-2017
Department of Materials Engineering (MTM)
University of Leuven (KU Leuven)
Belgium

List of Publications

Muralidharan, G. K. and B. Verlinden (2016). "Novel severe plastic deformation technique—accumulated extrusion (AccumEx)." Materials Science and Technology: **32**(6), 547-555.

Muralidharan, G. K. and B. Verlinden (2015). "AccumEx -- A New SPD Technique for Fabricating Lamellar Materials." Acta Physica Polonica, A **128**(4): 523.